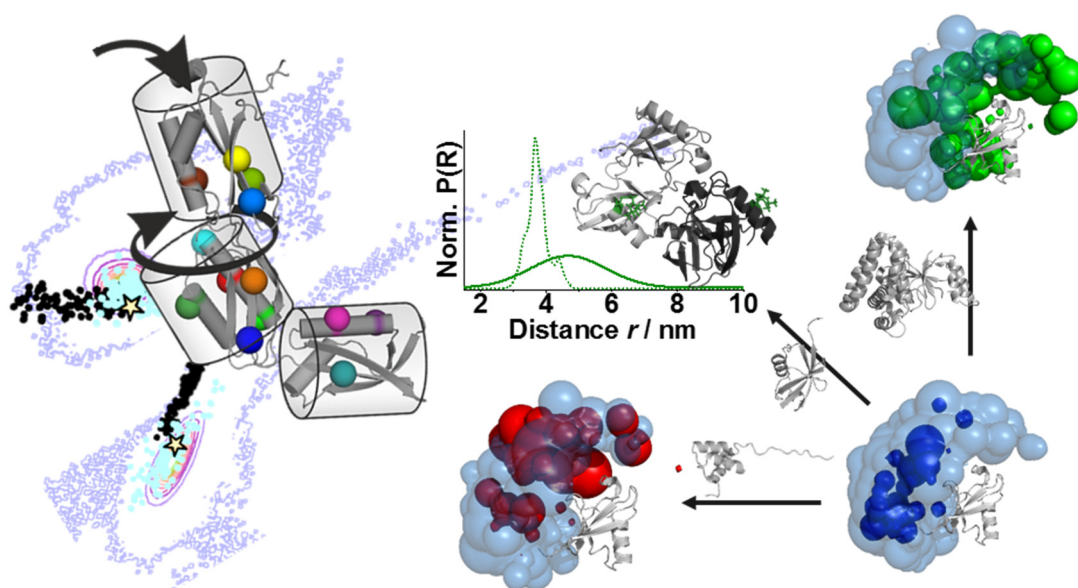


Conformational flexibility of multi-domain proteins determined by pulsed EPR spectroscopy

Bestimmung der konformellen Flexibilität von
multi-Domänen Proteinen mittels gepulster EPR Spektroskopie



Dissertation

zur Erlangung des Doktorgrades der Naturwissenschaften

vorgelegt beim Fachbereich 14

der

Johann Wolfgang Goethe-Universität Frankfurt am Main

von

Denise Schütz

aus Frankfurt am Main

Frankfurt am Main 2017

Denise Schütz

Geboren am 16.04.1986 in Frankfurt am Main

Matrikelnummer: 3148794

Dekan: Prof. Dr. Michael Karas

Gutachter: Prof. Dr. Thomas F. Prisner

Prof. Dr. Volker Dötsch

Datum der Disputation: 10.11.2017

*„Komm reg dich nich auf über Steine im Weg.
Wer hat denn gesagt das es einfach so geht und läuft es mal von selbst,
oh Mann dann bedank dich,
mach ‘n knicks und fall auf die Knie,
sei froh das Es von selber ging,
denn Sowas passiert selten bis nie”*

Ingo Pohlmann

Abstract

Structural biology often employs a combination of experimental and computational approaches to unravel the structure-function paradigm of biological macromolecules. This thesis aims to approach this combination by the application of Pulsed Electron-Electron Double Resonance (PELDOR/DEER) spectroscopy and structural modelling. In this respect, PELDOR spectroscopy in combination with site-directed spin labelling (SDSL) of proteins is frequently used to gain distance restraints in the range from 1.8 to 8 nm. The inter-spin distance and the flexibility of the spin labelled protein domains are encoded in the oscillation and the dampening of the PELDOR signal. The intrinsic flexibility of the commonly used MTSSL (1-Oxyl-2,2,5,5-tetramethylpyrroline-3-methyl) spin label itself can be an obstacle for structural modelling if the flexibility of the label is large compared to the flexibility of the protein domains. In this thesis the investigation of two multi-domain proteins by the 4-pulse PELDOR sequence is presented. At first, the N-terminal polypeptide transport-associated (POTRA) domains of *anaOmp85*, a rigid three domain protein, giving well-defined PELDOR distance restraints, is investigated. The experimental restraints are used for structure refinement of the X-ray structure and reveal a strong impact of the intrinsic flexibility of MTSSL on the accuracy of structural refinement. The second example, K48-linked diubiquitin, is a highly flexible multi-domain protein on which the flexibility of MTSSL is of minor impact on structural modelling. In this case, the distance restraints are utilized to determine conformational ensembles. Due to the high intrinsic flexibility already characterizing diubiquitin the recently developed 7-pulse Carr-Purcell (CP) PELDOR sequence was applied to investigate longer ubiquitin chains. This sequence enables to measure dipolar oscillations with an extended time window, allowing a good separation between inter- and intramolecular contributions even for long distance and broad conformational distributions, thereby providing an increased accuracy of the obtained distance distributions.

Corrections

Page 14,	Equation 2.18,	bracket before $\sin\theta$
Page 15	line 12-13	The rule of thumb for the maximal distances until which the mean distance between two spins A and B (Eq. 2.21) or the distribution width (Eq. 2.22) can be correctly determined for a given time window are [29]:
Page 15	Equation 2.21,	$r_{A,B}$ must be $r_{max, \langle r \rangle}$
	Equation 2.22,	$\sigma_{A,B}$ must be $r_{max, \sigma}$
Page 16	Figure 2.6	t should be T
Page 46	Figure 3.15, caption	(A,C,F) should be (B, D, F)
	line 7	(B,D,G) should be (C, E, G)
Page 107	Figure 6.18 C and F	σ_{max} should be $r_{max, \sigma}$
		r_{max} should be $r_{max, \langle r \rangle}$

Table of Contents

Abstract.....	i
Corrections	iii
Table of Contents	v
Chapter 1 Introduction.....	1
1.1 Motivation and Aim.....	4
Chapter 2 Theoretical Background.....	5
2.1 Electron Paramagnetic Resonance.....	5
2.2 Pulsed electron-electron double resonance spectroscopy.....	13
2.2.1 4-pulse PELDOR.....	13
2.2.2 7-pulse CP PELDOR.....	16
2.3 Data analysis.....	18
2.4 <i>In silico</i> prediction of inter-spin distances.....	21
Chapter 3 Results and Discussion	23
3.1 Cyanobacterial Omp85 POTRA domains – a rigid system.....	24
3.1.1 PELDOR distance restraints versus rotamer library-prediction.....	25
3.1.1.1 Validation of the intra-POTRA domain architecture.....	25
3.1.1.2 Relative domain-domain orientation in frozen liquid solution.....	29
3.1.2 Comparison to Molecular Dynamics Simulations.....	37
3.1.3 Influence of spin label flexibility on structure refinement.....	40
3.1.4 Conformational space of the refined ensembles and MD simulations.....	45
3.1.5 Relevance of the restricted flexibility of <i>ana</i> Omp85 POTRA domains	48
3.2 K48-linked ubiquitin chains – a flexible system	51
3.2.1 Identification of spin labelling sites with restricted flexibility.....	52
3.2.2 Conformational ensemble of the flexible K48-linked diubiquitin	53
3.2.3 Alterations of the conformational ensemble of K48-linked diubiquitin	57
3.2.3.1 Conformational selection upon Cue1 binding	59

3.2.3.2 Conformational remodelling upon OTUB1 binding	63
3.2.4 Influence of a large inter-domain flexibility on PELDOR restraints.....	65
3.2.5 Evaluation of the compact fold of tetraubiquitin	67
3.2.6 Conformational changes of highly flexible polyubiquitin chains.....	70
3.2.7 Relevance of the flexibility of K48-linked chains for recognition	72
Chapter 4 Conclusion and Perspectives	77
Chapter 5 Deutsche Zusammenfassung	83
5.1 Einfluss der Nitroxid-Marker Flexibilität auf Strukturverfeinerungen.....	84
5.2 Konformelle Ensembles von flexiblen multi-Domänen Proteinen.....	86
5.3 PELDOR an hoch flexiblen multi-Domänen Proteinen	87
5.4 Abschließende Diskussion und Ausblick	88
Chapter 6 Appendix	91
6.1 Supplemental Material	91
6.2 Materials and Methods	113
6.2.1 Sample preparation and purification.....	113
6.2.2 X-Band CW EPR Measurements.....	115
6.2.3 PELDOR Data Collection and Data Analysis	116
6.2.4 <i>In silico</i> prediction of PELDOR distance restraints.....	118
6.2.5 Structural Refinement of the X-ray structure of the POTRA domains.....	119
6.2.6 Generation of a structural ensemble of K48-linked diubiquitin	120
6.2.7 Molecular Dynamic simulations of POTRA domains	122
Bibliography.....	124
List of Amino Acids.....	138
List of Figures	139
List of Tables	143

Chapter 1

Introduction

More than 70% of the eukaryotic proteins [1], and especially membrane proteins, consist of multiple domains whose relative orientation and potential flexibility/rigidity are strongly associated with their function [2]. Thus, gathering structural and dynamical information is of utmost importance in unravelling the structure-function paradigm and in establishing an understanding of biochemical processes within all organic life forms. Several methods are available to address these questions, such as X-ray crystallography, SAXS¹, Cryo-EM², FRET³ NMR⁴- and EPR⁵-spectroscopy.

X-ray crystallography allows high resolution (0.12 nm) atomistic structure determination. Unfortunately, it is not possible to obtain information about structure and dynamics of molecules in their natural environment using X-ray structure analysis [3-5]. In addition, the inherent conformational flexibility of proteins, and especially of multi-domain proteins, hampers or even prevents crystallisation. This drawback is overcome by SAXS [6]. Here, a homogeneous dilute buffer solution of macromolecules, e.g. proteins, up to a size of several mega-Dalton can be investigated in real time enabling the determination of the entire conformational ensemble. However, this comes at the cost of low resolution (1-2 nm; [7]).

Cryo-EM has recently emerged as a frequently applied tool for structure determination of complex molecular structures. This is due to advances in detector hardware and image-processing software, which led to a tremendous increase of the resolution limit (~ 0.3 nm; [8]). Now it is possible to investigate molecular complexes of a molecular weight as low as ~135 kDa [9], and under perfect imaging conditions, a theoretical limit of 38 kDa is indicated [10]. Similar to SAXS the molecule of interest can be studied in a buffer solution, however with the restriction of fast freezing this solution to cryogenic temperatures. This results in a static picture of several conformations of e.g. multi-domain proteins.

¹ Small Angle X-ray Scattering

² Cryo-Electron Microscopy

³ Förster Resonance Energy Transfer

⁴ Nuclear Magnetic Resonance

⁵ Electron Paramagnetic Resonance; also ESR = Electron Spin Resonance

In contrast to the aforementioned techniques, NMR spectroscopy simultaneously yields atomistic structural and dynamical information [11, 12]. However, high resolution liquid state NMR is restricted to systems below ~ 50 kDa [13]. The drawback of the molecular size limit can be somewhat overcome by the application of SSNMR⁶ in combination with MAS⁷ [14]. The intrinsically low sensitivity of both liquid and SSNMR, due to the small energy splitting of the nuclear spin states and thus a small Boltzmann polarization, can be addressed by DNP⁸ [15]. DNP allows transferring the high polarization of an electron spin to a nuclear spin, e.g. ^1H or ^{13}C , thereby increasing the intensity of the NMR signal. Nevertheless, the usual technique to obtain inter-proton distance restraints is the NOESY experiment, yielding NOE⁹ restraints of less than 0.5–0.7 nm [16]. In order to obtain long-range orientational or distance restraint via NMR experiments, RDCs¹⁰ or PREs¹¹ (~ 3.5 nm) are detected, respectively. In the case of RDCs, the investigated protein needs to be embedded in an anisotropic medium, which provides partial alignment with respect to the external magnetic field and should exhibit a certain rigidity, in order to maintain anisotropy within the sample. Under these conditions, the angular orientation of e.g. the β -strands and the α -helix in ubiquitin with respect to the external magnetic field can be determined, which can be calculated back to the relative orientations of these secondary structure elements [17, 18]. The observation of PREs is only possible for proteins either containing a paramagnetic metal centre or artificially spin labelled, e.g. with the nitroxide label MTSSL¹². This technique is predominantly used to investigate low populated conformations ($\geq 1\%$) of conformational equilibria with a flat energy landscape [19]. Yet, two criteria have to be matched: (i) the distance between the electron spin and the relaxation enhanced nuclei in the low populated conformation needs to be significantly shorter than in the major conformation; (ii) the conformational exchange should be fast ($\tau_{exchange} < 250 \mu\text{s}$; [20]).

Complementary biophysical techniques to determine distance restraints are FRET [21] and EPR spectroscopy [22, 23], which do not depend on the size of the biomolecule under investigation. Yet, they are restricted to local information on either fluorophore or paramagnetic spin labels, respectively. The application of CW¹³ EPR allows the determination of distance up to 1.5 nm

⁶ Solid-State NMR

⁷ Magic Angle Spinning

⁸ Dynamic Nuclear Polarization

⁹ Nuclear Overhauser Effect

¹⁰ Residual Dipolar Couplings

¹¹ Paramagnetic Relaxation Enhancement

¹² 1-Oxyl-2,2,5,5-tetramethylpyrroline-3-methyl

¹³ Continuous Wave

[24, 25], while both FRET and pulsed EPR spectroscopy, e.g. PELDOR¹⁴ [26, 27], are able to determine long-range distances restraints in the range of 1.5-8 nm [28, 29], thus exceeding the distances restraints observable via NMR. In a FRET experiment, an acceptor and a donor fluorophore have to be attached to the biomolecule of interest via a flexible linker. The efficiency of the resonance energy transfer between the fluorophores is thereby dependent on the inter-fluorophore distances and orientation [21]. Nevertheless, due to the high sensitivity, these measurements can be accomplished on a single molecule.

Compared to FRET, EPR spectroscopy has several advantages. First, there is no need for two different labels, leading to a facilitated SDSL¹⁵ labelling scheme for the commonly used spin label MTSSL ([25, 30], Figure 1.1).

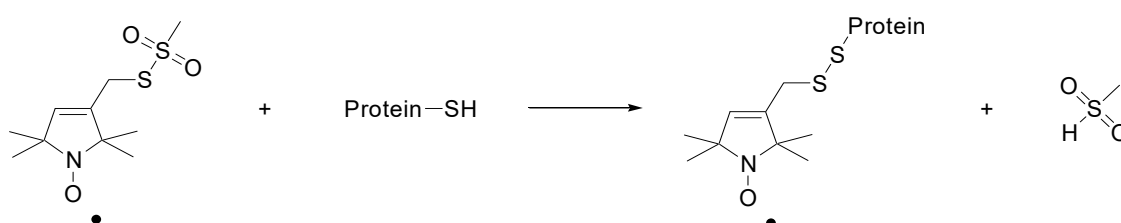


Figure 1.1: SDSL scheme of an EPR active label. The reaction of the MTSSL spin label with cysteine to generate the disulphide-linked nitroxide side chain to a protein. This labelling scheme is also utilized in PRE experiment.

Second, the labels are small compared to fluorescent tags and have a shorter linker, which increases the accuracy of the observed distance distributions. Furthermore, it has been shown that MTSSL introduces less or even no structural perturbations [31].

The collection of several PELDOR distance restraints in conjunction with structural modelling, utilizing programs like Modeller [32, 33], Rosetta [34, 35] or CYANA¹⁶ [36, 37], can yield relative domain-domain orientations, information about the type of motion underlying a conformational change as well as protein-protein interactions. However, the application of the restraints in structural modelling requires a suitable approximation of the intrinsic flexibility of the spin label. Other than for the fluorescent labels there have been many attempts to estimate the flexibility of either the free spin label [38] or of the spin label attached to a small peptide fragment or protein [31, 39-44] *in silico*. The most popular approach is the rotamer library-prediction.

Beside these experiment-based approaches, structural and especially dynamical investigations are nowadays often carried out by MD¹⁷ simulations [2]. A comparison of these simulations

¹⁴ Pulsed ELelectron-electron DOuble Resonance; also called Double Electron-Electron Resonance (DEER)

¹⁵ Site-Directed Spin Labelling

¹⁶ Combined Assignment and dYnamics Algorithm for NMR Applications

¹⁷ Molecular Dynamics

with the long-range restraints can further aid to identify the type of inter-domain motion, e.g. swing/hinge or twist.

1.1 Motivation and Aim

PELDOR spectroscopy in combination with SDSL of proteins is frequently used to obtain long-range distance restraints, which are hardly available by any other technique. The application of these distance restraints in structural modelling is particularly interesting in the case of multi-domain proteins to gain valuable information on the domain-domain orientation, conformational flexibility, and potential conformational changes. Yet, it has to be kept in mind that the distance restraints are measured between the unpaired electrons of two covalently attached flexible MTSSLs. This means that the experimental PELDOR signal comprises information on the domain-domain orientation only indirectly by means of inter-spin distances, the flexibility of the protein and the flexibility of the spin label linker. Thus, a combination of the flexibility of the spin label linker, a large intrinsic protein flexibility, and long inter-spin distances rises some challenges in terms of structure calculations and analysis of the experimental time traces, which might eventually affect the conclusions involving the structure-function paradigm.

These challenges shall be addressed in this thesis by the use of two different types of soluble multi-domain proteins. First, the influence of the accuracy of the *in silico*-predicted flexibility of MTSSL on structure refinement of the conformational space of a multi-domain protein will be elucidated by the three N-terminal POTRA¹⁸ domains from cyanobacterial Omp85 of *Anabaena sp.* PCC 7120¹⁹ (*anaOmp85*). Second, the capability of PELDOR spectroscopy to determine conformational ensembles of multi-domain proteins, and especially changes of these ensembles upon protein-protein interactions, shall be tested by the use of free and UBD²⁰ bound K48-linked diubiquitin to unravel distinct binding mechanisms. Furthermore, the experimental challenges arising from highly flexible proteins and large inter-spin distances shall be illustrated by K48-linked ubiquitin chains (> 2 ubiquitin moieties). Beside the challenges, it was possible to evaluate whether the compact fold of tetraubiquitin is the predominant conformation of this chain.

¹⁸ **P**Oly-peptide **T**Ransport Associated

¹⁹ *Anabaena species* Pasteur Culture Collection 7120

²⁰ Ubiquitin **B**inding **D**omain

Chapter 2

Theoretical Background

The theoretical background of EPR and especially PELDOR spectroscopy will be elucidated with in this chapter guided by standard textbooks and research/review articles [29, 45-48]. The nitroxide radical will be taken as an example to underline the descriptions, as it is the utilized radical in this thesis. In the case of EPR the spin system S - I is an intramolecular system, in which both spins I and S belong to the same molecule, for example, a ^{14}N nuclei ($I = 1$) and an electron spin ($S = 1/2$) within a nitroxide radical. In terms of dipolar EPR-spectroscopy, more precisely PELDOR spectroscopy, the dipolar interactions between neighbouring electron spins need to be considered. For this reason, the descriptive Hamiltonians and the relevant terms will be introduced and briefly discussed.

2.1 Electron Paramagnetic Resonance

The Total-Spin-Hamiltonian, Eq. 2.1, introduced by Abragam and Pryce [49, 50] describes the interactions of two electron spins S ($S=1/2$) with each other and the interaction of each of those electron spins S with a nuclear spins I ($I = 1$) in an external magnetic field.

$$\begin{aligned}
 \hat{H} = & \underbrace{\mu_B \vec{B} (g_A \hat{S}_A + g_B \hat{S}_B)}_{\text{Electron-Zeeman-Interaction}} - \underbrace{g_I \mu_I \vec{B} (\hat{I}_A + \hat{I}_B)}_{\text{Nuclear-Zeeman-Interaction}} + \underbrace{\hat{S}_A \underline{A} \hat{I}_A + \hat{S}_B \underline{A} \hat{I}_B}_{\text{Hyperfine-Interaction}} \\
 & + \underbrace{\hat{I}_A \underline{P} \hat{I}_A + \hat{I}_B \underline{P} \hat{I}_B}_{\text{Nuclear-Quadropol-Interaction}} + \underbrace{\hat{S}_A \underline{D}_{Dip} \hat{S}_B}_{\text{Dipol-Dipol-Interaction}} - \underbrace{2 \hat{J} \hat{S}_A \hat{S}_B}_{\text{Exchange-Interaction}}
 \end{aligned} \tag{Eq. 2.1}$$

In the course of this chapter, the six terms in Eq. 2.1 will be discussed in closer detail. At specific points, the descriptions will be explained using the example of a nitroxide radical.

The first two terms are the electron and nuclear Zeeman interactions.

The **electron-Zeeman term** describes the interaction of the electron spin characterized by the operator \hat{S} given by the Pauli spin matrixes

$$\hat{S}_x = \frac{1}{2} \begin{pmatrix} 0 & 1 \\ 1 & 0 \end{pmatrix}, \hat{S}_y = \frac{1}{2} \begin{pmatrix} 0 & -i \\ i & 0 \end{pmatrix}, \hat{S}_z = \frac{1}{2} \begin{pmatrix} 1 & 0 \\ 0 & -1 \end{pmatrix}$$

With an external magnetic field vector $\vec{B}_0 = (0, 0, B_0)$. μ_B , is the Bohr magneton²¹, which can be expressed as,

$$\mu_B = \frac{e\hbar}{2m_e} = \frac{\gamma_S \hbar}{g_e} \quad \text{Eq. 2.2}$$

Where e is the electron charge²² and m_e the electron mass²³. Eq. 2.2 further contains $\hbar = h/2\pi$, with h the Planck constant²⁴, and the gyromagnetic ratio²⁵ of an electron γ_S . For an electron within a molecule, this isotropic g-factor g_e ²⁶ can become anisotropic due to the distribution of the electron within the molecule. The g-factor must therefore be given as a tensor \underline{g} .

$$\underline{g} = \begin{pmatrix} g_{xx} & 0 & 0 \\ 0 & g_{yy} & 0 \\ 0 & 0 & g_{zz} \end{pmatrix} \quad \text{Eq. 2.3}$$

Within the principal axis system (PAS), which can be obtained via matrix transformation of the laboratory coordinate system using a rotation around the Euler angles $\Omega(\alpha, \beta, \gamma)$.

The splitting of the energy levels according to this interaction is shown in Figure 2.1. The energy difference of the two resulting energy-levels is given by

$$\Delta E = \underline{g}\mu_B |\vec{B}_0| \Delta m_s = h\nu \quad \text{Eq. 2.4}$$

Where m_s is the magnetic quantum number, can take two values $m_s = \pm 1/2$ as demonstrated by the Stern-Gerlach-Experiment [51, 52]. $|\vec{B}_0|$ in Eq. 2.4 is the external magnetic field in z-orientation.

²¹ $\mu_B = 9.274015 \cdot 10^{-24} \text{Am}^2$

²² $e = 1.602177 \cdot 10^{-19} \text{C}$

²³ $m_e = 9.109390 \cdot 10^{-31} \text{kg}$

²⁴ $h = 6.626076 \cdot 10^{-34} \text{J}$

²⁵ $\gamma_S = -1.760859644 \cdot 10^{11} \text{ s}^{-1}\text{T}^{-1}$

²⁶ $g_e = 2.002319$

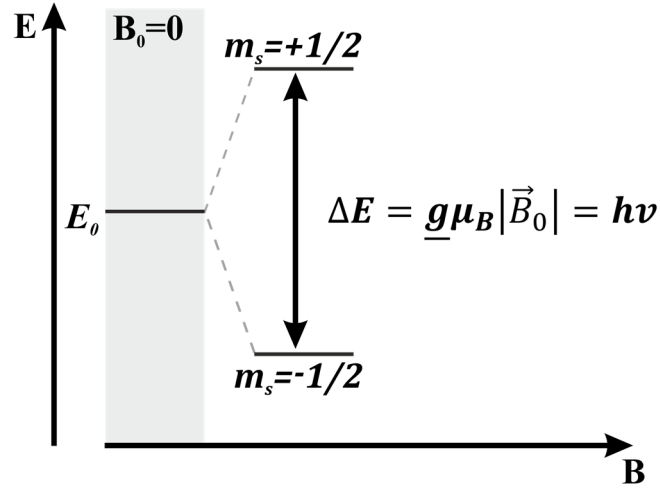


Figure 2.1: Electron-Zeeman splitting of the energy levels of an electron spin within a magnetic field. Indicating the magnetic quantum number m_s of each state and their energy difference.

Cw- or pulsed EPR can measure a resonance absorption by applying a continuous or a pulsed alternating electromagnetic field in the microwave region if the energy difference between the two states matches the selection rule $\Delta m_s = 1$. The first observation of this resonance absorption was made by Zavoisky in 1944. [53, 54]

In analogy, the **nuclear-Zeeman term** describes the interaction of the nuclear magnetic moments \hat{I} with the external magnetic field \vec{B} . The nuclear magneton is represented by μ_I and can be expressed by:

$$\mu_I = \frac{\gamma_I \hbar}{g_I} \quad \text{Eq. 2.5}$$

The nuclear-Zeeman interaction is predominantly relevant for NMR phenomena. It has no bearing on the description of the EPR experiments with the selection principles $\Delta m_s = \pm 1$ and $\Delta m_I = 0$, because it only leads to an equidistant displacement of the energy levels.

The third in Eq. 2.1 term is the **hyperfine interaction**, which consists of an isotropic part (*Fermi-contact-interaction* [55]) and an anisotropic part (*dipole-dipole-interaction* between nuclear spin I and electron spin S).

$$\hat{H}_{\text{Hyperfine}} = \hat{H}_{N,\text{Fermi}} + \hat{H}_{N,\text{Dip}} = \hat{\underline{S}} \hat{\underline{A}} \hat{\underline{I}} \quad \text{Eq. 2.6}$$

The **Fermi-contact-interaction** arises from the electron density $|\psi_0(r=0)|^2 > 0$ at a particular nucleus. This is usually limited to an s-Orbital. However, if the electron resides in a

p-Orbital, e.g. in a nitroxide residue, significant isotropic interactions can be caused by configuration interactions or spin polarization mechanisms [46]. The interaction is independent of the relative orientation of the molecule to the external magnetic field.

$$\hat{H}_{N,Fermi} = A_{iso} \hat{S} \hat{I} \quad \text{Eq. 2.7}$$

The isotropic hyperfine coupling constant A_{iso} is given as

$$A_{iso} = \frac{2\mu_0}{3\hbar} \mu_B \mu_I g_e g_I |\psi_0(\mathbf{r} = \mathbf{0})|^2 \quad \text{Eq. 2.8}$$

With μ_0 is the permeability of vacuum.

The anisotropic part of the hyperfine term occurs from the **dipole-dipole interaction** of the nuclear spin I and the electron spin S .

$$\hat{H}_{N,Dip} = \hat{S} \underline{T} \hat{I} \quad \text{Eq. 2.9}$$

The dipolar coupling tensor components T_{ij} are given by the following equation

$$T_{ij} = \frac{\mu_0}{4\pi\hbar} \mu_B \mu_I g_e g_I \left\langle \psi_0 \left| \frac{3r_i r_j - \delta_{ij} r^2}{r^5} \right| \psi_0 \right\rangle \quad \text{Eq. 2.10}$$

where r_i and r_j are components of the interconnecting electron nucleus vector and ψ_0 is the ground state wave function. In this case, the tensor \underline{T} is traceless and neglects spin orbit coupling. Taking into account that the magnetic moment of the nuclear spin I is small, we have to consider that their interactions are much weaker than those of the electron spin S .

The combination of the isotropic and the anisotropic part leads to the overall hyperfine-coupling tensor \underline{A} .

$$\underline{A} = A_{iso} \underline{1}_3 + \underline{T} \quad \text{Eq. 2.11}$$

$\underline{1}_3$ is a (3x3) unit matrix and A_{iso} is given as:

$$A_{iso} = \frac{1}{3} (A_{xx} + A_{yy} + A_{zz}) = \frac{1}{3} \text{Tr}(\underline{A}) \quad \text{Eq. 2.12}$$

The hyperfine term of the Hamiltonian has to be included for each coupled nuclei.

In the case of a nitroxide radical, e.g. MTSSL, A_{iso} is found to be larger than the Larmor Frequency of the ^{14}N nucleus resulting in the energy-level scheme represented in Figure 2.2A.

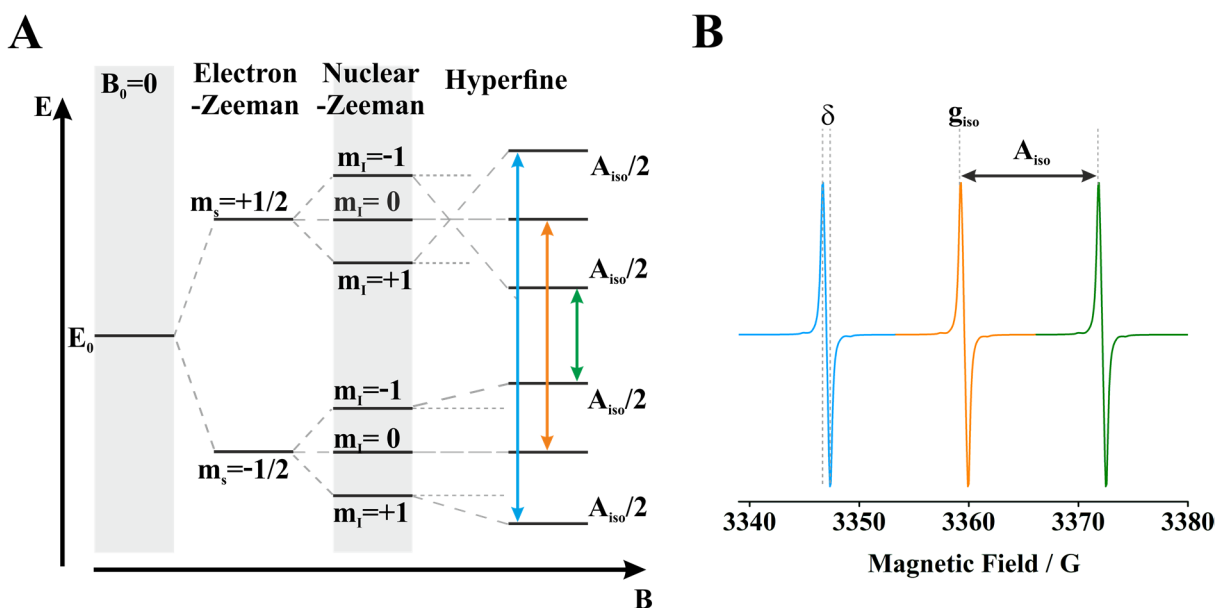


Figure 2.2: Interactions of the electron spin $S = 1/2$ in a nitroxide radical with the nuclear spin I of ^{14}N ($I=1$). A) Energy-level-diagram for a nitroxide radical, indicating the three resonance transitions (blue, orange, and green). B) CW EPR-spectrum of a nitroxide radical under fast motion with the isotropic g -tensor g_{iso} and the isotropic hyperfine coupling A_{iso} and the linewidth δ .

Irradiation with monochromatic microwaves²⁷ and a sweeping magnetic field at room temperature leads to an absorption spectrum when the resonance condition is full-filled. Yet, the usually detected CW EPR spectrum is the first derivative of this absorption-spectrum, due to field modulation and phase sensitive detection (Figure 2.2B). The cw-EPR spectrum already contains information about the surrounding and the dynamics of a nitroxide radical. For measurements accomplished at X-band (~ 9.5 GHz), like in this work, the anisotropy of the hyperfine interaction dominates the dynamic effects in the spectrum. In the case of fast dynamics (rotational correlation time $\tau_r \leq 10^{-9}$ s; [25]), the \underline{g} - and \underline{A} -tensor (Eq. 2.3 and 2.11) are averaged to the isotropic values g_{iso} and A_{iso} and the line-width δ , becomes equal for all three lines (Figure 2.2B). In the case of slow motion ($10^{-9} \leq \tau_r \leq 10^{-6}$ s; [25]), e.g. radical attached to a protein, the random orientation of the molecules with respect to the magnetic field has to be taken into account. Each statistical oriented radical gives a spectral line at a certain position according to its orientation with respect to the magnetic field. The observed spectrum is broad due to the interference of the lines of all radicals (Figure 2.3). Within this regime the complete

²⁷ The Zeeman-splitting of the energy levels typically corresponds to the typically used EPR magnetic field strength energies in microwave range.

g-tensor as well as the complete hyperfine coupling A have to be taken into account. The maximum of this anisotropic spectrum bears several orientations.

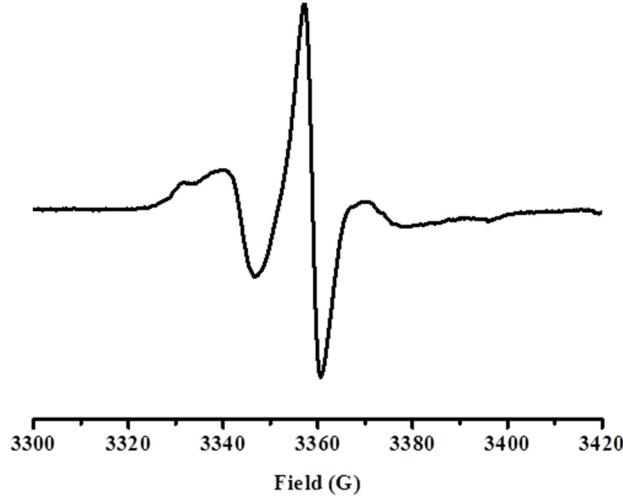


Figure 2.3: Anisotropic CW EPR spectrum of the nitroxide spin label MTSSL attached to a protein.

The fourth term of the Hamiltonian is the **nuclear-quadrupole interaction**. If a nucleus has a spin $I > 1/2$ and the distribution of an electron density different from spherical symmetry quadrupole interactions occur. This interaction leads to a shift of the nuclear spin sublevels on the magnetic field axis. In the case of a nitroxide radical analysed at X-band, this shift is negligible. Therefore, this term of the spin Hamiltonian does not have to be taken into account.

The two terms **dipole-dipole interaction** and **exchange interaction** in Eq. 2.1 can be summed up as **electron-spin-spin interactions**, which occur when paramagnetic centres/molecules are relatively close to each other.

The **dipole-dipole interaction** of two electron spins is the foundation for the dipolar spectroscopy utilized in this thesis. Given that the point-dipole-approximation²⁸ is valid, the interaction can be written as:

$$\hat{H}_{DD} = \frac{\mu_0 g_A g_B \mu_B^2}{4\pi\hbar} \left[\frac{\hat{\mathbf{S}}_A \hat{\mathbf{S}}_B}{|\vec{r}_{A,B}|^3} - \frac{3(\vec{r}_{A,B} \hat{\mathbf{S}}_A)(\vec{r}_{A,B} \hat{\mathbf{S}}_B)}{|\vec{r}_{A,B}|^5} \right] = \hat{\mathbf{S}}_A \underline{\underline{D_{Dip}}} \hat{\mathbf{S}}_B \quad \text{Eq. 2.13}$$

The interaction is inversely proportional to $|\vec{r}_{A,B}|^3$ and thus can be used for the determination of the distance between two electron spins.

²⁸ Distance between spins is larger than the width of distribution.

The relative orientation of the two electron spins \hat{S}_A and \hat{S}_B is commonly defined by the spherical coordinates θ , ϕ and $\vec{r}_{A,B}$. Therefore, Eq. 2.13 is often state as:

$$\hat{H}_{DD} = \frac{\mu_0 g_A g_B \mu_B^2}{4\pi\hbar} \frac{1}{|\vec{r}_{A,B}|^3} (\hat{A} + \hat{B} + \hat{C} + \hat{D} + \hat{E} + \hat{F}) \quad \text{Eq. 2.14}$$

The terms $\hat{A} - \hat{F}$, are the dipolar alphabet given in Table 2.1.

Table 2.1: Dipolar alphabet. The difference of the magnetic quantum number ΔM describes the character of the EPR-transition: $\Delta M = \pm 1$ are single-quantum transitions and $\Delta M = \pm 2$ are double-quantum transitions. $\hat{S}_+ = \hat{S}_x + i\hat{S}_y$ and $\hat{S}_- = \hat{S}_x - i\hat{S}_y$ are the raising and lowering operator, respectively.

Term	Operator	Orientation	ΔM
\hat{A}	$\hat{S}_z^A \hat{S}_z^B$	$(1 - 3\cos^2\theta)$	0
\hat{B}	$-\frac{1}{4}(\hat{S}_+^A \hat{S}_-^B + \hat{S}_-^A \hat{S}_+^B)$	$(1 - 3\cos^2\theta)$	0
\hat{C}	$-\frac{3}{2}(\hat{S}_+^A \hat{S}_z^B + \hat{S}_z^A \hat{S}_+^B)$	$\sin\theta\cos\theta \cdot e^{-i\phi}$	+1
\hat{D}	$-\frac{3}{2}(\hat{S}_-^A \hat{S}_z^B + \hat{S}_z^A \hat{S}_-^B)$	$\sin\theta\cos\theta \cdot e^{i\phi}$	-1
\hat{E}	$-\frac{3}{4}(\hat{S}_+^A \hat{S}_+^B)$	$\sin^2\theta \cdot e^{-2i\phi}$	+2
\hat{F}	$-\frac{3}{2}(\hat{S}_-^A \hat{S}_z^B)$	$\sin^2\theta \cdot e^{2i\phi}$	-2

Upon application of an external magnetic field \vec{B}_0 , which is significantly larger than D_{Dip} (high-field approximation) only terms \hat{A} and \hat{B} have to be considered for the description of dipolar spectroscopy experiments. In addition, for a spin system, e.g. a doubly nitroxide labelled protein, within the weak coupling limit²⁹ and the quantization of the two electron spins along the direction of \vec{B}_0 only term \hat{A} has to be taken into account. Thus, Eq. 2.13 reduces to:

$$\hat{H}_{DD} = \underbrace{\frac{\mu_0 g_A g_B \mu_B^2}{4\pi\hbar} \frac{1}{|\vec{r}_{A,B}|^3}}_{\omega_D} \cdot (1 - 3\cos^2\theta) \cdot \hat{S}_z^A \hat{S}_z^B \quad \text{Eq. 2.15}$$

Thereby, ω_D is the dipolar coupling frequency:

$$\omega_D = 2\pi\nu_D \quad \text{Eq. 2.16}$$

²⁹ $|\omega_{S_A} - \omega_{S_B}| \gg D_{Dip}$

Implementing the dipolar coupling constant D_{Dip} 15 becomes:

$$\hat{H}_{DD} = \frac{D_{Dip}}{|\vec{r}_{A,B}|^3} \cdot (1 - 3\cos^2\theta) \quad \text{Eq. 2.17}$$

The value of D_{Dip} is $2\pi \cdot 52 \text{ MHz/nm}^3$, with $g_A = g_B = g_e = 2$.

Form Eq. 2.17 it is obvious that ω_D varies from $\frac{-2D_{Dip}}{r_{A,B}^3}$ to $\frac{+D_{Dip}}{r_{A,B}^3}$.

This is true for a rotation of dipolar axis r parallel ($\theta = 0^\circ$) and perpendicular ($\theta = 90^\circ$) to the external magnetic field \vec{B}_0 . Additionally Eq. 2.17 reveals the absolute value of the dipolar interaction is zero in the case of a random orientation of a molecule [56], e.g. which is rotating very fast in comparison to the inverse coupling strength. Furthermore the dipolar interaction disappears for the magic angle of $\theta = 54.7^\circ$.

For a given orientation of the molecule, e. g. a single crystal, the dipolar coupling of the two electron spins leads to a splitting of the EPR line (Figure 2.4A). In contrast to that, spectra of frozen samples show a superposition of spectra taken from randomly distributed biradicals. The spectrum taken from randomly oriented biradicals is called Pake pattern (Figure 2.4). The distance between the edges of the spectrum matches the dipolar coupling of molecules with an angle of $\theta = 0^\circ$. The distance between the laces is the dipolar coupling of molecules with an angle of $\theta = 90^\circ$.

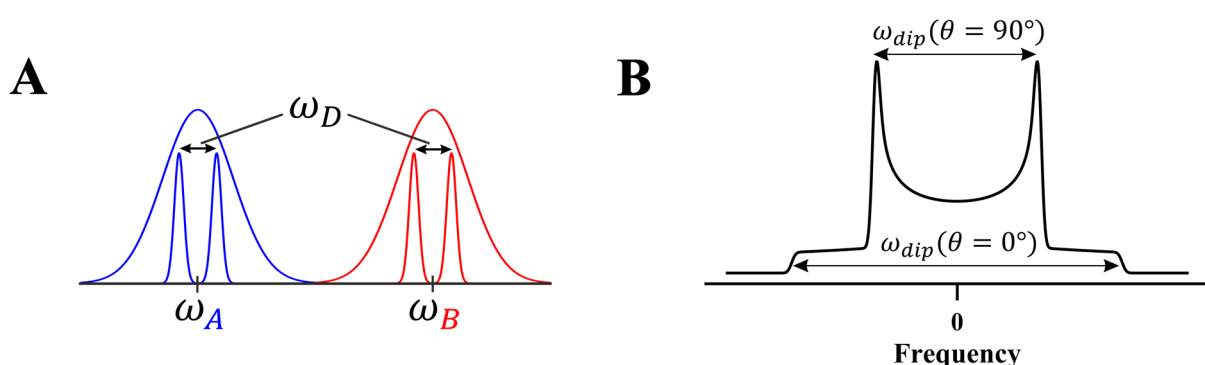


Figure 2.4: The effect of the dipolar coupling between two electron spins A and B. A) Schematic CW EPR spectrum of two dipolar coupled electron spins A and B, whose splitting is covered by the inhomogeneous/natural linewidth. B) Simulated Pake pattern for a spin $S=1/2$. Arrows indicate the splitting between the two peaks $\omega_D(\theta = 90^\circ)$ and the two edges $\omega_D(\theta = 0^\circ) = 2\omega_D(\theta = 90^\circ)$. In the case of pulsed EPR experiments like PELDOR the peaks appear at $\pm\omega_D$ and $\pm 2\omega_D$.

Unfortunately, in the case of spin labelled biomolecules, the splitting is in the case of CW EPR often covered by the inhomogeneous line broadening, due to relatively large inter-spin distances

($r > 1.5\text{-}2\text{ nm}$). In order to resolve this interaction pulsed EPR methods like Pulsed Electron-Electron Double Resonance spectroscopy needs to be applied (Chapter 2.2).

If the distance between the paramagnetic centres is smaller than 1 nm or for the case that conjugated bridges appear between the radicals the **exchange interaction J** has to be taken into account. In the course of this thesis, this interaction can be neglected, due to the usage of disulphide-linked nitroxide spin labels, which were used as markers to investigate multi-domain proteins. The disulphide bond prevents the distribution of electron spin density within the system. In addition, the labelling positions were chosen such that distance shorter than 1 nm are rather unlikely.

2.2 Pulsed electron-electron double resonance spectroscopy

Since the introduction of PELDOR by Milov in 1981 [26, 57] it is possible to separate the dipolar coupling from line-broadenings and other effects like separated hyperfine couplings and the anisotropy of the g -tensor. [26, 27] This method allows the determination of long-range distances and their distribution in spin labelled macromolecules. Thus, providing valuable information on conformational changes [58, 59] as well as distance restraints (1.8 nm to 6–10 nm in deuterated samples) for structural modelling [34, 35, 60-63].

2.2.1 4-pulse PELDOR

The 4-pulse PELDOR experiments [64, 65] were performed with the sequence shown in Figure 2.5.

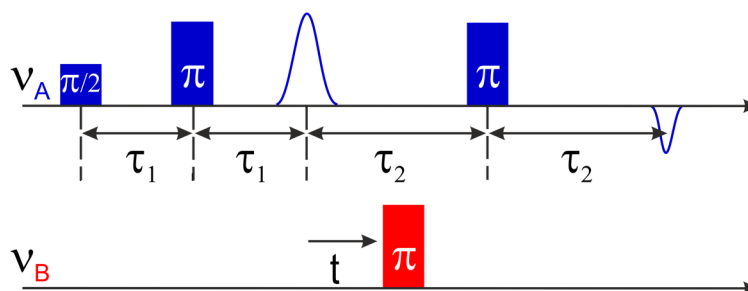


Figure 2.5: Dead-time free 4-pulse PELDOR sequence. This sequence is an extension of the 3-pulse PELDOR sequence, which was introduced by Milov in 1981.

The sequence consist of pulses with detection frequency ν_A and and a pump frequency ν_B . The spins influenced by ν_A are called observer spins (A) whereas those influenced by ν_B are called pumped spins (B). In the course of biological applications like in this work the A and B spins are provide by identical nitroxide spectra, whose differentiation is achieved by the large A_{zz} hyperfine component of ~ 34 G. To obtain an optimum pumping efficiency the pump frequency usually coincides with the maximum of the nitroxide powder spectrum for a given spectrometer frequency (e.g. X-band (~ 9.5 GHz) or Q-band (~ 33 GHz)).

The detection sequence (frequency ν_A) of the 4-pulse PELDOR experiment is a refocussed Echo-sequence. The 90° pulse ($\pi/2$ -pulse) in the beginning of the sequence flips the equilibrium magnetization (z magnetization) of the spins A into the transversal plane. During the time interval τ_1 the spins start to precess with different frequencies dependent on the inhomogenty of nitroxide spectrum. Due to the second pulse of 180° (π -pulse) the magnetization is refocussed. Within the subsequent interval τ_1 a primary Echo is built up. The π -pulse in the pump sequence (frequency ν_B) is applied a time t after the first pulses, selectively inverts the B spins within the system. This inversion leads to a change of the local magnetic field of the A spins or their Lamor frequency of $\pm\omega_D$ respectively. This results in a different transversal precession of the A spins and therefore in a non-perfectly refocused Hahn-Echo. Due to this dependence, the detected signal $V(t)$ is the product of the echo in the absences of dipolar interactions V_0 and the periodic modulation according to the time t of the pump pulse. In the case of proteins labelled with MTSSL, in a first approximation no orientation selection is to be expected, due to the flexibility of the spin label and biomolecule. Thus, the signal can be described as an average over all orientations.

$$V_{intra}(t) = \iint V_0(1 - \lambda_B + \lambda_B \cos(\omega_D t) \sin\theta) \cdot P(r) d\theta dr \quad \text{Eq. 2.18}$$

With λ_B being the inversion efficiency of pump pulse (for further information see chapter 2.3).

This signal, usually called dipolar evolution function or time trace, is dominated by the oscillation with the angular frequency ω_D ($\theta = 90^\circ$). Applying a Fourier-transformation to the observed signal one obtains the Pake pattern (Figure 2.4). The observed time trace is characterized by a fast damping of the dipolar oscillations. In the case of the flexible nitroxide radical, MTSSL, this damping is due to the distribution of r .

Up to this point, only two dipolar coupled electron spins within one molecule were considered. However, within a macroscopic sample not only the intramolecular $V_{intra}(t)$ (Eq. 2.18) but also the intermolecular $V_{inter}(t)$ interactions contribute to the observed 4-pulse PELDOR signal $V(t)$. [57, 66, 67]

$$\mathbf{V}(t) = \mathbf{V}_{intra}(t) \cdot \mathbf{V}_{inter}(t) \quad \text{Eq. 2.19}$$

For soluble proteins /molecules in solution a three dimensional distribution can be assumed. Furthermore, with the negligence of excluded volumes $V_{inter}(t)$ can be described as:

$$\mathbf{V}_{inter}(t) = e^{\left(-\frac{2\pi g_A g_B \mu_B^2 \mu_0}{9\sqrt{3}\hbar} c \lambda_B t\right)} \quad \text{Eq. 2.20}$$

with c is the radical concentration in m^{-3} [68].

In the case of a large conformational flexibility of a biomolecule and/or long inter-spin distances ($> 6\text{nm}$) the differentiation between $V_{intra}(t)$ and $V_{inter}(t)$ contributions becomes ambiguous for shorter time windows. The rule of thumbs for the correct determination of a distance $r_{A,B}$ (Eq. 2.21) or distribution width $\sigma(r_{A,B})$ (Eq. 2.22) for a given time window are [29]:

$$r_{A,B} = 5 \cdot \sqrt[3]{\frac{\text{time window}}{2\mu\text{s}}} \text{nm} \quad \text{Eq. 2.21}$$

$$\sigma(r_{A,B}) = 4 \cdot \sqrt[3]{\frac{\text{time window}}{2\mu\text{s}}} \text{nm} \quad \text{Eq. 2.22}$$

In order to overcome this drawback a recently developed 7-pulse CP³⁰ PELDOR sequence [48] can be utilized, substantially prolonging the observation time window and thereby increasing the upper limit and accuracy of the observable distance distributions.

³⁰ Carr-Purcell

2.2.2 7-pulse CP PELDOR

The 7-pulse CP PELDOR [48] experiments were performed with the sequence shown in Figure 2.6. This chapter is a short narration of the technique presented in [48]

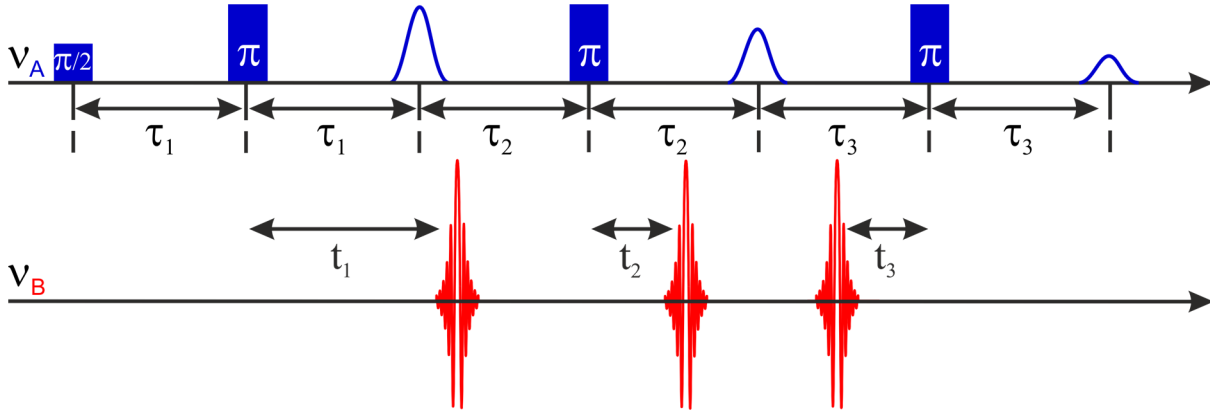


Figure 2.6: 7-pulse CP PELDOR sequence. This sequence is an extension of the dead-time free 4-pulse PELDOR sequence [65]. The sequence uses sech/tan pulses instead of classical rectangular pulses as pump pulse. In addition, the sequence is extended by three pulses (an additional refocusing pulse in the detection sequence, creating a CP sequence, (operating on ν_A) and two pump pulses (operating on ν_B)).

As the conventional 4-pulse PELDOR [65] the 7-pulse CP PELDOR [48] is a double frequency technique consisting of a detection frequency ν_A and a pump frequency ν_B .

The detection sequence (frequency ν_A) of the 7-pulse CP PELDOR sequence is a Carr-Purcell sequence, which uses a series of three rectangular refocussing pulses. For a maximal intensity of the refocussed echo at the end of the CP sequence the delay times τ_1, τ_2, τ_3 are of approximately the same length. This allows a prolongation of the observable time window of the dipolar evolution. The pump sequence (frequency ν_B) consists of three sech/tan pulses, which accompany the three refocussing pulses of the detection sequence. The sech/tan pulse shape is necessary to obtain a uniform inversion efficiency of the pump pulses compared to conventional rectangular pulses. The first and second pump pulse, are applied after a time T_1 or T_2 after the first and second refocussing pulse, respectively. The third pump pulse is applied at a time T_3 before the last refocussing pulse to prevent an overlap of the pump pulse with the detected echo. The time axis, t , of the experiment is given as:

$$t = \tau_1 + \tau_2 + \tau_3 - (|T_1| + |T_2| + |T_3|) \quad \text{Eq. 2.23}$$

As for the conventional 4-pulse PELDOR sequence, the observed signal is a product of intra- and intermolecular contributions (Eq. 2.19). However, the multiple pump pulses lead to an

increased number of dipolar pathways and thus a complicated intermolecular decay function. This is because not every B spin that has been inverted by the first pulse is again inverted by one or both following pump pulses. In total seven pathways may occur with different weights and the following phases:

$$\begin{aligned}\varphi_{1\bar{2}\bar{3}} &= (|\tau_1 - T_1|)\omega_D, \varphi_{\bar{1}2\bar{3}} = (|\tau_2 - T_2|)\omega_D, \varphi_{\bar{1}\bar{2}3} = (|\tau_1\tau_3 - T_3|)\omega_D, \\ \varphi_{\bar{1}\bar{2}3} &= (|\tau_1 + \tau_2 - T_1 - T_2|)\omega_D, \varphi_{1\bar{2}3} = (|\tau_2 - T_1 - T_2|)\omega_D, \\ \varphi_{\bar{1}23} &= (|\tau_2 + \tau_3 - T_2 - T_3|)\omega_D \text{ and } \varphi_{123} = (|\tau_2 + \tau_3 - T_2 - T_3|)\omega_D; \text{ the pure 7-pulse} \\ &\text{CP PELDOR signal.}\end{aligned}$$

Thus the intra- and intermolecular signal are:

$$\begin{aligned}V_{intra}(t) &= \lambda_B \bar{p}^2 (\cos(\varphi_{1\bar{2}\bar{3}}) + \cos(\varphi_{\bar{1}2\bar{3}}) + \cos(\varphi_{\bar{1}\bar{2}3})) + \\ &\lambda_B p \bar{p} (\cos(\varphi_{1\bar{2}3}) + \cos(\varphi_{\bar{1}23}) + \cos(\varphi_{\bar{1}\bar{2}3})) + \\ &\lambda_B p^2 (\cos(\varphi_{123})) + 1 - \lambda_B\end{aligned} \quad \text{Eq. 2.24}$$

With λ_B the fraction of B spins inverted by one pump pulse, p the probability of a B spin being inverted by a second pump pulse and $\bar{p} = 1 - p$.

$$V_{inter}(t) = \exp\left(-\lambda_B \frac{2\pi g_A g_B \mu_B^2 \mu_0}{9\sqrt{3}\hbar} cS\right) \quad \text{Eq. 2.25}$$

With c the radical concentration and S being defined as:

$$\begin{aligned}S &= \bar{p}^2 (|\tau_1 - |T_1|| + |\tau_2 - |T_2|| + |\tau_3 - |T_3||) + \\ &p \bar{p} \left(|\tau_1 + \tau_2 - |T_1| - |T_2|| + |\tau_3 - \tau_1 + |T_1| - |T_3|| \right) + \\ &p^2 (|\tau_1 + \tau_2 + \tau_3 - |T_1| - |T_2| - |T_3||)\end{aligned} \quad \text{Eq. 2.26}$$

The probability p is a crucial parameter and needs to be larger than 0.7, in order to obtain a signal that is mostly due to the wanted dipolar pathway (φ_{123}). The additional dipolar pathways are then only a perturbation ('artefacts') to the true dipolar evolution function.

2.3 Data analysis

In order to retrieve the intramolecular distance information from the primary PELDOR time trace $V(t)$ (Eq. 2.19, Figure 2.7), $V_{intra}(t)$ describing all spins within a spin labelled macromolecule needs to be separated from $V_{inter}(t)$ being the decay of the signal due to the homogeneous distribution of the cluster within the sample (background). The intermolecular dipole-dipole interaction (Eq. 2.20) bears information about the spin concentration and the local dimensionality of the distribution of the spin labels. To remove the intermolecular contribution in 4-pulse PELDOR the signal is divided by a monoexponential (Figure 2.7), while in terms of 7-pulse CP PELDOR division by the function described by Eq. 2.25 and Eq. 2.26 needs to be applied.

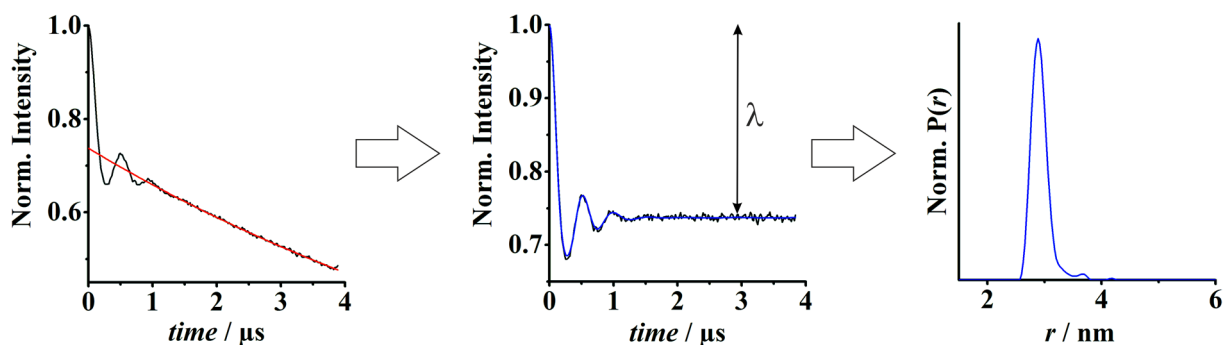


Figure 2.7: Conventional PELDOR data analysis. Left: Primary PELDOR time trace showing the intermolecular contribution in red. Middle: Dipolar evolution function after background-correction indicating the modulation depth parameter λ . The fit from Tikhonov regularization is shown in blue. Right: Distance distribution obtained from Tikhonov regularization. In some case model based analysis like Gaussian model fitting can be applied.

Due to the ‘artefacts’ in the dipolar evolution function of the 7-pulse CP PELDOR, the standard analysis must be extended by an iterative correction procedure, which aims to subtract the additional traces with their appropriate weights, zero times and time increments [48].

After the appropriate correction procedure either for 4-pulse PELDOR (Figure 2.7) or 7-pulse CP PELDOR the intramolecular dipolar evolution function is obtained (4-pulse PELDOR: Eq. 2.19; 7-pulse CP PELDOR: Eq. 2.25). This function includes information about electron-electron distances, distance distributions, labelling efficiency and the number of coupled spins within a system (*spin-counting*) [69]. The modulation depth λ is a product of the pump pulse efficiency λ_B and the labelling efficiency x .

$$\lambda(\text{sample}) = \lambda_B \cdot x \quad \text{Eq. 2.27}$$

For a system with 100% labelling efficiency, the modulation depth is given by the pump pulse efficiency. For standard experiments on a nitroxide with a 12 ns pump pulse and an offset of 70 MHz, λ has values of 0.45 / 0.53 (dependent on the resonator) at X-band. At Q-band using a 20 ns pump pulse and an offset of 70 MHz λ was found to be 0.25 (see Figure 6. 1 for calibration). To extract the distance information from the dipolar evolution function a Tikhonov regularization, implemented in the MATLAB software package DeerAnalysis [70] is utilized, which shall be introduced briefly. Additional information can be found in [71].

In the case of MTSSL labelled proteins the intramolecular part of the PELDOR signal $V_{intra}(t)$ can be described by a Fredholm integral equation of the first kind (Eq. 2.28), due to the flexibility of both spin label and protein.

$$V_{intra}(t) = \int_{R_{min}}^{R_{max}} K(r, t) \cdot P(r) dr \quad \text{Eq. 2.28}$$

With $K(r, t)$ being a kernel function (Eq. 2.29), giving the average of the dipolar coupling over all orientations with a given distance r , with respect to the magnetic field, and $P(r)$ the distance distribution between the two spin labels.

$$K(r, t) = \int_0^{\pi/2} \cos[(1 - 3\cos\theta^2)\omega_D] \sin\theta d\theta \quad \text{Eq. 2.29}$$

However, in a case were the orientation of the interspin vector r and the nitroxide magnetic tensors (\underline{g} and \underline{A}) are correlated the kernel function presented in Eq. 2.29 is no longer valid. In this case, the PELDOR signal is orientation selective, meaning that the signal at a given spectral position depends on the geometry of the biomolecule. Thus, in order to retrieve the “true” $P(r)$ a sum over multiple frequency offsets is required. This situation is found for example in the case of DNA or RNA strands spin labelled with the rigid spin label C-spin, yet also strong interactions of the MTSSL spin label with the protein backbone or neighbouring side chains might cause this orientation dependency of the experimental signal. Nevertheless, in both cases the determination of the underlying distance distribution $P(r)$ is an *ill-posed* problem, since small experimental variations (e.g. noise) can lead to significant deviations in the observed distance distribution $P(r)$.

A well-suited method to solve this *ill-posed* problem is the Tikhonov regularization, which stabilizes the solution of Eq. 2.28 by the introduction of the regularization parameter α .

The resulting $P(r)$ minimizes the following functional:

$$\Phi_{\alpha}(\mathbf{P}(\mathbf{r})) = \|\mathbf{V}(\mathbf{t}) - \mathbf{K}(\mathbf{t}, \mathbf{r})\mathbf{P}(\mathbf{r})\|^2 + \alpha\|\mathbf{L}\mathbf{P}(\mathbf{r})\|^2 \quad \text{Eq. 2.30}$$

With L being either the identity $LP(r) = P(r)$ or the second derivative operator $LP(r) = P(r)''$

The distance distribution obtained for the minimum of Eq. 2.30, additionally considering the restraint $P(r) \geq 0$, is given by:

$$\mathbf{P}_{\alpha}(\mathbf{r}) = (\mathbf{K}(\mathbf{t}, \mathbf{r})^T \mathbf{K}(\mathbf{t}, \mathbf{r}) + \alpha \mathbf{L}^T \mathbf{L})^{-1} \cdot \mathbf{K}(\mathbf{t}, \mathbf{r})^T \mathbf{V}(\mathbf{t}) \quad \text{Eq. 2.31}$$

From this it becomes obvious that for an appropriate value of α the first term in Eq. 2.30 will install compatibility with the experimental data, while the second term gives a smoothed estimate of the solution. However, for too large or too small values of α , the result will be either over-smoothed or obstructed by ‘artefact’ peaks, respectively. Thus, it is necessary to apply a reliable method for the determination of the regularization parameter α , to achieve the best quality of the solution, which is, in this case, the L-curve criterion. The L-curve is a logarithmic plot of the smoothness $\eta(\alpha)$ versus the mean square deviation $\rho(\alpha)$ of the result. These quantities are given by the following equations:

$$\eta(\alpha) = \|\mathbf{V}(\mathbf{t}) - \mathbf{K}(\mathbf{t}, \mathbf{r})\mathbf{P}_{\alpha}(\mathbf{r})\|^2 \quad \text{Eq. 2.32}$$

$$\rho(\alpha) = \left\| \frac{d^2}{dr^2} \mathbf{P}_{\alpha}(\mathbf{r}) \right\|^2 \quad \text{Eq. 2.33}$$

The optimal α is found at the corner of the L-curve, giving a reasonable balance between the compatibility to the experimental time trace and the smoothness of the solution.

Another way of finding the solution of the *ill*-posed problem is fitting the data to a model, e.g. assuming a distance distribution of one or two Gaussians [70]. This allows a simplified representation of the unknown distance distribution $P(r)$, thereby facilitating the interpretation of the result. However, the application of such models implies a certain knowledge about the studied molecule and should be validated against the result of the Tikhonov regularization.

2.4 *In silico* prediction of inter-spin distances

One limitation to PELDOR measurements using SDSL is the unknown position of the electron spin with respect to the backbone. Unfortunately, very few experimental data sets on the conformations of the spin label attached to proteins [38] are available in order to use this information to create a so called rotamer library of the MTSSL side chain. Thus, the ‘golden standard’ of an *in silico* estimation/prediction of likely conformations is still based on long Molecular Dynamics (MD) simulations on either free MTSSL or bound to model peptides, as the computational effort of sufficiently long whole spin labelled protein simulations is too high. The conformations sampled during these runs are then clustered to give a representative ensemble of possible conformations, “the rotamer library”. Over the last decade, several rotamer libraries have emerged, of which only a small selection shall be introduced as they were considered in this thesis. Thereby especially libraries obtained by MD simulations using force fields customized to accurately consider possible interactions of the spin label with the protein backbone are of interest.

The prediction of the spin label flexibility at given position in a static protein structure (X-ray, NMR) is achieved by *in silico* spin labelling. Hereby, the fraction of rotamers in the ‘rotamer library’ applicable to this site is calculated by applying a Lennard-Jones potential [38], to estimate the interaction energy between the rotamer and the protein backbone.

The first approach is implemented in the MATLAB base software Multiscale modelling of macromolecular systems, short MMM [38, 72]. The rotamer libraries chosen in this thesis are directly available for the use in MMM. The rotamer libraries under comparison are the standard libraries in MMM2013.2 in 298K and 175K mode, the libraries from Hubbell (Warsh, [73]) and Sezer [40]. The standard libraries of MMM2013.2 are obtained from MD simulations at 298K and 175K of the free spin label and iterative projection onto a set of canonical dihedral angles resulting in ~210 possible rotamers for each library. [38] The rotamer libraries by Deniz Sezer are made on the basis of an MD simulation of the MTSSL side chain attached to a 14 residue poly-alanine α -helix using a force field especially developed for a reliable description of the MTSSL side chain. The library Sezer12 uses populations of χ_1 and χ_2 (Figure 2.8) as extracted from the MD trajectories, whereas in Sezer13 the populations are conditioned on the state of χ_3 .

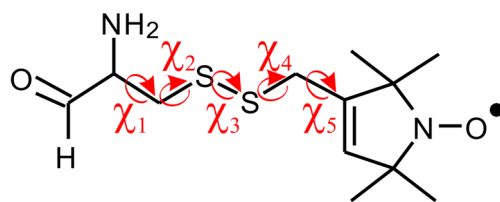


Figure 2.8: The five torsion angles ($\chi_1 - \chi_5$) of the MTSSL side chain.

The rotamer library Warsh is obtained by DFT calculations on an MTSSL side chain on a model 10 residue polyglycine α -helix. The resulting library considers interactions of the label side chain with the protein backbone, intra-residue $C\alpha-H\cdots S\delta$ interactions, solvation energies, as well as the χ_1, χ_2 probabilities that are in good agreement to those obtained from X-ray studies. [42]

To consider the complementary “tether-in-a-cone” approach [74] MtsslWizard a PyMOL plugin was used. Hereby the search for rotamers without sterical clashes with the protein is accomplished by defining a “vdW cut-off” (different tolerance can be used by the thoroughness parameter). In contrast to MMM MtsslWizard does not make assumptions about rotamer probabilities or the estimation of interaction energies. [43, 44]

The interspin distance between one rotamer at position 1 in the protein to all rotamers at position 2 and vice versa are calculated, thereby creating a distribution of distance. The width of this distribution gives the inaccuracy produced by the intrinsic flexibility of the spin label. Unfortunately, this approach excludes backbone flexibility, domain movement and especially side chain rearrangements upon spin labelling.

Chapter 3

Results and Discussion

Structural investigations of biomolecules, e.g. multi-domain proteins, by PELDOR spectroscopy can be very challenging. Yet, being aware of those challenges allows elucidating domain-domain architectures, conformational flexibilities as well as conformational changes. Within this chapter, two studies of multi-domain proteins are presented, which demonstrate potential pit-falls and evaluate the applicability of the experimental results for structure determination.

The difficulties arising from the intrinsic flexibility of MTSSL upon structure determination will be discussed using the example of the three *anaOmp85* POTRA domains [75] which were found to give strongly oscillating PELDOR time traces similar to model compounds (Figure 6.2 and Figure 6.5). A main focus will be on the comparison of different rotamer libraries as well as MD simulations of spin labelled *anaOmp85* POTRA domains with the experimental data. This will be the basis for the evaluation of the accuracy of the predicted spin label flexibility and its impact on the resolution of structure refinements.

The capability of utilizing spin labelling positions, which lead to a restricted spin label flexibility for the determination of conformational ensembles and changes by means of PELDOR distance restraints will be demonstrated on the example of diubiquitin chains. Yet, this was only possible since the inaccuracies in rotamer library-predictions were found to be of minor importance due to the flexibility of the diubiquitin chains.

The challenges emerging with a large conformational flexibility of the biomolecule and large inter-spin distances will be illustrated by the use of longer ubiquitin chains. The main issue here is the accessibility of a sufficient length of the time window to accurately determine the intermolecular background decay. This issue will be addressed by the application of the recently developed 7-pulse CP PELDOR sequence [48]. Hereby, enabling the detection of conformational changes even for such flexible systems.

Last but not least the biological relevance of the results will be discussed in the third paragraph of this chapter.

3.1 Cyanobacterial Omp85 POTRA domains – a rigid system

The POTRA³¹ domains *anaP1*, *anaP2*, *anaP3* (Figure 3.1) are the soluble N-terminal extension of the polypeptide-transporting β -barrel protein (PTB) *anaOmp85*. These domains display a characteristic β - α - α - β - β fold, where the two helices are packed from the same side against the 3-stranded β -sheet [75-79]. The X-ray structure of these domains (hereafter 3MC8,) was published in 2010 by Koenig et al.[75]. The internal architecture of the domains was rather unquestioned. However, the MD simulation published along with the X-ray structure suggested an additional relative orientation of the domains, especially *anaP1* and *anaP2*. Seven intra- and twenty inter-POTRA domain variants were expressed and purified (Figure 3.1) to investigate them by means of PELDOR spectroscopy.

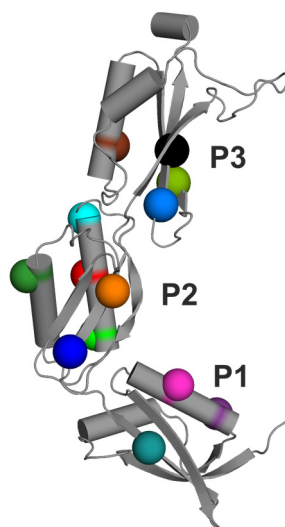


Figure 3.1: Ribbon representation of 3MC8 indicating the spin labelled residues. Spin labelled residues in *anaP3*: V460C (black), Q429C (brown), V457C (light blue) and L448C (light green); *anaP2*: Q374C (orange), V370C (blue), E344C (red) and A319C (green); *anaP1*: I292C (dark cyan), N265C (magenta) and Q259C (violet). Intra-POTRA domain variants were expressed, purified and spin labelled by Eva-Maria Bouwer, a former Ph.D. student in the lab of Prof. Enrico Schleiff at the Goethe-University.

The majority of the measured distance restraints, using PELDOR spectroscopy at X-band frequencies (~9.8 GHz, also see Chapter 6.2.3), were performed and analysed by Dr. Reza Dastvan (Figure 6.2, Figure 6.4, Figure 6.5 and Figure 6.6), who was a former PhD student in the group of Prof. Thomas F. Prisner and is currently a Postdoctoral researcher at Vanderbilt University in the group of Prof. Hassane S. Mchaourab. Exceptions are stated in the caption of Figure 6.5. The restraints will be compared to simulations using the rotamer library or the tether-in-a-cone approach to validate the structural integrity of the individual domains. In

³¹ Polypeptide Transport-associated domains

addition, the relative orientation of the *anaOmp85* POTRA domains in frozen liquid solution will be elucidated. Since this comparison does not include any backbone movement, the experimental results will be compared to MD simulations of spin labelled *anaOmp85* POTRA domains and REMD³² simulations of wild type domains (for details see Chapter 6.2.7 and [63]), to include the effects of protein dynamics. Based on the high quality of the observed PELDOR distance restraints the influence of the spin label flexibility on structure refinement will be evaluated using two different approaches: (i) treating the individual POTRA domains as rigid bodies and (ii) using an all-atom refinement of the structure to examine the relative orientation of these domains in frozen liquid solution.

Parts of this chapter were published in Dastvan et al. 2016. Biophys J 110:2195-2206.

3.1.1 PELDOR distance restraints versus rotamer library-prediction

The structural investigation of biomolecules by PELDOR often includes the comparison to available atomistic structures obtained by other techniques such as X-ray crystallography or NMR spectroscopy. To compare, these static structures with the experimentally observed PELDOR data, *in silico* modelling of the internal flexibility of MTSSL, by the approaches and libraries introduced in chapter 2.5, will be employed. This is beneficial compared to α -distance distributions since it includes the length and flexibility of the MTSSL side chain. However, the accuracy of these predictions needs to be evaluated in detail before the experimental results can be applied in the refinement of an existing structure.

3.1.1.1 Validation of the intra-POTRA domain architecture

All seven intra-POTRA domain PELDOR time traces showed well-defined oscillations within the observed time window. This allowed a clear differentiation between intra- and intermolecular dipolar interactions, enabling the extraction of well-resolved distance distributions by Tikhonov regularization (Chapter 6.4.1, Figure 6.2). These results point out a confined backbone flexibility of the individual domains. Large deviations in the mean distance of the experimental data and the predictions, based on the rotamer library, would indicate a different intra-domain architecture. Thus, a careful validation of the intra-domain architecture

³² Replica Exchange Molecular Dynamics simulations

has to be done before differences in the relative domain-domain orientation could be investigated. The background-corrected PELDOR time traces and the distance distributions of the seven intra-POTRA domain variants were compared with 3MC8 using different rotamer libraries (Figure 3.2 and Figure 3.3), in order to evaluate the quality of the predictions.

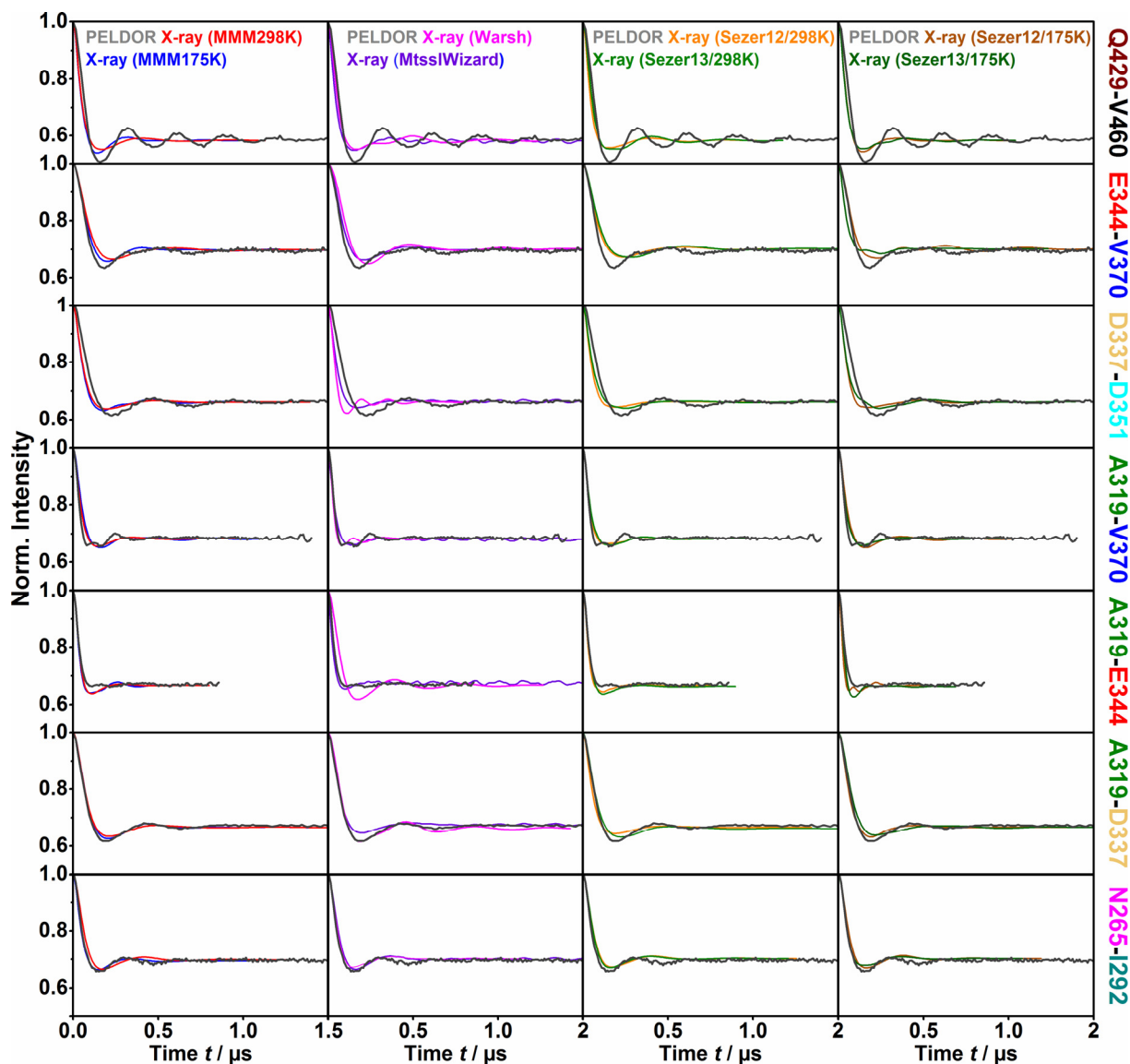


Figure 3.2: Comparison of intra-POTRA domain PELDOR time traces generated by MMM and MtsslWizard with experimental traces. Time traces were generated on 3MC8 by the standard rotamer libraries of MMM2013.2 [38] in 298 K mode (red), in 175 K mode (blue), Warsh library (magenta), Sezer12 in 298K mode (orange), Sezer12 in 175K mode (green), Sezer13 in 298K mode (brown) and Sezer13 in 175K mode (dark green) were directly obtained from MMM software package. While time traces for distance distributions from MtsslWizard using thorough search and loose vdW restraints (cut-off 2.5Å, 5 clashes allowed) (violet) were obtained by a home-written MATLAB® script. The background-corrected experimental data is shown in (grey).

Especially for intra-domain spin labelled pairs in *anaP1* (N265C/I292C) and *anaP2* (A319C/D337C and A319C/E344C), the initial decay as well as the dampening of the predicted time traces were in good agreement with the experimental results (Figure 3.2). Thus leading to a large overlap of the experimental and predicted distances distributions (Figure 3.3).

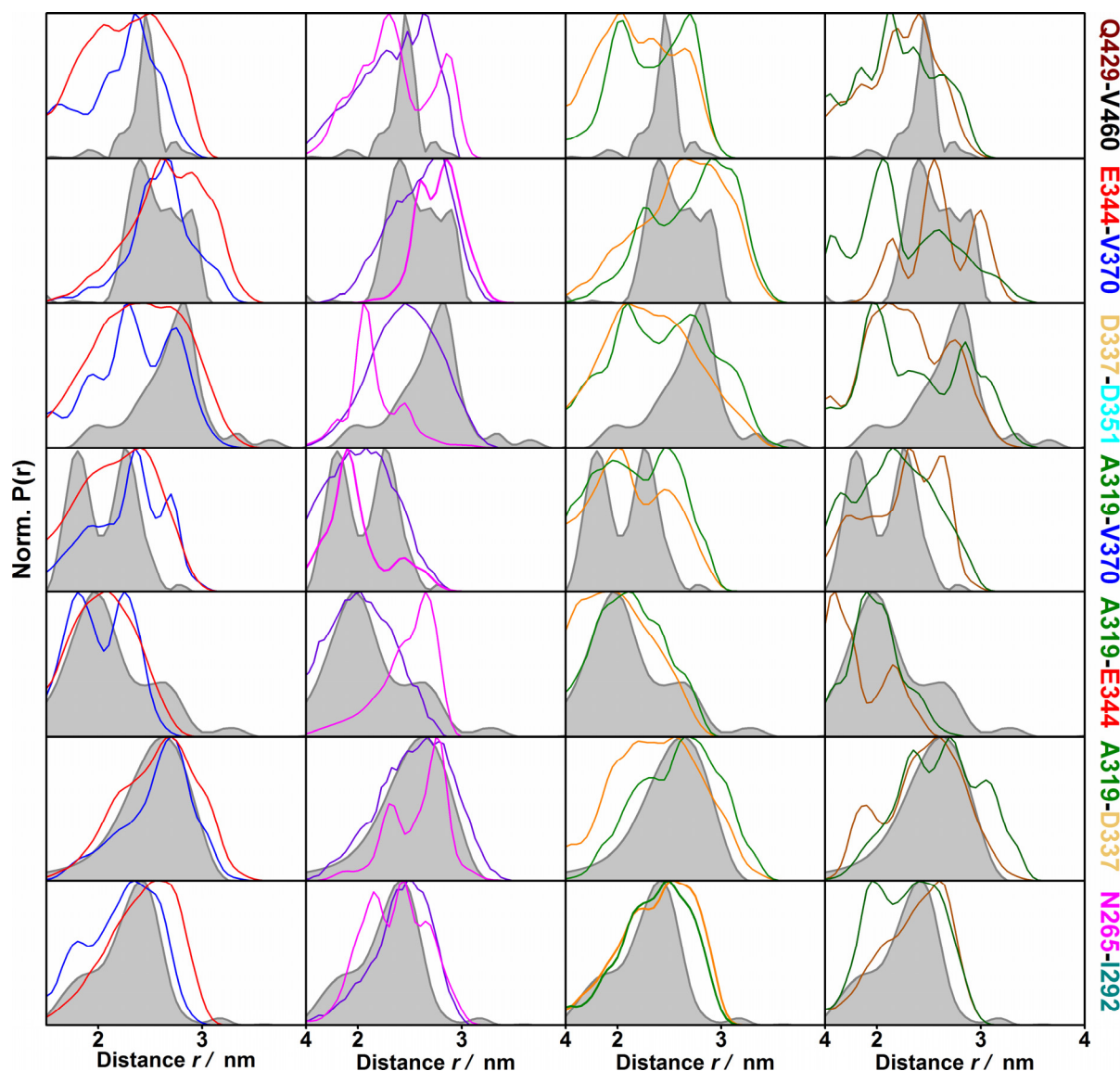


Figure 3.3: Comparison of experimentally obtained intra-POTRA domain distance distributions with distributions generated by MMM and MtsslWizard. Distance distributions generated on 3MC8 by MMM in 298 K mode (red), in 175 K mode (blue), Warsh library (magenta), Sezer12 in 298K mode (orange), Sezer12 in 175K mode (green), Sezer13 in 298K mode (brown), Sezer13 in 175K mode (dark green) and MtsslWizard using thorough search and loose vdW restraints (violet) are compared to the obtained distance distributions by Tikhonov regularization (grey).

This indicates that the rotamer libraries for these spin labelling positions are suitable to reflect the true distance and flexibility of the spin labels in these pairs with high precision. However, the experimental time traces for intra-domain spin labelled pairs in *anaP3* (Q429C/V460C), as well as the *anaP2* (D337C/D351C), exhibited stronger oscillations than predicted by any of the rotamer libraries (Figure 3.2). Therefore, the experimental distance distributions were much narrower than those predicted (Figure 3.3), indicating a small backbone flexibility of the *anaOmp85* POTRA domains as well as a restricted flexibility of MTSSL. In addition, time traces of similar dampening but different oscillation frequencies and thus distances distributions of similar width but different shape compared with the predictions for spin labelled pairs related to residue 370 in *anaP2* (Figure 3.3) were observed. The rigidity of the spin label at this position was also observed in liquid solution via CW EPR (Figure 6.3).

All these aforementioned deviations of experiment and prediction are most likely due to a more confined rotamer flexibility of at least one partner in the spin label pair within the experiment. In addition, even the libraries, which take into account backbone interactions and $C\alpha-H\cdots S\delta$ interactions or solvation energies, do not enhance the overall compatibility. This qualitative result was further underlined by using a deviation factor (DF) defined as:

$$DF = \frac{1}{N} \left(\frac{\sum_R (P_{exp}(R) - P_{sim}(R))^2}{\sum_R (P_{exp}(R))^2} \right) \quad \text{Eq. 3.1}$$

With N being the number of experimental data sets.

Table 3.1: Deviation factor DF (Eq. 3.1) of the experimental and predicted distance distributions from different rotamer libraries for all intra-POTRA domain variants (N=7).

MMM175K	MMM298K	MtsslWizard	Warsh
0.43	0.99	0.91	0.77
Sezer12/175K	Sezer12/298K	Sezer13/175K	Sezer13/298K
0.73	1.09	0.79	0.85

Nevertheless, it could be concluded that the architecture of the individual domains in frozen solution is very similar to 3MC8, allowing the assumption that the individual domains can be treated as rigid bodies. Furthermore, this result indicates, that potential differences observed for the inter-POTRA domain variants can be attributed to a different domain-domain orientation.

3.1.1.2 Relative domain-domain orientation in frozen liquid solution

The structural integrity of the individual domains was evaluated by the seven intra-POTRA domain variants. Yet, deviations between the width of experimental and rotamer library based distance distributions were observed. These deviations indicated a confined flexibility of the spin label in frozen liquid solution compared to the *in silico* flexibility, especially for residues V370C, Q429C, and V460C. This observation needs to be kept in mind when (i) comparing the twenty inter-POTRA domain restraints (Figure 3.4) with the predictions based on 3MC8 and (ii) drawing conclusion on the relative domain-domain orientation.

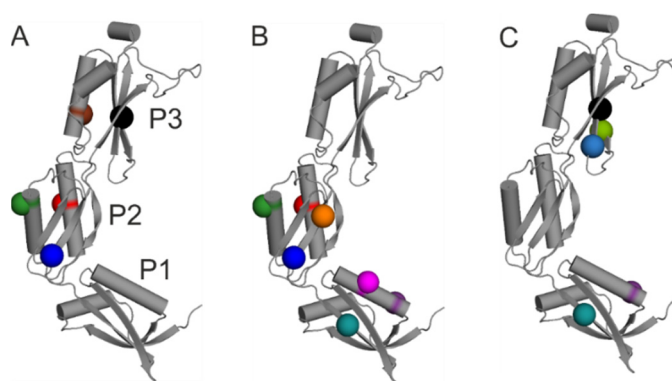


Figure 3.4: Cartoon representation of 3MC8 indicating the spin labelled residues in each domain for the inter-domain variants. A) Spin labelled residues in *anaP3* and *anaP2*: V460C (black), Q429C (brown), V370C (blue), E344C (red), and A319C (green). B) Spin labelled residues in *anaP2* and *anaP1* creating the inter-domain variants between those domains: Q374C (orange), V370C (blue), E344C (red), A319C (green), I292C (dark cyan), N265C (magenta) and Q259C (violet). C) Spin labelled residues in *anaP3* and *anaP1*: V460C (black), V457C (light blue), L448C (light green), I292C (dark cyan) and Q259C (violet). The spin labelling positions for the inter-POTRA domain restraints were selected such that a triangulation of a position in *anaP1* or *anaP3* with a position in *anaP2* and a direct correlation of *anaP1* and *anaP3* was possible. Inter-POTRA domain variants were expressed, purified and spin labelled by Eva-Maria Bouwer, a former Ph.D. student in the lab of Prof. Enrico Schleiff at the Goethe-University.

Similar to the intra-POTRA domain PELDOR data, the majority of the inter-POTRA domain spin labelled pairs exhibited pronounced dipolar oscillations within the observed time window (Figure 6.5), leading to well-resolved inter-spin distances (Figure 6.6) ranging from ~ 2.4 nm (N265C/E344C) to ~ 5.7 nm (I292C/V460C). Comparison of the experimental inter-POTRA domain restraints with 3MC8 using the previously introduced rotamer libraries and temperatures was done for all POTRA domain pairs.

The predictions for the inter-POTRA domain distance restraints between *anaP2-anaP3* based on 3MC8 showed a high degree of consistency with the experimental intramolecular dipolar evolution functions (Figure 3.5; page 30). Especially for spin labelled pairs of residue 429, the dipolar frequency, as well as the dampening of the dipolar evolution function, were reproduced

by the rotamer libraries, only a minor deviation in the pattern of the oscillations was observed. Thus, the distance distributions overlap nicely (Figure 3.6, page 31).

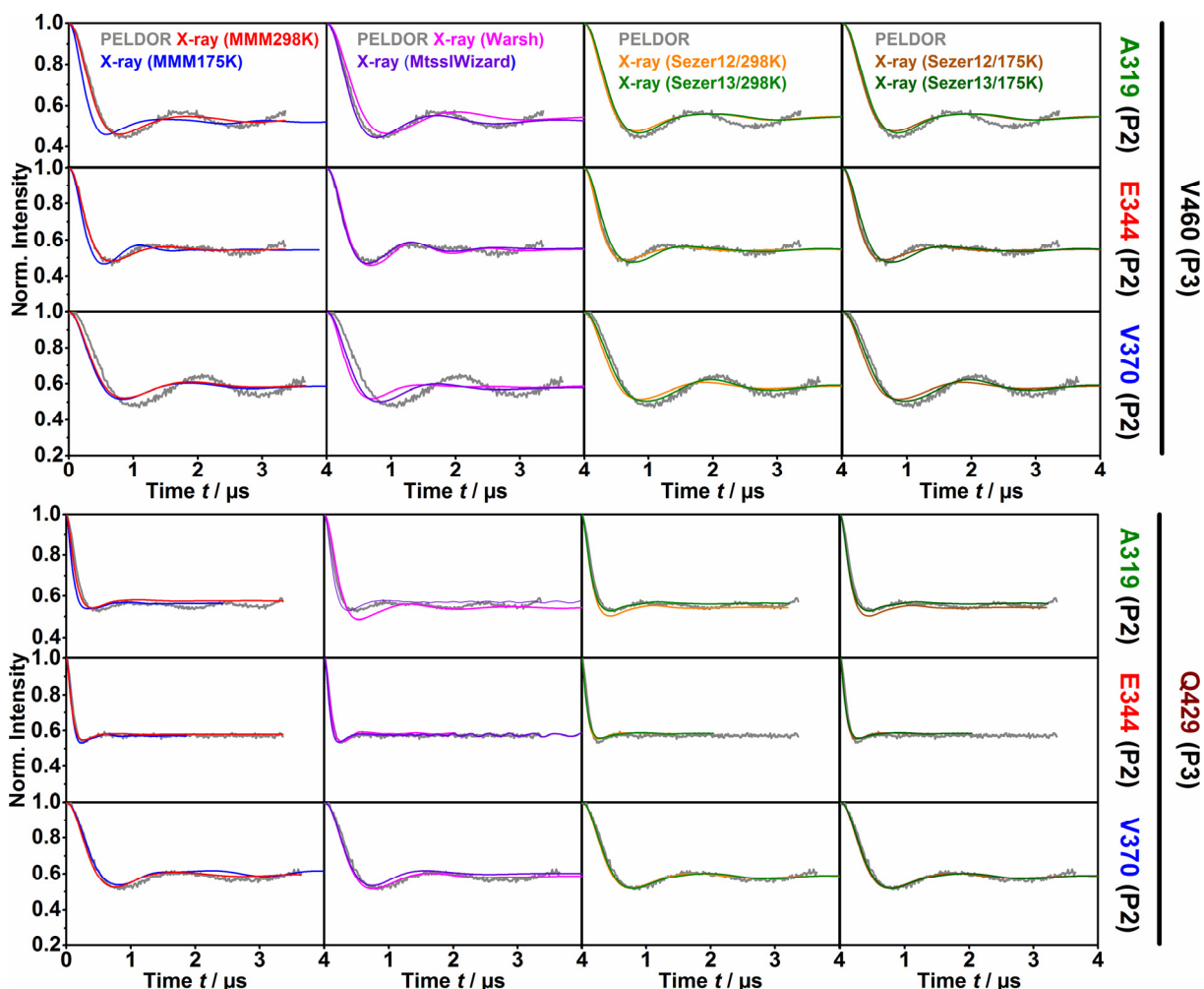


Figure 3.5: Comparison of inter-POTRA domain PELDOR time traces for *anaP3* and *anaP2* generated by MMM and MtsslWizard with the experimental traces. Time traces generated on 3MC8 by the standard libraries of MMM2013.2 in 298 K (red) and 175 K (blue) mode, Warsh (magenta), Sezer12 in 298K (orange) and 175K (green) mode, Sezer13 in 298K (brown) and 175K (dark green) mode were obtained from MMM. While time traces for distance distributions from MtsslWizard (violet) using thorough search and loose vdW restraints (cut-off 2.5Å, 5 clashes allowed) were obtained by a home-written MATLAB® script. The background-corrected experimental data is shown in grey.

This agreement was seen for restraints belonging to residue 460 as well. However, the spin labelled pair V370C/V460C exhibited stronger dipolar oscillation than predicted and therefore, a narrower experimental distance distribution than predicted by *in silico* labelling. An exception to this finding were the Sezer rotamer libraries. Furthermore, the spin labelled pair E344C/V460C yielded a bimodal experimental distance distribution, which was not reproduced by any of the rotamer libraries. These observations were in line with the intra-domain results, where distances involving residues 370 or 460 showed deviations between experiment and rotamer library prediction, emphasizing that the spin label flexibility is strongly hindered at

these positions. Nevertheless, the restrictions were not strong enough to cause orientation selection (Figure 6.7).

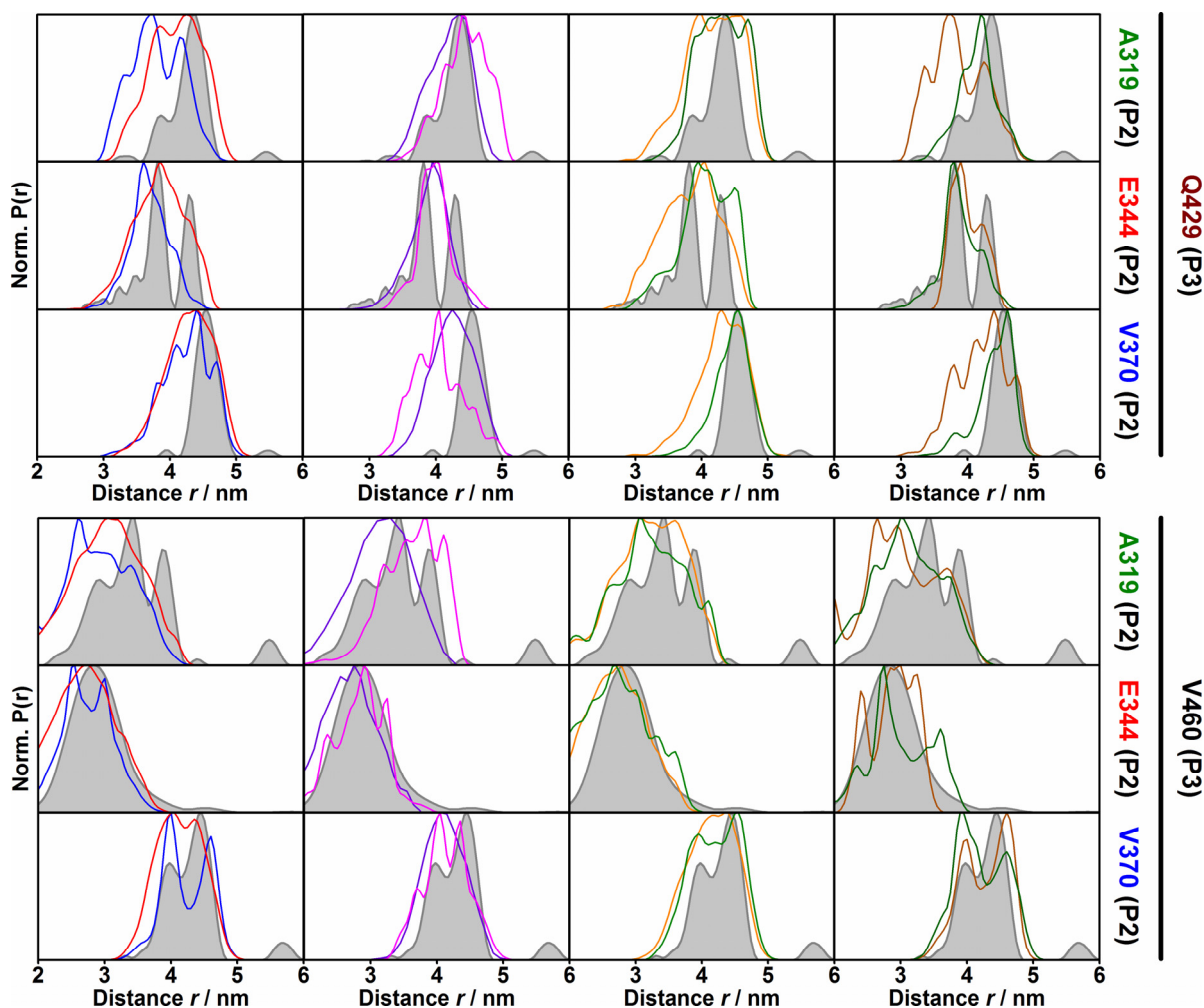
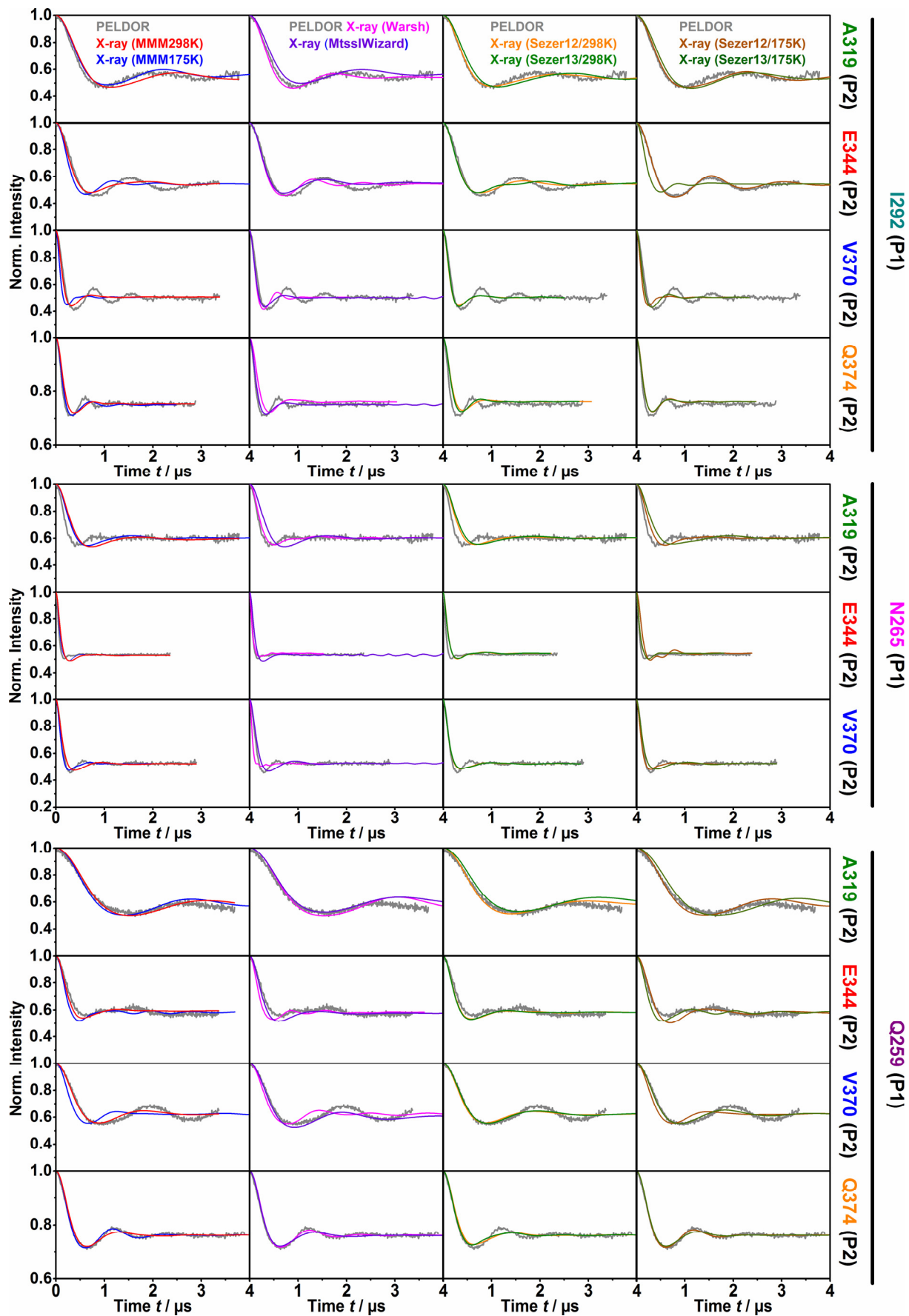


Figure 3.6: Comparison of inter-POTRA domain distance distributions for *anaP3* and *anaP2* generated by MMM and MtsslWizard with experimental distance distributions. Distance distributions generated on 3MC8 by the standard libraries of MMM2013.2 in 298 K mode (red), in 175 K mode (blue), Warsh library (magenta), Sezer12 in 298K mode (orange), Sezer12 in 175K mode (green), Sezer13 in 298K mode (brown) and 175K mode (dark green) and MtsslWizard using thorough search and loose vdW restraints (violet) are compared to the distance distributions from Tikhonov regularization (grey).

In-depth inspection of the experimental dipolar evolution functions for *anaP1-anaP2* revealed that the predicted time traces exhibited a stronger damping and a shift in dipolar coupling frequency (Figure 3.7; page 32), leading to some deviations of the experimental and predicted mean distances (Figure 3.8; page 33).

Figure 3.7: Comparison of inter-POTRA domain PELDOR time traces for *anaP1* and *anaP2* generated by MMM and MtsslWizard with experimental traces. Time traces generated on 3MC8 by the libraries of MMM2013.2 in 298 K (red) and 175 K (blue) mode, Warsh library (magenta), Sezer12 in 298K (orange) and 175K (green) mode, Sezer13 in 298K (brown) and 175K (dark green) mode were directly obtained from MMM software package. Time traces for distance distributions from MtsslWizard using thorough search and loose vdW restraints (cut-off 2.5Å, 5 clashes allowed) (violet) were obtained by a home-written MATLAB® script. The background-corrected experimental data is shown in (grey).



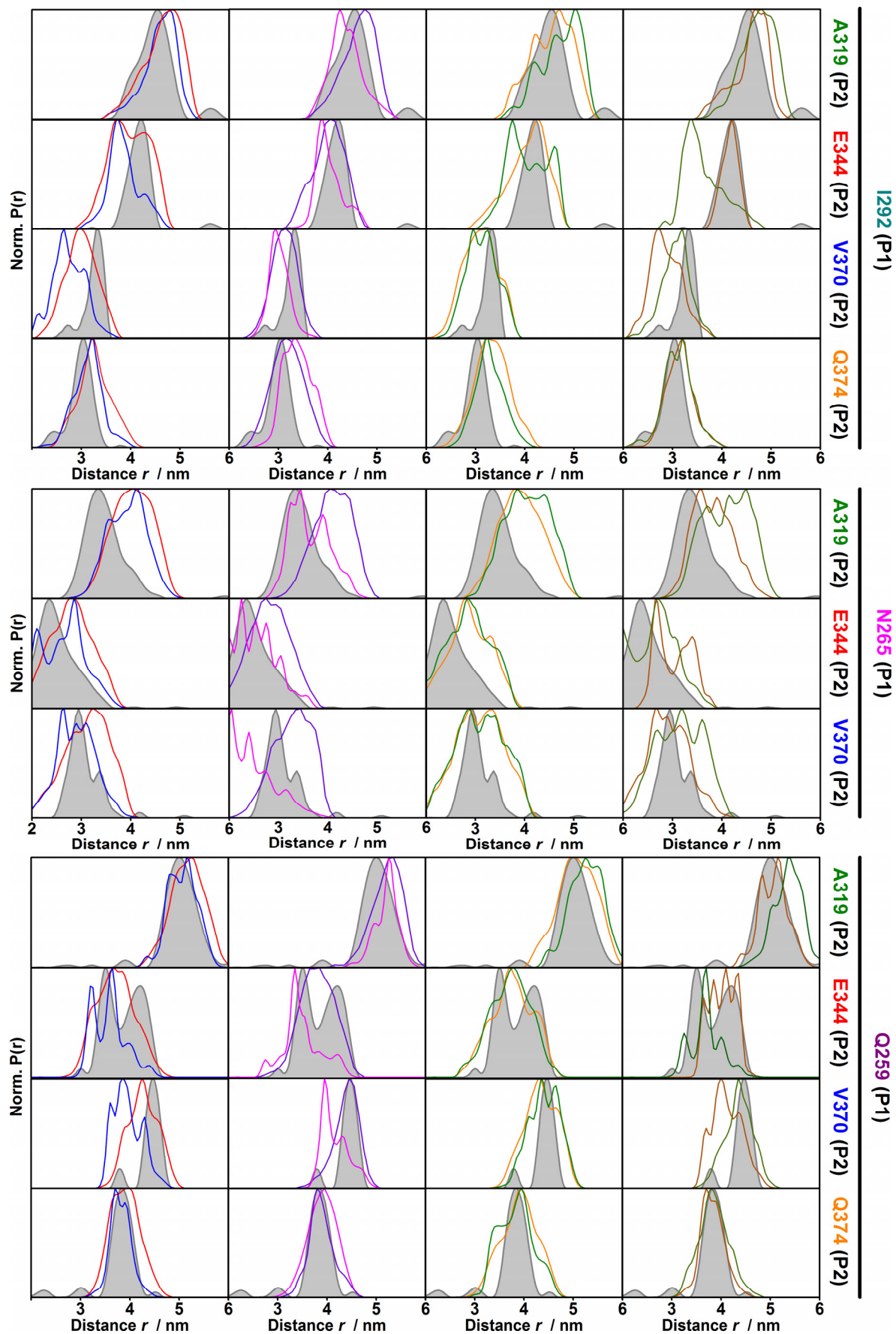


Figure 3.8 Comparison of inter-POTRA domain PELDOR distance distributions for *anaP1* and *anaP2* generated by MMM and MtsslWizard with experimental traces. Distance distributions generated on 3MC8 by the standard libraries of MMM2013.2 in 298 K mode (red), in 175 K mode (blue), Warsh library (magenta), Sezer12 in 298K mode (orange), Sezer12 in 175K mode (green), Sezer13 in 298K mode (brown) and Sezer13 in 175K mode (dark green) and MtsslWizard using thorough search and loose vdW restraints (violet) are compared to the obtained distance distributions by Tikhonov regularization (grey).

In terms of restraints connected to residue 259, the predicted dipolar evolution functions revealed some differences in dipolar coupling frequency for the spin labelled pairs Q259C/E344C and Q295C/V370C. This was most likely due to small population differences in the rotamer library-predictions compared to the MTSSL conformations at these sites in frozen liquid solution. In addition, none of the rotamer libraries reflected the dampening for the spin labelled pairs N265C/V370C and I292C/V370C (Figure 3.7; page 32), leading to distance distributions broader than observed experimentally (Figure 3.8; page 33). Interestingly the predicted and experimental mean distances for spin labelled pair N265C/V370C were in good agreement, with the only exception being the Warsh library. While for the other spin labelled pairs connected to residue 265, a shift in dipolar coupling frequency to a longer period and thus larger mean distance was observed except for the Warsh library. Since residue 265 showed a reasonable agreement of experiments and predictions for the intra-POTRA domain restraints the observed differences in the inter-POTRA domain restraints might be due to a slightly different orientation of the domains, rather than rotamer inaccuracy. For restraints involving residue 292, the most intriguing differences were observed for spin labelled pairs I292C/V370C and I292C/Q374C. In both cases, the strong dipolar oscillations could not be mirrored by the rotamer libraries leading to discrepancies in the distribution widths. The finding that all *anaP1-anaP2* spin labelled pairs with residue 370 as partner beard a narrower distance distribution compared to the predicted distributions was most likely due to a smaller selection of rotamer states of the spin label. This limited flexibility was not only observed in frozen liquid solution but as well by liquid state CW EPR (Figure 6.3). Residue 370 is located within an inter β -strand loop, this specific location might have led to interactions with the protein backbone of *anaP2*, which could not be reproduced by the rotamer libraries. This was in line with the results on the intra-POTRA domain restraints as well as the POTRA domain pair *anaP3-anaP2*.

Taking together all deviations between predicted and experimental restraints and the narrow width of the experimental distributions, a distinct but slightly different relative domain-domain orientation of *anaP1-anaP2* compared to 3MC8 was observed by PELDOR spectroscopy. These difference in the inter-POTRA domain orientation of *anaP1-anaP2* should as well lead to an altered relative orientation of the N-terminal *anaOmp85* POTRA domain *anaP1* with

respect to the C-terminal POTRA domain *anaP3*, compared to 3MC8. Albeit, most of the rotamer library-predictions of the dipolar evolution functions between *anaP1* and *anaP3* showed a reasonable agreement with the experiment (Figure 3.9).

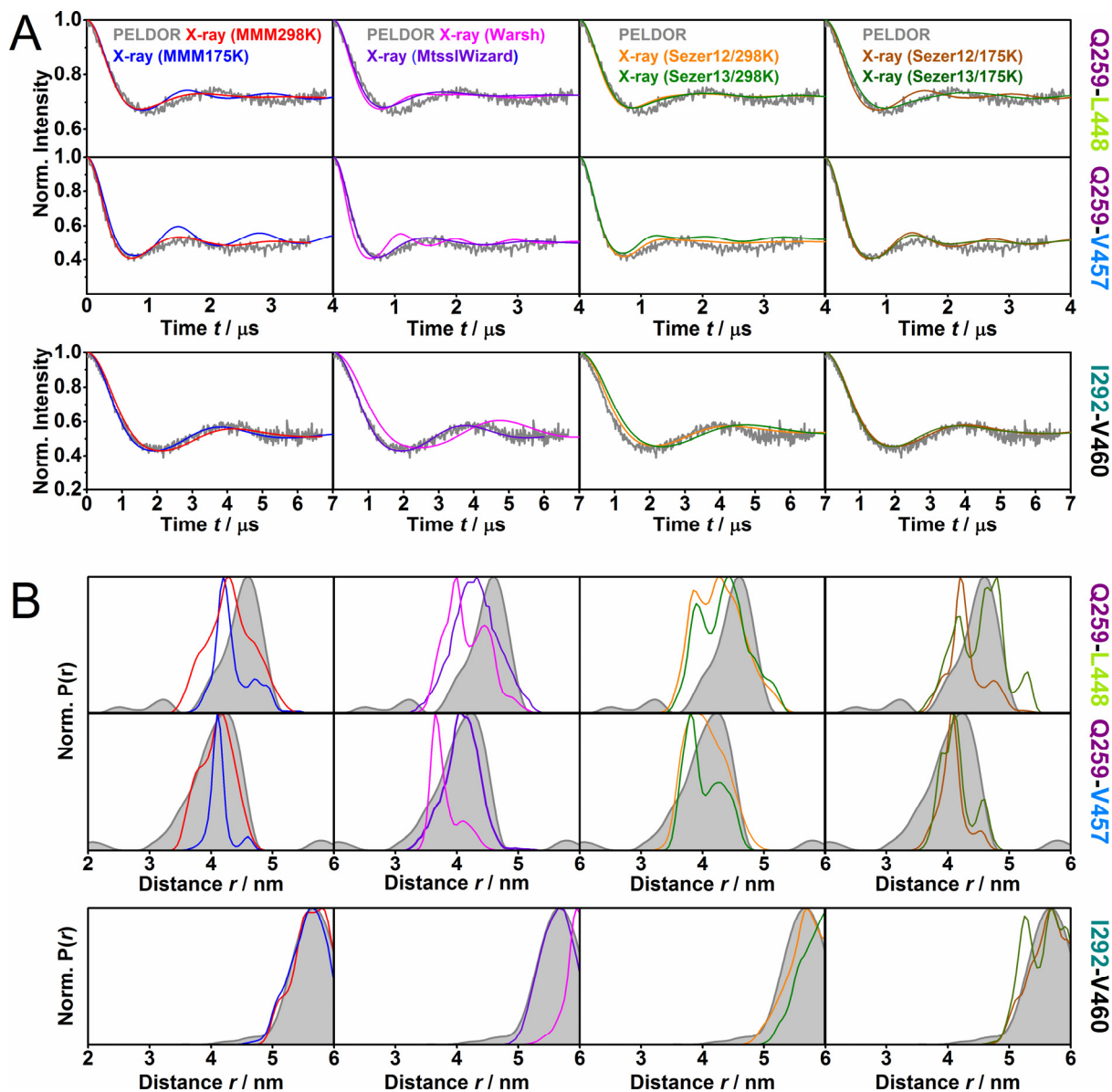


Figure 3.9: Comparison of inter-POTRA domain time traces and distance distributions for *anaP3* and *anaP1* generated by MMM and MtsslWizard with the experimental data. A) Time traces generated on 3MC8 by the standard libraries of MMM2013.2 in 298 K (red) and 175 K (blue) mode, Warsh library (magenta), Sezer12 in 298K (orange) and 175K (green) mode, Sezer13 in 298K (brown) and 175K (dark green) mode were directly obtained from MMM software package. While time traces for distance distributions from MtsslWizard using thorough search and loose vdW restraints (cut-off 2.5Å, 5 clashes allowed) (violet) were obtained by a home-written MATLAB® script. The background-corrected experimental data is shown in (grey). B) Corresponding distance distributions generated on X-ray structure compared to the experimental distance distributions obtained by Tikhonov regularization (grey).

Nevertheless, the experimental mean distance for the spin labelled pair Q259C/L448C was slightly longer than predicted on the 3MC8. However, this might be caused by population differences of the rotamers at these positions. In addition, the standard library of MMM and Sezer12 in 175K mode exhibited stronger dipolar oscillations (Figure 3.9A; page 35) leading to distance distributions narrower than experimentally observed (Figure 3.9B; page 35). This was as well the case for the spin labelled pair Q259C/V457C, yet for this spin labelled pair, the rotamer libraries Warsh and Sezer libraries in 175K mode showed a similar behaviour. The spin labelled pair I292C/V460C had the best agreement between experimental results and simulations on the 3MC8, except for rotamer libraries Sezer13 in 298K mode and Warsh, with slower dipolar oscillations and thus longer distances (Figure 3.9; page 35).

In summary, the experimental inter-POTRA domain distances restraint revealed minor deviations from 3MC8. However, as for the intra-POTRA domain restraints, an overestimation of the spin label flexibility, reflected by broader distance distributions is observed, potentially covering the differences in the relative domain-domain orientation compared to 3MC8. Consideration of intra-residue $C\alpha-H\cdots S\delta$ interactions slightly reduces the width of the distributions but changed the most probable distances. Thus, overall agreement of predicted and experimental distance distributions for all inter-POTRA domain restraints was not greatly increased, which can be quantified by DF (Eq. 3.1; page 28) between the experimental and predicted distance distributions.

Table 3.2: Deviation factor DF (Eq. 3.1) of the experimental and predicted distance distributions from different rotamer libraries for all inter-POTRA domain variants (N=20).

MMM175K	MMM298K	MtsslWizard	Warsh
0.59	0.53	0.46	0.56
Sezer12/175K	Sezer12/298K	Sezer13/175K	Sezer13/298K
0.49	0.53	0.45	0.94

These results might be an indication for rather small inter-domain rearrangements or rearrangements leading to non-varying inter-domain distance. Thus, an analysis of the conformational dynamics, as well as the spin label flexibility at the respective positions, is inevitable for the determination of the relative orientation of the domains.

3.1.2 Comparison to Molecular Dynamics Simulations

The comparison of the experimental PELDOR results with 3MC8 using the rotamer library approach revealed that the usage of a static model prevents an accurate prediction of the flexibility of the MTSSL side chain. To overcome this drawback, multiple Molecular Dynamics (MD) simulations on *in silico* spin labelled *anaOmp85* POTRA domains with a total length of 1.9 μ s were performed by Dr. Oliver Mirus, a former Postdoctoral researcher in the group of Prof. Dr. Enrico Schleiff at the Goethe-University. This approach should help to account for side chain rearrangement and an appropriate description of the spin label and backbone flexibility. Thus, leading to more realistic distance distributions and dipolar evolution functions. In the case of the *anaP2-anaP3* spin labelled pair E344C/V460C the MD simulations did reflect the shape of the experimental time trace and distance distributions better than predictions based on 3MC8 using the standard rotamer library of MMM in 298K mode (Figure 3.10; page 38).

A reason for this might have been that rotamer libraries were calculated based on the structure 3MC8 using a “simple” Lennard-Jones potential to account for interactions with the protein, while MD simulations allowed to account for side chain rearrangements as well as putative tertiary interactions with the protein. Unfortunately, this improvement in rotamer library-prediction was not observed as a general trend, e.g., the spin labelled pairs Q259C/E344C, N265C/A319C, V370C/V460C (Figure 3.10 and Figure 3.11; pages 38 and 39).

The distance distributions for the POTRA domain pair *anaP1* and *anaP2*, extracted from the MD simulation, were of similar width than those calculated with the rotamer library. Both have an increased dampening of the simulated dipolar evolution function (Figure 3.11) compared to the experimental time traces. This promoted the picture that the conformational flexibility of the domains and the spin label is more confined in frozen liquid solution. The deviations in mean distance between 3MC8 and experimental data observed for *anaP1-anaP2* spin label pairs related to residue 265 were attributed to a potential difference in the domain-domain orientation. Interestingly, this was not confirmed by the MD simulations on spin labelled domains, which revealed distance distributions for spin label pairs of residue 265 similar to those predicted by the rotamer libraries (Figure 3.10 and Figure 3.11; pages 38 and 39).

Yet, for the spin label pair N265C/V370C a bimodal distance distribution was observed, which might be a hint that also the flexibility of the spin label at position 265 was influenced by backbone fluctuations and sidechain rearrangements of the protein.

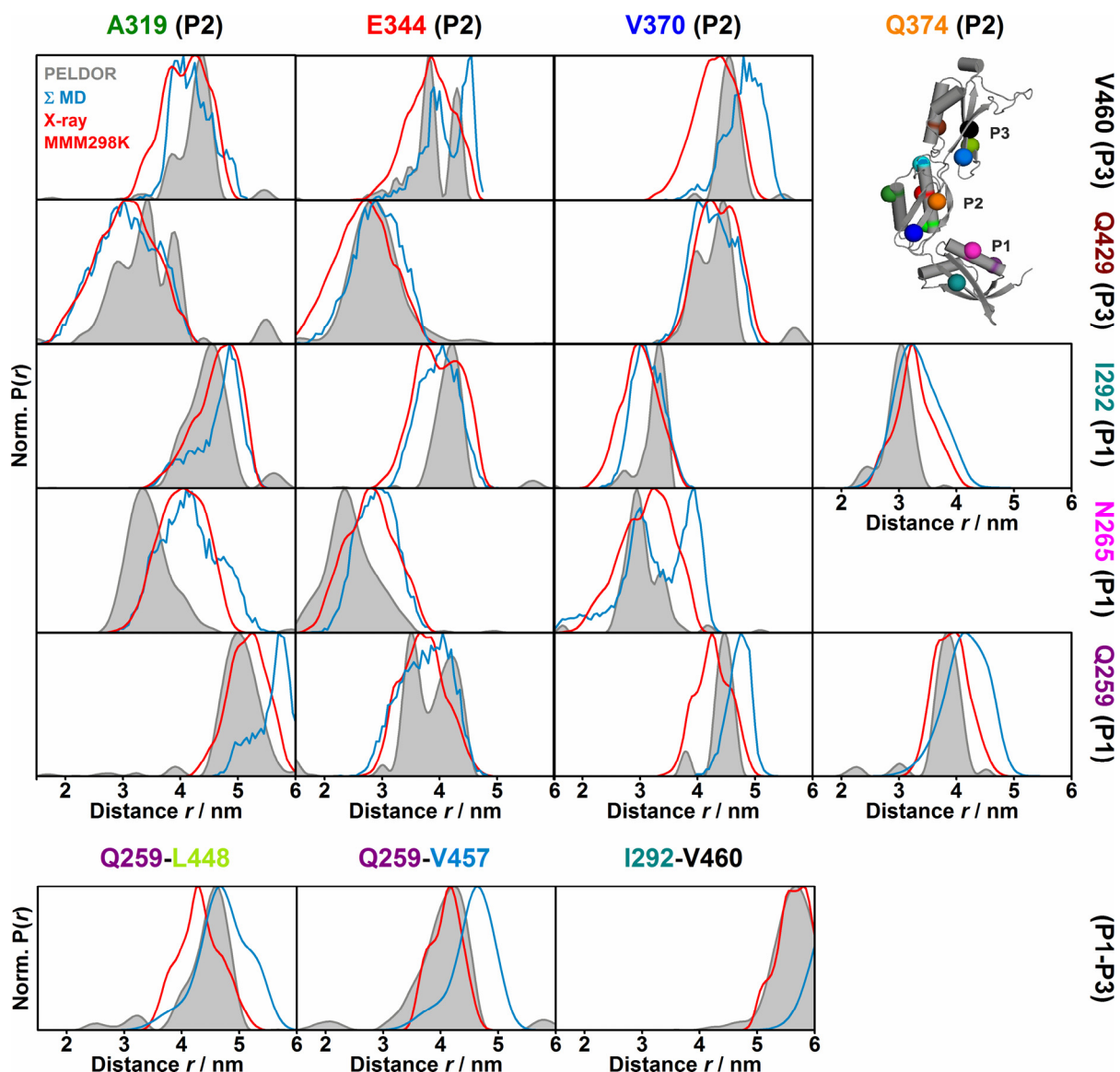


Figure 3.10: Comparison of experimental and simulated intra-molecular distance distributions from MD and the X-ray structure 3MC8. The summed distance distribution over all MD simulations on *in silico* spin label *anaOmp85* (blue) are compared to the experimental distance distributions (grey) as well as those generated on 3MC8 using the standard libraries of MMM2013.2 in 298 K (red). The ribbon representation of 3MC8 indicating the spin labelling positions is given as inset. MD simulations on *in silico* spin labelled *anaOmp85* POTRA domains were performed by Dr. Oliver Mirus, a former Postdoctoral researcher in the group of Prof. Dr. Enrico Schleiff at the Goethe-University.

Interestingly the distance distributions extracted from our MD simulations on spin labelled domains *anaP1* and *anaP3* showed differences in mean distances for the spin labelled pairs Q259C/V457C and I292C/V460C (Figure 3.10 and Figure 3.11; pages 38 and 39) compared to both rotamer library-predictions and experimental restraints. These deviations might be due to a lower sampling of these distances within the MD simulations (only 3 out of 15 MD trajectories for each spin label pair).

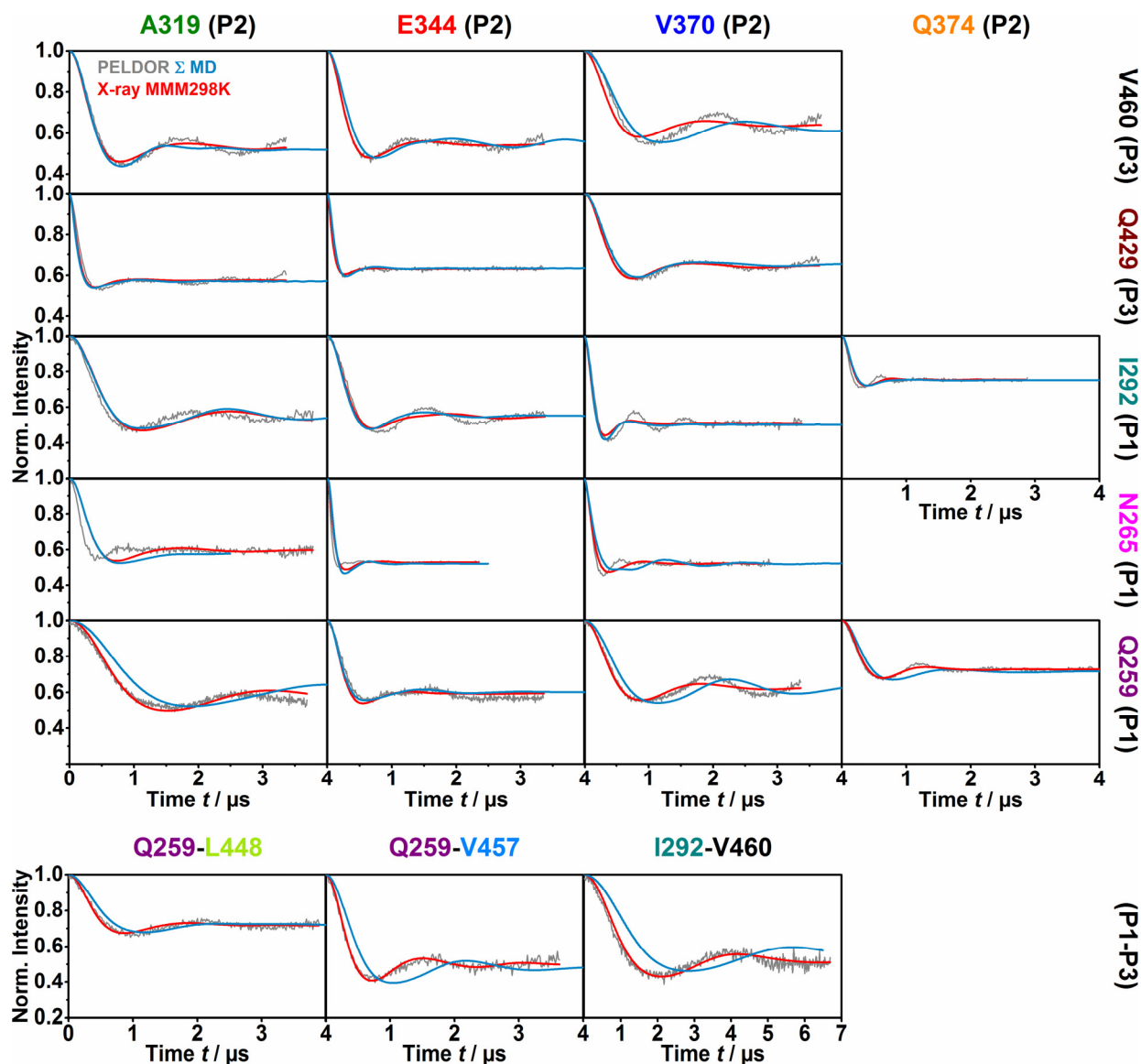


Figure 3.11: Comparison of experimental and simulated intra-molecular dipolar evolution functions from MD and 3MC8. The MD simulations on *in silico* spin label *anaOmp85* were performed by Dr. Oliver Mirus, while simulations of the dipolar evolution functions based on the extracted distance distributions (blue) were performed by the author herself using a home-written MATLAB script. The experimental dipolar evolution functions (grey), as well as those generated on 3MC8 using the standard libraries of MMM2013.2 in 298 K (red), are shown for comparison.

In summary, the MD simulations on *in silico* spin labelled *anaOmp85* POTRA domains, unfortunately, showed only minor improvements in the prediction of spin label flexibility. In addition, the distribution widths of the MD-based distributions were only slightly increased compared to the experimental and those of the rotamer library-predictions. This is a further indication of rather a confined flexibility of the domains and especially for *anaP2* and *anaP3*, with a conformation comparable to the 3MC8. Yet, the deviations in mean distances of restraints related to residue 265 and distribution widths for restraints related to residue 370 were preserved in the MD simulations, indicating a different domain-domain orientation of *anaP1-anaP2* in combination with a more confined spin label flexibility in frozen liquid solution

compared to both simulation approaches. Nevertheless, the overall DF (0.7180) was even increased compared to the predictions based on 3MC8.

3.1.3 Influence of spin label flexibility on structure refinement

The well-defined experimental distance distributions and the deviations in *anaP1* and *anaP2* distances, which were preserved for both rotamer library-predictions and MD simulations on spin labelled *anaOmp85* POTRA domains, are a good basis for a structure refinement. Yet, the overestimation of the spin label flexibility by the rotamer libraries might be a limiting factor in unravelling the orientation of *anaP1* and *anaP3* with respect to *anaP2* in frozen liquid solution. In a first simplified approach, the relative domain-domain orientation of 3MC8 will be refined assuming the individual POTRA domains as rigid bodies, according to the results on the intra-domain restraints and the similarity to the 3MC8. In the second approach, the potential backbone movements, as well as side chain rearrangements of the *anaOmp85* POTRA domains, are taken into account. In a first step, the conformational space sampled by the MD simulations is screened to extract an ensemble of start structures, which are further subjected to a Rosetta relax protocol. This should help to account for protein flexibility and putative tertiary interactions of the spin label with the protein.

Both approaches will be evaluated and compared in terms of their accuracy to give advice for future studies.

In the case of the rigid body refinement, the standard rotamer libraries of MMM in 175K and 298K mode, as well as a self-made library based on the MD simulations on *in silico* spin labelled *anaOmp85* POTRA domains were considered to account for spin label flexibility at a specific site. All libraries showed similar observations (Figure 6.8, Figure 6.9 and Table 3.3), thus the results will be discussed exemplarily by the use of the commonly applied standard rotamer library of MMM in 298K mode. In order to refine the relative orientation of the individual of the *anaOmp85* POTRA domains with respect to 3MC8, the domains (rigid bodies) will be translated and rotated (Figure 3.12; page 41) to minimize the RMSD between the experimental and simulated distance distributions of pairs of rotamer bundles. Hereby, the NO-coordinates of the rotamer ensembles are fixed relative to the individual POTRA domain they are attached to (for details see Chapter 6.2.5).

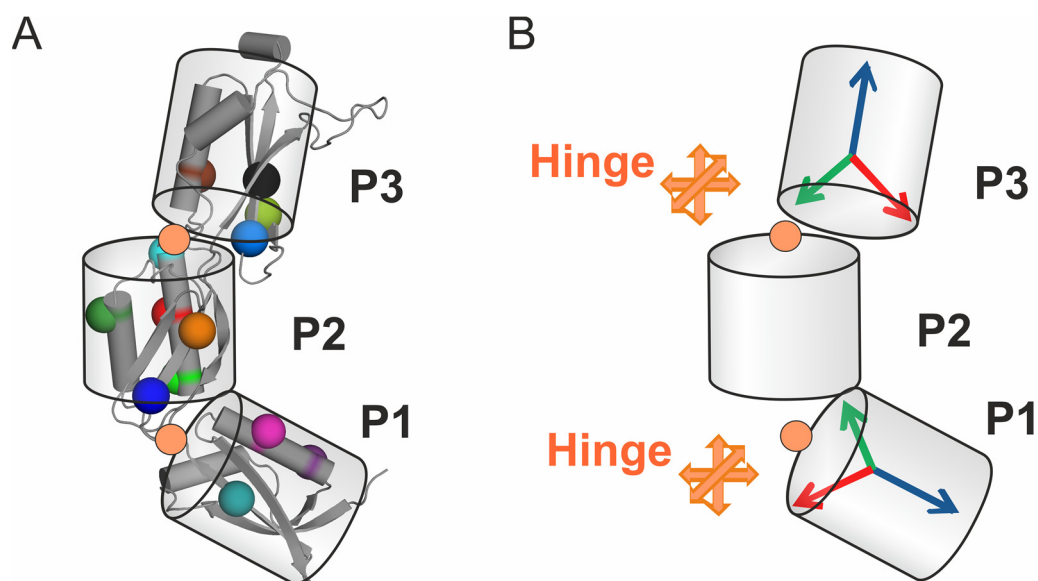


Figure 3.12: Illustration of the rigid body refinement. A) Ribbon representation of 3MC8 indicating the spin labelling positions in the individual domains. The individual domains are assumed as rigid bodies, which is depicted by cylinders. B) Cartoon of the translational and rotational motions executed during the rigid body refinement. The rotational motions occur at hinge points (orange) which mimic the flexible linkers between the domains.

The mean distance for the *anaP2-anaP3* spin labelled pair A319C/V460C and its dipolar oscillation frequency was slightly better reproduced in comparison to any of the previous calculations. Yet, the width of the distribution and therefore the dampening of the dipolar evolution function for the spin labelled pair V370C/V460C was increased (Figure 3.13 and Figure 3.14, pages 42 and 43). Hence, the rigid body refinement did not lead to an overall improvement for restraints between *anaP2-anaP3*, indicating that the arrangement of those domains is close to that of 3MC8.

Comparison of the refined distance distributions for ‘the best model’ of the rigid body refinements revealed that especially distances for the *anaP1-anaP2* spin labelled pairs N265C/A319C and N265C/E344C, which showed deviations in mean distance compared to rotamer library-prediction, were shifted to match the experimental distribution (Figure 3.13; page 42). This is even more obvious by looking at the time domain signal (Figure 3.14; page 43). In addition, an enhanced consistency between dipolar oscillation frequencies was observed for the spin labelled pair I292C/Q374C. Nevertheless, the width of the simulated distributions was mainly unchanged, especially for the spin labelled pairs N265C/V370C and I292C/V370C; preserving the increased dampening of the dipolar oscillations of the time domain signal (Figure 3.14; page 43).

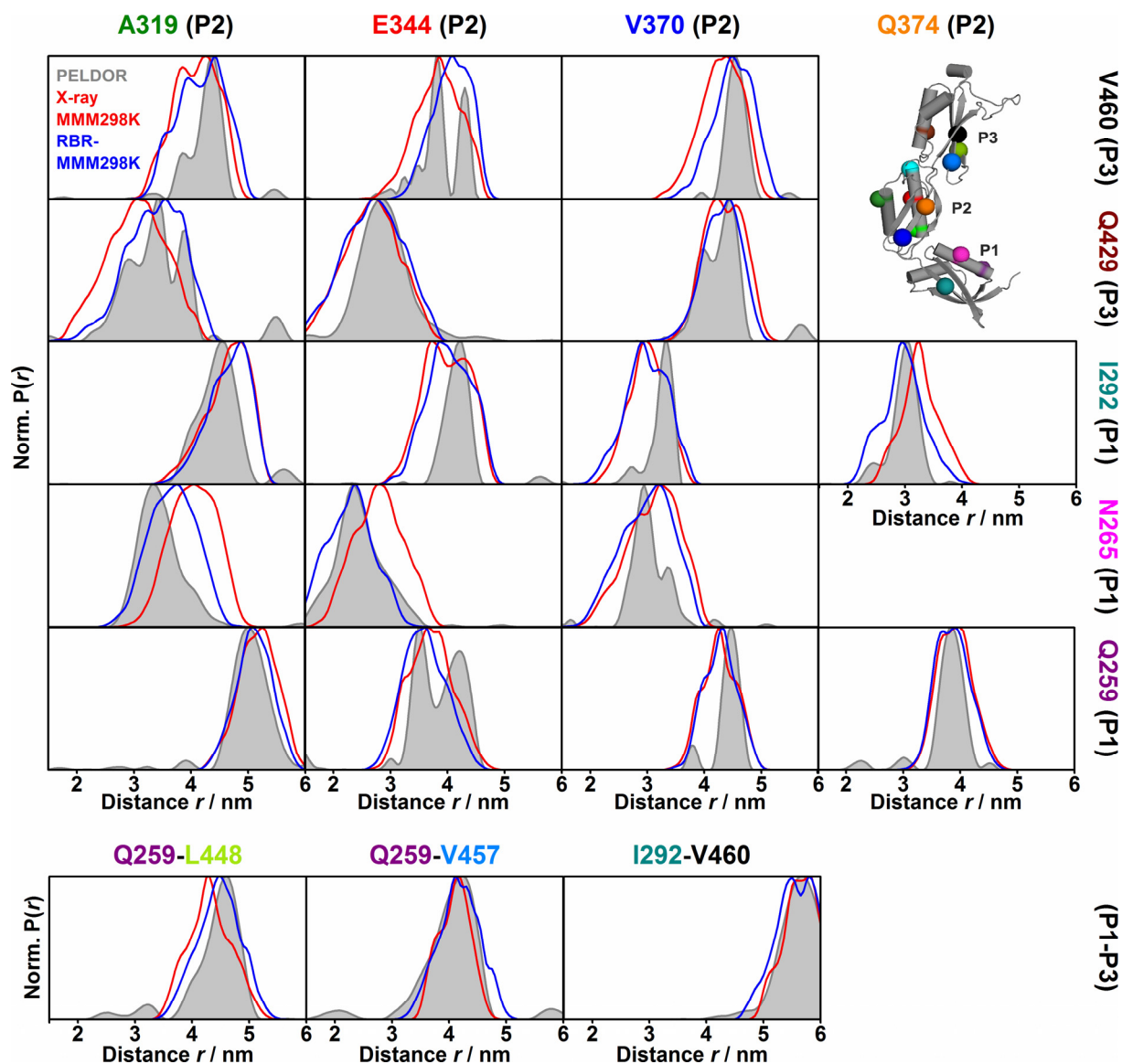


Figure 3.13: Comparison of experimental (grey) and simulated intra-molecular distance distributions from the rigid body refinement for all inter-POTRA domain restraints. Distance distributions obtained for the best model of the rigid body refinements using the standard library of MMM2013.2 in 298 K mode (red), generated on 3MC8 is compared to the distance distributions obtained by Tikhonov regularization (grey). The rigid body refinement was conducted by Prof. Dr. Thomas Prisner at the Goethe-University. The ribbon representation of 3MC8 indicating the spin labelling positions is given as inset.

Due to the slight change in the conformation *anaP1-anaP2*, the agreement of simulated and experimental distance distributions / dipolar evolution functions for restraints between *anaP1-anaP3* was slightly increased. Especially, the mean distance, as well as width of the distribution for the spin labelled pairs Q259C/L448C and Q259C/V457C were in better accordance with the experimental data. This was in line with the enhanced accuracy observed for the spin labelled pair Q259C/E344C.

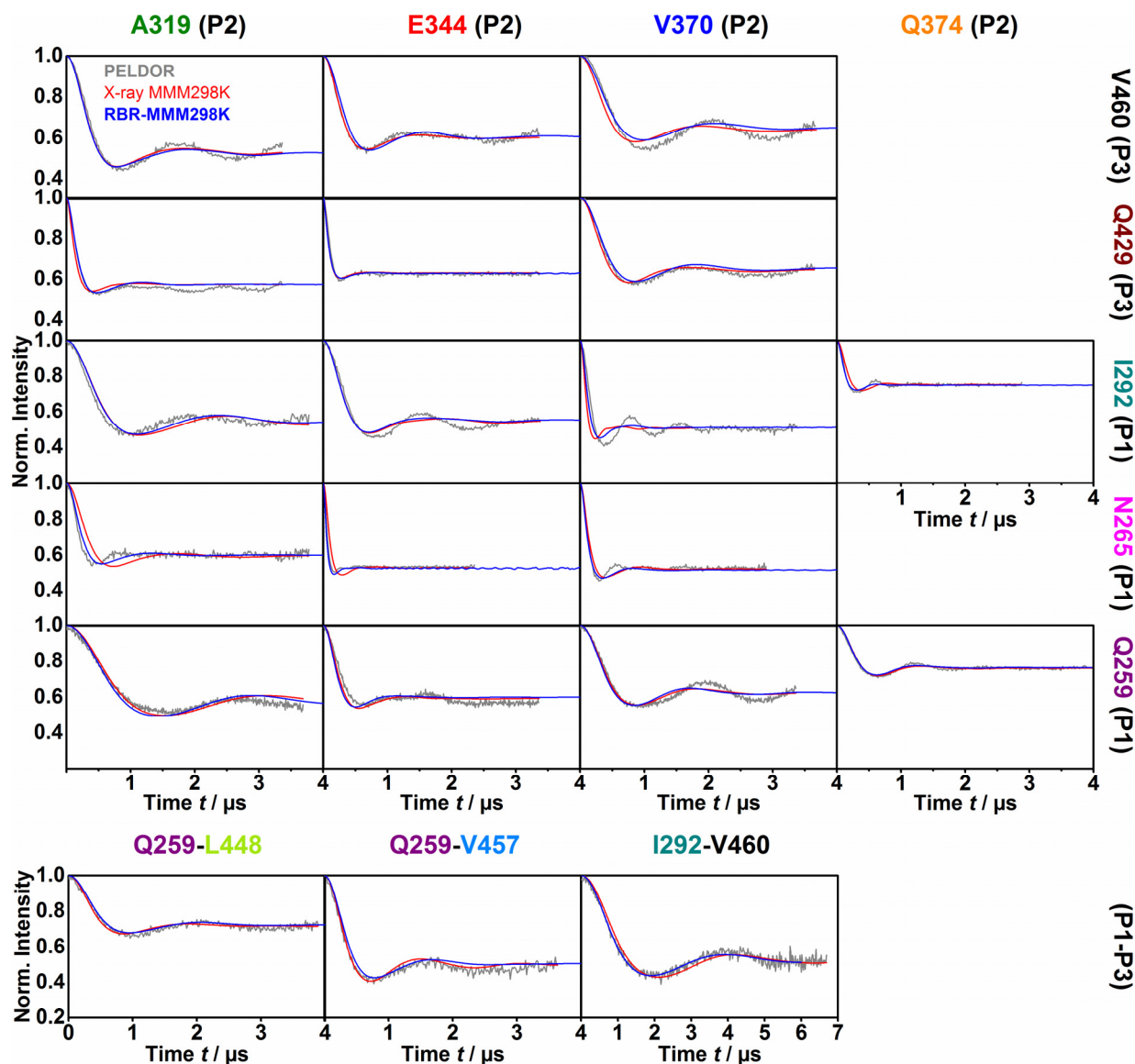


Figure 3.14: Comparison of experimental (grey) and simulated intramolecular dipolar evolution functions from the rigid body refinement for all inter-POTRA domain restraints. Dipolar evolution functions obtained for the best model of the rigid body refinements using the standard libraries of MMM2013.2 in 298 K mode generated on 3MC8 is compared to the background-corrected experimental dipolar evolution functions (grey). Simulations of the dipolar evolution functions for the distance distributions obtained by rigid body refinement were done by the author herself. The rigid body refinements were conducted by Prof. Dr. Thomas Prisner at the Goethe-University

Nevertheless, the over estimation of the spin label flexibility by the rotamer library, which was reflected by broader distance distributions, led to several solutions giving similar good RMSDs between experimental and simulated distance distributions, which were below the error of Tikhonov regularization. Thus, this approach was strongly dependent on the quality of the rotamer library-prediction. Even a self-made rotamer library from the MD simulations of *in silico* spin labelled *anaOmp85* POTRA domains did not lead to a general increase in the similarity of the distance distributions (Figure 6.8 and Figure 6.9). This indicates that even full MD simulations of *in silico* spin labelled proteins were not able to represent the necessary

interaction and the true label flexibility. Thus, none of the rotamer libraries utilized for rigid body refinement results in a better overall agreement of predicted and experimental distributions. This becomes even more obvious when comparing the SF of the distance distributions based on 3MC8 and the best model of the refinements (Table 3.3).

Table 3.3 Comparison of the deviation factor (DF; Eq. 3.1) of the distance distributions predicted for different rotamer libraries and the refined distributions for all inter-POTRA domain variants (N=20).

	MMM 175K	MMM 298K	MD
X-ray	0.59	0.53	0.72
refined	0.43	0.40	0.37

A more realistic refinement approach was perused by Dr. Oliver Mirus using Rosetta. Other than the simplified assumption of the individual domains as rigid bodies, this approach accounts for protein flexibility, side chain rearrangements and putative tertiary interactions of the spin label with the protein. Unfortunately, the inherent flexibility of the spin label flexibility is initially described by a Rosetta in-built rotamer library. Yet, during the refinement process, one single rotamer for each labelling site will be selected to match the experimental restraints for a specific model structure. This might aid to overcome the inherent inaccuracy of the rotamer libraries (for details see Chapter 6.2.5). Furthermore, the correlation of each position by two different sites or even trilateration reduced the degrees of freedom introduced by the MTSSL side chain drastically. A drawback of this approach was the invisibility of the distribution width. The best Rosetta refined model gave an almost complete agreement (~98%) with the most probable distances of the experimental distributions (Figure 6.2 orange lines). Unfortunately, the precision of the Rosetta rotamer library, as well as the increased degrees of freedom due to full protein flexibility, allowed multiple models with a similar good agreement (Top 100 models fall into a score range of ~ 0.6%) with the experimental results in frozen solution.

Thus, both refinement approaches contain a resolution limit due to the underlying rotamer library, resulting in conformational ensembles. Yet, comparison of the conformational space of these ensembles with the conformational space sampled during MD simulations of *anaOmp85* POTRA domains can be beneficial to evaluate the size of this ensemble and the influences of the intrinsic flexibility of the *anaOmp85* POTRA domains on the resolution limit of structure refinement.

3.1.4 Conformational space of the refined ensembles and MD simulations

The MD simulations on spin labelled *anaOmp85* POTRA domains showed only minor deviations in the distribution width. A possible explanation was that the conformational space was not fully sampled by the simulation. Thus, the total possible conformational space was additionally estimated by replica-exchange molecular dynamics (REMD) simulations. In the course of these simulations wild type POTRA domains were simulated simultaneously at various different temperatures and after a certain simulation period, the models (replica) exchanged between the different temperatures (for details see Chapter 6.3.7). In order to visualize the conformational space, twist and swing angles of the simulated structures were calculated. Hereby, the twist angle described a rotational motion about the main axis of the respective domain *anaP1* or *anaP3*. The swing angle described a bending of either *anaP1* or *anaP3* from the main axis of *anaP2*. Comparison of the orientational space to this of the MD simulations *in silico* spin labelled *anaOmp85* POTRA domains showed a large overlap of the orientational space for all domain pairs (Figure 3.15B-G; page 46), especially of the most populated region. This was also the case for the previously published MD simulations (43); however, the present simulations enabled a more comprehensive view due to their multitude, time length and an enhanced sampling method. Therefore, it could be concluded that the total length of the MD on spin labelled *anaOmp85* POTRA domains is sufficient to describe the conformational dynamics of the protein backbone.

The top 100 models of both refinement strategies were located within the conformational space sampled by MD and REMD simulations, by that again showing consistency between the MD simulation approaches (Figure 3.15B-G; page 46). Yet, the conformational space of the *anaOmp85* POTRA domain in frozen solution yielded by both refinement approaches is rather restricted compared to that sampled by the MD simulations on spin labelled POTRA domains and REMD simulations (Figure 3.15B-G; page 46). This is especially observed for the full range of twist motion of *anaP1* with respect to *anaP2* explored during the REMD simulation in a small corridor bounded by the swing angle mostly between 80° and 100° (Figure 3.15 E; page 46).

The small angular spread observed for the orientational ensemble of *anaP2-anaP3* of 40° and 30° for the rigid-body (standard rotamer library of MMM in 298K mode) and Rosetta refinement, respectively, (Figure 3.15B, C; page 46) was in line with the well-defined oscillations of the dipolar evolution functions obtained for these restraints (Figure 6.5).

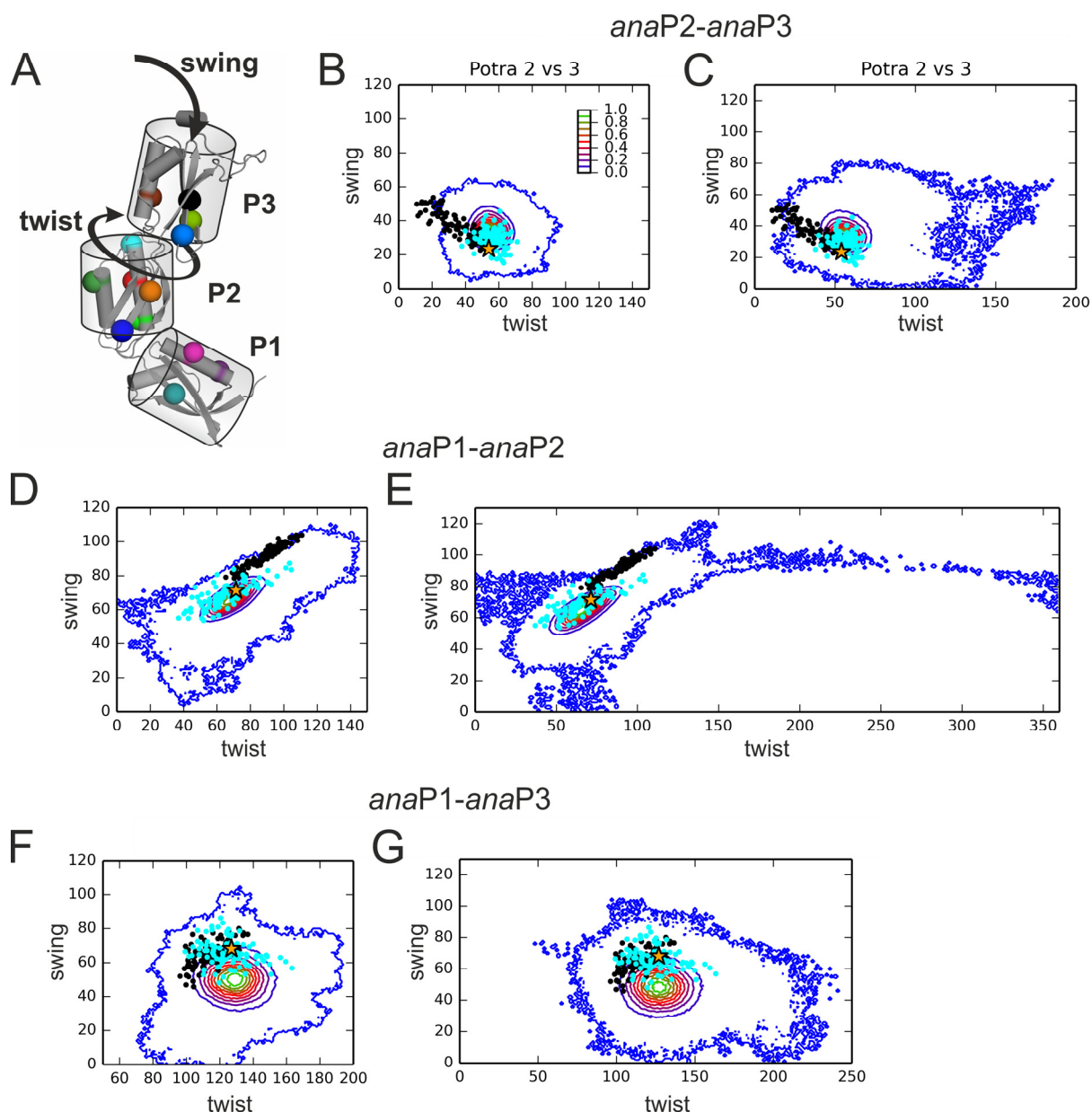


Figure 3.15: Comparison of the orientational space of pairs of *anaOmp85*-POTRA domains obtained by MD simulations of spin labelled POTRA domains and REMD simulations to models obtained from structure refinements using the experimental PELDOR distance restraints. A) Cartoon representation of 3MC8 indicating the rigid bodies, twist and swing angles describing the relative orientation of the domains and labelling positions. B-G) The density maps (10 contour levels) indicate the relative population of the orientational space between adjacent *anaOmp85*-POTRA domains determined by MD simulations of spin labelled POTRA domains (A, C, F) and REMD simulations (B, D, G). In all plots, the asterisk indicates the conformation of the respective domains in 3MC8. The refined structures obtained by rigid body refinement standard MMM2013.2 rotamer library in 298K mode (black dots) and Rosetta refinement (cyan dots) are indicated. The REMD simulations were performed and the angular plots created by Dr. Oliver Mirus and kindly provided for the use in this thesis.

Furthermore, the $C\alpha$ distance distributions of the investigated inter-domain restraints in the REMD simulation were very narrow compared to the experimental distributions confirming the assumption of small backbone movements of these domains during the time course of the simulation (Figure 6.10). Thus, the flexibility of the spin label was large compared to the inter-

domain flexibility and the inaccuracy in orientation prediction mostly due to the inaccuracy in the prediction of the spin label flexibility in both approaches. Nonetheless, the orientation of this domain pair in 3MC8 resembles the putative orientation in frozen liquid solution.

The conformational ensemble of *anaP1* with respect to *anaP2* was larger compared to *anaP2-anaP3* ensemble and described an ellipse with a swing angle dispersion of 30° and 40°, and a twist angle dispersion of 50° and 70° for the rigid-body and Rosetta refinement, respectively (Figure 3.15D, E; page 46). In particular, large twist angle dispersion and the discrepancy in the ellipse centres (rigid body: twist 90°, swing 92°; Rosetta: twist 66°, swing 69°) seemed to be in contradiction with the experimentally observed pronounced dipolar oscillations for restraints of this domain pair (Figure 6.5). Yet, the underlying motion caused only a minor broadening of the C α distance distributions related to residue 374, leading to widths comparable to those of the PELDOR restraints (Figure 6.10). Thus, the underlying flexibility of the domains was still covered by the resolution limit of the rotamer library. Nevertheless, *anaP1-anaP2* were found to be connected in a bit more flexible fashion than *anaP2-anaP3*. This was in accordance with the larger interface between *anaP2-anaP3* [75].

For both POTRA domain pairs the models of the Rosetta refinement showed a larger overlap with the most populated orientations in the MD simulations. Therefore, this refinement approach seemed to be favourable compared to the rigid body approach since it gave a better representation of the ensemble in frozen liquid solution.

The relative orientations obtained for *anaP1* and *anaP3* showed a similar spread of twist/swing angles for both strategies, which was similar to the one observed for the domain pair *anaP2* and *anaP3* (Figure 3.15F, G; page 46). However, the overlap of the refined ensembles was much bigger than observed for *anaP2* and *anaP3*. Looking at the relative orientation of *anaP1* and *anaP3* by MD and REMD simulations reveals a circular orientational space; however, the diameter of the space was $\sim 20^\circ$ larger than the one observed for *anaP2-anaP3*. With the orientational space of the most populated conformations being of the same size as for the model ensembles obtained by both refinement approaches. A more stringent selection of allowed models significantly reduces the spread in angular space of the Rosetta models, which in the case of the rigid body refinement was not true for the orientation of *anaP2-anaP3* (Figure 6.11). Interestingly, the refined ensembles, as well as the conformation of 3MC8, were slightly shifted to larger swing angles. Therefore, it could be concluded that the relative orientation of *anaP1* and *anaP3* present in 3MC8 bear a close resemblance to the refined model ensembles (Figure 3.15 F, G; page 46).

In summary, it can be concluded, that the resolution limit introduced by the rotamer libraries prevents the determination of an explicit relative orientation of the *anaOmp85* POTRA domains in frozen liquid solution. Furthermore, this observation is benefited by the small intrinsic flexibility of the *anaOmp85* POTRA domains observed in the REMD simulations. Thus, especially the slight differences in the domain-domain orientation of *anaP1-anaP2* compared to 3MC8 are hidden. Yet, particularly the Rosetta refinement allowed the identification of a restricted conformational ensemble compared to the MD simulations, with a slightly larger flexibility of *anaP1-anaP2*, which is in good agreement with the experimental results.

3.1.5 Relevance of the restricted flexibility of *anaOmp85* POTRA domains

The three POTRA domains (*anaP1*, *anaP2*, and *anaP3*) are the soluble N-terminal extension of the β -barrel type Omp85³³ of cyanobacterium *Anabaena sp.* PCC 7120 (*anaOmp85* [80]) encode by *alr2269*. *AnaOmp85* is a class II PTBs³⁴ [81] and belongs to the Omp85-TpsB³⁵ superfamily. It is considered the most abundant Omp85 protein in the outer membrane of cyanobacteria [82] and catalyses the insertion of β -barrel proteins into the outer membrane, while the POTRA domains were found to regulate the pore gating of the β -barrel from the periplasmic side of the outer membrane (OM, [75, 80, 83]). The length of the linker between the individual domains in combination with the domain-domain interface determines the flexibility and relative orientation of the domains, which are supposed to be of functional relevance [84, 85]. In contrast to the five POTRA domains of the related Omp85 Bama³⁶ in *E.coli* (*ecP1*, *ecP2*, *ecP3*, *ecP4*, and *ecP5*) the *anaOmp85* POTRA domains bare an N-terminal proline-rich domain (PRD; residues 145–219), for which structural information does not exist [75, 86].

The conformational ensembles of the *anaOmp85* POTRA domains obtained by structure refinement using PELDOR distance restraints showed a small intrinsic flexibility of the three *anaOmp85* POTRA domains and especially *anaP2-anaP3*. In addition, the orientation of these domains in the X-ray structure (3MC8) seems to be a good representative of this refined ensemble. The restricted flexibility of *anaP2-anaP3* is in line with earlier findings Bama, where the most C-terminal POTRA domains *ecP3* to *ecP5* were assumed to bear a rigid architecture

³³ Outer-Membrane Protein of 85 kDa

³⁴ polypeptide-transporting β -barrel protein

³⁵ Omp85 – Two-partner secretion B

³⁶ β -barrel assembly machinery; formerly YaeT.

[87]. This was partially validated for *ecP4-ecP5* in lipid bilayers as well as in detergent by solution- or solid-state NMR and SAXS [87-89], revealing an orientation similar to the X-ray structure of those domains. However, recent X-ray structures (5AYW, 5EKQ, 5D0O) of assembled BAM complexes challenge this assumption [90-92].

The observed restricted flexibility of *anaP1-anaP2* contradicts a switch between different conformations as reported for the five POTRA domains of BamA, which revealed a fishhook-like arrangement of the POTRA domains with a kink between rigid architectures of *ecP5-ecP3* and *ecP2-ecP1* [77], as well as an extended conformation [78]. A similar conformational change was proposed for the two POTRA domains of the class I PTB FhaC³⁷ in *Bordetella pertussis* (*bp*) by PELDOR spectroscopy [93]. Yet, solution and solid state NMR, EPR or SAXS measurements of truncated BamA constructs revealed a reorientation of *ecP2-ecP3*, which is slow or even not present on the timescales of these experiments, especially in lipid bilayers [88, 94-96].

The POTRA domains of BamA interact with all components of the BAM complex [90, 92], thereby providing a scaffold for the complex assembly. Both 5AYW and 5D0O imply that the relative orientation of the POTRA domains and the relative orientation of especially *ecP5* to the β -barrel are an important factor for the proper architecture of the entire complex. A similar observation was made for FhaC, where a 2-amino acid insertion between the two POTRA domains decreased the recognition of the substrate [84].

Unfortunately, the reconstitution of full-length *anaOmp85* into an artificial lipid membrane was unsuccessful. Thus, the orientation of C-terminal POTRA domain *anaP3* relative to the β -barrel remains elusive. Yet, it is possible to infer the potential orientation using the available X-ray structures of full-length BamA (5AYW, 5EKQ, 5D0O) or FhaC (4QKY) and aligning the most C-terminal POTRA domains (BamA: *ecP5*, *anaOmp85*: *anaP3* and FhaC: *bpP2*).

Embedding these models and the experimentally observed restricted flexibility into the context of the outer membrane gives a first insight into the relation between flexibility and the dimension of the PGL³⁸ (Figure 3.16; page 50). The PGL is a porous network [97, 98], which is in close vicinity [99-101] to the outer membrane from the periplasmic side [102, 103]. In *Anabaena* sp. it was found to be 14±2 nm while [104], while in *E. coli* the PGL spans only about ~ 6nm [105].

³⁷ Filamentous emAgglutinin transporter protein

³⁸ Peptidoglycane Layer

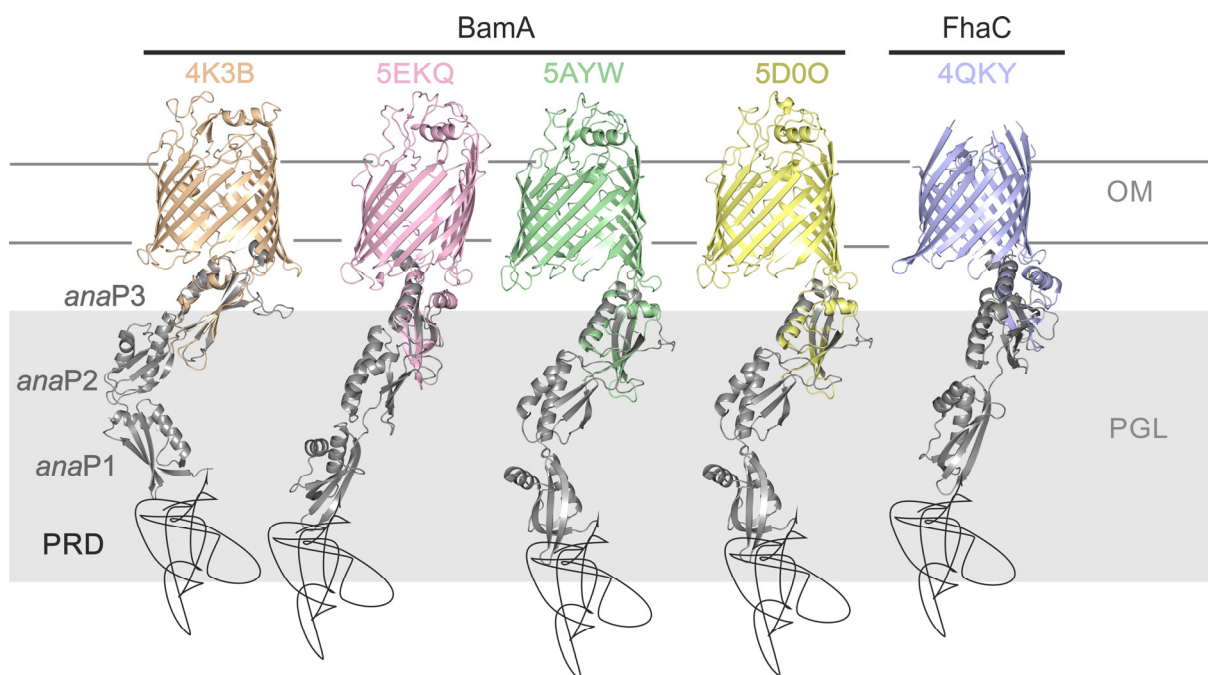


Figure 3.16: Putative orientation of the *anaOmp85* POTRA domains to the β -barrel and integration into the cellular environment. To mimic the potential orientation of the *anaOmp85* POTRA domain with respect to the β -barrel *anaP3* is aligned to *ecP5* of various full-length BamA structures (4K3B (gold); 5EKQ (rose; Complex of BamA, C, D and E); 5AYW (green; Entire BAM complex), 5D00 (yellow, Entire BAM complex)) or *bpP2* of full-length FhaC (4QXY, blue; superseded 2QDZ). ‘PRD’ denotes the proline-rich domain of *anaOmp85*, for which no structural information is available. The models are embedded into the cellular context using a true to scale schematic representation of the outer leaflet of cyanobacteria [104]. The β -barrel is situated in the outer membrane (OM), which is followed by the peptidoglycan-layer after a small spacing.

Using these dimensions, the *anaOmp85* POTRA domains (length in 3MC8 = 9.5 nm) reach only about 6.5 nm into the PGL, leaving them embedded in this confined cellular environment. This would be in good agreement with the restricted flexibility of the domains, only allowing for small thermal fluctuations. In addition, the positioning of the domains within the PGL explains the absence of a kink between *anaP1-anaP2*. The last ~ 6 nm are potentially covered by the PRD³⁹, which are supposed to function as a stiff 'sticky arm', binding rapidly (because of the small surface area and flexibility involved) and reversibly to other proteins [106] acting as an antenna for the incoming substrate as well as a mediator for the oligomerization in membranes.

³⁹ Proline-Rich Domain

3.2 K48-linked ubiquitin chains – a flexible system

Ubiquitination and especially polyubiquitination is one of the most versatile posttranslational modifications, which leads to a multitude of cellular signalling functions such as proteasomal degradation, destabilization, an altered localization or a functional manipulation of the target protein [107, 108]. The information content of ubiquitination is encoded by the linkage type as well as by the chain length, which determine the conformational space of a ubiquitin chain [109]. The linkage type is defined by the K⁴⁰ residue of ubiquitin that is bound to the C-terminus of the previous ubiquitin. One possible linkage type is by K48. Ubiquitin chains of this linkage type were discovered as a signal for proteasomal degradation [110-113], yet the mechanisms of signal recognition are under debate, especially for longer chains [114]. Studying the conformational space of these chains in more detail could lead to a deeper understanding of the aforementioned mechanisms. The large number of published structures of diubiquitin suggests a rather high flexibility of these chains [115-121]. As discussed in the previous chapter, structure refinement or estimation of the conformational flexibility of multi-domain proteins are strongly dependent on the spin label flexibility at a given protein site, when the inherent flexibility of the label exceeds the inter-domain flexibility. For multi-domain proteins with a high intrinsic flexibility the choice of labelling positions that are prone to exhibit a restricted flexibility might be beneficial for the determination of the conformational flexibility. For this purpose, in a first step suitable labelling positions with a restricted flexibility have to be identified. Second, the conformational space of free K48-linked diubiquitin chains will be investigated and, connected to this topic, the capability of PELDOR spectroscopy to determine conformational changes will be demonstrated. Third, the complications arising from highly flexible multi-domain systems will be discussed by the use of polyubiquitin chains. In the last step, the mechanisms involved in the translation of the encoded signal into a cellular response will be explored by the use of UBDs⁴¹ or DUBs⁴².

⁴⁰ K = Lysine; Three letter code Lys

⁴¹ ubiquitin binding domains

⁴² deubiquitinating enzymes

3.2.1 Identification of spin labelling sites with restricted flexibility

Helical secondary structure elements have often been shown to lead to a decreased spin label flexibility, thus minimizing the contribution of backbone flexibility [122-124]. This was observed for *ana*Omp85 POTRA domains as well [63]. Two double-Cys variants T22C/E34C and N25C/E34C, located on the alpha 1 helix of ubiquitin or a nearby position (Figure 3.17), were used to estimate the flexibility of the spin label and secondly to probe the length of the helix and, thereby, the structural integrity of monoubiquitin.

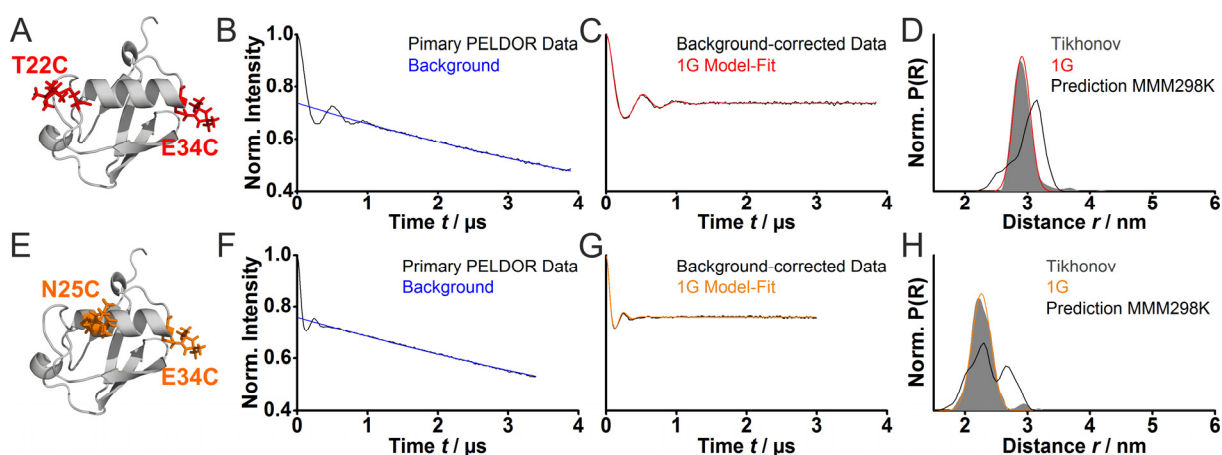


Figure 3.17: Spin label flexibility in doubly spin labelled Cys-variants in monoubiquitin. A) Monoubiquitin variant T22C/E34C; B) Primary 4-pulse PELDOR data with the 3D background shown in blue. C) Background-corrected 4-pulse PELDOR time traces with fit from a single Gaussian model (red). D) Distance distributions obtained by single Gaussian model fitting (red) and Tikhonov regularization ($\alpha=1$; grey) with the distance distributions generated on the X-ray structure (1UBQ) by MMM2015.2 in 298K mode (black). E) Monoubiquitin variant N25C/E34C; F) Primary 4-pulse PELDOR data with the 3D background shown in blue. G) Background-corrected 4-pulse PELDOR time traces with fit from a single Gaussian model (orange). H) Distance distributions obtained by single Gaussian model fitting (orange) and Tikhonov regularization ($\alpha=10$; grey) compared with the distance distributions generated on 1UBQ (black). Ubiquitin variants were assembled, purified and spin labelled by Andreas Kniss from the Lab of Prof. Volker Dötsch at the Goethe-University.

For both double-Cys variants, well-defined oscillations were observed which allowed a clear differentiation between intra- and intermolecular dipolar interactions (Figure 3.17). Such time traces enable the extraction of well-resolved distance distributions by Tikhonov regularization (Figure 3.17) and can be resembled by a single Gaussian distance distribution. These narrow distributions are indicative of a confined flexibility of the spin labels at the chosen positions and also confirmed the rigid structure of helix 1.

Comparison to the X-ray structure (1UBQ) in addition confirmed the confined flexibility since the width of distance distributions predicted based on the standard rotamer library of MMM in 298K mode is similar to that experimentally observed. Furthermore, only a small number of possible rotamers are predicted for the spin labelled positions based on 1UBQ (T22C = 76 rotamers, N25C = 52 rotamers, E34C = 21 rotamers; ~200 rotamers in entire library).

3.2.2 Conformational ensemble of the flexible K48-linked diubiquitin

The confined flexibility observed for the restraints within helix 1 of ubiquitin was very useful for determining the conformational flexibility of K48-linked diubiquitin. Furthermore, labelling within the beta-sheets, which would also lead to a confined label flexibility as well (e.g. residue 370 in *anaP2*), would, in this case, interfere with molecular recognition over the hydrophobic patch [125]. Thus, five variants with spin labelling positions along helix 1 in the proximal⁴³ (p) and the distal⁴⁴ (d) K48-linked ubiquitin moieties were synthesized to characterize the conformational space. (Figure 3.18A).

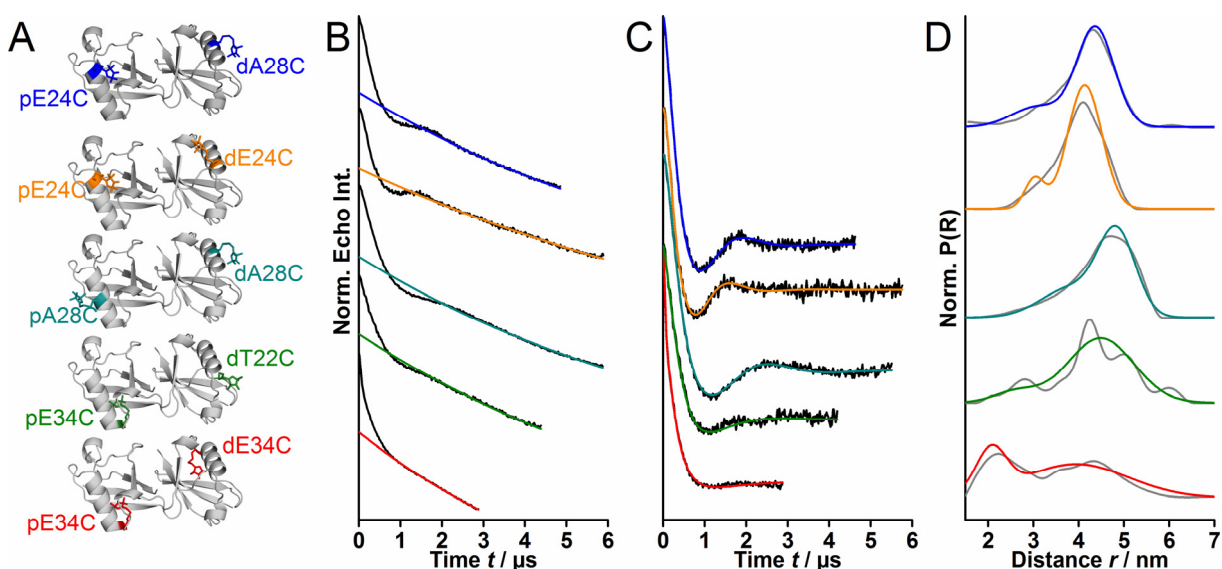


Figure 3.18: Experimental PELDOR Data for five K48-linked diubiquitin variants. A) The labelling positions for each restraint are indicated on the NMR structure 2PEA. B) Primary 4-pulse PELDOR data. The 3D background is indicated pE24C/dA28C (blue), pE24C/dE24C (orange), pA28C/dA28C (cyan), pE34C/dT22C (green) and pE34C/dE34C (red). C) Background-corrected time traces with fits from two Gaussian model fitting. D) Distance distributions from two Gaussian model fitting. Fits from Tikhonov with a regularization parameter of 100 are given for comparison and model validation (grey; Table 6.3). Diubiquitin variants were assembled, purified and spin labelled by Andreas Kniss from the Lab of Prof. Volker Dötsch at the Goethe-University.

Three variants (pE24C/dA28C, pE24C/dE24C, pA28C/dA28C) showed a dipolar oscillation at the beginning, which was already damped after the first oscillation. Nevertheless, the observation time windows of up to 6 μ s were sufficient to enable for a reliable background-correction (Figure 3.18B, C). The broad yet structured distance distributions by Tikhonov regularization could be resembled by the simplified assumption of two-Gaussian distributions (Figure 3.18D). The fast dampening is a strong indication of a flexible connection of both monoubiquitin moieties, e.g. compared to the observations on *anaOmp85* POTRA, where most

⁴³ First ubiquitin in a chain.

⁴⁴ Last ubiquitin in a chain.

of the experimental time traces showed pronounced dipolar oscillations. The other two variants (pE34C/dT22C, pE34C/dE34C) exhibited an even stronger dampening, resulting in an even broader distance distributions. Unfortunately, the PELDOR time window was a bit short for variant pE34C/dE34C. This short time window was related to a rather short phase memory time T_M of this variant (Figure 6.12), which is most likely due to the orientation of the spin label at position 34, which is pointing towards the inside of a ubiquitin moiety.

Comparison of the experimental distance distributions of these inter-ubiquitin domain restraints to structure-based *in silico*-predicted distance distributions shows that the observed flexibility was in accordance with the large number of different published structures of K48-linked diubiquitin in the RCSB⁴⁵ Protein Data Bank [115-121, 126-130] (Figure 3.19).

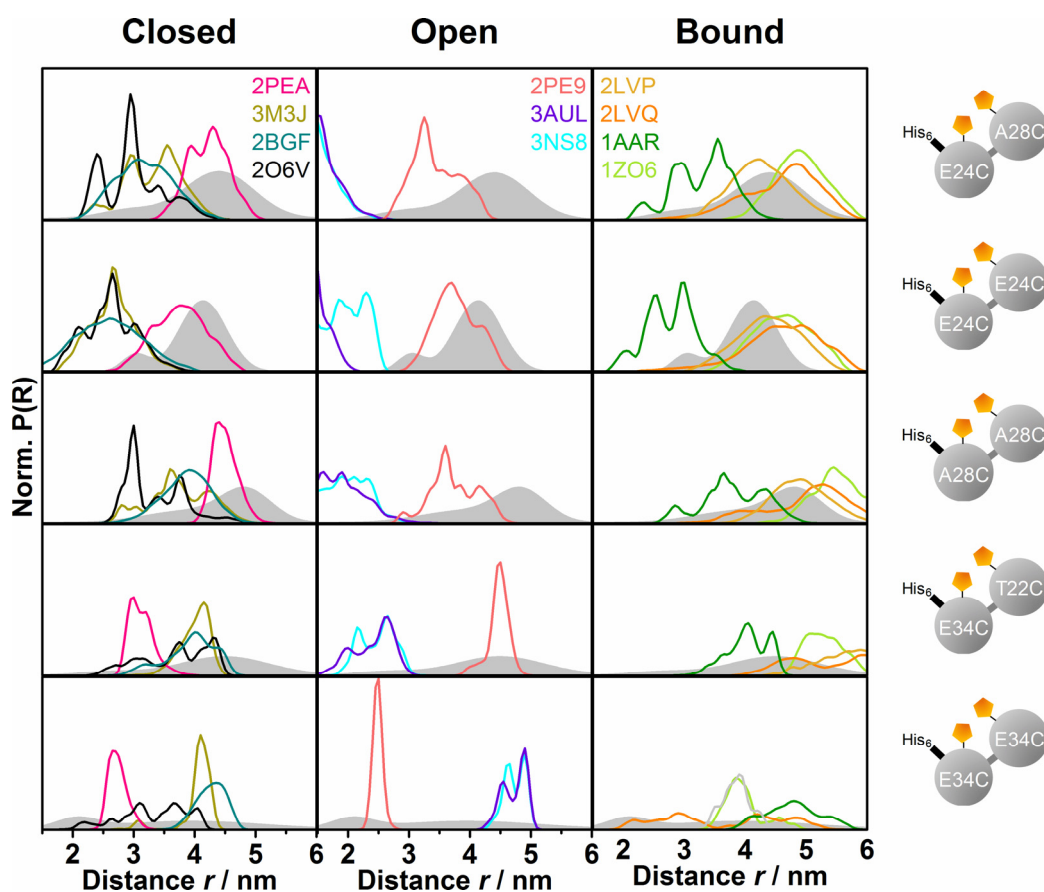


Figure 3.19: Comparison of the experimental inter-ubiquitin distance distributions for various diubiquitin variants to distance distributions generated by MMM2015.2 [38] in 298K mode. The experimental distributions are shown as grey areas (grey). The PDB⁴⁶ structures are classified in close (2PEA, 3M3J, 2BGF, 2O6V), open (2PE9, 3AUL, 3NS8) and bound (2LVP, 2LVQ, 1AAR and 1ZO6) conformations, according to the relative distance of the I44 centred hydrophobic patches.

⁴⁵ Research Collaboratory for Structural Bioinformatics

⁴⁶ Protein Data Bank

However, the rather closed conformation (as defined by the relative distance of the I44-centered hydrophobic patches) observed in 2PEA [117, 118] showed the closest resemblance of the most probable distance. While the closed conformations observed in 2BGF, 3M3J and 2O6V, involving extensive hydrophobic patch interactions [116, 119, 129], and 1AAR, diubiquitin in complex with E2 [115], do not satisfy most PELDOR distance restraints (Figure 3.19). The largest deviations were observed for elongated chain conformations, as seen in the X-ray structures 3AUL and 3NS8 [121]. Yet, interestingly the “open” conformations in 2PE9 [117, 118] or the UBD bound HADDOCK⁴⁷ models 2LVP, 2LVQ [130] and 1ZO6 [128] were in quite good agreement compared to the highly closed conformations. Remarkably, in contrast to the observations on the *anaOmp85* POTRA domains, the widths of the simulated distance distributions are narrower than those experimentally observed. An exception to this were the predicted distance distributions for the UBD bound HADDOCK models 2LVP and 2LVQ [130], however, this is not due to the inaccuracy in rotamer library-prediction but to the inaccuracy of the protein model ensemble (the complete model ensemble are given in Figure 3.22 on page 67). This underlines that the inaccuracy in rotamer library-prediction does not obstruct the determination of inter-domain flexibility but rather, that the lower intrinsic flexibility of the spin labels along helix 1 is beneficial for these investigations.

The resolution limit, observed in the case of *anaOmp85* POTRA domains, should be of minor importance to structural modelling here since the inaccuracy in the predicted flexibility of the spin label was found to be small compared to the inter-domain flexibility.

As in the case of *anaOmp85* POTRA domains, a rigid body assumption for the backbone of the individual domains was pursued. In the present case, mobile side chains are assumed. The rigid bodies were connected via a flexible linker containing ubiquitin residues 72-76 (Figure 6.13). The maximal flexibility of the spin label was given by the rotamer library created with MMM in 298K mode at the given position. During the modelling one single rotamer out of this library, as in the Rosetta refinement, was chosen for a specific model. The software CYANA¹⁶ was employed [37], instead of the home-written MATLAB code to prevent non-biophysical linker conformations or steric clashes. Furthermore, the experimental distance restraints were not used to refine any of the published structures, but as a filtering tool for structural modelling. In an initial step, 10⁶ structural models were calculated by translational and rotational movement of the distal ubiquitin with respect to the proximal one. The first filtering step was the exclusion of models exhibiting sterical clashes, resulting in an ensemble of $\sim 3.7 \times 10^5$ conformers (Figure

⁴⁷ High Ambiguity Driven biomolecular DOCKing

6.14). The second filtering step utilizes the combined probability (Eq. 6.1) of all five experimental distance distributions. Each conformation with a combined probability <1% was dropped, yielding a representative structural ensemble of $\sim 1.4 \times 10^5$ models consistent with the experimental restraints (Figure 6.14; for detail to the structural modelling see Chapter 6.2.6). Out of this ensemble, 3000 individual models were chosen as representative models for visualization (Figure 3.20).

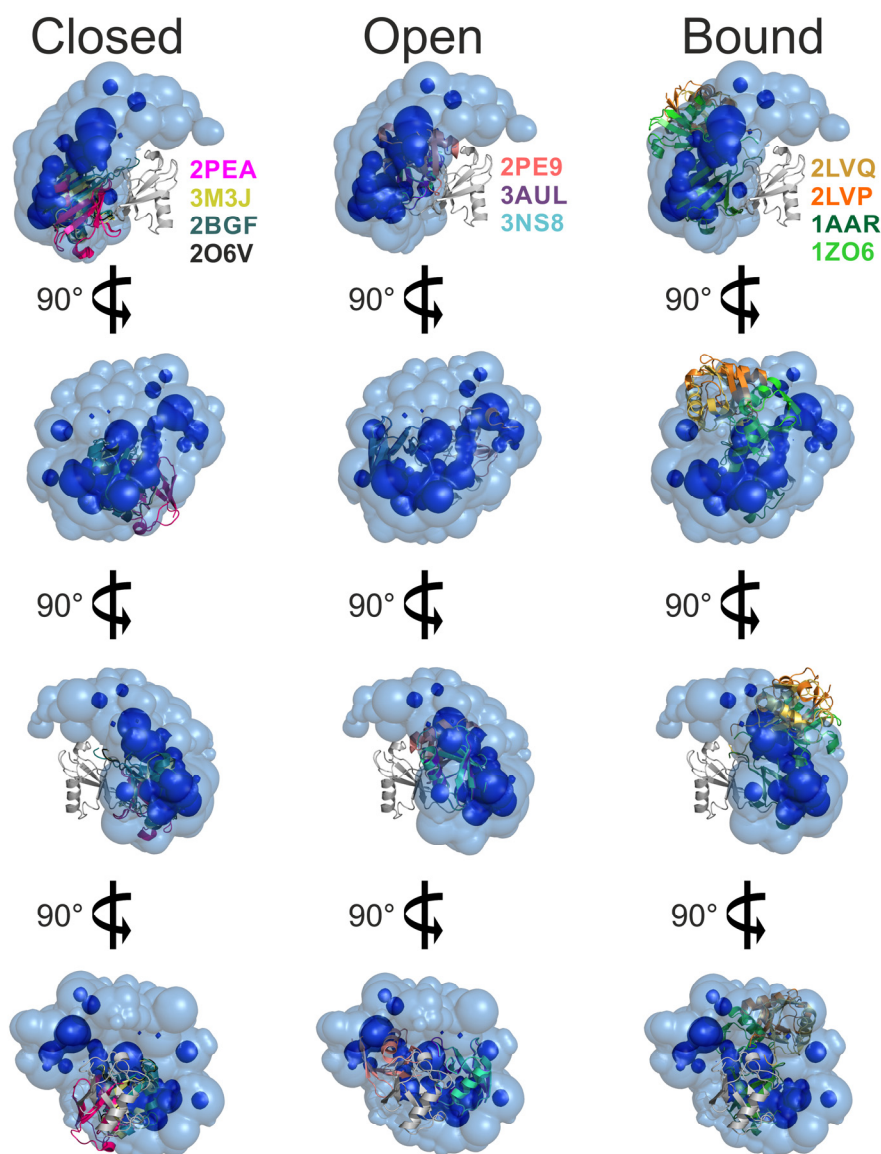


Figure 3.20: Analysis of the conformational space of K48-linked diubiquitin. The conformational ensemble of the distal ubiquitin moiety obtained by CYANA is given for two combined probability cut-offs (light blue, 0.12 and dark blue 0.4) with respect to the proximal moiety (grey). A comparison of the conformational ensemble of the available structures of closed/open free and UBD bound K48-linked diubiquitin is given. The proximal ubiquitin of the structures is aligned onto the reference proximal ubiquitin of the CYANA ensemble. In the case of the diverse NMR structure ensembles, 2LVP and 2LVQ additional overlays with all models are shown in Figure 3.22. Structural modelling employing CYANA was done by Dr. Sina Kazemi from the Güntert Lab at Goethe-University.

In each of these diubiquitin molecules, a sphere represents the centre of mass of ubiquitin (Figure 6.13), indicating the position of the distal ubiquitin with respect to the proximal one and the size of the spheres represents the combined probability of a certain (for details see Chapter 6.3.6). This calculation resulted in a “flower bouquet”-shaped conformational space (combined probability cut-off 0.12 (light blue); Figure 3.20), however with highly populated sub spaces (combined probability cut-off 0.4 (dark blue); Figure 3.20). Comparison of the modelled conformational space to the previously reported structures in the RCSB Protein Data Bank revealed that both ‘closed’ (2PEA, 2O6V, 2BGF and 3M3J; [116, 117, 119, 129]) and ‘open’ (2PE9; [117]) structures showed conformations of the distal ubiquitin moiety at different locations within the highly populated subspace (Figure 3.20; dark blue ensemble). Furthermore, the conformations of published UBD bound structures (2LVQ, 2LVP, 1ZO6 and 1AAR; [115, 128, 130]) are possible but fall into a lower populated conformational subspace (Figure 3.20). This could indicate that binding of certain UBDs uses conformational selection as recognition mechanism. Similarly, compact structures with accessible hydrophobic patches (3NS8 and 3AUL; [120, 121]) are located in less probable regions of the conformational ensemble.

3.2.3 Alterations of the conformational ensemble of K48-linked diubiquitin

The investigation of conformational changes of multi-domain proteins upon their recognition, transport function or due to intracellular conditions is of utmost importance to unravel the structure-function relationship. In terms of diubiquitin, the investigation of effects of different UBDs on the conformation and conformational flexibility might aid to draw conclusions about the mechanisms of molecular recognition. The diubiquitin variant pE24C/dA28C (Figure 3.18), which showed a pronounced yet fast damped dipolar oscillation in free diubiquitin, was used to study the effect of potential interaction partners. First, the effect of the CUE⁴⁸ domains of yeast Cue1 (from here on Cue1; [131]), of the homologous CUE domain of the human E3 ligase gp78 [130] and of yeast Cue2 [132] was probed. The UBDs were all found to have similar binding modes, interacting with the hydrophobic patch of an individual ubiquitin moiety ([133]; Figure 3.21; further information on the UBDs can be found in Chapter 3.2.7).

⁴⁸ Coupling of Ubiquitin-conjugation to endoplasmatic reticulum (ER) degradation

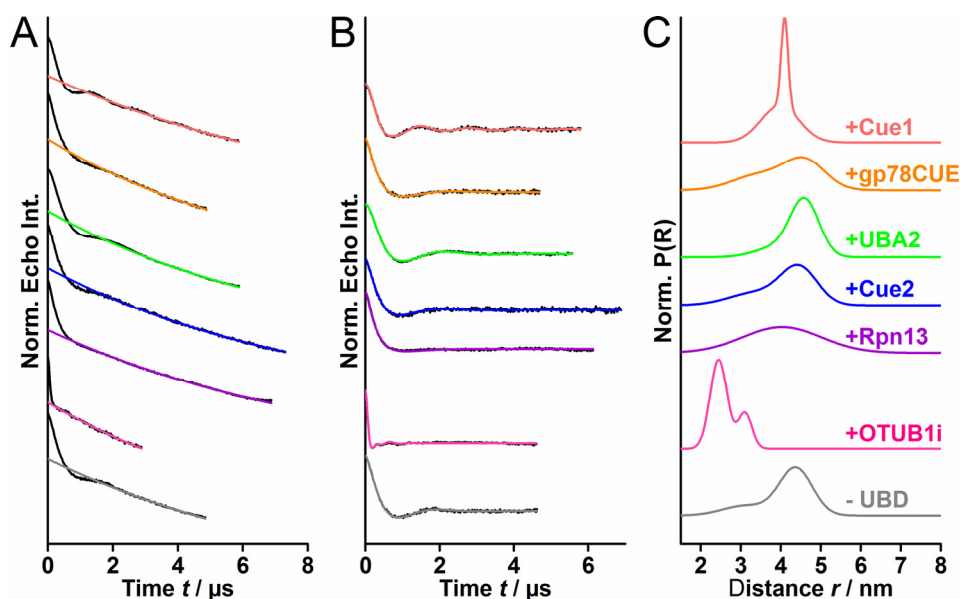


Figure 3.21: The effect of ubiquitin binding domains (UBDs) and deubiquitinating enzymes (DUBs) on the conformational flexibility of diubiquitin. A) Primary 4-pulse PELDOR data of doubly spin labelled K48-linked diubiquitin variant pE24C/dA28C alone (grey) and in complex with the UBDs of Cue1 (light red), gp78CUE (orange), Cue2 (green), UBA2 (blue) and the DUB OTUB1i (pink), indicating the 3D background. B) Corresponding background-corrected 4-pulse PELDOR time traces with fits using a two Gaussian model (Table 6.3), which resemble the distance distributions obtained by Tikhonov regularization. C) Distance distributions obtained by two Gaussian model fitting. K48-linked diubiquitin variant pE24C/dA28C was assembled, purified and spin labelled as well as the UBDs and the DUB utilized in this study by Andreas Kniss from the Lab of Prof. Volker Dötsch at the Goethe-University.

Only the addition of Cue1 was found to have a stabilizing effect on the conformational flexibility of diubiquitin, leading to a bimodal distance distribution with a contribution of $\sim 70\%$ of a broad Gaussian and $\sim 30\%$ of a narrow Gaussian with an error $\pm 5\%$, which was obtained by background-variation. Thus, Cue1 seems to have a unique stabilizing effect within this class of UBDs. The so-called UBA2⁴⁹ domain of human Rad23 [128] was added to diubiquitin to test whether an alternative binding mode, for example binding of the K48-linkage, leads to a conformational change. However, binding of this domain had only minor effects on the conformational flexibility. A similar observation was made in the case of the proteasomal receptor Rpn13⁵⁰, which was shown to interact with the isopeptide linkage connecting the individual ubiquitin moieties [134, 135].

Finally, the effect of a DUB on the conformational flexibility of diubiquitin was investigated. Since DUBs regulated the specific hydrolysis of the inter-ubiquitin linkage [136], all measurements were obtained using a variant with an inactivated catalytic centre (see Chapter 6.2.1) to prevent diubiquitin cleavage. Binding of the inactivated variant of the K48-linkage

⁴⁹ Ubiquitin-associated

⁵⁰ Regulatory Particle Non-ATPase 13

specific DUB, OTUB1⁵¹ ([137]; hereafter OTUB1i), to diubiquitin led to a significant change in the inter-spin distances reducing the mean distance by ~1.5 nm. (Figure 3.21).

The conformational changes introduced by either Cue1 or OTUB1i on the five variants of diubiquitin, which were used to determine the initial flexibility of diubiquitin, were reinvestigated to gain further insights into the underlying binding mechanisms.

3.2.3.1 Conformational selection upon Cue1 binding

Binding of Cue1 to the diubiquitin variants pE24C/dA28C, pE24C/dE24C and pA28C/dA28C shifted the conformational equilibrium of diubiquitin to a distinct conformation of ~30% of the total probability distribution of K48-linked diubiquitin, while the conformational distribution of the pE34C/dE34C variant was shifted to larger distance (Figure 3.22A; page 60). The background-correction for this restraint was achieved by applying a similar background compared to the free variant. The only distance restraint that was nearly unaffected by Cue1 binding is the pE34C/dT22C variant (Figure 3.22A; page 60). The five restraints of Cue1 bound diubiquitin were subjected to structural modelling with CYANA, as the restraints of free diubiquitin, to visualize the differences in the conformational ensembles. For the restricted populations of the Cue1 bound state, the inaccuracy in rotamer library-prediction of the spin label flexibility might introduce a resolution limit. However, due to the broad underlying population of ~70%, this should have a minor effect on the overall size of the ensemble of modelled with CYANA. The reduced conformational space was readily seen in the number of conformations (4.1×10^4 conformations; ~30%; Figure 6.15; page 106) out of the original collision free ensemble ($\sim 3.7 \times 10^5$ conformations) that were in agreement with the five PELDOR restraints (Figure 3.22B; page 60). A representative ensemble of 3000 structures depicts the conformational distribution of the distal moiety of diubiquitin in this complex in Figure 3.22E. The conformational space for a combined probability cut-off of 0.12 includes the underlying broad population, while sub spaces for a combined probability cut-off of 0.4 give an estimate for the conformationally restricted population (Figure 3.22B; page 60).

The size of this sub ensemble might be overestimated due to the inaccuracy in the rotamer library-prediction. Comparison of the conformational ensemble of free and Cue1-bound K48-linked diubiquitin underlined that Cue1 binds under the mechanism of conformational selection, leading to conformations comparable to those observed in 2LVP, 2LVQ [130].

⁵¹ Ovarian Tumor Deubiquitinase, Ubiquitin Aldehyde Binding 1

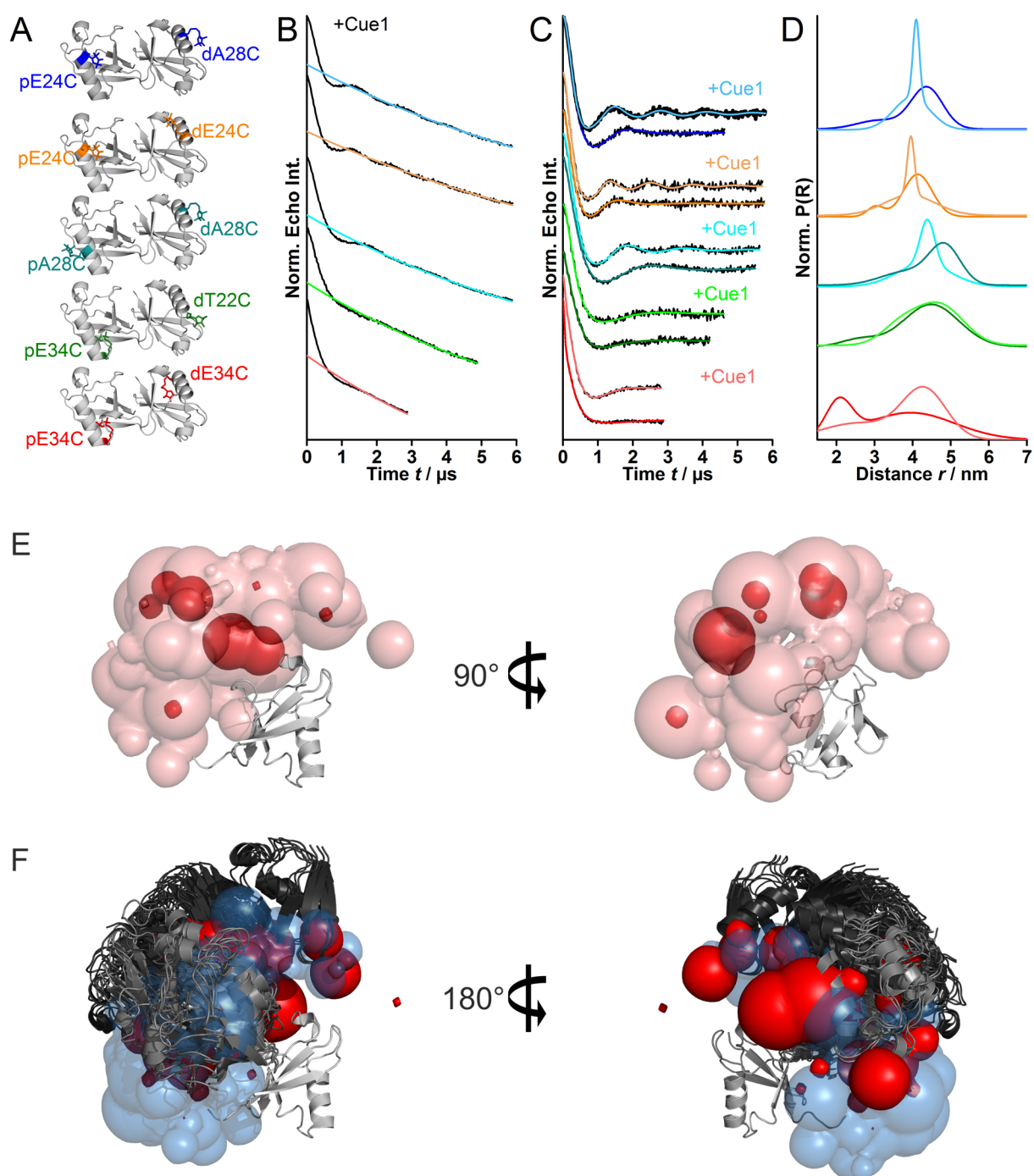


Figure 3.22: The effect of Cue1 on the conformational space of K48-linked diubiquitin. A) The labelling positions for each restraint are displayed on the NMR structure 2PEA. B) Primary PELDOR data. The 3D background is indicated pE24C/dA28C (light blue), pE24C/dE24C (light orange), pA28C/dA28C (light cyan), pE34C/dT22C (light green) and pE34C/dE34C (light red). C) Background-corrected dipolar evolution functions of five different doubly spin labelled diubiquitin variants in complex with Cue1. D) Corresponding distance distributions (dark coloured lines; Table 6.3) in comparison to the distance distributions obtained for the respective unbound diubiquitin variants (light coloured lines). E) The conformational ensemble of the distal ubiquitin moiety obtained by CYANA is given for two combined probability cut-offs (light blue, 0.12 and dark blue 0.4) with respect to the proximal moiety (grey) for the Cue1 bound state. F) Comparison of the conformational ensemble of free (blue) and Cue1-bound (red) diubiquitin at a cut-off 0.2, indicating a conformational selection. Furthermore, the HADDOCK model ensembles of 2LVQ (grey) and 2LVP (black) are depicted for comparison. K48-linked diubiquitin variants, as well as Cue1, were prepared by Andreas Kniss from the Lab of Prof. Volker Dötsch at the Goethe-University. Structural modelling employing CYANA was done by Dr. Sina Kazemi from the Güntert Lab at Goethe-University.

The observed changes could not be attributed to differences in rotamer populations in the course of Cue1 binding since Cue1 binds to the hydrophobic patches [131] centred in the beta-sheets of ubiquitin, which are located opposite to the spin labelling positions in helix 1. Furthermore, the effect could be modulated by binding deficient variants of diubiquitin. The introduction of an Alanine mutation at residues 42 or 70 in either or both the proximal or distal moiety was used to prevent Cue1 binding (Figure 3.23 and Figure 6.16).

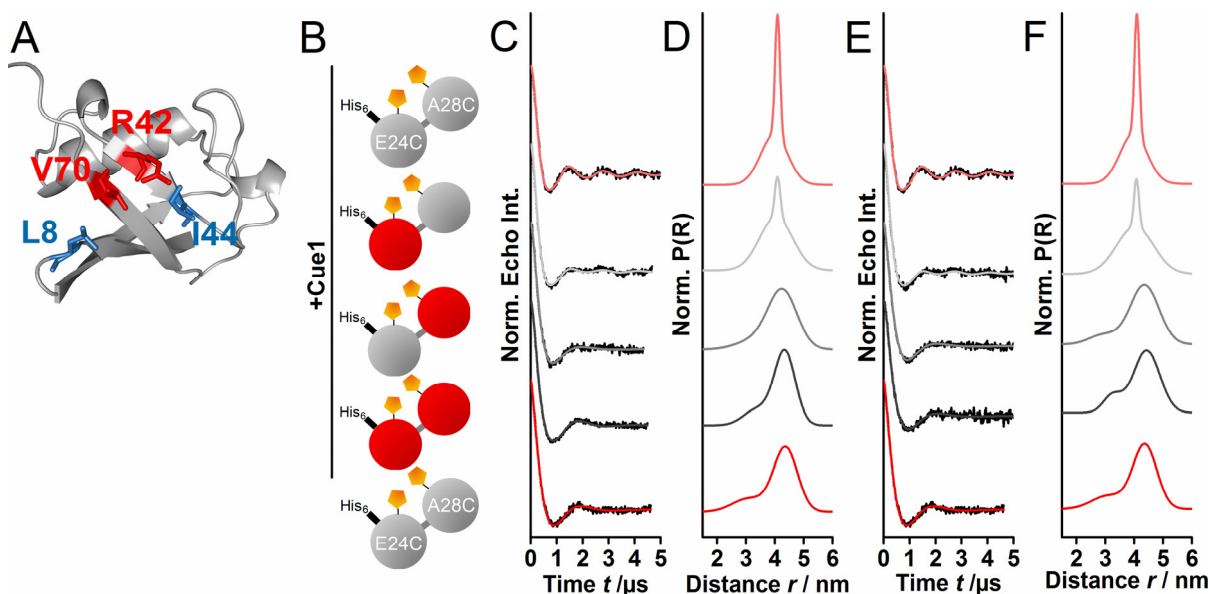


Figure 3.23 Investigation of Cue1 binding deficient pE24C/dA28C K48-linked diubiquitin variants. A) NMR structure of ubiquitin (1UBQ) indicating the hydrophobic patch residues L8, I44 (blue) and V70 (red) as well as R42 (red). R42 and V70 were replaced by A, to create a binding deficiency. B) Schematic representation of diubiquitin variant pE24C/dA28C, indicating the ubiquitin moiety with the binding deficient mutation (red). C) Background-corrected PELDOR time traces of diubiquitin bearing the Cue1 binding deficient mutation R42A in either or both ubiquitin moieties in the presence of Cue1. D) Corresponding distance distributions obtained by two-Gaussian model fitting (Table 6.3). E) Background-corrected PELDOR time traces of diubiquitin bearing the Cue1 binding deficient mutation V70A in either or both ubiquitin moieties in the presence of Cue1. F) Corresponding distance distributions obtain by two-Gaussian model fitting (Table 6.3). Binding deficient pE24C/dA28C diubiquitin variant, as well as Cue1, were prepared by Andreas Kniss from the Lab of Prof. Volker Dötsch at the Goethe-University.

For the proximal R42A⁵² / V70A⁵³ mutations [128, 131], a reduction of the stabilizing effect by ~50% was observed, leading to a bimodal distance distribution with a broad Gaussian of ~90% and a narrow Gaussian of ~10%, with a minor variation of $\pm 2\%$ upon different background-corrections. (Figure 3.23B, C, Table 6.3 and Figure 6.16) However, distal R42A / V70A mutations led to a complete abolishment of the stabilizing effect, indicating that binding of the distal moiety is of importance for the stabilizing effect of Cue1. The efficiency of the binding inhibition was probed with double R42A / V70A variants of diubiquitin, showing time

⁵² R = Arginine; Three letter code Arg.; A = Alanine; Three letter code Ala.

⁵³ V = Valine; Three letter code Val.

traces similar to free diubiquitin. These results were compared to a simple equilibrium-binding model for two independent binding sites on a protein. This allowed estimating the equilibrium concentrations of the possible species of free and Cue1 bound diubiquitin in frozen liquid solution (Figure 3.24).

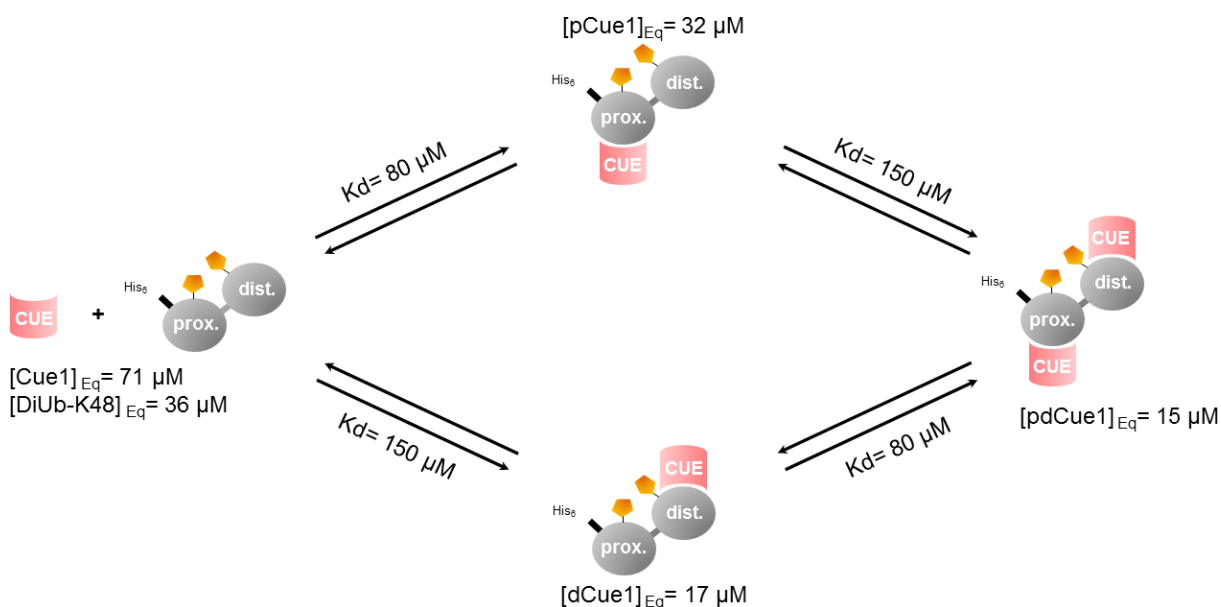


Figure 3.24: Equilibrium binding model for diubiquitin using two independent Cue1 binding sites. The equilibrium concentrations of the possible species of free and Cue1 bound ubiquitin are estimated using the K_d s for proximal and distal binding reported by Delbrück et al. [131] and initial concentrations of Cue1 of $150 \mu M$ and $100 \mu M$ of diubiquitin.

Taking into account that purely proximal binding of Cue1 did not reveal a stabilizing effect in the experiment and purely distal binding led to a 50% reduction of the stabilizing effect, the possible species could be sorted into two groups. First, sum of the equilibrium concentrations of free ubiquitin and the purely proximal bound chain ($[DiUb-K48]_{Eq} + [pCue1]_{Eq}$) which was roughly 70% of the available ubiquitin concentration ($100 \mu M$) and second, the purely distal bound and double bound diubiquitin chain ($[pCue1]_{Eq} + [pdCue1]_{Eq}$), which contributed to about 30%. This was perfectly in line with the experimental distance distribution for the pE24C/dA28V variant with no binding deficiency. In an adapted binding model of an inhibited proximal binding site, purely distal binding made up ~50% of the ubiquitin species, which was in line with the experimentally observed reduction of the conformational stabilization.

3.2.3.2 Conformational remodelling upon OTUB1 binding

Binding of an inactivated variant of the thiol and K48-linkage specific DUB, OTUB1 of the Otubain (OTU) protease family, to diubiquitin variant pE24C/dA28C led to a strong effect, shifting the distance distribution to shorter distances and a narrower distribution (Figure 3.21 and Figure 3.25B-D; page 64). A similar effect was observed for the pE24C/dE24C variant (Figure 3.25A-D; page 64), leading to a narrow population of the distance distribution of about ~70% of the overall population. The shortening of the inter-spin distance was as well observed for variant pA28C/dA28C, yet the restrictive effect as seen for the previous variants was not observed. A narrowing of the distance distribution was again monitored for the pE34C/dE34C variant, however the inter-spin distances increases (Figure 3.25A-D; page 64). As for the case of Cue1 binding, the distance restraint that was least affected by OTUB1 binding was the pE34C/dT22C variant (Figure 3.25A-D; page 64).

The observed narrowing of the distance distributions for the variants pE24C/dA28C, pE24C/dE24C and pE34C/pE34C could introduce a resolution limit in the structural modelling by CYANA, as observed for the *anaOmp85* POTRA domains since the overestimation of the spin label flexibility by the rotamer library might exceed the protein flexibility. Nevertheless, the decrease in the chain flexibility was also revealed by a reduced number of structural models (1.2×10^4 models, Figure 6.17), which were compatible with all five distances restraints for this complex, compared to the free diubiquitin ensemble. A representative ensemble of 3000 structures depicts the conformational distribution of the distal moiety of diubiquitin in this complex (Figure 3.25E; page 64). The overlay of the conformational space of free and OTUB1 bound diubiquitin underlined the observed shift and narrowing of the conformational space (Figure 3.25F; page 64), indicating that OTUB1 binds under conformational remodelling. Hereby, it should be mentioned, that the probability cut-off of 0.2 chosen for the comparison might be an overestimation of the real conformational space of the distal ubiquitin in the OTUB1 bound complex. A comparison to a previously reported X-ray structure of OTUB1 in complex with two individual ubiquitin moieties (4DDI), but with a close vicinity of K48 in first (proximal) moiety and the C-terminus of the second (distal) moiety, showed that this conformation lies on the outer edge of the ensemble (Figure 3.25F; page 64).

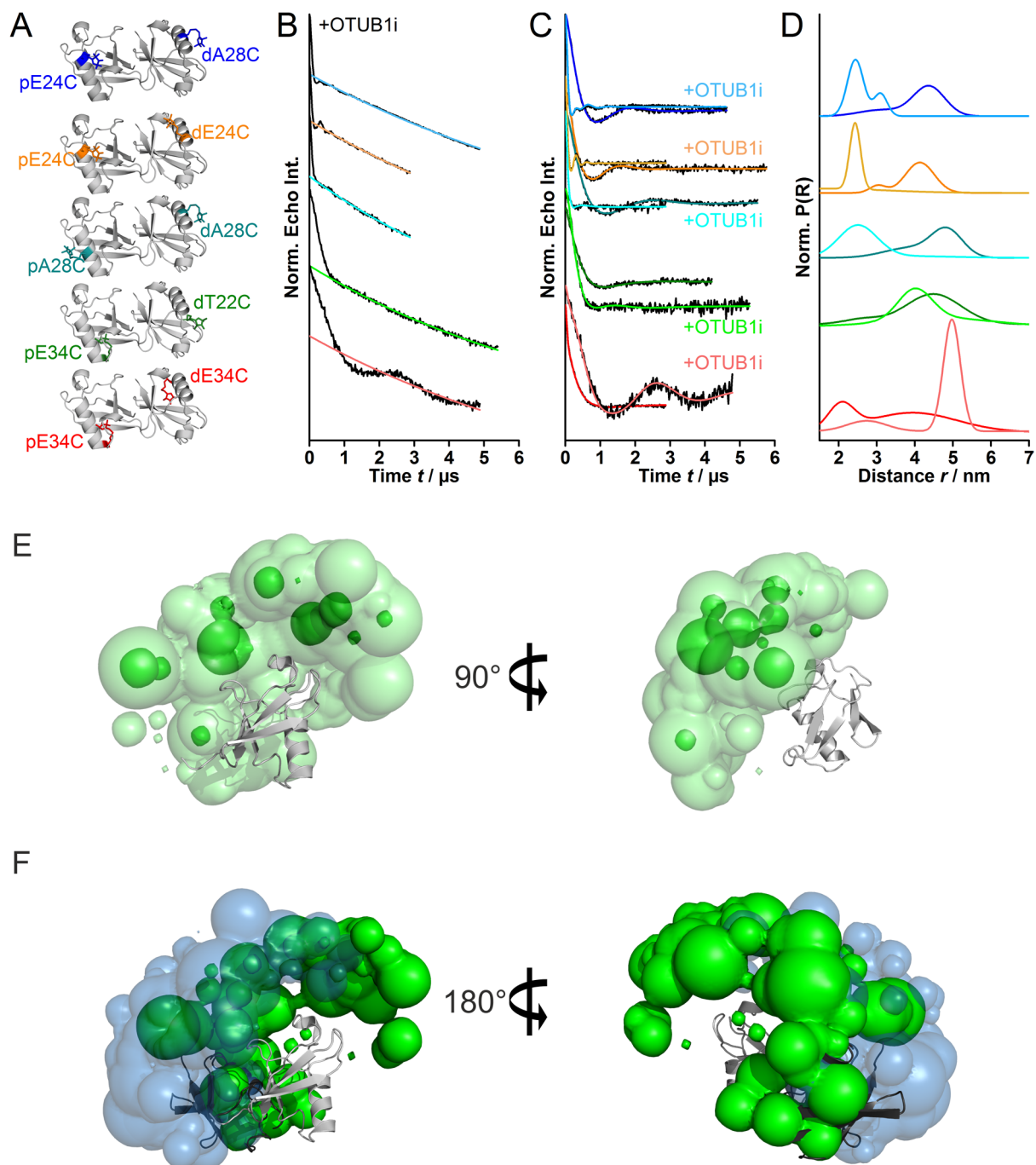


Figure 3.25: The Effect of OTUB1i on the conformational space of K48-linked diubiquitin. A) The labelling positions for each restraint are displayed on the NMR structure 2PEA. B) Primary PELDOR data. The 3D background is indicated pE24C/dA28C (light blue), pE24C/dE24C (light orange), pA28C/dA28C (light cyan), pE34C/dT22C (light green) and pE34C/dE34C (light red). C) Left: Background-corrected dipolar evolution functions of five different doubly spin labelled diubiquitin variants in complex with OTUB1i. D) Corresponding distance distributions (dark coloured lines; Table 6.3) in comparison to distance distributions obtained for the respective unbound diubiquitin variants (light coloured lines; Table 6.3). E) The conformational ensemble of the distal ubiquitin moiety obtained by CYANA is given for two combined probability cut-offs (light green, 0.12 and dark green 0.4) with respect to the proximal moiety (grey) for the OTUB1i bound state. F) Overlay of the conformational ensemble of free (blue) and OTUB1i-bound (green) diubiquitin at a cut-off 0.2, indicating a conformational selection. In addition, the possibly “distal” ubiquitin in complex 1 of 4DDI (black) is shown for comparison. K48-linked diubiquitin variants, as well as OTUb1, were prepared by Andreas Kniss from the Lab of Prof. Volker Dötsch at the Goethe-University. Structural modelling employing CYANA was done by Dr. Sina Kazemi from the Güntert Lab at Goethe-University.

3.2.4 Influence of a large inter-domain flexibility on PELDOR restraints

The observations on K48-linked diubiquitin chains showed that a hindered flexibility of the spin label is beneficial for the investigation of flexible multi-domain proteins since it will not or only slightly contribute to the observed dampening of the dipolar evolution function. This provided the possibility to study the conformational flexibility of larger multi-domain proteins such as longer ubiquitin chains (> 2 moieties), whose conformational space might depend on the chain length. To evaluate this hypothesis double-Cys variants of tri- and tetraubiquitin chains were synthesized, carrying a spin label on the proximal and the distal ubiquitin (Figure 3.26A). The preparation of pure double-Cys variants at the desired ubiquitin moieties was controlled during chain elongation (see Chapter 6.2.1).

The dipolar evolution functions of tri- and tetraubiquitin obtained with the 4-pulse PELDOR sequence revealed an increased dampening in combination with a prolongation of the initial signal decay, compared to mono- and diubiquitin, leading to an enlarged mean distance and a broadening of the distributions (Figure 3.26B and D, Figure 6.18 and Figure 6.19).

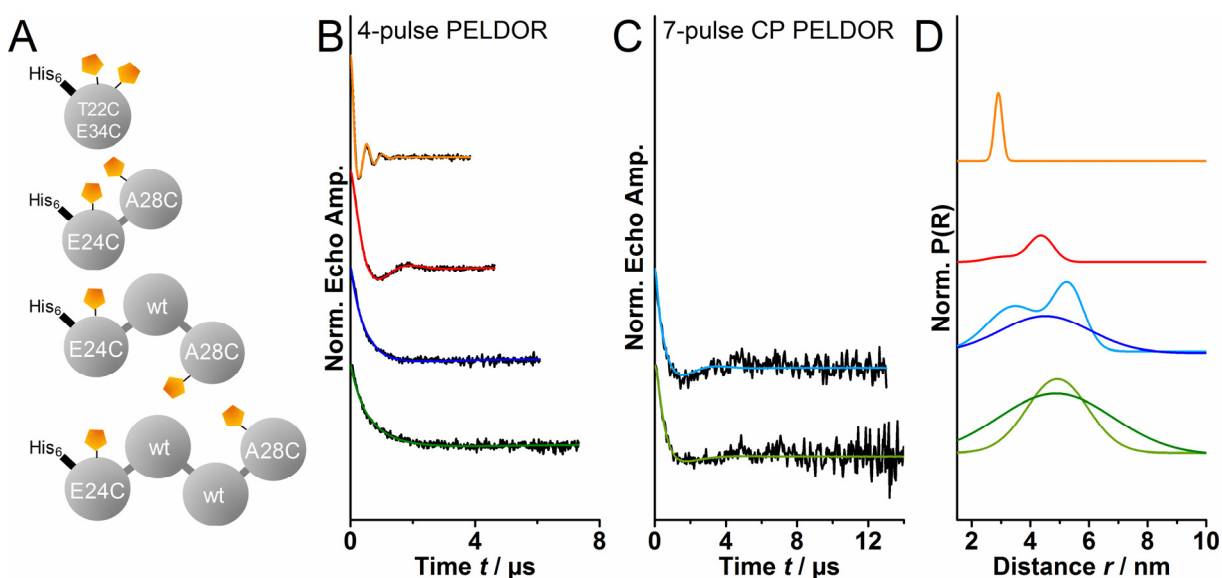


Figure 3.26: Conformational flexibility of K48-linked polyubiquitin chains. A) Schematic representation of monoubiquitin variant T22C/E34C, diubiquitin variant pE24C/dA28C, triubiquitin variant pE24C/dA28C and tetraubiquitin variant pE24C/dA28C. B) Background-corrected 4-pulse PELDOR time traces of doubly spin labelled K48-linked polyubiquitin chains labelled at position pE24C and dA28C in comparison to the monoubiquitin variant T22C/E34C (orange). C) Background- and ‘artefact’-corrected 7-pulse CP PELDOR time traces of tri- and tetraubiquitin labelled at position pE24C and dA28C. The modulation depth is scaled to ~ 0.25 . D) Corresponding distance distributions obtained by one or two Gaussian fits. For tri- and tetraubiquitin the distance distributions obtained by 4-pulse and 7-pulse CP PELDOR are overlaid for comparison (Table 6.3). The 7-pulse CP PELDOR measurements were obtained in collaboration with Dr. Philipp E. Spindler, a Postdoctoral researcher in the group of Prof. Thomas F. Prisner at the Goethe-University. The tri- and tetraubiquitin variants were assembled, purified and spin labelled by Andreas Kniss from the Lab of Prof. Volker Dötsch at the Goethe-University.

This was indicative of a strong rise in chain flexibility as well as a larger distance between the spin labels. Especially, large distances can look like a damped dipolar evolution function if the time window is too short to observe a full dipolar oscillation for a reliable differentiation between inter- and intra-molecular contributions (Figure 6.18).

The utilization of 7-pulse CP PELDOR [48] enabled to enlarge the dipolar evolution time window, thereby leading to a more reliable background-correction (Figure 6.19) and a shift of the boundaries given by Eq. 2.21 and Eq. 2.22. However, it needs to be kept in mind that for an appropriate use of the ‘artefact’ correction procedure, the probability of a double spin inversion p has to be larger than ~ 0.7 (Chapter 2.2.2, [48]). This condition was full-filled for all tri- and tetraubiquitin variants (see Figure 6.19). With the applied experimental conditions, accurate distance and distribution width can be determined up to 9.5 nm and 7.6 nm, respectively ([29]; Eq. 2.21 and Eq. 2.22). The measurements revealed a longer yet fast damped oscillation period for triubiquitin, compared to the diubiquitin variant, which was probably removed in the case of the 4-pulse PELDOR experiment by an underestimation of the intermolecular contributions (Figure 6.18, red background-correction). In the case of tetraubiquitin, the 7-pulse CP PELDOR time trace was strongly damped, yet a completely unmodulated signal as in the 4-pulse PELDOR experiment was not observed, leading to a slightly narrower distance distribution for the 7-pulse CP PELDOR experiment. The modulations visible from $t = 4-8 \mu\text{s}$ were a remnant of the approximate iterative correction procedure, which aims to subtract the additional traces with their appropriate weights, zero times and time traces [48], and were therefore not taken into account for the analysis using a Gaussian model. Nevertheless, the clearly visible oscillation in the case of triubiquitin showed that the application of the recently developed 7-pulse CP PELDOR sequence enabled the determination of a more reliable background-correction, thus allowing the investigation of highly flexible multi-domain proteins and the reliable determination of large inter-spin distance distribution.

3.2.5 Evaluation of the compact fold of tetraubiquitin

The enhanced time window due to the application of 7-pulse CP PELDOR enabled the evaluation of the compact fold of tetraubiquitin as seen in the published X-ray structures [129]. This fold was as well proposed to be the predominant conformation in liquid solution by PRE¹¹ measurements [129]. However, the result on the tetraubiquitin variant pE24C/dA28C challenged this conclusion. Additional triubiquitin (pE34C/dA28C) and tetraubiquitin variants (pA28C/dS57C, pE34C/dA28C) were synthesized (Figure 3.27).

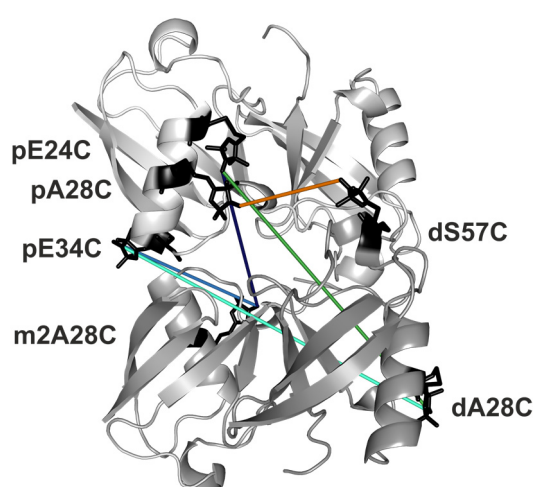


Figure 3.27: PELDOR distance restraints indicated on the X-ray structure of tetraubiquitin (2O6V). The triubiquitin variants pE24C/dA28C (dark blue) and pE34C/dA28C (light blue) are mimicked by *in silico* spin labelling of the second last ubiquitin (abbreviated by m2) moiety in the X-ray structure. *In silico* spin labelling of tetraubiquitin variants, pE24C/dA28C (dark green) and pE34C/dA28C (light green) was pursued at positions as in the EPR samples. The colour code matches that of Figure 3.28. The tri- and tetraubiquitin variants were assembled, purified and spin labelled by Andreas Kniss from the Lab of Prof. Volker Dötsch at the Goethe-University.

The experimental restraints will be compared with distance distributions predictions based on the X-ray structure 2O6V (hereafter 2O6V), which is the only structure of a chain with four ubiquitin bearing all moieties in the asymmetric unit, to evaluate the compact fold as the predominant conformation in frozen solution as well. The other three structures in the RCSB Protein Data Bank either show only two moieties in the asymmetric unit (1TBE, 1F9J; [126, 127]) or bear a cyclic connection (3ALB; [138]). Thus, only 2O6V will be compared to the experimental PELDOR restraints of tri- and tetraubiquitin. In order to mimic a triubiquitin chain *in silico* spin labels were attached to the second last ubiquitin moiety (abbreviated by m2) in 2O6V (Figure 3.27). All variants (Figure 3.27, Figure 3.28A) exhibited strongly damped time traces, which were fitted by broad single Gaussian distributions (exception triubiquitin variant pE24C/dA28C; Figure 3.28; page 71 and Figure 6.19).

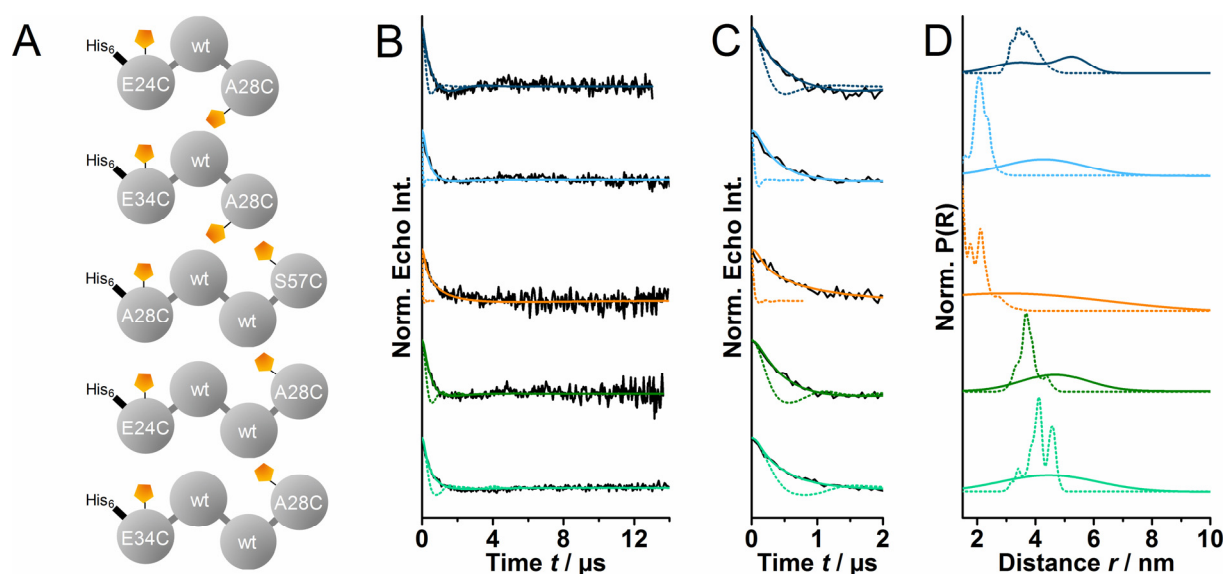


Figure 3.28 Conformational flexibility of K48-linked polyubiquitin chains. A) Schematic representation of the investigated tri- and tetraubiquitin variants. B) Background-corrected 7-pulse CP-PELDOR time traces of two spin labelled triubiquitin variants (pE24C/dA28C (blue), pE34C/dA28C (light blue), and three tetraubiquitin variants (pA28C/dS57C (orange), pE24C/dA28C (green); pE34C/dA28C (cyan)) in comparison to the simulated dipolar evolution functions generated on 2O6V (dotted lines). C) Zoom into early times of the dipolar evolution function for better comparison to the simulation. D) Corresponding distance distributions obtained by one- or two-Gaussian model fitting (solid lines) compared with the simulated distance distributions generated on 2O6V (dotted lines). This reveals a broad conformational space for ubiquitin chains > 3 moieties. The model based analysis of the experimental data was applied to facilitate the interpretation of the results. The respective Tikhonov regularization analysis showed broad, but spiky distributions due to the noise level of some of the datasets. The tri- and tetraubiquitin variants were assembled, purified and spin labelled by Andreas Kniss from the Lab of Prof. Volker Dötsch at the Goethe-University.

The large widths of the distances for longer polyubiquitin chains are strongly indicative of a very broad conformational space. The broadest distribution was observed for the tetraubiquitin variant pA28C/dS57C. A reason for this might be the properties of residue 57, this residue is located in a small alpha-helical segment within a rather long loop connecting the beta-strands 4 and 5. This potentially introduces a further layer of flexibility, leading to an additional expansion of the conformational distribution. Superposition of the simulated and experimental dipolar evolution functions shows a strong discrepancy in dipolar frequency as well as dampening (Figure 3.28B, C and Figure 6.19). Nevertheless, due to the broad experimental distribution, an overlap with the simulated distance distributions was always observed (Figure 3.28D). In contrast to the *anaOmp85* POTRA domains, where both simulated and experimental distribution widths were found to originate predominately from the spin label flexibility, the distribution widths in the case of polyubiquitin chains have different origins. While the rotamer library approach is based on a static structure, hence only taking into account the inherent flexibility of the spin label, the experimental distributions of the polyubiquitin chains are

dominated by the protein flexibility. Thus, a quantitative comparison of the overlap integrals of both distributions, as done for the *anaOmp85* POTRA domains, is not valid.

Elongation of the doubly-spin labelled diubiquitin variant pE24C/dA28C with wildtype ubiquitin to tri- and tetraubiquitin only led to minor effects on the conformational space of diubiquitin, which were within the resolution limit (Figure 3.29A-C and Figure 6.20).

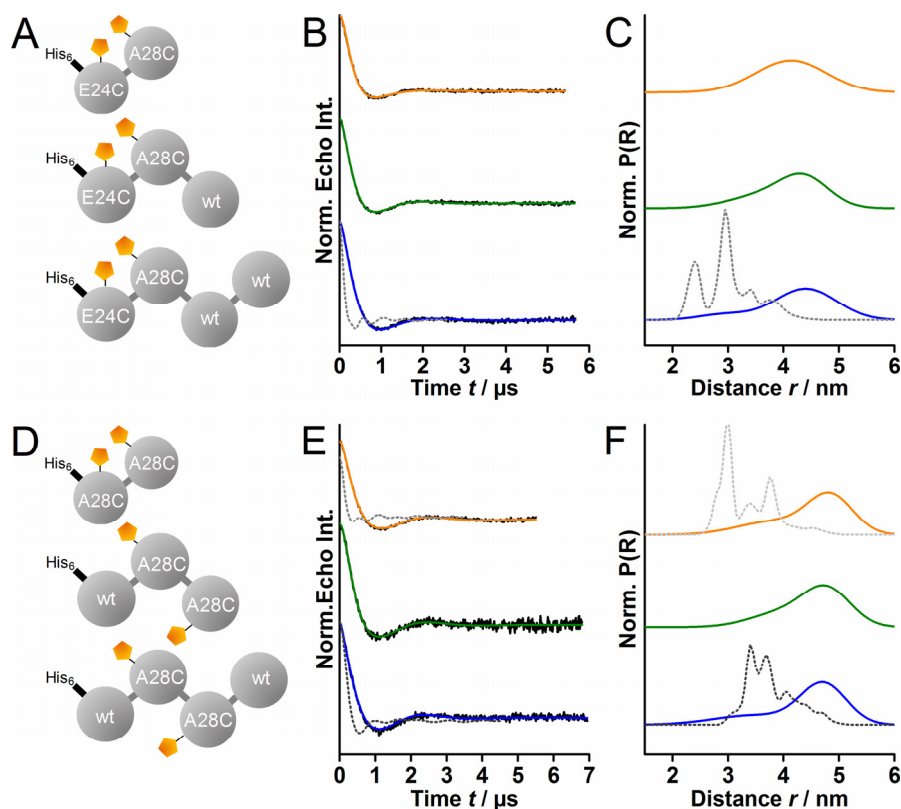


Figure 3.29: Influence of chain length and diubiquitin position within a chain on the conformational flexibility of diubiquitin. A) Schematic representation of diubiquitin variant pE24C/dA28C, triubiquitin variant pE24C/mA28C and tetraubiquitin pE24C/m1A28C. B, C) Experimental PELDOR data and corresponding distance distributions (one or two Gaussian model fits) for distal elongation of diubiquitin variant pE24C/dA28C with wildtype ubiquitin. For the pE24C/m1A28C tetraubiquitin variant (blue) a comparison to the dipolar evolution function and distance distributions generated on 206V at respective positions by MMM2015.2 in 298K mode (grey, dotted line) is shown. D) Schematic representation of diubiquitin variant pA28C/dA28C, triubiquitin variant mA28C/dA28C and tetraubiquitin m1A28C/m2A28C. E, F) Experimental PELDOR data and distance distributions (two Gaussian model fits) for diubiquitin variant pA28C/dA28C, proximal elongation to triubiquitin variant mA28C/dA28C and proximal/distal elongation to tetraubiquitin variant m1A28C/m2A28C. Data for the diubiquitin variant pA28C/dA28C are compared to the dipolar evolution functions and the distance distributions generated on 206V at positions pA28C/m1A28C (light grey, dotted line) MMM2015.2 in 298K mode. The experimental data of tetraubiquitin variant m1A28C/m2A28C is compared to the dipolar evolution function and the distance distributions generated on 206V at respective positions (grey, dotted line) by MMM2015.2 in 298K mode. The di-, tri- and tetraubiquitin variants were assembled, purified and spin labelled by Andreas Kniss from the Lab of Prof. Volker Dötsch at the Goethe-University.

Furthermore, the triubiquitin variant mA28C/dA28C and the tetraubiquitin variant m1A28C/m2A28C showed dipolar evolution functions and distance distributions similar to those of the pA28C/dA28C diubiquitin variant (Figure 3.29D-F and Figure 6.20). Thus, a stabilization of the conformational space of diubiquitin upon chain elongation could be

excluded. This observation was confirmed by comparison to the *in silico* predictions of the respective restraints based on 2O6V. These results indicated that the compact conformation of tetraubiquitin seen in 2O6V is not the predominant conformation in frozen liquid solution at a physiological pH of 7.2. This was as well true for a pH of 4.5 (Figure 6.21), which was reported to facilitate less compact conformations [139]. Revisiting the PRE measurements published alongside with 2O6V, allowed an alternative interpretation of the conformational space sampled in liquid solution. The exchange between the ‘open’ and ‘closed’ conformations of diubiquitin was found to occur on a timescale of 10 ns [117, 118]. Even if the timescale of the exchange would be hundreds of ns in tetraubiquitin the exchange would still be fast on the timescale of the PRE experiment ($\tau_{exchange} < 250 \mu s$, [20]). Under these conditions PRE experiments are usually applied to study sparsely populated conformations of down to 1% of the overall population. Such a sparsely populated state would be perfectly in line with the broad conformational distribution of those chains in frozen liquid solution and a flat energy landscape of the conformational exchange, excluding a conformational restriction due to a slow freezing rate. Nevertheless, also a significant contribution of a completely elongated chain conformation (pearl-on-a-string model; diameter of pearl/ubiquitin 27 Å and string sections/linkage ~15 Å) to the conformational ensemble could be excluded, since the distance between both spin labels in such a conformation would be larger than 10 nm.

3.2.6 Conformational changes of highly flexible polyubiquitin chains

Even with the reliability of the background-correction due to the application of the 7-pulse CP PELDOR sequence, the observed distance distributions were too broad to be considered for structural modelling purposes. This was in strong contrast to the experiments on diubiquitin. Nevertheless, it might be at least possible to observe changes upon binding of UBDs or DUB. This could still aid to understand the binding modes of the individual binding domains.

The strong effects of Cue1 and OTUB1i on the conformational flexibility of diubiquitin gave reason to also investigate complexes of those binders with longer polyubiquitin chains. Complexes of the pE24C/dA28C variants of tri- and tetraubiquitin with either Cue1 or OTUB1i were measured using 7-pulse CP PELDOR. The background-corrected time traces of tri- and tetraubiquitin in complex with Cue1 only showed a prolonged dipolar oscillation while the dampening was unchanged compared to the time trace of the free variant (Figure 3.30A, C and Figure 6.22). This led to distance distributions of similar shape in combination with a shift to

larger inter-spin distances between the proximal and distal ubiquitin (Figure 3.30B, D). However, the conformational selection observed for diubiquitin vanished with increasing chain length. For the homologous CUE domain gp78CUE, which is also involved in chain elongation, no stabilizing effect on the conformational flexibility of diubiquitin was observed.

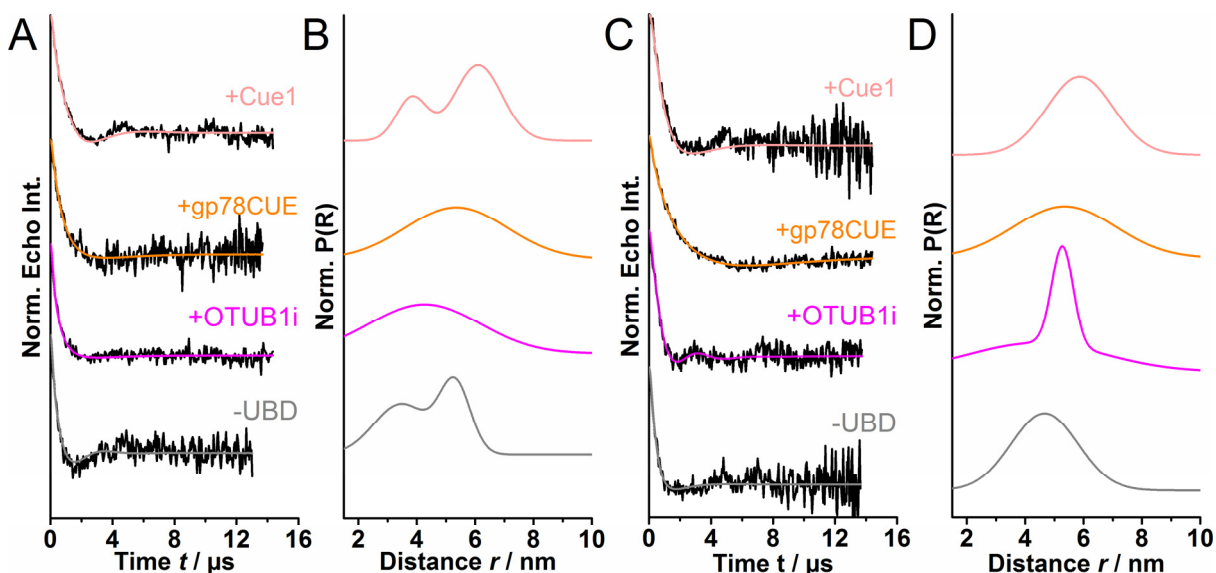


Figure 3.30: The effect of different UBDs and a DUB on the conformational flexibility of K48-linked tri- and tetraubiquitin chains. A) Background- and ‘artefact’-corrected 7-pulse CP PELDOR dipolar evolution functions of spin labelled triubiquitin variant pE24C/dA28C free (grey) and in complex with Cue1 (light red), gp78CUE (orange) and OTUB1i (magenta). B) Corresponding distance distributions. C) Background- and ‘artefact’-corrected 7-pulse CP PELDOR dipolar evolution functions of spin labelled tetraubiquitin variant pE24C/dA28C free (grey) and in complex with Cue1 (light red), gp78CUE (orange) and OTUB1i (magenta). D) Corresponding distance distributions. The tri- and tetraubiquitin variants, as well as Cue1, gp78CUE, and OTUB1i, were prepared by Andreas Kniss from the Lab of Prof. Volker Dötsch at the Goethe-University.

In terms of tri- and tetraubiquitin, the oscillation frequency of the dipolar evolution function was even increased and a stronger dampening was observed compared to the free polyubiquitin chains. This resulted in increased mean distances and broadened distance distributions. Nevertheless, the effects of both UBDs on polyubiquitin chains > 2 ubiquitin moieties are shallow. Only the addition of OTUB1i to K48-linked tetraubiquitin variant pE24C/dA28C resulted in a conformational stabilization of tetraubiquitin leading to a narrower peak at 5.3 nm for about $\sim 40\%$ of the overall population (Figure 3.30D; Table 6.3: Fitting parameters for data analysis with Gaussian model fits.). This conformation is distinct from the conformation in 2O6V with a mean distance of 3.8 nm and a width of 0.4 nm. Other than for diubiquitin, where binding of OTUB1 introduced a conformational remodelling (Figure 3.25), 7-pulse CP PELDOR on tetraubiquitin implied a conformational selection rather than an active remodelling of the entire topological arrangement of tetraubiquitin. The broadening effect on the pE24C/dA28C triubiquitin variant could be explained by the binding mode of OTUB1i as well

as its size (31 kDa) compared to the triubiquitin chain (25.5 kDa). Thus, it was unlikely that two individual DUBs can simultaneously bind the two isopeptide linkages in triubiquitin, leaving always one ubiquitin molecule highly mobile.

3.2.7 Relevance of the flexibility of K48-linked chains for recognition

The 76-amino acid protein ubiquitin (Figure 3.31) is a key player in the posttranslational modification in eukaryotic cells, since ubiquitination and especially polyubiquitination of proteins leads to a multitude of proteolytic and non-proteolytic signalling functions such as proteasomal degradation, destabilization, an altered localization or a functional manipulation of the target protein [107, 108]. A malfunction of any of these can lead to pathological diseases, e.g. Parkinson's disease, cystic fibrosis or an altered immune response [140].

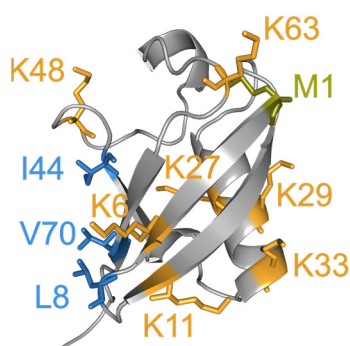


Figure 3.31: Ribbon representation of the X-ray structure 1UBQ of monoubiquitin. The eight lysine residues (orange), the methionine M1 (yellow) as well as the three hydrophobic patch residues (blue) are indicated

Eight different linkage types (K6⁵⁴, K11, K27, K29, K33, K48, K63 or M1⁵⁵), of highly diverse conformations, chain types (homotypic, heterotypic or branched) and chain lengths build the so called ‘Ubiquitin Code’ [108]. The highly complex pool of ubiquitin-modifications is ‘written’ by the concerted action of ubiquitin-activating enzymes (E1), ubiquitin conjugating enzymes (E2) and ubiquitin ligases (E3) [111, 141]. Thereby the E2 enzymes mainly specify the linkage type, while E3 enzymes are the primary determinants of substrate specificity [142, 143]. The resulting ubiquitin chains are recognized and the contained signal is ‘read’ by ubiquitin binding domains (UBDs, [125]) using either the canonical hydrophobic I8⁵⁶, I44, V70⁵⁷-containing patch of ubiquitin or the specific linkage type. The chain length can be sensed when multiple UBDs are arranged in tandem [144]. The ubiquitination of proteins is a reversible process,

⁵⁴ K = Lysine; Three letter code Lys

⁵⁵ M = Methionine; Three letter code Met.

⁵⁶ I = Isoleucine; Three one letter code Ile.

⁵⁷ V = Valine, Three letter code Val.

which is regulated by an ‘erase’ process specifically hydrolysing the ubiquitin chains by deubiquitinating enzymes (DUBs) [136].

The most abundant linkage type is via K48 [145], which is related to proteasomal degradation [112], with tetraubiquitin as ‘minimal’ signal for an efficient targeting of proteins to the 26S proteasome. The predominant conformation of those chains at near physiological pH of 7.2 was found to be compact and ‘closed’, with the hydrophobic patches buried at the domain-domain interface [116, 117, 129]. However, this conformation would prevent efficient binding of ubiquitin binding proteins [109], e.g. during the sequential assembly of ubiquitin chains by E2 enzymes [146] or interaction with the receptors on the proteasome [129, 137]. Thus, both cases would be strongly interfered or would require an active remodelling of the chains. Fortunately, a rapid conformational exchange was observed by NMR⁴, FRET³ or SAXS¹ studies [117, 120, 129, 137, 147]. Nevertheless, due to the timescale of the experiments or the experimental conditions the entirety of the conformational space of the K48-linked chains and with that the mechanisms of ubiquitin binding during the ‘writing, reading or erasing’ processes (ubiquitination, recognition, and deubiquitination) remain elusive [137].

Embedding the results reported in chapter 3.2 into the biological context might shed light on the binding mechanisms underlying the assembly, recognition or disassembly of K48-linked ubiquitin chains as well as the relevance of chain flexibility for ubiquitin binding.

The large conformational space sampled by K48-linked diubiquitin in frozen liquid solution unifies the previously reported structures as part of an even larger structural ensemble. This indicates a flat energy landscape with no major preference of a certain conformation, which would hint on the relevance of this flexibility for molecular recognition. The effect of interacting proteins, as well as their potential binding mechanism, shall now be discussed by their occurrence in the proteasomal degradation pathway.

Two UBDs, which are involved in the ‘writing’ process of K48-linked ubiquitin chains during the ERAD⁵⁸ pathway in yeast and in mammals, are the CUE domains of Cue1 [148, 149] and gp78 [130], respectively. Cue1 is bound to the E2 enzyme Ubc7 via a U7BR⁵⁹, thus Cue1 takes part in the conjugation step of the ubiquitination, while gp78CUE is part of the E3 enzyme gp78 which catalyses the transfer of ubiquitin from the E2 enzyme (Ube2g2) to a lysine residue of the substrate protein or the K48 of another ubiquitin moiety. The interaction side of both domains on ubiquitin was found to be via the hydrophobic patch. This could also suggest a similar binding mechanism. However, the so different the steps are in which these domains are

⁵⁸ endoplasmic reticulum (ER)-associated protein degradation

⁵⁹ Ubc7 – binding region

involved so different are their effects on the conformational space of K48-linked ubiquitin. While gp78CUE was found to have a minor effect on the conformational space of K48-linked diubiquitin, Cue1 lead to a restriction of the conformational space towards ‘open’ conformations via a conformational selection mechanism. This selection of an ‘open’ conformation is in line with the previous observations by von Delbrück *et al.*, where Cue1 was found to accelerate ubiquitination by orienting the distal ubiquitin moiety relative to the E2 enzyme Ubc7, acting in an E4-like manner [131]. The mild effect of gp78CUE can be attributed to the differential organization of the ubiquitination complexes as this CUE domain is directly located in the E3 ligase. Furthermore, gp78CUE was found to have a ~ 10 fold lower Kd [130], as compared to Cue1 (150 μ M; [131]). Nevertheless, it has to be mentioned that one PELDOR restraint might not be enough to exclude that gp78CUE uses a similar mechanism only selecting a different conformation of the chain.

The recognition of ubiquitin chains and the deciphering of the encoded signal is for example accomplished by the ubiquitin-associated (UBA) domain UBA2 of the proteasomal shuttling factor hHR23A⁶⁰ [128] or a subunit of the regulatory particle of the proteasome such as Rpn13 [134, 135]. Both preferentially bind K48-linked chains in a chain length-dependent manner [150-153]. The results obtained on the pE24C/dA28C of diubiquitin in complex with either UBA2 or Rpn13 show a minor stabilizing effect for UBA2 and even a further increase of the conformational flexibility in terms of Rpn13. Thus, contradicting the picture of a distinct remodelling of the chain conformation for an efficient recognition of the ubiquitin chain. Yet, the minimal length of the K48-linked ubiquitin chain for efficient targeting to the proteasome contains four ubiquitin moieties [112]. The very large conformational flexibility of both tri- and tetraubiquitin are in strong contrast to the reported compact conformation of K48-linked tetraubiquitin involving secondary interactions apart from interactions between hydrophobic patches, where diubiquitin units are stacked onto one another [129] suggesting that no distinct structural motif is generated. Thus, no major structural rearrangement seems to be required for efficient proteasomal recognition by Rpn10 and Rpn13 [154]. Furthermore, it suggests that a long and flexible conformation facilitates the simultaneous binding to both Rpn10 and Rpn13 which were found to be separated by approximately 10 nm [152].

The regulatory step, which opposes the ‘writing’ process is the disassembly of the ubiquitin chains. In order to efficiently hydrolyse an ubiquitin chain DUBs need direct access to the isopeptide linkage between the individual ubiquitin moieties, thus binding necessarily requires

⁶⁰ hHR23A = human homolog of yeast Rad23a

an ‘open’ conformation. A K48-linkage specific DUB is OTUB1 [155, 156], a member of the thiol specific Otubain (OTU) protease family. The observed PELDOR restraints of K48-linked diubiquitin chains in complex with an inactivated mutant of OTUB1 (OTUB1i) together with structural modelling suggest a binding mechanism with an initial conformational selection accompanied by a specific remodelling of the chain conformation to allow proteolytic cleavage. This mechanism is evident by the population of chain conformations, which are weakly or even unpopulated in free K48-linked diubiquitin. The action of OTUB1 is especially important in terms of longer chains since the length of K48-linked chains can control the degradation efficiency [131] and the duration of proteasomal degradation [157]. The interaction of K48-linked tetraubiquitin and OTUB1i, yielded a pronounced stabilization of the conformational space, yet leaving the most probable interspin distance almost unaffected. This stabilization might suggest a simultaneous binding of two OTUB1i enzymes, which fixate the ubiquitin chain in an ‘open’ extended conformation for efficient hydrolysis. In contrast, the UBDs involved in chain assembly or recognition only slightly influenced the large conformational space of longer ubiquitin chains, yet leading to an increased mean distance between both spin labels in diubiquitin. This suggests a further unwinding of longer K48-linked chains during elongation processes with local stabilization effects of the distal moieties being more likely as those facilitate chain elongation as observed for the complex of diubiquitin and Cue1.

In summary, ubiquitin chains and especially the minimal degradation signal K48-linked diubiquitin were shown to bare a high conformational flexibility instead of a linkage specific ‘closed’ conformation. This leaves the existence of a conformation dependent degradation signal under question. The investigation of the ubiquitin binding proteins with ubiquitin chains revealed two distinct mechanisms of ubiquitin chain binding such as conformational selection and conformational remodelling during the assembly and disassembly of the chains, respectively. Yet, the conformational selection during chain assembly seems to be more relevant for diubiquitin. Nevertheless, such an interplay of these mechanisms to accomplish protein complex formation has been proposed earlier [114].

Chapter 4

Conclusion and Perspectives

The relative orientation, as well as the conformational flexibility of two multi-domain proteins, were examined within the scope of this thesis. The influence of the intrinsic flexibility of the commonly used spin label MTSSL⁶¹ on structural modelling/refinement, as well as the influence of a large inter-domain flexibility on the interpretability of PELDOR⁶² distance restraints, were evaluated. The thorough analysis of these influences allowed to estimate the applicability of PELDOR spectroscopy in combination with SDSL⁶³ for the investigation of multi-domain proteins to elucidate the structure-function relationship.

PELDOR investigation of the three N-terminal POTRA⁶⁴ domains from cyanobacterial Omp85⁶⁵ of *Anabaena sp.* PCC 7120⁶⁶ (*anaOmp85*) showed pronounced dipolar oscillations for intra- and inter-POTRA domain time traces, leading to narrow distance distribution. This was indicative of a confined intra-, inter-POTRA domain flexibility as well as of a limited/restricted spin label flexibility. Comparison of the experimental intra-POTRA domain distance restraints with the X-ray structure 3MC8 via *in silico* prediction of the distance distribution using the different rotamer libraries revealed an overestimation of the spin label flexibility for the predictions, reflected by broader distance distributions. Nevertheless, it could be concluded that the architecture of the individual domains in frozen liquid solution is very similar to 3MC8, supporting the assumption that the individual domains can be treated as rigid bodies. A similar comparison of the inter-POTRA domain restraints to 3MC8 showed a distinct but slightly different relative domain-domain orientation for the POTRA domain pair *anaP1-anaP2* compared to 3MC8. However, the overestimation of the spin label flexibility by the predictions of the rotamer library approach potentially covered the real magnitude of the differences in the relative domain-domain orientation compared to 3MC8. The consideration of intra-residue C α —H \cdots S δ interactions in the rotamer library slightly reduced the width of the predicted distance distributions, which leads to a closer similarity to the experimentally

⁶¹ 1-Oxyl-2,2,5,5-tetramethylpyrroline-3-methyl

⁶² Pulsed ELection-electron DOuble Resonance; also called Double Electron-Electron Resonance (DEER)

⁶³ Site-Directed Spin Labelling

⁶⁴ POly-peptide TRansport Associated

⁶⁵ Outer Membrane Protein of 85 kDa

⁶⁶ *Anabaena species* Pasteur Culture Collection 7120

observed widths. However, a change in the most probable distances was observed which are different from those observed experimentally. Thus, it was concluded that none of the rotamer libraries was able to give a reliable estimation of the spin label flexibility. Furthermore, the results indicated rather small inter-POTRA domain rearrangements or inter-POTRA domain rearrangements leading to non-varying inter-domain distances, e.g. a concerted reorientation of *anaP1* and *anaP3*. In order to overcome the obstacles related to the use of a static model for an accurate prediction of the flexibility of the MTSSL side chain, as well as to obtain a better estimation of the protein flexibility, MD⁶⁷ simulations of *in silico*-spin labelled *anaOmp85* POTRA domain were performed. Unfortunately, these showed only minor improvements in the prediction of spin label flexibility. In addition, the distribution widths of the MD-based distributions were only slightly broadened compared to the experimental and the rotamer library-predicted distributions, which was a further indication of a confined flexibility of the spin label as well as of the protein backbone. Nevertheless, the deviations in *anaP1* and *anaP2* distances were preserved. These deviations were addressed by structure refinement using two approaches. The first simplified approach refined the relative domain-domain orientation of 3MC8 assuming the individual POTRA domains as rigid bodies, according to the results on the intra-POTRA domain restraints and the similarity to the 3MC8. In this approach the flexibility of the spin label was taken into account by rotamer libraries, keeping the NO-coordinates of the rotamers fixed relative to the individual POTRA domain. The second approach took into account potential backbone movements as well as side chain rearrangements of the *anaOmp85* POTRA domains by first screening the conformational space of the MD simulations to extract an ensemble of starting structures, which were then *in silico*-spin labelled by the internal RosettaEPR Rotamer library and further subjected to a Rosetta relax protocol. This then chose a single rotamer pair for a given structural model. Both refinement approaches resulted in conformational ensembles rather than in an explicit structure with a different orientation of the POTRA domain pair *anaP1-anaP2*. Comparison of these ensembles with the whole possible orientational space, which was estimated by REMD⁶⁸ simulations, led to the conclusion that, in terms of systems with a low intrinsic inter-domain flexibility (narrow C α distribution), the inaccuracy in the *in silico* prediction of the spin label flexibility leads to a resolution limit of structural refinement. This is especially pronounced for labelling position with a more restricted flexibility in the real sample than predicted by the rotamer libraries. The resolution limit could be lowered by designing of new rigid spin labels that can be incorporated into the backbone of

⁶⁷ Molecular Dynamics

⁶⁸ Replica-Exchange Molecular Dynamics

the protein, which would make the prediction of the sidechain conformation unneeded. Furthermore, the force fields utilized in the MD simulations could be improved in order to increase the accuracy of predictions.

In the case of a high inter-domains flexibility, as observed for K48-linked diubiquitin, the resolution limit introduced by the prediction of the flexibility of MTSSL has a minor effect on the determination of the conformational ensemble of these domains. For the investigation of such multi-domain proteins, PELDOR spectroscopy in conjunction with structural modelling is thus found to be a valuable tool. Thereby, the size of the individual domain does not determine the flexibility, since a POTRA domain and a single ubiquitin are of similar size/weight (~8 kDa).

The low impact of the spin label flexibility on the determination of conformational space of flexible multi-domain proteins even vanishes when the inter-domain flexibility leads to a highly unstructured quaternary fold of the multi-domain protein. This is the case for polyubiquitin chains longer than two ubiquitin moieties. Here, the vast flexibility of these multi-domain proteins causes a strong dampening of the PELDOR signal due to the broad distribution of the inter-spin distances. This leads to difficulties in the differentiation between inter- and intramolecular contributions, even within the time window of ~7 μ s obtained with the standard 4-pulse PELDOR experiment at Q-band (34 GHz) in deuterated buffer solution. In this work, it was shown that application of the recently developed 7-pulse CP⁶⁹ PELDOR sequence to highly flexible soluble proteins in deuterated buffer solution provides a significant extension of the observable time window (~15 μ s). This enables a reliable background-correction even for time traces with strongly damped dipolar oscillations, thus increasing the accuracy in determining distance distributions between both spin labels. Thus, it can be concluded that the application of 7-pulse CP PELDOR enables a reliable investigation of highly flexible multi-domain proteins and their conformational distributions.

The procedures described above allowed to draw conclusions about the biological relevance of the PELDOR results and to give an outlook for possible future investigations to enhance the understanding of the structure-function paradigm.

In the case of the *anaOmp85* POTRA domains, the conformational ensemble exhibits a rather small angular spread, which is comparable to the most populated region observed during REMD⁷⁰ simulations. This restricted inter-domain flexibility could be rationalized by the

⁶⁹ Carr-Purcell

⁷⁰ Replica Exchange Molecular Dynamics

location of the *anaOmp85* POTRA domain within the PGL⁷¹, which is a porous network in the close vicinity of the periplasmic side of the outer membrane. A future perspective of this study would be the investigation of the orientation of the POTRA domains with respect to the *anaOmp85* β -barrel using a full-length construct. Here, the application of 7-pulse CP PELDOR will not only allow to address long distances, e.g. between *anaP1* and the β -barrel but also overcome the challenges arising from the lipid environment, e.g. short dipolar evolution time windows due to short T_M times.

The K48-linked diubiquitin chains and especially longer K48-linked ubiquitin chains revealed broad conformational distributions, indicative of a flat energy landscape of the conformational space of these chains. The increasing flexibility only allowed the application of the restraints obtained for K48-linked diubiquitin to structural modelling with a combination of the approaches utilized for the *anaOmp85* POTRA domains within the software CYANA¹⁶, instead of the home-written MATLAB code to prevent non-biophysical amino acid chain conformations or steric clashes of the ubiquitin moieties. The backbone of the ubiquitin moieties was assumed to be a rigid body while the side chains and the inter-domain linker are allowed to move freely. The flexibility of the spin label was resembled by an initial rotamer library. Yet, during the modelling one single rotamer out of this library, as in the Rosetta refinement, was chosen for a specific model. This gave a reasonable model of the conformational space of K48-linked diubiquitin, which is in agreement with the multitude of structures in the RCSB⁷² Protein Data Bank.

Besides, the determination of the conformational ensemble of free K48-linked diubiquitin, it was possible to reveal two distinct mechanisms involved in ubiquitin binding during either generation or disassembly of ubiquitin chains.

The CUE⁷³ domain of Cue1, which takes part in the assembly of ubiquitin chains, uses the mechanism of conformational selectio to stabilize ~30% of the conformational ensemble of diubiquitin in an ‘open’ conformation in order to facilitate chain elongation. Furthermore, it was even possible to estimate the ratio of the possible species of proximally or distally bound Cue1 in frozen liquid solution using a simple equilibrium-binding model for two independent binding sites on a protein. Other than Cue1, the deubiquitinating enzyme OTUB1⁷⁴ uses the

⁷¹ PeptidoGlycane Layer

⁷² Research Collaboratory for Structural Bioinformatics

⁷³ Coupling of Ubiquitin-conjugation to ER degradation

⁷⁴ Ovarian Tumor Deubiquitinase, Ubiquitin Aldehyde Binding 1

mechanism of conformational remodelling to generate a relative orientation of the ubiquitin moieties which would allow an efficient cleavage of the isopeptide linkage.

The application of 7-pulse CP PELDOR to tri- and tetraubiquitin chains revealed a remarkable, yet reliable, broadness of the inter-spin distance distributions of these chains, thanks to the enlarged dipolar evolution time window. This allowed drawing conclusions about the conformational space and its biological role, even if structural modelling does not give conclusive results, due to the high inter-domain flexibility. The broadness of the distance distribution of the proximally- and distally-labelled tri- and tetraubiquitin chains strongly contradicts the accepted model of the compact conformation of the X-ray structure of tetraubiquitin (2O6V) as the major conformation in frozen liquid solution. Furthermore, any diubiquitin moiety within a tri- or tetraubiquitin chain revealed distance distributions similar to that of the corresponding diubiquitin variant. Thus, extensive inter-moiety interactions stabilizing a 'closed' diubiquitin conformation, as seen in 2O6V, were not observed.

Furthermore, it was possible to determine conformational changes of both tri- and tetraubiquitin upon interaction with either Cue1 or OTUB1. This showed that the stabilizing effect of Cue1 on the conformational space of diubiquitin was not transferred to tri- and tetraubiquitin chains. By contrast, the interaction of OTUB1 with tetraubiquitin led to a strong effect, yet more resembling a conformational selection than a remodelling. Along these lines, 7-pulse CP PELDOR could be utilized to probe the conformation of tetraubiquitin or even longer ubiquitin chain upon simultaneous binding to the proteasomal receptors Rpn10 and Rpn13⁷⁵, whose inter-domain distance was found to be ~ 10 nm [152].

As the 'Ubiquitin Code' contains seven further linkage types (K6, K11, K27, K29, K33, K63 or M1) apart from K48-linked chains, the conformational space and especially the conformational changes of these chains upon interaction with specific binding partners is a large field with plenty of open questions. Preliminary experiments on free K11- and K63-linked diubiquitin in comparison the K48-linked diubiquitin already revealed that 4-pulse PELDOR spectroscopy is not only able to determine conformational changes upon ubiquitin binding (Chapter 3.2.3), but also to determine distinct differences in the conformational distributions of these linkage types (Figure 4.1).

⁷⁵ Regulatory Particle Non-ATPase 10 and 13

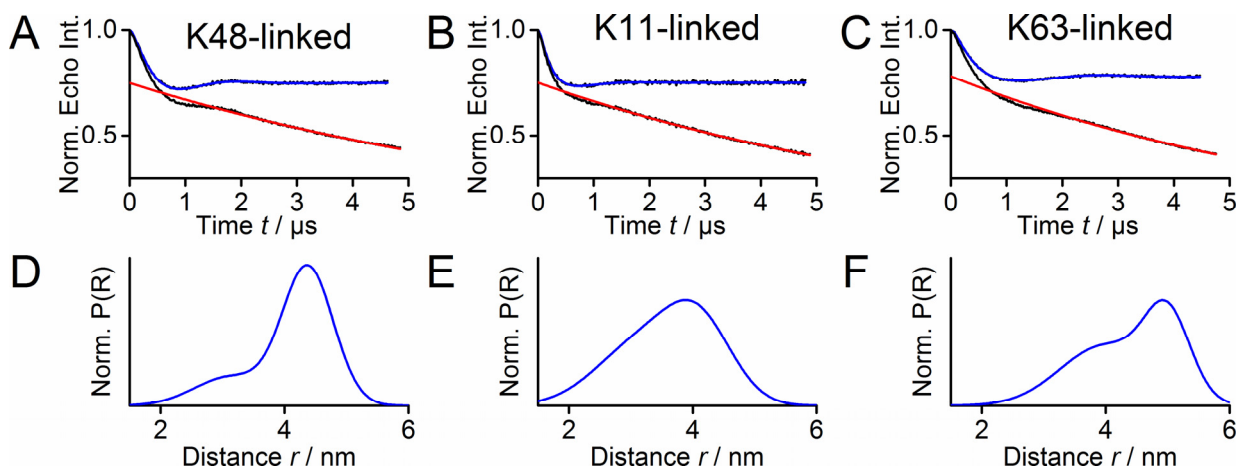


Figure 4.1: Conformational diversity of differently linked diubiquitin chains. A-C) 4-pulse PELDOR time traces of doubly spin labelled K48-, K11- and K63-linked diubiquitin variants pE24C/dA28C. D-F) Resulting distance distributions obtained by two-Gaussian model fitting.

Therefore, it should be possible to gain a deeper knowledge about the structure-function paradigm of the entire ubiquitin code with the benchmarks and methodologies discussed in this thesis.

Chapter 5

Deutsche Zusammenfassung

Die heutige Strukturbiologie verwendet häufig eine Kombination aus experimentellen Datensätzen und computergestützten rechnerischen Methoden, um das Struktur-Funktion Paradigma von biologische Makromolekülen, wie zum Beispiel multi-Domänen Proteinen, zu entschlüsseln. In dieser Arbeit wird dieser kombinierte Ansatz mittels der Anwendung von PELDOR⁷⁶ Spektroskopie und der computergestützten Modellierungen von Konformationsräumen verfolgt. Die PELDOR Spektroskopie in Kombination mit SDSL⁷⁷ ist eine häufig verwendete Methode, um Abstände zwischen zwei ungepaarten Elektronenspins, im Bereich von 1.8 bis 8 nm, und deren Verteilung zu bestimmen. Hierbei ist sowohl die inter-Spin Distanz als auch die Flexibilität des verwendeten Spin Markers und des Proteins im experimentellen PELDOR Signal in Form der Oszillationsfrequenz und deren Dämpfung kodiert.

In der vorliegenden Arbeit wurden die relative Domänen-Domänen Orientierung und die konformelle Flexibilität zweier multi-Domänen Proteine untersucht. Im Rahmen dieser Analyse wurden Hindernisse, die durch die intrinsische Flexibilität des gängigen Nitroxid-Markers MTSSL⁷⁸, eine hohe Flexibilität des Proteinrückgrates sowie große inter-Spin Abstände entstehen, evaluiert.

Zuerst wurden die drei N-terminalen POTRA⁷⁹ Domänen des β -Fass Proteins *anaOmp85* des Cyanobakteriums *Anabaena sp.* PCC 7120⁸⁰ untersucht und der Einfluss der Flexibilität von MTSSL auf eine Strukturverfeinerung, mittels PELDOR Abstandsverteilungen, diskutiert. Besonders im Vordergrund steht hierbei die Genauigkeit der Vorhersage der Flexibilität von MTSSL auf der Basis von Rotamer-Bibliotheken anhand eines statischen Modells (NMR, X-ray).

Als Zweites wurde der Konformationsraum von K48-verknüpften Ubiquitinketten sowie dessen Änderung durch die Bindung von UBDS⁸¹ oder eines DUBs⁸² ermittelt. Anhand dieser Systeme

⁷⁶ Pulsed Electron-Electron Double Resonance = Gepulste Elektronen-Elektronen Doppelresonanz

⁷⁷ Site-Directed Spin Labelling = Zielgerichtete Nitroxid-Markierung von Proteinen

⁷⁸ 1-Oxyl-2,2,5,5-tetramethylpyrroline-3-methyl

⁷⁹ Polypeptid TRansport-Associated = Polypeptid Transport-assoziiert

⁸⁰ *Anabaena species* Pasteur Culture Collection 7120

⁸¹ Ubiquitin Binding Domains = Ubiquitin Bindung Domänen

⁸² DeUBiquitinating Enzym = Deubiquitinierendes Enzym

wurde die Notwendigkeit eines hinreichenden Zeitfensters für die Untersuchung langer inter-Spin Abstände und breiter Abstandsverteilungen erörtert werden.

Die erhaltenen Ergebnisse werden zudem in den biologischen Kontext eingeordnet.

5.1 Einfluss der Nitroxid-Marker Flexibilität auf Strukturverfeinerungen

Die Untersuchung der drei *anaOmp85* POTRA Domänen mittels PELDOR Spektroskopie zeigte ausgeprägte dipolare Oszillationen der PELDOR Zeitspuren sowohl für Spin Marker Paare innerhalb einer POTRA Domäne (intra-POTRA Domäne) als auch zwischen zwei POTRA Domänen (inter-POTRA Domäne). Dies war ein erster Hinweis auf eine eingeschränkte intra-, inter-POTRA Domänen und MTSSL Flexibilität. Der Vergleich der experimentellen intra-POTRA Domänen Abstandsverteilungen mittels *in silico* Vorhersage der Verteilung unter Verwendung verschiedener Rotamer-Bibliotheken zeigte eine Überschätzung der Flexibilität von MTSSL durch die Simulationen, was in breiteren Abstandsverteilungen der Simulationen resultiert. Dennoch konnte die strukturelle Integrität der individuellen Domänen validiert und ihre Ähnlichkeit zur Kristallstruktur 3MC8 festgestellt werden, was die Annahme der einzelnen Domänen als starre Körper erlaubt. Im Falle der inter-POTRA Domänen Abstandsverteilungen zeigte der Vergleich mit 3MC8, insbesondere für das POTRA Domänen Paar *anaP1-anaP2*, eine leicht unterschiedliche Domänen-Domänen Orientierung. Jedoch wurde auch hier eine Überschätzung der Spin Marker Flexibilität durch die Simulationen beobachtet, welche den realen Umfang der Unterschiede in der Domänen-Domänen Orientierung im Vergleich zu 3MC8 überlagert. Die Verwendung von Rotamer-Bibliotheken die $C\alpha-H\cdots S\delta$ Wechselwirkungen des Spin Marker berücksichtigen, führten zu keiner merklichen Verbesserung der Vorhersage. Um die Hürden, zum Beispiel die Unbeweglichkeit der Seitenketten und des Proteinrückgrates, die bei der Verwendung eines statischen Modells (NMR, X-ray) zur Vorhersage der Flexibilität von MTSSL entstehen, zu überwinden, wurden MD⁸³ Simulationen von *in silico* Spin markierten *anaOmp85* POTRA Domänen durchgeführt. Leider führten diese Simulationen nur zu einer kleinen Verbesserung der Vorhersage der Flexibilität von MTSSL. Allerdings sprach die nur leichte Verbreiterung der Abstandsverteilungen gegenüber denen der Rotamer-Bibliotheken sowohl für eine eingeschränkte inter-Domänen, als auch MTSSL Flexibilität in gefrorenen Lösung. Des Weiteren blieben die beobachteten Unterschiede für das *anaOmp85* POTRA Domänen Paar

⁸³ Molekular Dynamics = Molekular Dynamik.

anaP1-anaP2 auch in den MD Simulationen erhalten. Diese Unterschiede wurden mittels zweier Strukturverfeinerungsansätze adressiert. Hierbei ist zu beachten, dass für die Implementierung der mittels PELDOR erhaltenen inter-Spin Abstandsverteilungen in den Verfeinerungsprozess eine *in silico* Vorhersage der Flexibilität von MTSSL benötigt wird. Die gängigste Methode für diese Vorhersage ist die Verwendung von Rotamer-Bibliotheken, welche aus langen MD Simulationen erzeugt wurden. Unter der Anwendung eines Lennard-Jones Potentials und einer bekannten statischen Struktur, zum Beispiel X-ray oder NMR⁸⁴, werden die Rotamere von MTSSL aus der Bibliothek ausgewählt, die an der gegebenen Position energetisch günstig sind. Der erste Ansatz nutzte, in Übereinstimmung mit den Ergebnissen der Intra-Domänen Abstandsmessungen und deren Ähnlichkeit zur Kristallstruktur 3MC8, die vereinfachende Annahme der einzelnen *anaOmp85* POTRA Domänen als starre Körper. In diesem Ansatz wurde die Spin Marker Flexibilität durch Rotamer-Bibliotheken berücksichtigt, wobei die NO-Koordinaten der Rotamere relativ zu denen der individuellen *anaOmp85* POTRA Domäne fixiert sind. Der zweite Verfeinerungsansatz bezog sowohl die Flexibilität des Proteinrückrates, als auch der Seitenketten mit ein. Hierzu wurde zunächst der Konformationsraum der MD Simulationen gefiltert und ein Bündel an Startstrukturen ermittelt die mit einer Rosetta eigenen Rotamer-Bibliothek *in silico* Spin markiert und anschließend einem Rosetta Relaxationsprotokoll unterzogen werden, um das endgültige Strukturbündel zu ermitteln, in dem jede Struktur ein einzelnes Rotamer-Paar enthält. Diese Vorgehensweise soll dazu beitragen die Flexibilität von MTSSL besser darzustellen, indem mögliche Interaktionen mit dem Protein und dessen Aminosäureseitenketten berücksichtigt werden. Bei der Analyse der Verfeinerungen stellte sich jedoch heraus, dass beide Ansätze nicht wie angestrebt in einer expliziten Struktur mit einer veränderten Domänen-Domänen Orientierung von *anaP1-anaP2* resultieren, sondern in mehreren Bündeln von Strukturen. Ein Vergleich dieser Bündel mit dem mittels REMD⁸⁵ Simulationen geschätzten vollständigen Konformationsraum zeigte, dass im Falle von multi-Domänen Proteinen mit eingeschränkter inter-Domänen Flexibilität (schmale $C\alpha$ Abstandsverteilungen) die Überschätzung der Flexibilität von MTSSL, durch die Rotamer-Bibliotheken, zu einem Auflösungslimit von Strukturverfeinerungen führte.

⁸⁴ Nuclear Magnetic Resonance = Kernmagnetische Resonanz; auch Kernspinresonanz.

⁸⁵ Replica Exchange Molecular Dynamics = Replika Austausch Molekular Dynamik.

5.2 Konformelle Ensembles von flexiblen multi-Domänen Proteinen

Die Studie der ‚starr‘ verknüpften *anaOmp85* POTRA Domänen hat gezeigt, dass die Genauigkeit von Strukturverfeinerungen und die Abschätzung der konformellen Flexibilität solcher multi-Domänen Proteinen stark von der Flexibilität von MTSSL an einer gegebenen Position abhängt. Im Falle von multi-Domänen Proteinen mit einer flexiblen Verknüpfung könnte die Wahl von Marker Positionen mit eingeschränkter Flexibilität jedoch von Vorteil sein, um die Proteinflexibilität bestimmen zu können. Daher wurden im ersten Schritt Marker Positionen mit eingeschränkter Spin Marker Flexibilität innerhalb der Helix 1 von Ubiquitin identifiziert. Für die Untersuchung von K48-verknüpften Diubiquitinketten wurden Spin Marker Positionen innerhalb der Helix 1 der proximalen (p) und distalen (d) Domäne gewählt. Die Messung mittels PELDOR Spektroskopie ergaben breite inter-Domänen Abstandsverteilungen, was auf eine flexible Verknüpfung der Domänen hinweist. Der Vergleich dieser Verteilungen mit Strukturen aus der RCSB⁸⁶ Protein Daten Bank mit Hilfe des Rotamer-Bibliotheken Ansatzes zeigte, dass die vorhergesagten Abstandsverteilungen schmäler als die experimentellen Verteilungen sind. Dies führt zu der Schlussfolgerung, dass die inter-Domänen Flexibilität von K48-verknüpften Diubiquitinen die durch Rotamer-Bibliotheken vorhergesagte Spin Marker Flexibilität übersteigt und die Spin Marker Flexibilität somit die Modellierung des Konformationsraumes nicht oder nur wenig beeinflusst. Die anschließend Modellierung wurde mit einem kombinierten Ansatz der Modellierungen der *anaOmp85* POTRA Domänen in der Software CYANA⁸⁷ durchgeführt. Hierbei wurde das Proteinrückrat als starr angenommen, die Flexibilität des inter-Domänen Linkers und der Seitenketten jedoch berücksichtigt. Die Flexibilität der MTSSL Seitenkette wurde durch eine Rotamer-Bibliothek vorgegeben. Während der Modellierung wurde jedoch jeweils ein Rotamer Paar für ein explizites Model ausgewählt. Der erhaltene Konformationsraum ist in Übereinstimmung mit der Vielzahl an bekannten Strukturen.

Neben der Bestimmung des Konformationsraumes von ungebundenen K48-verknüpften Diubiquitinketten wurden im Rahmen dieser Studie die Änderungen des Konformationsraumes durch die Bindung von UBDs und eines DUBs untersucht. Hierbei zeigten nur die CUE⁸⁸

⁸⁶ Research Collaboratory for Structural Bioinformatics = Forschungszusammenschluss für strukturelle Bioinformatik.

⁸⁷ Combined Assignment and dYnamics Algorithm for NMR Applications = Kombiniertes Zuordnungs- und Dynamik Algorithmus für NMR-Anwendungen.

⁸⁸ Coupling of Ubiquitin-conjugation to endoplasmatic reticulum (ER) degradation = Kopplung von Ubiquitin-Konjugation die endoplasmatische Retikulum assoziierte Degradation.

Domäne von Cue1 und das deubiquitinierende Enzym OTUB1⁸⁹ einen eindeutigen Effekt. Cue1, welche an den hydrophoben Bereich einer Ubiquitineinheit bindet, führte zu einer Verschiebung des konformellen Gleichgewichts von K48-verknüpftem Diubiquitin zu einer bestimmten Konformation die ~30 % der gesamten Wahrscheinlichkeitsverteilung ausmacht. Dieser stabilisierende Effekt zeigte sich in einer Reduktion des mit CYANA modellierten Konformationsraumes. Dieser Effekt ist zu ~50 % von der Bindung von Cue1 an die distale Ubiquitin Domäne abhängig. Anders als die Bindung von Cue1, bewirkte die Interaktion von K48-verknüpftem Diubiquitin mit dem DUB OTUB1 eine Verschiebung der Abstandsverteilungen zu vorher nicht oder nur gering populierten Abständen und einer Verschmälerung der Verteilung. Diese Veränderung des Konformationsraumes war in der anschließenden Modellierung mittel CYANA klar zu erkennen.

5.3 PELDOR an hoch flexiblen multi-Domänen Proteinen

Die beobachtete Flexibilität von K48-verknüpften Diubiquitinketten lässt eine Zunahme der Flexibilität mit der Kettenlänge vermuten. Bei der Untersuchung dieser Flexibilität ist eine eingeschränkte Flexibilität, wie im Falle der Marker Positionen in Helix 1 von Ubiquitin, von Vorteil, da die dann beobachtete Dämpfung des PELDOR Signals hauptsächlich durch die inter-Domänen Flexibilität gegeben ist. Um diese Hypothese zu prüfen wurden Tri- und Tetraubiquitinketten hergestellt, die jeweils in der Helix 1 des proximalen und distalen Ubiquitins einen Spin Marker tragen.

Anhand dieser Polyubiquitin Varianten zeigte sich, dass der Nutzen einer eingeschränkten Spin Marker Flexibilität verloren geht, wenn die inter-Domänen Flexibilität zu einer nahezu ungeordneten Quartärstruktur mit einer breiten inter-Spin Abstandsverteilung führt. Die breiten Verteilungen äußern sich in einer starken Dämpfung des PELDOR Signals. Diese Dämpfung führte sogar bei einem langen Zeitfenster von ~7 μ s, die mit der 4-pulse PELDOR Sequenz im Q-band (~34 GHz) an Proben mit deuteriertem Puffer erreicht wurden, zu Schwierigkeiten in der Unterscheidung von intra- und intermolekularen Signalanteile. Die Anwendung der kürzlich entwickelten 7-pulse CP⁹⁰ PELDOR Sequenz, auf Polyubiquitin Varianten in deuterierter Pufferlösung, ermöglichte eine signifikante Verlängerung des detektierbaren Zeitfensters (~15 μ s). Diese langen Zeitfenster erlaubten eine verlässliche Unterscheidung der

⁸⁹ Ovarian Tumor Deubiquitinase, Ubiquitin Aldehyde Binding 1 = Eierstock Tumor Deubiquitinase, Ubiquitin Aldehyd Bindung 1

⁹⁰ Carr-Purcell

intra- und intermolekularen Signalanteile und somit eine höhere Genauigkeit in der Bestimmung der inter-Spin Abstandsverteilungen. Die bemerkenswerte und dennoch verlässlich bestimmte Breite der inter-Spin Abstandsverteilungen erlaubten es Schlussfolgerungen über den zu Grunde liegenden Konformationsraum und dessen biologische Relevanz zu ziehen, auch wenn eine Visualisierung durch eine strukturelle Modellierung zu keinem aussagekräftigen Ergebnis führte. Die weitere Untersuchung von Spin markierten Diubiquitineinheiten in einer Tri- oder Tetraubiquitin Kette ergab Abstandsverteilungen, die mit denen der jeweiligen Diubiquitinvarianten vergleichbar sind. Dies war ein weiterer Hinweis, dass keine Stabilisierung der quartären Struktur von Tetraubiquitin durch starke inter-Domänen Wechselwirkungen vorhanden ist. Zudem war es möglich die Änderung des Konformationsraumes von Tri- und Tetraubiquitin durch die Interaktion mit Cue1 und OTUB1 zu beobachten. Hierbei zeigte sich, dass der stabilisierende Effekt von Cue1 auf Diubiquitin nicht auf Tri- und Tetraubiquitin übertragen wird. OTUB1 führt hingegen auch bei Tetraubiquitin zu einem stark stabilisierenden Effekt und einer Verlängerung des inter-Spin Abstandes und somit der proximalen und distalen Ubiquitineinheit.

5.4 Abschließende Diskussion und Ausblick

In dieser Arbeit wurden zum Einen die Einflüsse der intrinsischen Flexibilität von MTSSL auf Strukturmodellierungen/-verfeinerungen und zum Anderen die einer großen inter-Domänen Flexibilität auf die Interpretierbarkeit von PELDOR Abstandsmessungen evaluiert. Die eingehende Analyse dieser Einflüsse erlaubte die Anwendbarkeit von PELDOR Spektroskopie in Kombination mit SDSL auf die Untersuchung der Struktur-Funktion Beziehung von multi-Domänen Proteinen.

Die Untersuchung der drei *anaOmp85* POTRA Domänen ergab mehrere Bündel an Konformationen mit eingeschränkter inter-Domänen Flexibilität, die auch den am höchsten populierte Konformationen der REMD Simulationen ähneln. Diese eingeschränkte inter-Domänen Flexibilität lässt sich mit der zellulären Umgebung der *anaOmp85* POTRA Domänen im PGL⁹¹ erklären. Der PGL ist eine poröse Schicht, die sich auf der periplasmatischen Seite an die äußere Membran anschließt. Die *anaOmp85* POTRA Domänen ragen in die Poren dieser Schicht, können diese jedoch auf Grund ihrer Länge nicht überwinden. Daher befinden sich die Domänen in einer relativ eingeschränkten zellulären Umgebung, die keine größeren inter-

⁹¹ PeptidoGlycane Layer = Peptodoglycan Schicht

Domänen Bewegungen erlaubt. Eine Weiterführung dieser Untersuchung wäre die Bestimmung der relativen Orientierung der drei *anaOmp85* POTRA Domänen zum transmembranen β -Fass in einem Volllängenkonstrukt von *anaOmp85*. Die Anwendung von 7-pulse CP PELDOR würde hierbei nicht nur die Detektion von langen inter-Spin Distanzen, zum Beispiel zwischen *anaP1* und dem β -Fass, ermöglichen, sondern auch dazu beitragen die Herausforderungen die mit der Lipidumgebung einhergehen (kurze Zeitfenster auf Grund von kurzen T_M Relaxationszeiten) zu überwinden.

Die Untersuchung des Konformationsraumes von ungebundenen Diubiquitinketten oder deren Komplexen mit Interaktionspartnern ermöglichte die Bestimmung der unterschiedlichen Mechanismen der Ubiquitin Bindung im Rahmen des Aufbaus und des Abbaus von Ubiquitinketten. Die Bindung der CUE Domäne Cue1, die in den Aufbau von Ubiquitinketten involviert ist, nutzt den Mechanismus der konformelle Selektion um eine ‚offene‘ Konformation zu erzielen während das deubiquitinierende Enzym OTUB1, das den Abbau von Ubiquitinketten reguliert, zu einer konformationellen Remodellierung der Kette führt, die vermutlich den Zugang des Enzyms zur inter-Domänen Verknüpfung und somit deren Hydrolyse erleichtert.

Die Anwendung von 7-pulse CP PELDOR auf Tri- und Tetraubiquitin erlaubte eine verlässliche Abschätzung der inter-Domänen Flexibilität dieser Ketten. In diesem Zusammenhang konnte die kompakte Konformation der Kristallstruktur (2O6V) von K48-verknüpftem Tetraubiquitin evaluiert werden. Ein Vergleich der experimentellen und simulierten Abstandsverteilung zeigte, dass die kompakte Konformation von 2O6V zwar innerhalb der Verteilungsbreite liegt, jedoch nicht die vornehmliche Konformation von K48-verknüpftem Tetraubiquitin darstellt. Eine nochmalige Begutachtung der PRE⁹² Messungen die zusammen mit 2O6V veröffentlicht wurden, erlaubt eine alternative Interpretation des vorhandenen Konformationsraumes. Der Austausch zwischen der ‚geschlossenen‘ und der ‚offenen‘ Konformation von K48-verknüpftem Diubiquitin erfolgt auf einer Zeitskala von 10 ns. Selbst wenn dieser Austausch im Falle von Tetraubiquitin hunderte von ns dauern würde wäre dies immer noch im Rahmen des schnellen Austausches eines PRE Experimentes ($\tau_{exchange} < 250 \mu s$). Unter diesen Bedingungen werden PRE Experiment meist verwendet, um niedrig populierte Konformationen oder Protein-Protein Interaktionen von bis zu >1% zu beobachten. Ein solcher niedrig populierter Zustand wäre im Einklang mit den in dieser Arbeit erzielten Ergebnissen.

⁹² Paramagnetic Relaxation Enhancement =Paramagnetische Relaxationssteigerung

Des Weiteren erlaubte die Anwendung von 7-pulse CP PELDOR die Detektion von Konformationsänderungen von Tri- und Tetraubiquitinketten durch die Bindung von Cue1 oder OTUB1. Der Effekt von OTUB1 auf Tetraubiquitin ähnelt jedoch eher dem Mechanismus einer konformellen Selektion als einer Remodellierung, wie für Diubiquitin beobachtet. In diesem Sinne könnte 7-pulse CP PELDOR auch verwendet werden, um die Konformationsänderung von K48-verknüpften Tetraubiquitin oder auch noch längeren Ketten durch die gleichzeitige Bindung an die proteasomalen Rezeptoren Rpn10 und Rpn13, welche einen Abstand von ~10 nm besitzen, zu beobachten.

Der ‚Ubiquitin Code‘ enthält neben K48-verknüpften Ketten sieben weitere Kettentypen. Die Untersuchung des Konformationsraum dieser Ketten und dessen Änderung durch die Bindung von spezifischen Bindungspartnern stellt ein breites Feld mit vielen offenen Fragen dar. Erste Experimente an freien K11- und K63-verknüpften Diubiquitinketten im Vergleich zu K48-verknüpften Diubiquitin haben gezeigt, dass 4-pulse PELDOR Spektroskopie nicht nur konformelle Änderungen durch Ubiquitinbindung, sondern auch eine Unterscheidung des Konformationsraumes unterschiedlicher Kettentypen erlaubt (Abbildung 4.1). Daher sollte es mittels der in dieser Arbeit beschriebenen Verfahren möglich sein einen tieferen Einblick in das Struktur-Funktions Paradigma des gesamten ‚Ubiquitin Codes‘ zu erhalten.

Chapter 6

Appendix

6.1 Supplemental Material

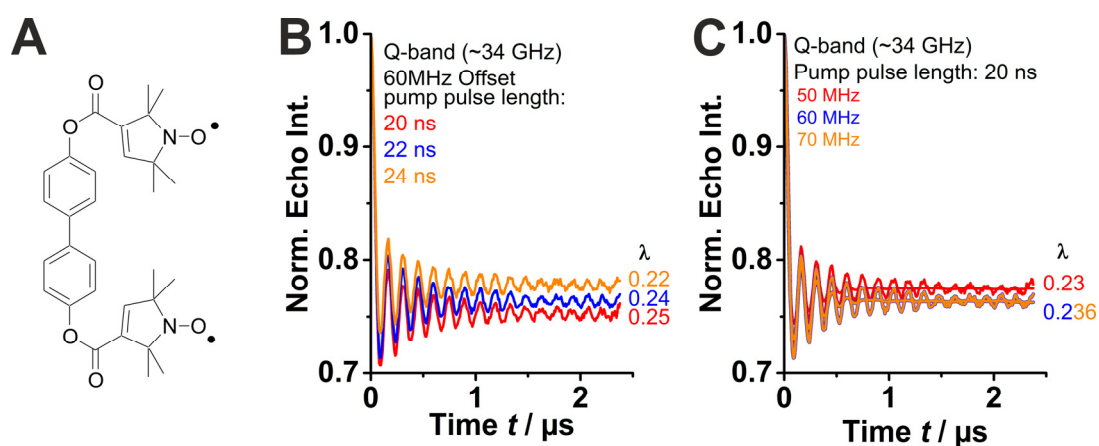


Figure 6. 1: Q-band calibration. This calibration was done in collaboration with Dr. Burkhard Endeward, who is a senior scientist in the Group of Pro. Thomas F. Prisner. A) Molecular Structure of Biphenyl-4,4'-diyl-bis(2,2,5,5-tetramethyl-1-oxyl-3-pyrroline-3-carboxylate (Labname: BiesterBi). Measurements were obtained for a concentration of 0.1 mM. B) Background-corrected PELDOR time trace obtained on BiesterBi for different pump pulse lengths and a given frequency-offset of 60 MHz between the pump and the probe pulse. C) Background-corrected PELDOR time trace obtained on BiesterBi for different frequency-offsets between the pump pulse and the probe pulse for a given pump pulse length of 20 ns.

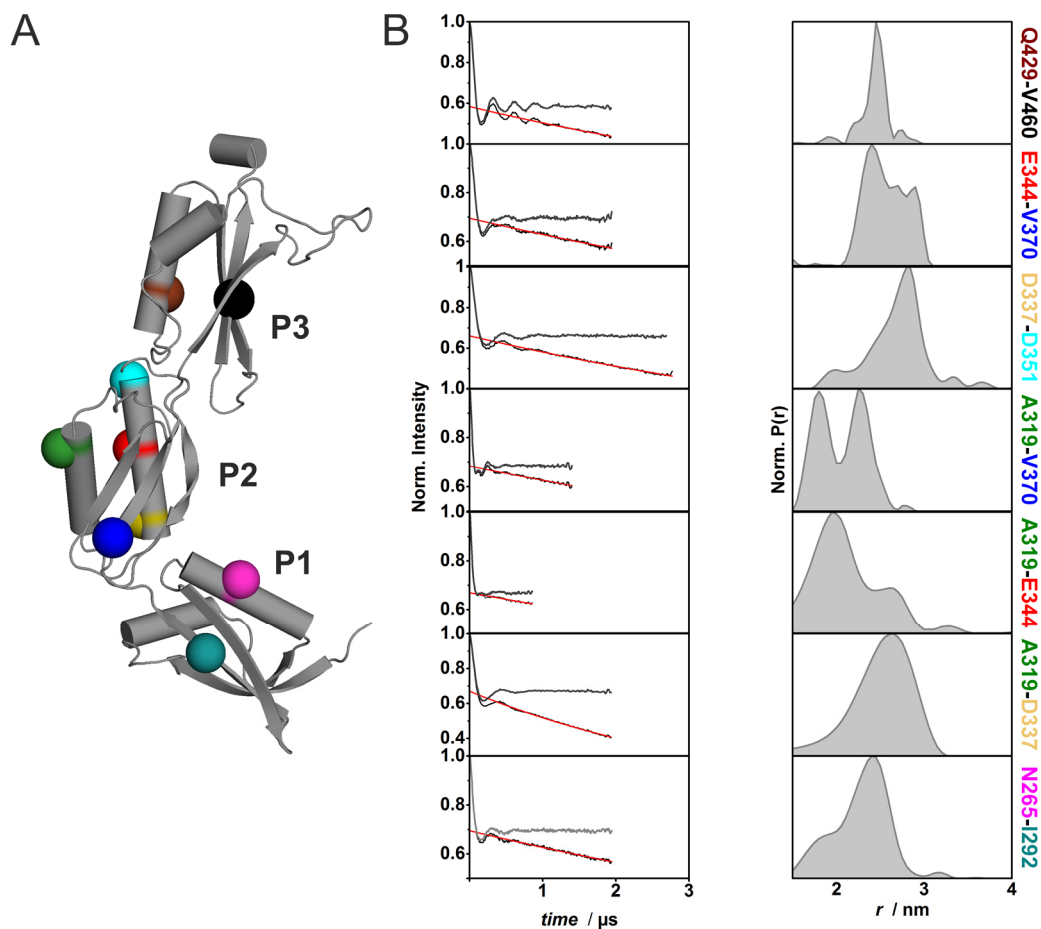


Figure 6.2: Experimental results on intra-POTRA domain restraints. A) The X-ray structure (3MC8) of the three POTRA domains (*anaP1*, *anaP2* and *anaP3*) indicating the spin labelled residues V460C (black), Q429C (brown), V370C (blue), D351C (cyan), E344C (red), D337C (sand/dark yellow), A319C (green), I292C (magenta) and N265C (dark cyan). B) Experimentally observed intra-domain PELDOR distance restraints. Left: The primary and background-corrected PELDOR time traces, obtained at X-band frequencies (~ 9.8 GHz), with fits from Tikhonov regularization (grey). The 3D backgrounds are shown in red. These experiments and the data analysis were performed by Dr. Reza Dastvan, a former Ph.D. student in the group of Prof. Thomas F. Prisner, who is currently a Postdoctoral researcher at Vanderbilt University in the group of Prof. Hassane S. Mchaourab. The intra-POTRA domain variants were expressed and purified by Eva-Maria Bouwer.

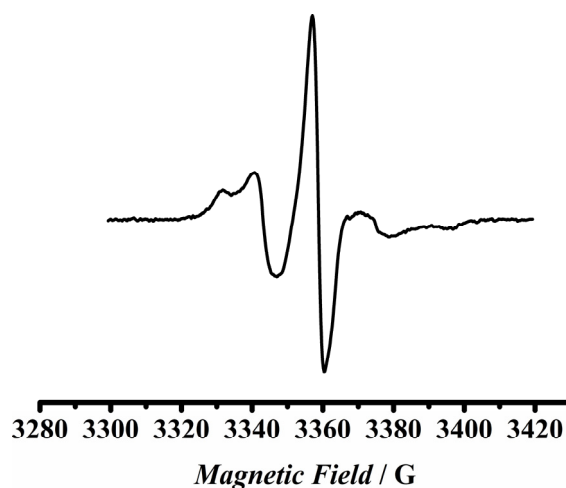


Figure 6.3: cw EPR spectrum of the single-Cys variant V370C in *anaP2*. This experiment was performed by Dr. Reza Dastvan. The variant was expressed, purified and spin labelled by Eva-Maria Bouwer, a former Ph.D. student in the lab of Prof. Enrico Schleiff at the Goethe-University.

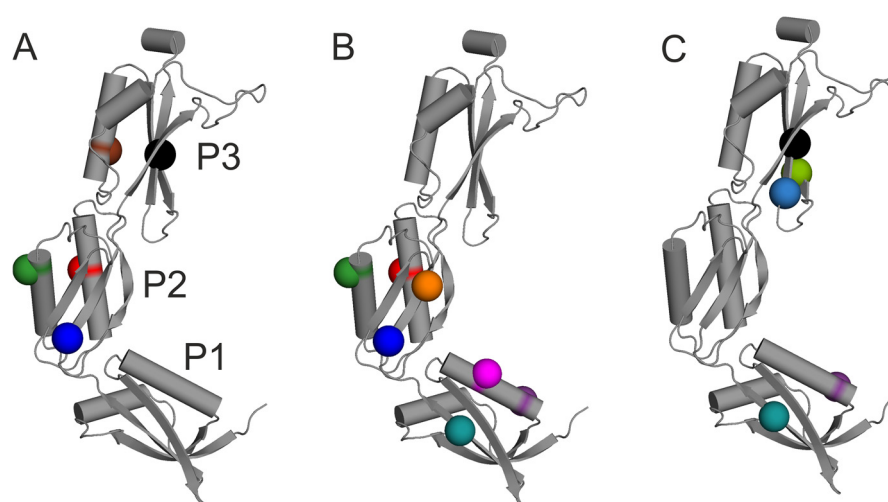


Figure 6.4: The X-ray structure of the three *anaOmp85* POTRA domains, indicating the spin labelled residues in each domain for the inter-domain residues. A) Spin labelled residues in *anaP3* and *anaP2* creating the inter-domain variants between those domains: V460C (black), Q429C (brown), V370C (blue), E344C (red), and A319C (green). B) Spin labelled residues in *anaP2* and *anaP1* creating the inter-domain variants between those domains: Q374C (orange), V370C (blue), E344C (red), A319C (green), I292C (dark cyan), N265C (magenta) and Q259C (violet). C) Spin labelled residues in *anaP3* and *anaP1*: V460C (black), V457C (light blue), L448C (light green), I292C (dark cyan) and Q259C (violet). The inter-POTRA domain variants were expressed and purified by Eva-Maria Bouwer.

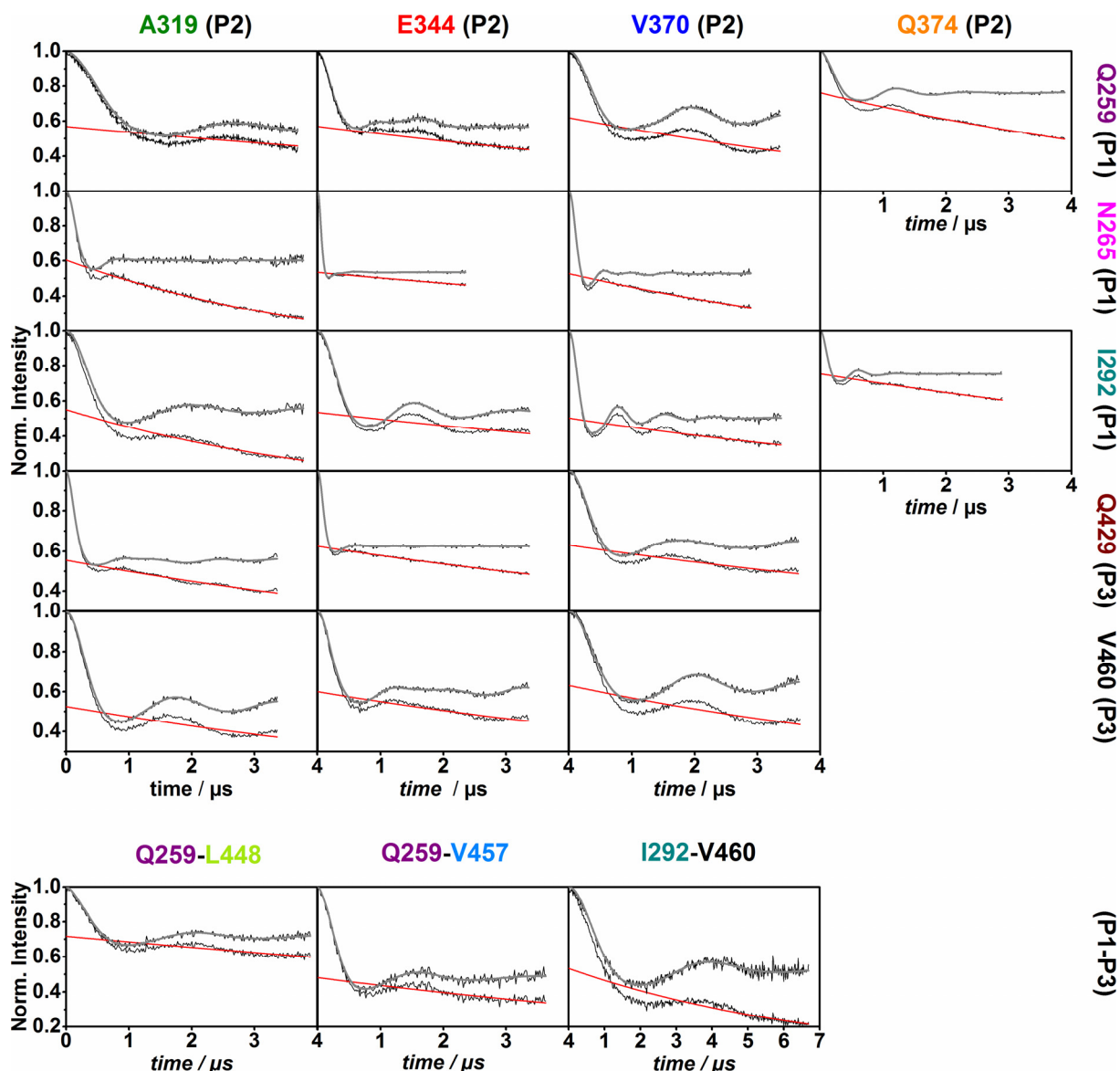


Figure 6.5: Experimental PELDOR data on inter-POTRA domain restraints. The primary and background-corrected PELDOR time traces for measurements on the inter-domain double variants with fits from Tikhonov regularization (grey) are shown. The 3D-backgrounds are shown in red. The lower modulation depth observed for spin label pairs I292C/Q374C, Q259C/Q374C and Q259C/L448C is due to the lower inversion efficiency of the pump pulse on utilized Q-band setup. The prolonged time window for the spin label pair I292C/V460C was obtained by matrix deuteration. These experiments were obtained and analysed by Dr. Reza Dastvan, a former Ph.D. student in the group of Prof. Thomas F. Prisner, who is currently a Postdoctoral researcher at Vanderbilt University in the group of Prof. Hassane S. Mchaourab. An exception to this were the *anaP1-anaP2* variants related to Q259C and Q374C and *anaP1-anaP3* variant Q259C-L448C, which were performed by the author herself.

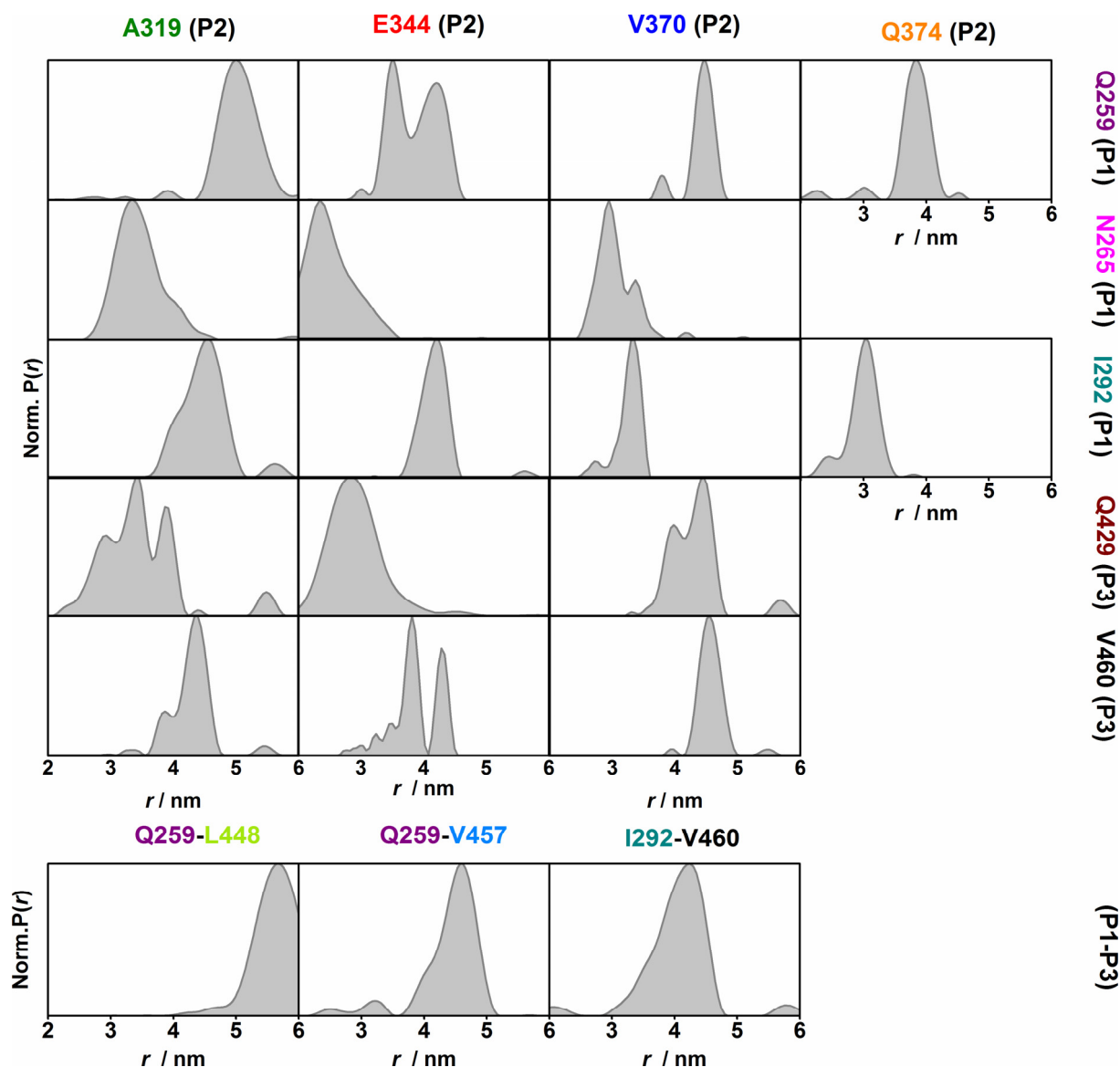


Figure 6.6: Inter-POTRA domain distance distributions obtained by Tikhonov. All distance distributions are normalized from [0-1]. The data analysis using DeerAnalysis2013 was performed analysed by Dr. Reza Dastvan, a former Ph.D. student in the group of Prof. Thomas F. Prisner, who is currently a Postdoctoral researcher at Vanderbilt University in the group of Prof. Hassane S. Mchaourab. An exception are the *anaP1-anaP2* variants related to Q259C and Q374C and *anaP1-anaP3* variant Q259C-L448C, which were analysed by the author herself.

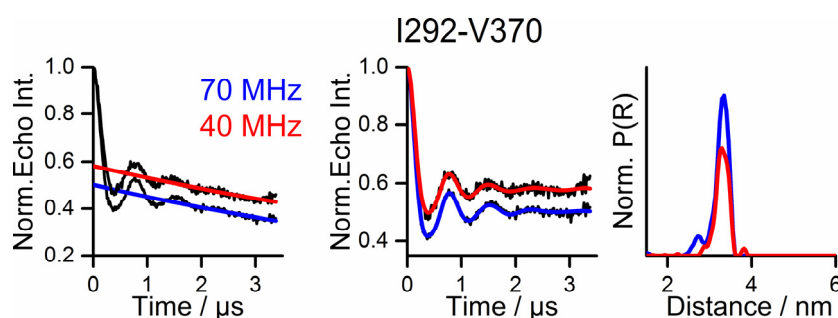


Figure 6.7: Orientation selectivity test for the inter-POTRA domain variant I292C/V370C. Left) Primary PELDOR time traces for different off-sets between the pump and probe pulses (40 MHz (red) and 70 MHz (blue)). Middle: Background-corrected PELDOR time traces for, showing virtually no difference. Right: Corresponding distance distributions. These experiments were performed by Dr. Reza Dastvan, a former Ph.D. student in the group of Prof. Thomas F. Prisner, who is currently a Postdoctoral researcher at Vanderbilt University in the group of Prof. Hassane S. Mchaourab.

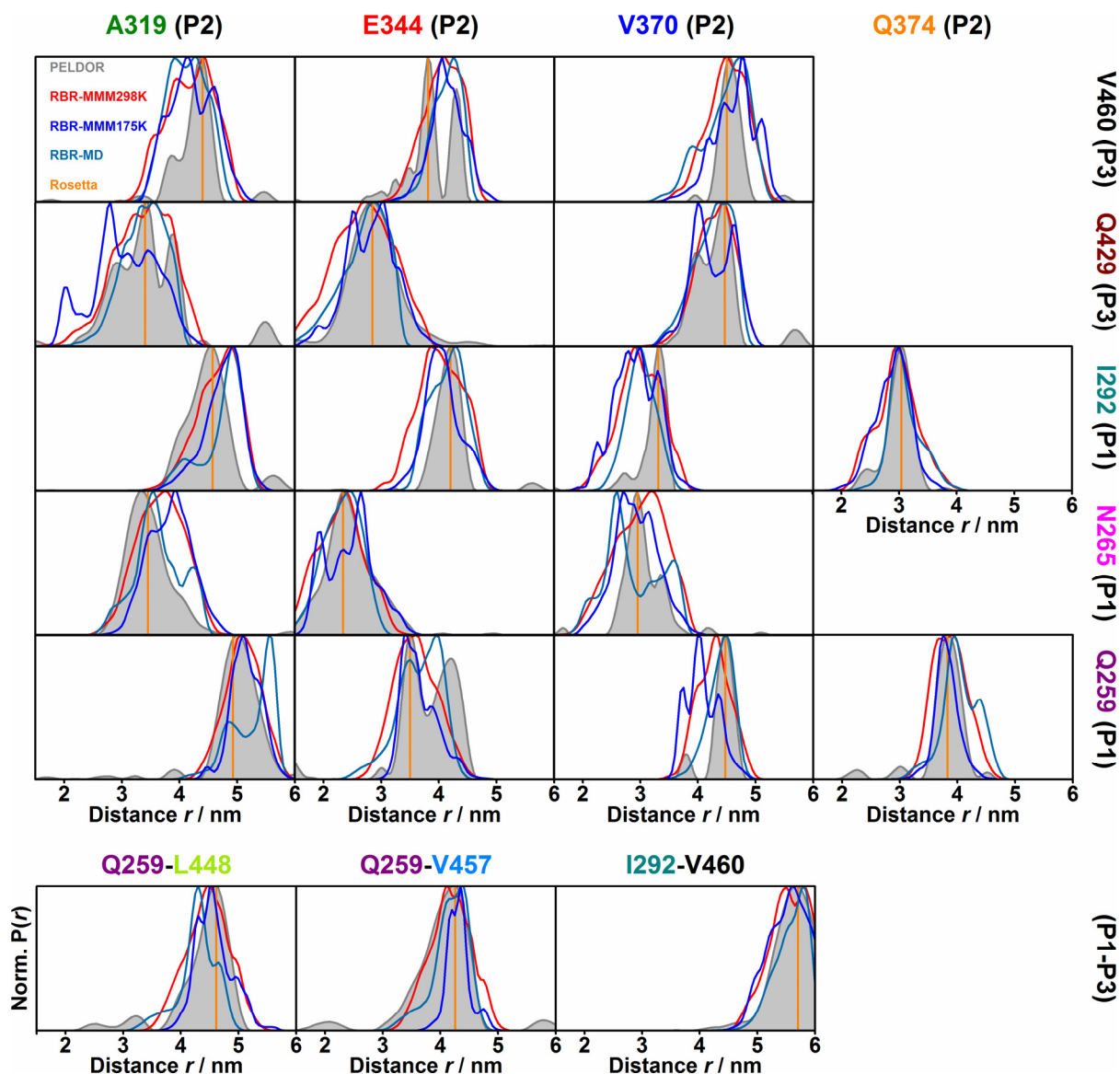


Figure 6.8: Comparison of experimental (grey) and simulated intra-molecular distance distributions from the rigid body and Rosetta refinement for all inter-POTRA domain restraints. Distance distributions obtained for the best model of the rigid body refinements using the standard library of MMM2013.2 [38] in 298 K mode (red), in 175 K mode (blue) generated on the X-ray structure and the rotamer library obtained by MD simulations of spin labelled POTRA domains (cyan) are compared to the obtained distance distributions by Tikhonov regularization (grey). The distances obtained for the best Rosetta refinement model are given as orange line, which matches the most probable distance of the individual inter-POTRA domain restraints. The rigid body refinements were conducted by Prof. Dr. Thomas F. Prisner at the Goethe-University and the Rosetta refinement by Dr. Oliver Mirus, a former Postdoctoral researcher in the group of Prof. Dr. Enrico Schleiff at the Goethe-University.

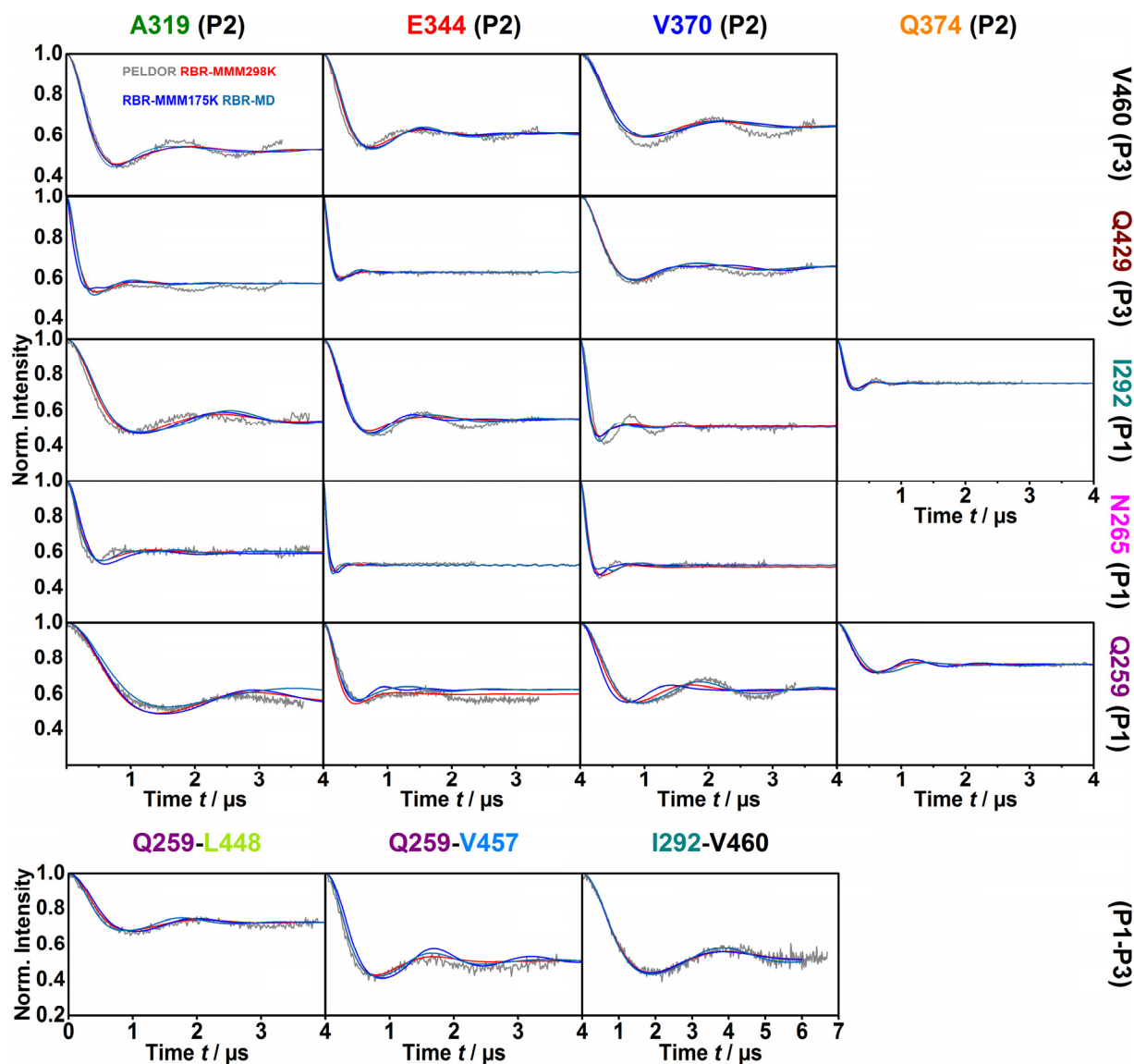


Figure 6.9: Comparison of experimental (grey) and simulated intramolecular dipolar evolution functions from the rigid body and Rosetta refinement for all inter-POTRA domain restraints. Dipolar evolution functions obtained for the best model of the rigid body refinements using the standard libraries of MMM2013.2 in 298 K mode (red), in 175 K mode (blue) generated on the X-ray structure and the rotamer library obtained by MD simulations of spin labelled POTRA domains (cyan) are compared to the background-corrected experimental dipolar evolution functions (grey). The distances obtained for the best Rosetta refinement model are given as orange line, which matches the most probable distance of the individual inter-POTRA domain restraints. Simulations of the dipolar evolution functions for the distance distributions obtained by rigid body refinement were done by the author herself. The rigid body refinements were conducted by Prof. Dr. Thomas Prisner and the Rosetta refinement by Dr. Oliver Mirus, a former Postdoctoral researcher in the group of Prof. Dr. Enrico Schleiff at the Goethe-University.

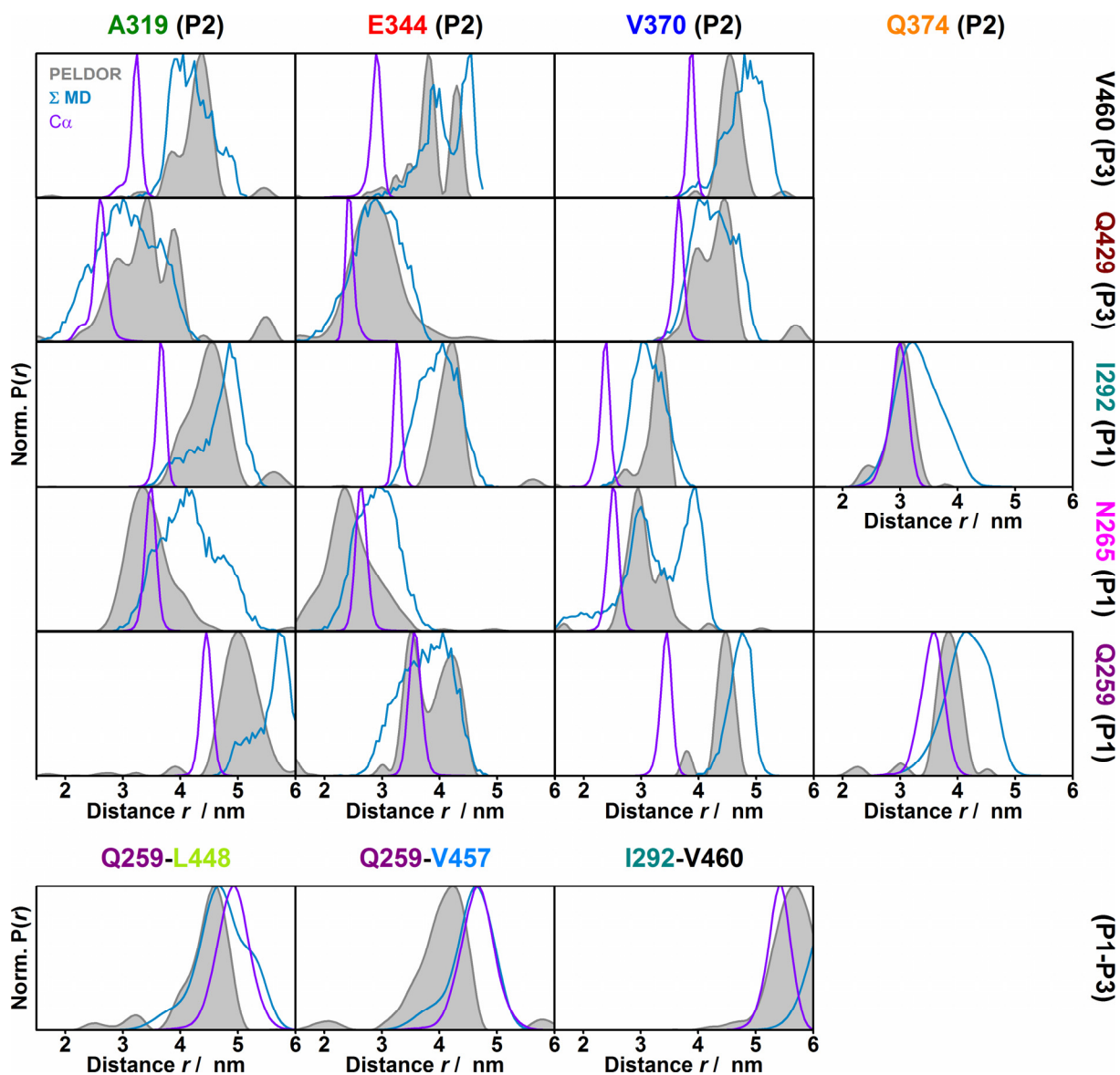


Figure 6.10: Comparison of experimental intra-molecular distance distributions for all inter-POTRA domain restraints in comparison to distributions obtained via MD or REMD simulations. The experimentally obtained distance distributions are shown in grey. The distance distributions between the two nitroxide labels obtained by MD simulations on spin labelled POTRA domains (blue) and the $C\alpha$ -distance distributions extracted from REMD simulations (purple) are shown as an estimation of the extent of the backbone movements of the *anaOmp85* POTRA domains. The MD and REMD simulations were performed by Dr. Oliver Mirus, a former Postdoctoral researcher in the group of Prof. Dr. Enrico Schleiff at the Goethe-University.

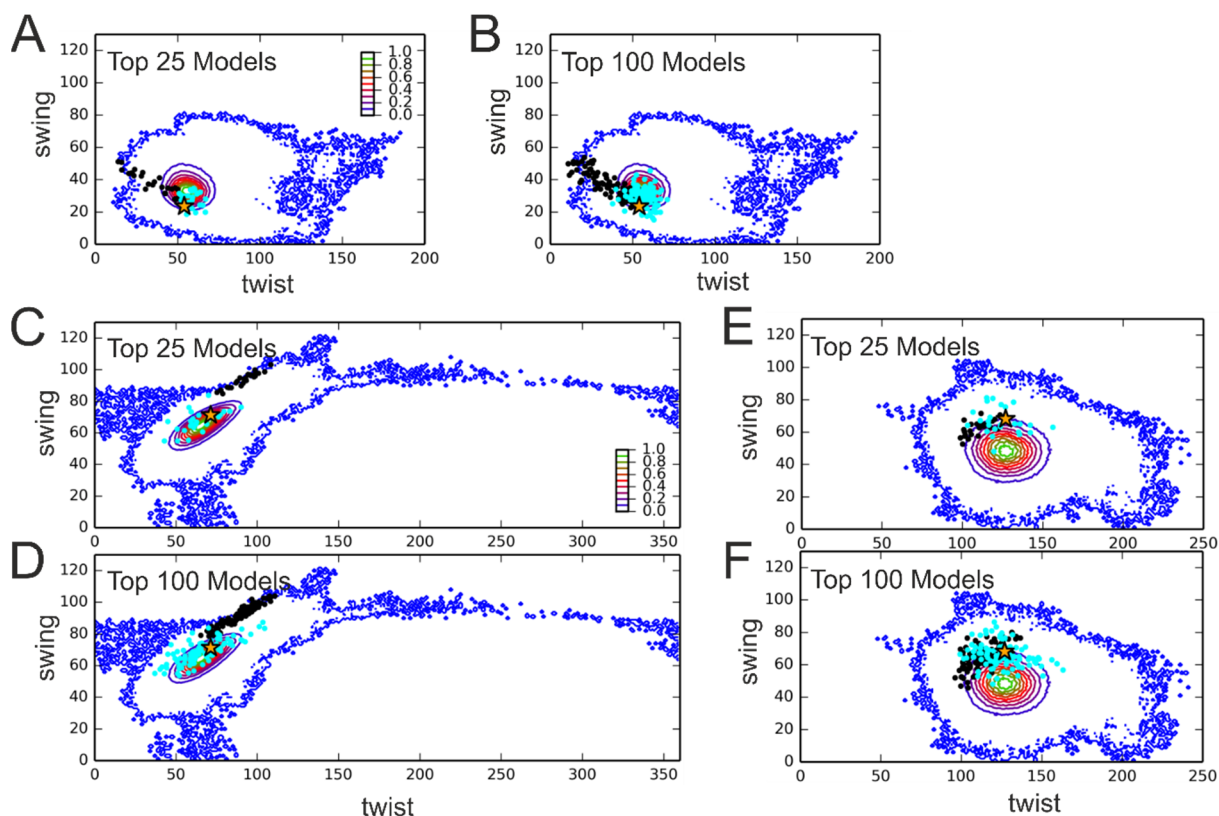


Figure 6.11: Orientational space of *anaOmp85* POTRA domains of wildtype Alr2269 sampled by REMD simulations in comparison to structure refinement. 2D contour plots show the frequency distribution of angular orientations of adjacent *anaOmp85* POTRA domain pairs from REMD simulations. (A and B) *anaP2-anaP3*. (C and D) *anaP1-anaP2*. (E and F) *anaP1-anaP3*. The top models from the rigid body (filled black circles) and Rosetta (filled cyan circles) refinement are mapped onto the contour plots. In panels A, C and E the top 25 are shown. In panels B, D and F the top 100 models are shown. In all plots, the asterisk indicates the conformation of the respective domains in the X-ray structure. The MD and REMD simulations were performed by Dr. Oliver Mirus, a former Postdoctoral researcher in the group of Prof. Dr. Enrico Schleiff at the Goethe-University.

Table 6.1: Comparison of simulated mean distances $\langle r \rangle$ obtained for different rotamer libraries on the basis of the X-ray structure 3MC8. The distance is given in nm with the standard deviation in parenthesis.

Pair	$\langle r \rangle_{\text{MMM175K}}$	$\langle r \rangle_{\text{Mtssl-wizard}}$	$\langle r \rangle_{\text{Sezer12-175K}}$	$\langle r \rangle_{\text{Sezer12-298K}}$	$\langle r \rangle_{\text{Sezer13-175K}}$	$\langle r \rangle_{\text{Sezer13-298K}}$	$\langle r \rangle_{\text{Hubbell-298K}}$
N265-I292	2.3 (0.4)	2.4 (0.4)	2.3 (0.4)	2.3 (0.4)	2.2 (0.4)	2.3 (0.4)	2.3 (0.3)
A319-D337	2.6 (0.4)	2.5 (0.4)	2.4 (0.4)	2.3 (0.5)	2.6 (0.4)	2.6 (0.4)	2.6 (0.3)
A319-E344	2.0 (0.4)	2.0 (0.4)	1.6 (0.4)	1.9 (0.4)	2.0 (0.3)	2.1 (0.4)	2.4 (0.3)
A319-V370	2.2 (0.4)	2.0 (0.5)	2.1 (0.5)	2.0 (0.5)	2.1 (0.4)	2.1 (0.5)	1.9 (0.4)
D337-D351	2.3 (0.4)	2.3 (0.4)	2.2 (0.4)	2.3 (0.5)	2.2 (0.6)	2.4 (0.5)	2.2 (0.3)
E344-V370	2.6 (0.3)	2.7 (0.3)	2.6 (0.4)	2.6 (0.4)	2.2 (0.5)	2.7 (0.4)	2.8 (0.2)
Q429-V460	2.2 (0.4)	2.2 (0.4)	2.2 (0.4)	2.1 (0.5)	2.1 (0.5)	2.3 (0.4)	2.3 (0.4)
I292-A319	4.6 (0.4)	4.6 (0.4)	4.6 (0.4)	4.5 (0.4)	4.7 (0.4)	4.7 (0.4)	4.4 (0.3)
I292-E344	3.9 (0.3)	4.0 (0.3)	4.2 (0.7)	4.0 (0.4)	3.6 (0.4)	4.0 (0.4)	4.0 (0.3)
I292-V370	2.8 (0.3)	3.1 (0.3)	2.9 (0.3)	3.3 (0.4)	3.1 (0.3)	3.1 (0.3)	3.0 (0.2)
N265-A319	3.9 (0.4)	4.1 (0.4)	3.8 (0.4)	3.9 (0.4)	4.1 (0.5)	4.0 (0.4)	3.6 (0.4)
N265-E344	2.7 (0.4)	2.8 (0.4)	3.0 (0.4)	2.9 (0.5)	2.6 (0.5)	2.8 (0.5)	2.4 (0.5)
N265-V370	2.9 (0.4)	3.2 (0.4)	2.9 (0.4)	3.1 (0.5)	3.1 (0.5)	3.1 (0.5)	2.5 (0.5)
Q259-A319	5.1 (0.3)	5.2 (0.3)	5.1 (0.3)	5.1 (0.4)	5.3 (0.3)	5.2 (0.4)	2.5 (0.6)
Q259-E344	3.6 (0.4)	3.8 (0.4)	4.0 (0.3)	3.7 (0.4)	3.7 (0.3)	3.7 (0.4)	3.5 (0.4)
Q259-V370	4.0 (0.3)	4.4 (0.3)	4.1 (0.3)	4.3 (0.3)	4.3 (0.3)	4.4 (0.3)	4.2 (0.3)
Q374-Q259	3.8 (0.2)	3.9 (0.3)	3.8 (0.3)	3.9 (0.4)	3.8 (0.4)	3.8 (0.4)	3.9 (0.3)
Q374-I292	3.1 (0.3)	3.2 (0.4)	3.2 (0.3)	3.3 (0.4)	3.3 (0.3)	3.3 (0.3)	3.4 (0.3)
V460-A319	3.9 (0.4)	4.2 (0.3)	3.8 (0.4)	4.2 (0.4)	4.1 (0.3)	4.3 (0.4)	4.4 (0.4)
V460-E344	3.8 (0.3)	3.9 (0.3)	4.0 (0.2)	3.8 (0.4)	3.9 (0.3)	4.0 (0.4)	4.0 (0.3)
V460-V370	4.2 (0.4)	4.2 (0.3)	4.2 (0.4)	4.3 (0.4)	4.4 (0.3)	4.4 (0.3)	4.0 (0.4)
Q429-A319	2.9 (0.6)	3.1 (0.5)	3.0 (0.6)	3.2 (0.5)	3.1 (0.5)	3.2 (0.5)	3.6 (0.4)
Q429-E344	2.7 (0.4)	2.7 (0.4)	2.9 (0.3)	2.7 (0.5)	3.0 (0.5)	2.7 (0.6)	2.8 (0.4)
Q429-V370	4.2 (0.4)	4.1 (0.4)	4.3 (0.4)	4.1 (0.4)	4.2 (0.4)	4.2 (0.4)	4.1 (0.4)
V460-I292	5.6 (0.3)	5.6 (0.3)	5.7 (0.4)	5.8 (0.4)	5.6 (0.4)	6.0 (0.4)	6.0 (0.3)
V457-Q259	4.1 (0.2)	4.0 (0.3)	4.2 (0.2)	4.0 (0.3)	4.1 (0.3)	4.0 (0.3)	3.8 (0.3)
L448-Q259	4.4 (0.3)	4.2 (0.4)	4.3 (0.3)	4.3 (0.4)	4.5 (0.4)	4.3 (0.4)	4.2 (0.4)

Table 6.2: Comparison of mean distance $\langle r \rangle$ of the PELDOR restraints with the X-ray structure, MD simulations of *in silico*-spin labelled *anaOmp85* POTRA domains and the best refined model of either rigid body or Rosetta refinement. The distances are given in nm. r_{pk} is the main distance of the distribution; the standard deviations are given in parentheses.

Pair	$\langle r \rangle_{\text{PELDOR}}/r_{pk}$	$\langle r \rangle_{\text{X-ray, MMM298K}}$	$\langle r \rangle_{\text{MD}}$	$\langle r \rangle_{\text{Rigid BodyMMM298K}}$	$\langle r \rangle_{\text{Rosetta}}$
N265-I292	2.3/2.4 (0.3)	2.4 (0.4)	n.d.	n.d.	2.4
A319-D337	2.5/2.6 (0.4)	2.6 (0.4)	n.d.	n.d.	n.d.
A319-E344	2.1/2.0 (0.5)	2.0 (0.4)	n.d.	n.d.	2.0.
A319-V370	2.1/1.8, 2.3 (0.3)	2.1 (0.5)	n.d.	n.d.	1.8.
D337-D351	2.7/2.8 (0.4)	2.4 (0.5)	n.d.	n.d.	n.d.
E344-V370	2.5/2.4 (0.3)	2.7 (0.4)	n.d.	n.d.	2.9
Q429-V460	2.4/2.5 (0.2)	2.2 (0.4)	2.1 (0.4)	n.d.	2.5
I292-A319	4.5/4.6 (0.5)	4.7 (0.4)	4.7 (0.4)	4.7 (0.4)	4.6
I292-E344	4.2/4.2 (0.3)	4.0 (0.4)	4.0 (0.3)	4.0 (0.5)	4.2
I292-V370	3.3/3.4 (0.2)	3.1 (0.3)	3.2 (0.3)	3.0 (0.4)	3.3
N265-A319	3.5/3.4 (0.4)	4.1 (0.4)	4.2 (0.5)	3.7 (0.6)	3.4
N265-E344	2.3/2.4 (0.4)	2.8 (0.4)	2.9 (0.3)	2.3 (0.5)	2.3
N265-V370	3.0/3.0 (0.4)	3.1 (0.5)	3.3 (0.6)	3.0 (0.6)	2.9
Q259-A319	5.3/ 5.0 (0.8)	5.2 (0.4)	5.6 (0.3)	5.1 (0.4)	4.9
Q259-E344	4.3/3.5, 4.2 (1.3)	3.7 (0.4)	3.8 (0.4)	3.6 (0.5)	3.5
Q259-V370	4.5/4.5 (0.5)	4.3 (0.3)	4.7 (0.2)	4.3 (0.4)	4.5
Q374-Q259	3.8/3.8 (0.4)	3.9 (0.3)	n.d.	3.9 (0.4)	3.9
Q374-I292	3.0/3.0 (0.3)	3.3 (0.4)	n.d.	3.0 (0.3)	3.1
V460-A319	4.4/4.4 (0.3)	4.2 (0.4)	4.2 (0.3)	4.2 (0.5)	4.4
V460-E344	3.9/3.8, 4.3 (0.5)	3.9 (0.4)	4.1 (0.4)	4.1 (0.5)	3.8
V460-V370	4.6/4.6 (0.2)	4.3 (0.4)	4.8 (0.3)	4.5 (0.4)	4.5
Q429-A319	3.4/3.4 (0.6)	3.1 (0.5)	3.1 (0.5)	3.4 (0.6)	3.4
Q429-E344	2.9/2.8 (0.5)	2.7 (0.5)	2.9 (0.4)	2.7 (0.7)	2.9
Q429-V370	4.3/4.5 (0.4)	4.1 (0.4)	4.3 (0.3)	4.3 (0.4)	4.5
V460-I292	5.7/5.7 (0.6)	5.7 (0.4)	6.4 (0.3)	5.6 (0.5)	5.7
V457-Q259	4.1/4.2 (0.8)	4.1 (0.3)	4.6 (0.4)	4.2 (0.4)	4.2
L448-Q259	4.3/4.6 (0.7)	4.3 (0.4)	4.7 (0.5)	4.5 (0.4)	4.6

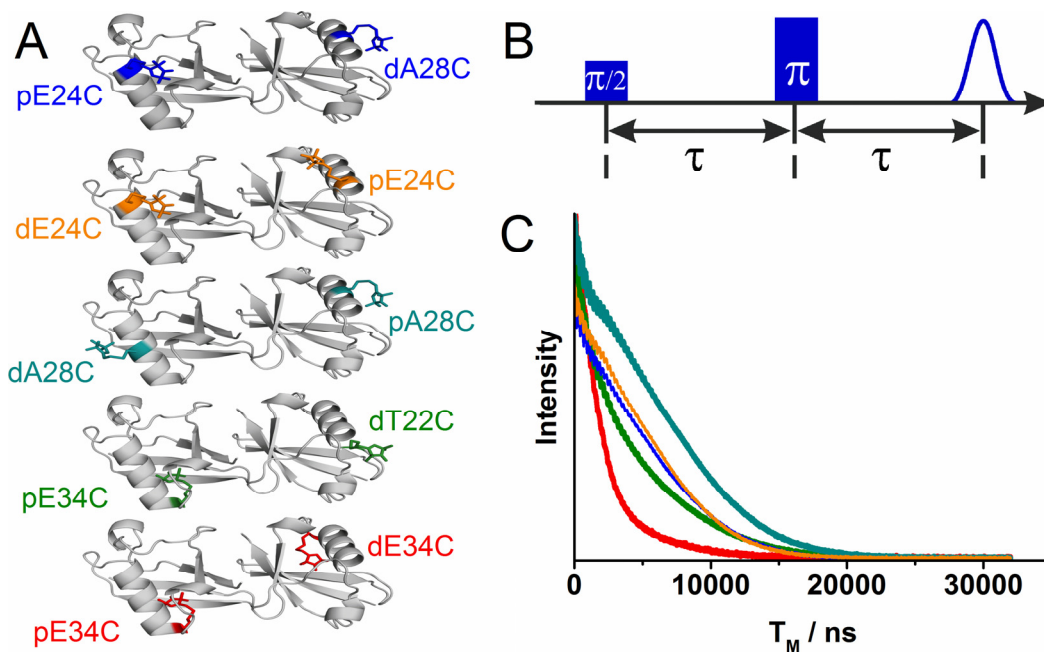


Figure 6.12: Hahn Echo experiment for the determination of T_M . A) The labelling positions for each restraint are displayed on the NMR structure 2PEA. B) The pulse sequence of the Hahn Echo experiment. The pulse lengths were 16 ns and 32 ns for the $\pi/2$ -pulse and the π -pulse, respectively. The initial delay τ between the pulses was 600 ns. The x-axis had 4000 points. The π -pulse is shifted in steps of 4 ns and the acquisition trigger in steps of 8 ns C) Hahn Echo Decay for the five diubiquitin variants indicated in A, using the same colour code.

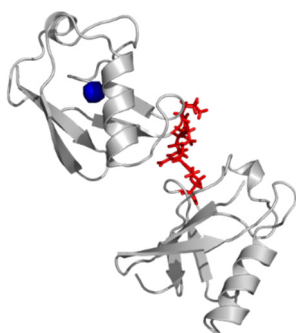


Figure 6.13: Structure of diubiquitin. Indicating the flexible residues 72-76 (red, stick representation) as well as the centre of mass of an individual ubiquitin molecule (blue) used for visualization of the conformational space.

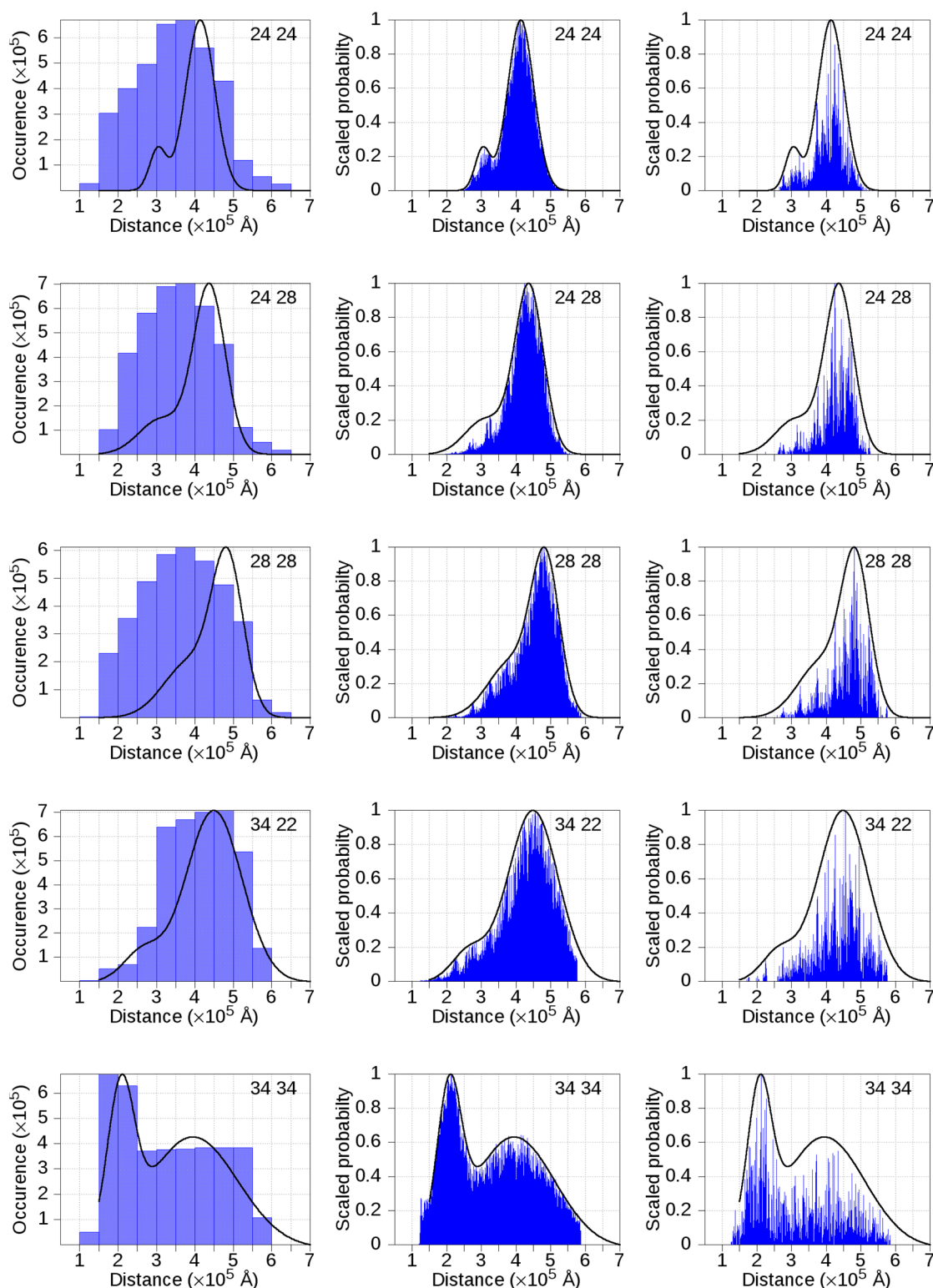


Figure 6.14: Modelling of the conformational space of K48-linked diubiquitin. Left: Number of conformations per distance interval of the collision-free conformational ensemble of 373,761 individual structures compared to the experimental distance distribution. Middle: Conformations of the collision-free ensemble weighted by a combined probability representing the occurrence of the specific structure with respect to all EPR distance distributions resulting in an ensemble of 144,520 structures above the probability threshold (for further information see Materials and Methods). Right: A representative ensemble of 3000 structures for visualization as probability hyper-surfaces.

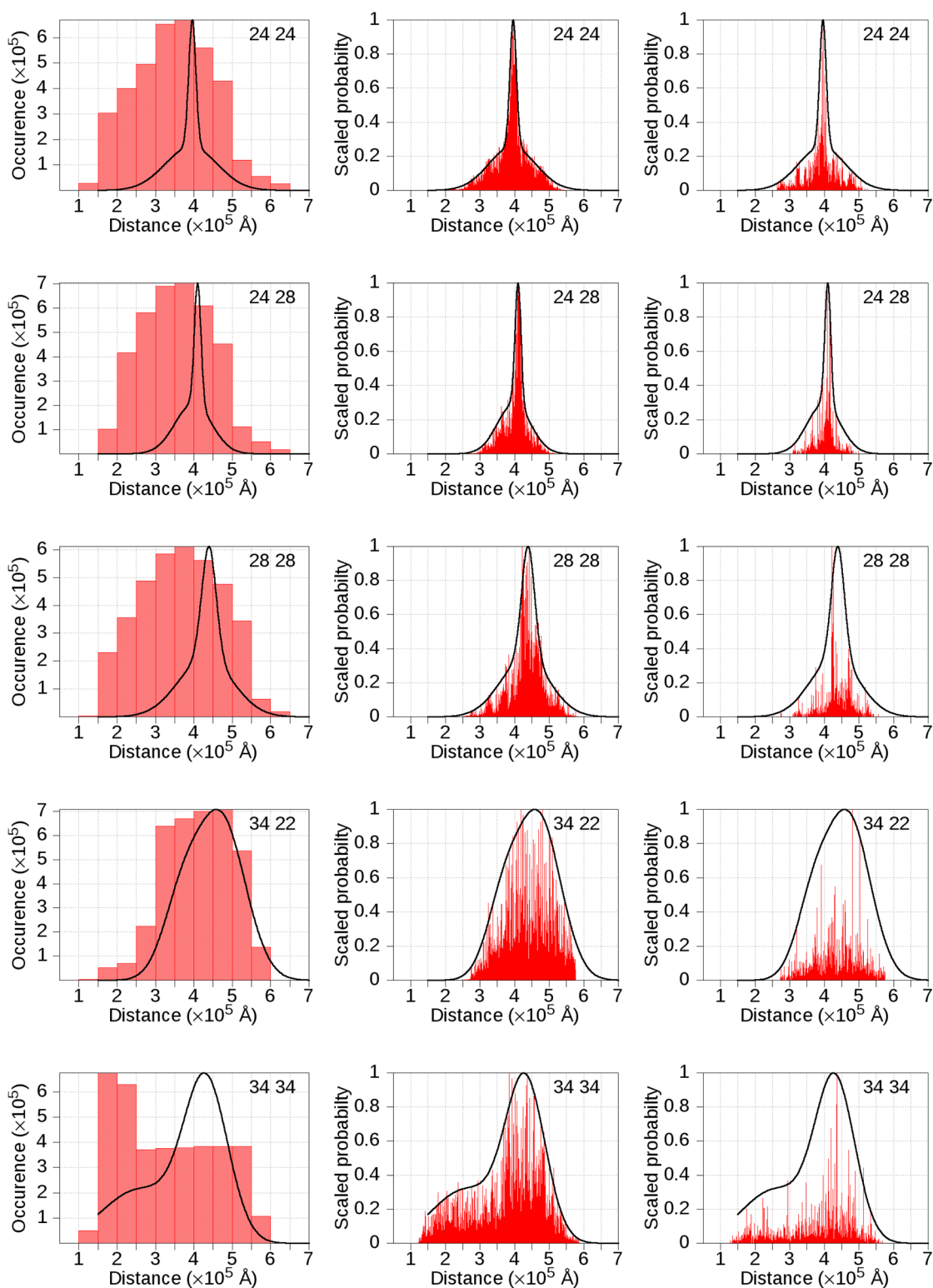


Figure 6.15: Modelling of the conformational space of K48-linked diubiquitin in complex with the CUE domain of Cue1. Left: Number of conformations per distance interval of the collision-free conformational ensemble with 373,761 individual structures compared to the experimental distance distribution. Middle: Conformations of the collision-free ensemble weighted by a combined probability representing the occurrence of the specific structure with respect to all EPR distance distributions resulting in an ensemble of 41,037 structures above the probability threshold (for further information see Materials and Methods). Right: A representative ensemble of 3000 structures for visualization as probability hyper-surfaces.

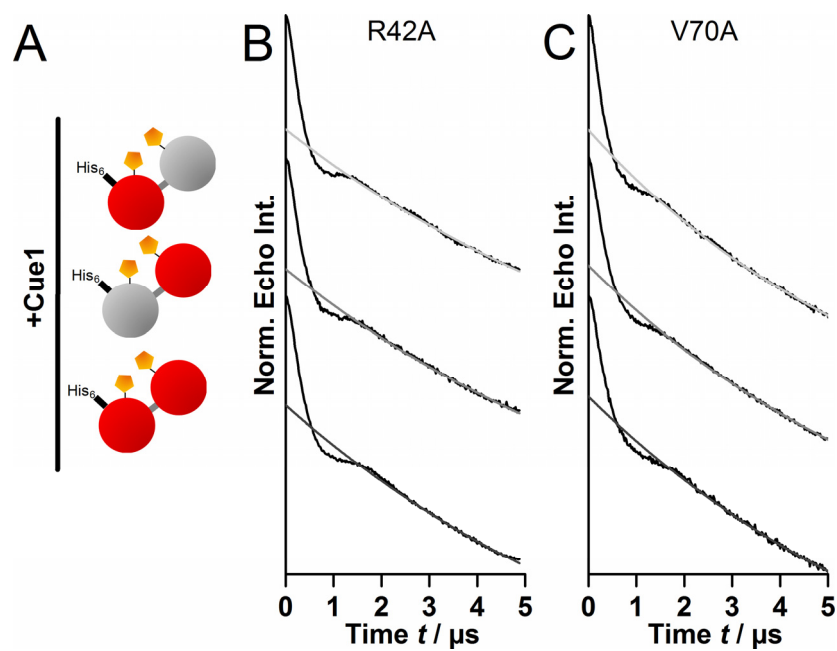


Figure 6.16: Primary 4-pulse PELDOR Data for the Cue1 binding deficient pE24C/dA28C K48-linked diubiquitin variants. A) Schematic representation of diubiquitin variant pE24C/dA28C, indicating the ubiquitin moiety with the binding deficient mutation (red). B) Primary PELDOR data of diubiquitin bearing the Cue1 binding deficient mutation R42A in either or both ubiquitin moieties in the presence of Cue1. C) Primary PELDOR data of diubiquitin bearing the Cue1 binding deficient mutation V70A in either or both ubiquitin moieties in the presence of Cue1.

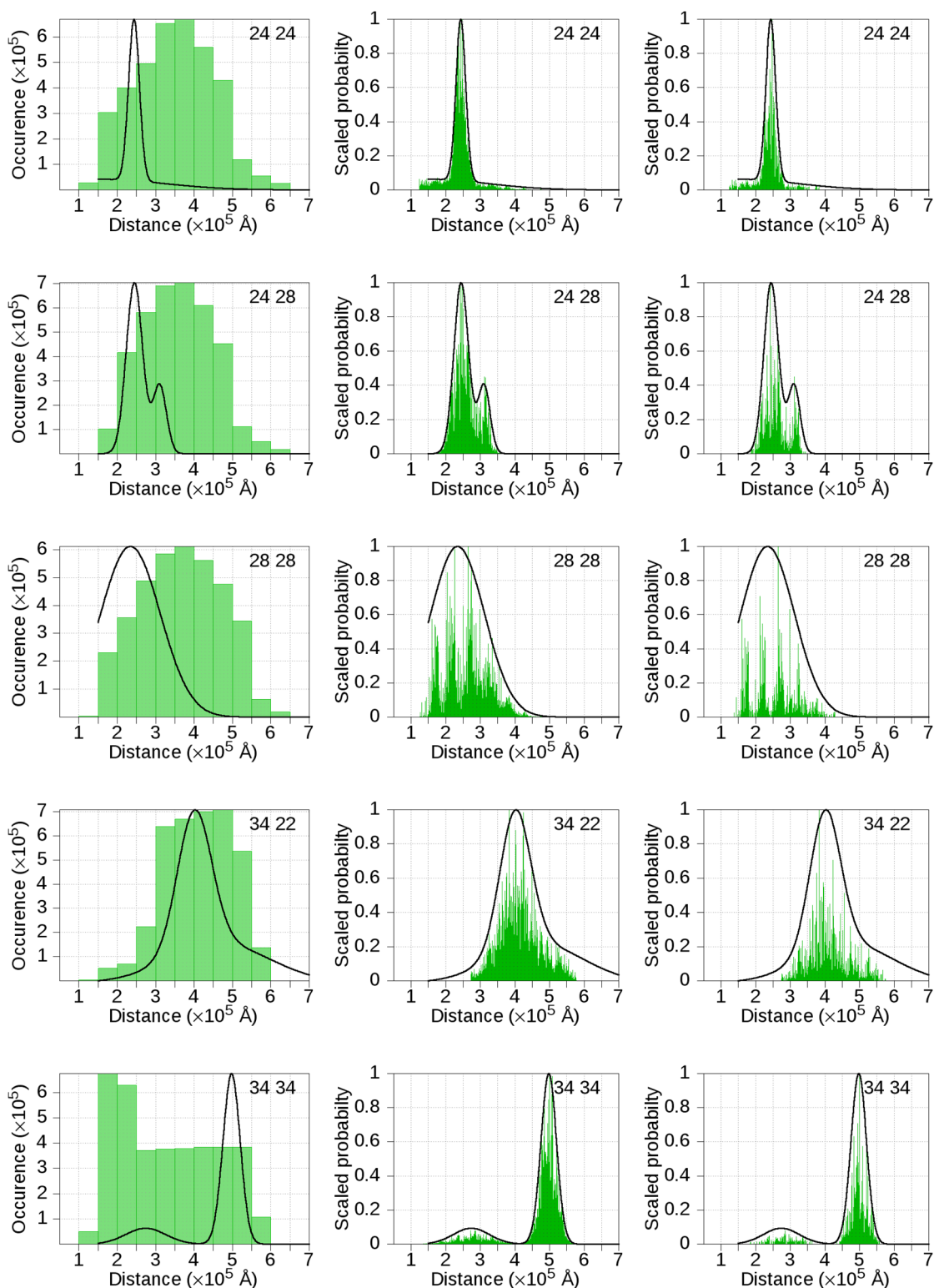


Figure 6.17: Modelling of the conformational space of K48-linked diubiquitin in complex with OTUB1i. Left: Number of conformations per distance interval of the collision-free conformational ensemble with 373,761 individual structures compared to the experimental distance distribution. Middle: Conformations of the collision-free ensemble weighted by a combined probability representing the occurrence of the specific structure with respect to the EPR distance distributions resulting in an ensemble of 12,432 structures above the probability threshold (for further information see Materials and Methods). Right: A representative ensemble of 3000 structures for visualization as probability hyper-surfaces.

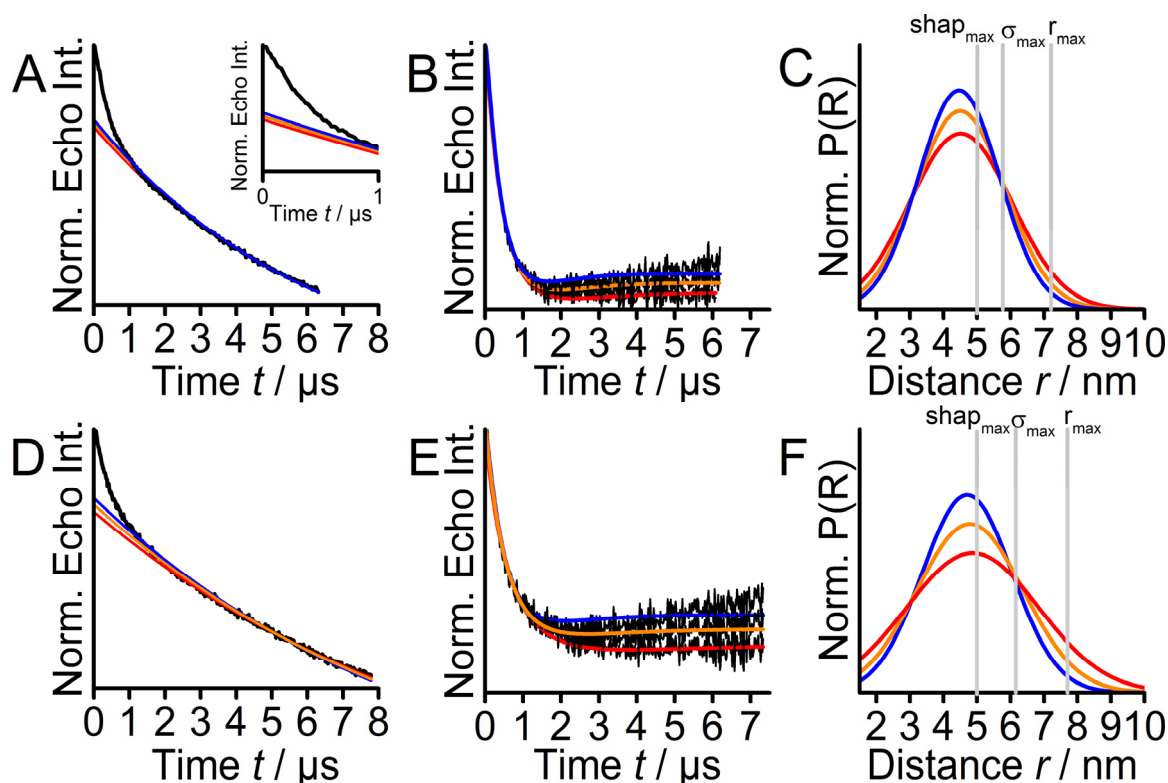


Figure 6.18: Analysis of 4-pulse PELDOR on doubly spin labelled tri- and tetraubiquitin variants pE24C/dA28C using different intermolecular decay functions. A) Primary 4-pulse PELDOR data for triubiquitin variant pE24C/dA28C indicating three different background-functions with starting times of 432 ns (blue), 736 ns (orange) and 1536 ns (red). A zoom into early times of the dipolar evolution function for better comparison to the simulation is given as inset. B) Background-corrected 4-pulse PELDOR time traces for the different background-functions in a. The single Gaussian model fit is shown in the colour code as in A. C) Corresponding distance distributions obtained by single Gaussian model fitting. The boundaries given by Eq. 2.21 and Eq. 2.22 are indicated. Additionally, the maximum distance (shape_{\max}) until which a reliable shape can be detected, as given in [29], is stated. D) Primary 4-pulse PELDOR data for tetraubiquitin variant pE24C/dA28C indicating three different background-functions with starting times of 400 ns (blue), 976 ns (orange) and 3380 ns (red). E) Background-corrected 4-pulse PELDOR time traces for the different background-functions in a. The single Gaussian model fit is shown in the colour code as in A. F) Corresponding distance distributions obtained by single Gaussian model fitting. The boundaries given by Eq. 2.21 and Eq. 2.22 are indicated. Additionally, the maximum distance (shape_{\max}) until which a reliable shape can be detected, as given in [29], is stated.

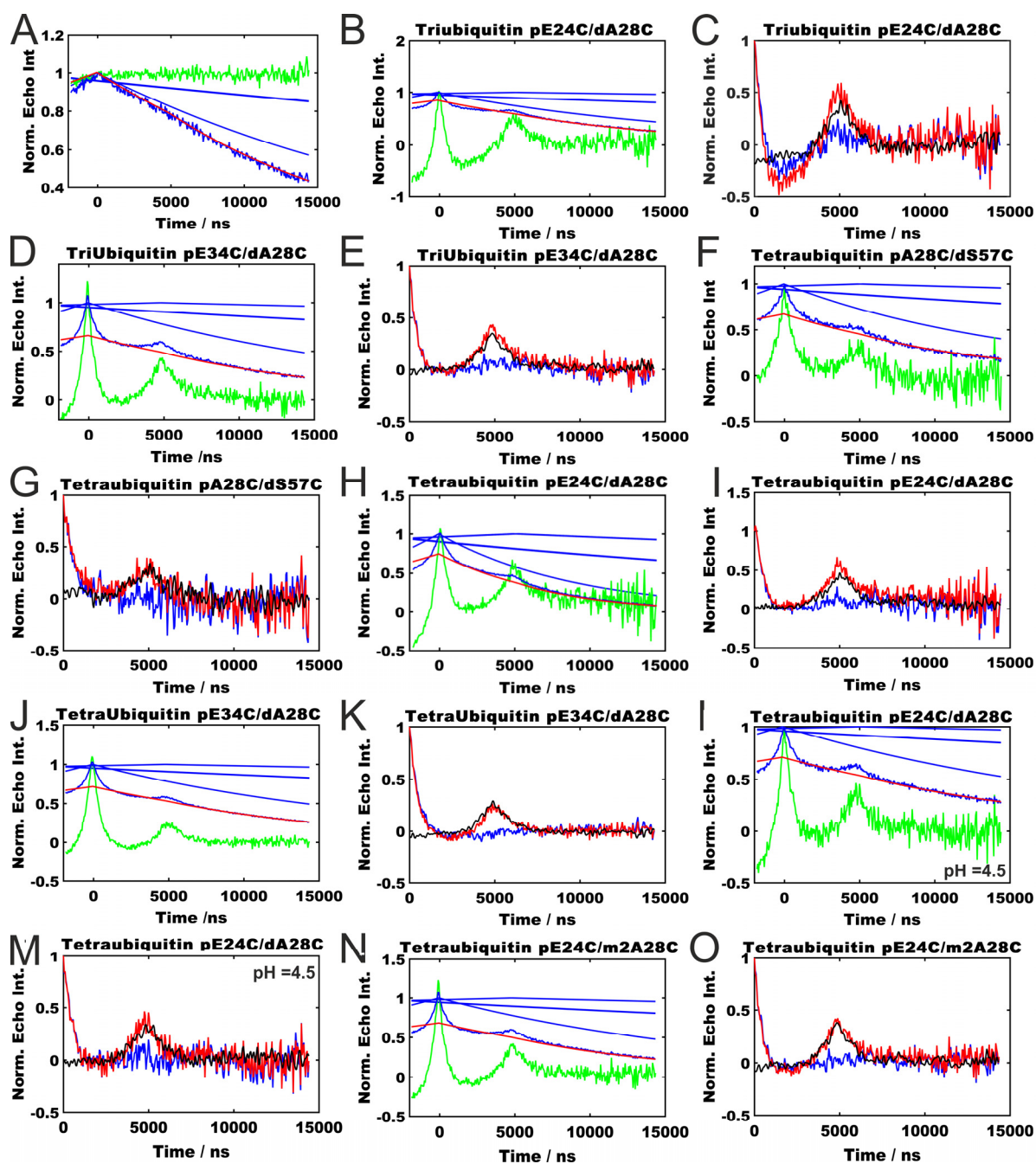


Figure 6.19: Primary 7-pulse CP PELDOR Data. A) 7-pulse CP PELDOR data obtained on singly labelled (pE24C) diubiquitin to verify the probability of double spin inversion p . B, D, F, H, J, L, N) Primary 7-pulse CP PELDOR data of doubly spin labelled tri- and tetraubiquitin variants spin labelled in the proximal and distal moiety fitted to the product (red) of all individual background decay functions (blue exponentials) times $(1-\lambda)$, with λ being the modulation depth of the signal. The background corrected dipolar signals after subtraction of the unmodulated part and renormalization are shown in green. C, E, G, I, K, M, O) Background-corrected 7-pulse CP PELDOR time traces of doubly spin labelled tri- and tetraubiquitin variants spin labelled in the proximal and distal moiety (red), sum of non 7-pulse dipolar signals (black) and extracted 7-pulse evolution (blue = red-black).

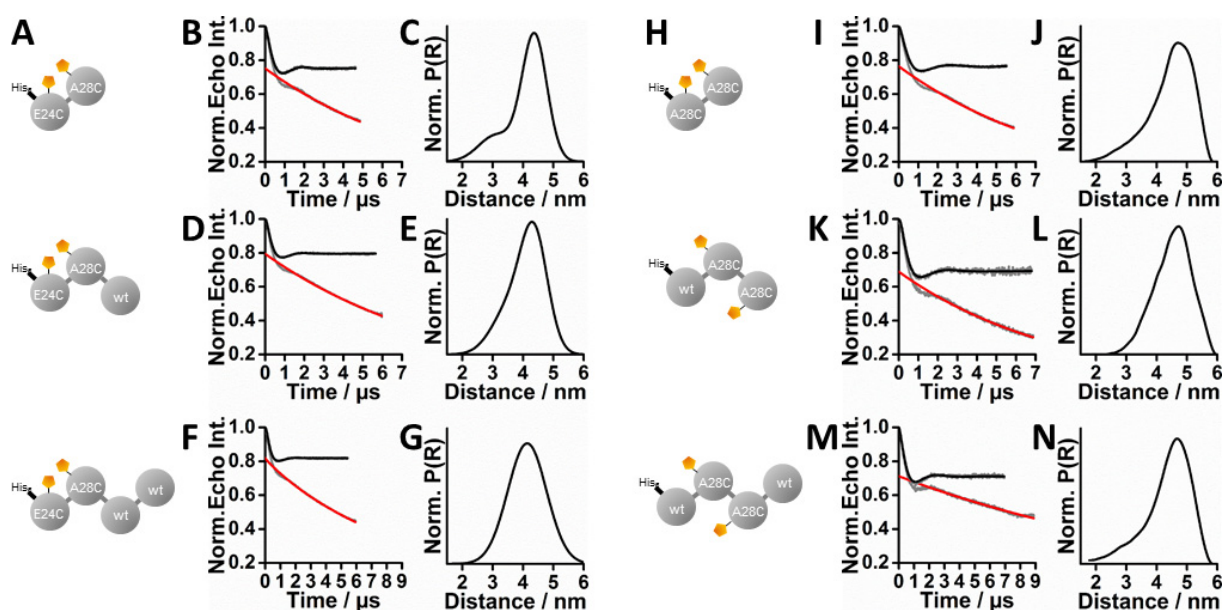


Figure 6.20: Primary PELDOR Data for the effect of chain elongation. A) Schematic representation of the investigated diubiquitin variant pE24C/dA28C, triubiquitin variant pE24C/mA28C and tetraubiquitin variant pE24C/m1A28C. B, D, F) Primary 4-pulse PELDOR data of doubly spin-labeled K48-linked ubiquitin chain variants in the order shown in A indicating the 3D background (red) and background-corrected PELDOR time trace with fit from 2 Gaussian model (black). C, E, G) Corresponding distance distributions obtain by 2 Gaussian model fitting. H) Schematic representation of the investigated diubiquitin variant A28C/dA28C, triubiquitin variant mA28C/dA28C and tetraubiquitin variant m1A28C/m2A28C. I, K, L) Primary 4-pulse PELDOR data of doubly spin-labeled K48-linked ubiquitin chain variants in the order shown in H indicating the 3D background (red) and background-corrected PELDOR time trace with fit from 2 Gaussian model (black). J, L, N) Corresponding distance distributions obtain by 2 Gaussian model fitting.

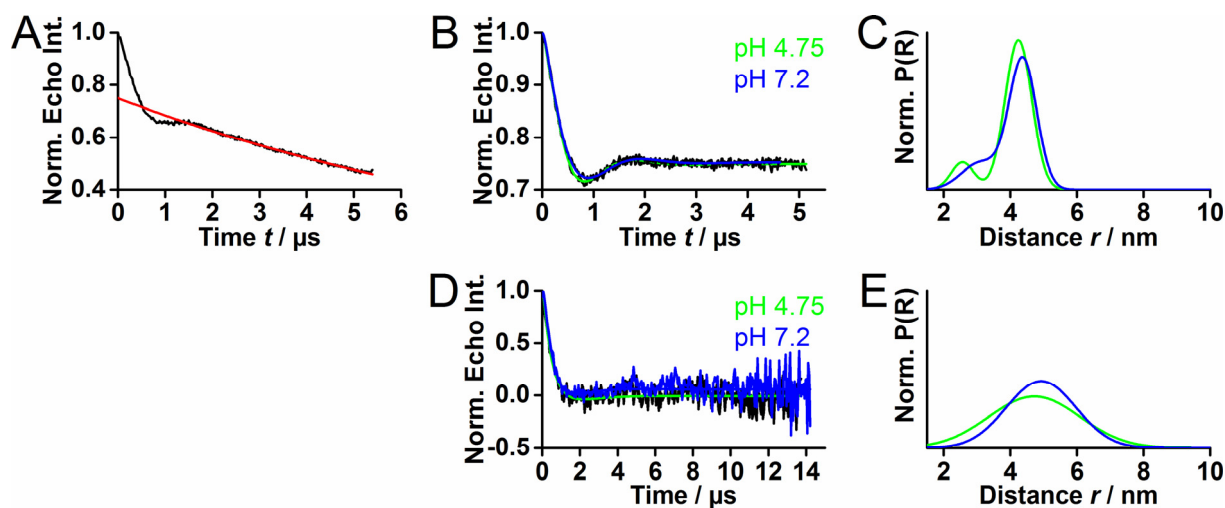


Figure 6.21: The effect of pH on the conformational space of di- and tetraubiquitin. A) Primary 4-pulse PELDOR data of doubly spin labeled K48-linked diubiquitin variant pE24C/dA28C at pH 4.5 indicating the 3D background (red). B) Background-corrected 4-pulse PELDOR time traces of diubiquitin variant pE24C/dA28C at pH 7.2 (blue) and 4.5 (green) with fit from a two Gaussian model. D) Background-corrected 7-pulse CP PELDOR time traces of doubly spin labeled K48-linked tetraubiquitin variant pE24C/dA28C at pH 7.2 (blue) and 4.5 (green) with fit from a two Gaussian model. The primary 7-pulse CP PELDOR Data is given in Figure 6.17. C, E) The corresponding distance distributions obtained by two Gaussian model fitting, showing virtually no difference.

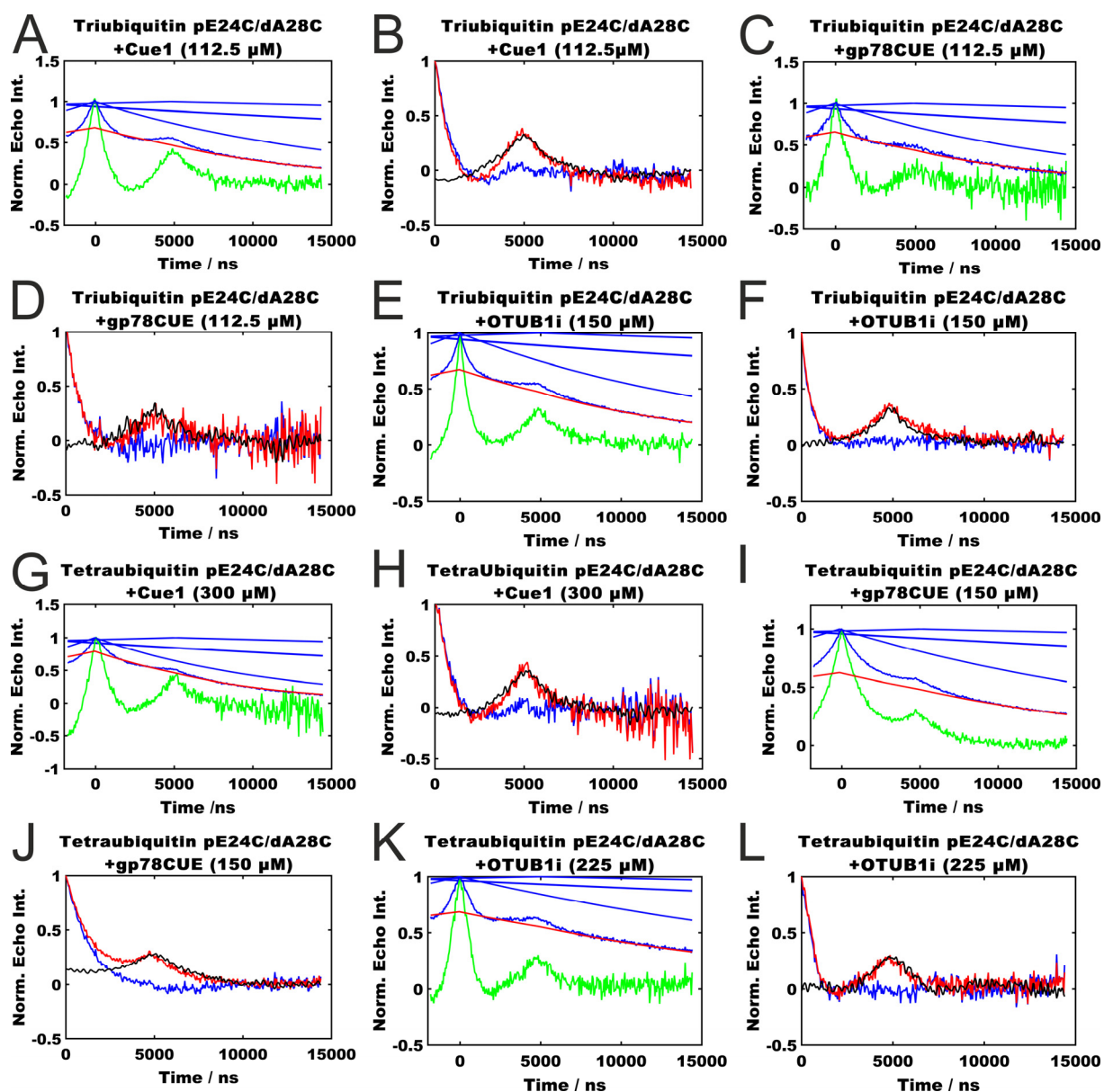


Figure 6.22: Primary 7-pulse CP PELDOR Data for the effect of Cue1, gp78CUE and OUTB1i on the conformational space on tri- and tetraubiquitin. A, C, E, G, I, K) Primary 7-pulse CP PELDOR data of doubly spin labelled tri- and tetraubiquitin variants spin labelled in the proximal and distal moiety fitted to the product (red) of all individual background decay functions (blue exponentials) times $(1-\lambda)$, with λ being the modulation depth of the signal. The background corrected dipolar signals after subtraction of the unmodulated part and renormalization are shown in green. B, D, F, H, J, L) Background-corrected 7-pulse CP PELDOR time traces of doubly spin labelled tri- and tetraubiquitin variants spin labelled in the proximal and distal moiety (red), sum of non 7-pulse dipolar signals (black) and extracted 7-pulse evolution (blue = red-black).

Table 6.3: Fitting parameters for data analysis with Gaussian model fits. Data listed are as mean of a single Gaussian (R1 and R2) with the standard deviations σ_1 and σ_2 , respectively. The population of each Gaussian distribution is given by P1 and P2, respectively. The mean distance of the entire distribution is given by $\langle R \rangle$ and the corresponding standard deviation by σ , Obtained from Approximate pake transformation.

Variant	Addition	R1 / nm	σ_1 / nm	P1 / %	R2 / nm	σ_2 / nm	P2 / %	$\langle R \rangle$	σ
Ubiquitin (100 μM)									
Ubiquitin T22C/E34C		2.91	0.19	100	-	-	-	2.91	0.13
Ubiquitin N25C/E34C		2.26	0.22	100	-	-	-	2.26	0.15
K48-linked Diubiquitin (100μM)									
pE24C/dA28C		3.12	0.82	22.5	4.38	0.59	77.5	4.09	0.69
pE24C/dA28C	Low pH (pH=4.5)	2.57	0.49	13.6	4.24	0.57	86.4	4.02	0.70
pE24C/dA28C	+Cue1 (150 μ M)	3.98	0.68	69.4	4.10	0.12	30.6	4.02	0.40
pE24C/dA28C	+gp78CUE (150 μ M)	3.45	0.95	40	4.60	0.73	60	4.14	0.81
pE24C/dA28C	+Cue2 (600 μ M)	3.39	0.97	34.3	4.46	0.64	65.7	4.10	0.74
pE24C/dA28C	+UBA2 (120 μ M)	3.90	0.77	21.2	4.60	0.51	78.8	4.45	0.50
pE24C/dA28C	+OTUB1i (150 μ M)	2.45	0.31	75.4	3.11	0.25	24.6	2.61	0.35
pE24C/dA28C	+Rpn13 (150 μ M)	4.03	1.39	100	-	-	-	4.04	0.96
pE24C/dE24C		3.03	0.31	12.2	4.14	0.53	87.8	4.00	0.51
pE24C/dE24C	+Cue1 (150 μ M)	3.96	0.13	28.7	3.93	0.96	71.3	3.94	0.57
pE24C/dE24C	+OTUB1i (150 μ M)	1.5	2.39	28.6	2.44	0.20	71.5	2.55	0.59
pA28C/dA28C		3.86	0.96	37.5	4.85	0.58	62.5	4.48	0.71
pA28C/dA28C	+Cue1(150 μ M)	4.39	0.26	33.9	4.30	1.01	66.1	4.33	0.59
pA28C/dA28C	+OTUB1i (150 μ M)	2.51	0.71	88.5	3.77	1.79	11.5	2.96	0.73
pE34C/dT22C		2.62	0.69	10.2	4.49	1.03	89.8	4.30	0.90
pE34C/dT22C	+Cue1 (150 μ M)	3.96	0.71	26.8	4.71	0.88	73.2	4.44	0.75
pE34C/dT22C	+OTUB1i (150 μ M)	4.01	0.63	54.4	4.66	1.88	45.6	4.32	0.99
pE34C/dE34C		2.07	0.48	26.8	3.95	1.65	73.2	3.49	1.28
pE34C/dE34C	+Cue1 (150 μ M)	2.57	1.37	32.9	4.31	0.81	67.1	3.82	0.96
pE34C/dE34C	+OTUB1i (150 μ M)	2.74	0.74	17.7	4.98	0.32	82.3	4.58	0.90
pE24C/pR42A/dA28C		3.62	0.82	35.6	4.45	0.55	64.4	4.15	0.61
pE24C/pR42A/dA28C	+Cue1	4.10	0.13	11.3	4.05	0.81	88.7	4.05	0.54
pE24C/dA28C/dR42A		3.67	0.84	38.5	4.44	0.51	61.3	4.14	0.59
pE24C/dA28C/dR42A	+Cue1	3.26	0.88	14.9	4.27	0.71	85.1	4.12	0.63
pE24C/pR42A/dA28C/ dR42A		3.52	0.86	34.0	4.41	0.52	66.0	4.11	0.63
pE24C/pR42A/dA28C/ dR42A	+Cue1	3.40	0.66	22.0	4.35	0.52	78.0	4.14	0.56
pE24C/pV70A/dA28C		3.12	0.56	19.0	4.38	0.55	81.0	4.14	0.63
pE24C/pV70A/dA28C	+Cue1	4.08	0.12	12.0	4.04	0.91	88.0	4.04	0.60

pE24C/dA28C/dV70A		3.06	0.44	11.2	4.40	0.62	88.8	4.24	0.60
pE24C/dA28C/dV70A	+Cue1	2.95	0.71	14.0	4.36	0.71	86.0	4.16	0.70
pE24C/pV70A/dA28C/ dV70A		3.15	0.36	12.0	4.43	0.62	88.0	4.27	0.59
pE24C/pV70A/dA28C/ dV70A	+Cue1	3.26	0.46	16.6	4.43	0.66	83.4	4.24	0.62
K48-linked Triubiquitin (50 μM)									
pE24C/dA28C [§]		3.47	1.33	56.2	5.31	0.75	43.8	4.30	1.17
pE24C/dA28C		4.51	2.17	100	-	-	-	4.60	1.44
pE24C/dA28C [§]	+Cue1 (112.5 μ M)	3.84	0.75	27.1	6.11	1.15	72.9	5.49	1.26
pE24C/dA28C [§]	+gp78CUE (112.5 μ M)	5.36	2.47	100	-	-	-	5.40	1.65
pE24C/dA28C [§]	+OTUB1i (150 μ M)	4.27	2.68	100	-	-	-	4.54	1.64
pE24C/mA28C [§]		3.57	0.83	34.6	4.37	0.63	65.4	4.09	0.63
mA28C/dA28C		3.96	0.81	33.5	4.78	0.61	66.5	4.51	0.62
pE34C/dA28C		4.28	1.32	100	-	-	-	4.34	1.29
K48-linked Tetraubiquitin (50 μM)									
pE24C/dA28C [§]		4.93	1.5	100	-	-	-	4.93	1.04
pE24C/dA28C		4.87	2.80	100	-	-	-	5.04	1.76
pE24C/dA28C [§]	Low pH (pH=4.5)	4.73	1.94	100	-	-	-	4.76	1.33
pE24C/dA28C [§]	+Cue1 (150 μ M)	5.78	1.18	100	-	-	-	5.88	1.14
pE24C/dA28C [§]	+gp78CUE (150 μ M)	6.96	4.28	100	-	-	-	6.35	2.11
pE24C/dA28C [§]	+OTUB1i (225 μ M)	4.39	3.92	61.6	5.28	0.52	38.4	4.99	1.50
pE24C/m1A28C		4.14	0.91	100	-	-	-	4.14	0.64
pA28C/dS57C [§]		2.95	5	100	-	-	-	4.68	2.10
pE34C/dA28C [§]		4.47	2.36	100	-	-	-	4.54	1.44
m1A28C/m2A28C		3.48	1.04	29.7	4.72	0.58	70.3	4.35	0.77
K11-linked Diubiquitin (100μM)									
pE24C/dA28C		3.20	1.05	55.1	4.11	0.76	49.9	3.62	0.78
K63-linked Diubiquitin(100μM)									
pE24C/dA28C		3.99	1.03	59.5	5.00	0.52	40.5	4.40	0.78
^a Obtained from Approximate pake transformation [*] Distance distribution from Tikhonov Regularization [§] 7-pulse CP PELDOR									

6.2 Materials and Methods

6.2.1 Sample preparation and purification

The *anaOmp85* POTRA domain variants were expressed, purified and spin labelled by Eva-Maria Bouwer, a former Ph.D. student in the lab of Prof. Enrico Schleiff at the Goethe-University. The experimental procedures stated below were already published in Dastvan et al. 2016. *Biophys J* 110:2195-2206 and are reprinted in this thesis for completeness.

The residues of *anaOmp85* POTRA domains, which were chosen as spin labelling sites, were substituted by cysteine via Quick-change PCR using a construct containing residues 161–467 of *anaOmp85* as described in (19). Transformed *E. coli* BL21 DE3 (Invitrogen) were inoculated in LB at 37°C. The expression was induced by addition of 1 mM isopropyl 1-thio- β -D-galactopyranoside (IPTG) at A600 = 0.8. After an incubation of 4h, the cells were harvested and resuspended in a lysis buffer (25mM HEPES/KOH pH 7.0; 250 mM NaCl; 5mM MgCl₂). The cells were lysed via sonication. The proteins were immobilized on Ni-NTA (Qiagen) after 30 min centrifugation at 25,000 x g and washed with a wash buffer (25mM HEPES/KOH pH 7.0; 250 mM NaCl; 5 mM MgCl₂; 10 mM Imidazole). The *anaOmp85* POTRA domain variants were spin labelled with MTSSL (Enzo) within the wash buffer overnight at 4°C. After extensively washing the labelled *anaOmp85* POTRA domain variants were eluted with an elution buffer (25 mM HEPES/KOH pH 7.0; 250 mM NaCl; 500 mM Imidazole). The concentration of the *anaOmp85* POTRA domain variants was determined using the Bradford reagent (Bio-Rad). The concentration was adjusted to 100 μ M for the PELDOR samples, in PELDOR buffer (25mM HEPES/KOH pH 7.0; 250 mM NaCl; 500mM Imidazole, 30% Glycerol). X-Band samples (180 μ l or 40 μ l with 100 μ M protein concentration) were transferred to standard 4 mm or 2.8 mm diameter quartz EPR tubes (Wilmad) and shock-frozen in liquid nitrogen. The Q-Band samples (10 μ l with 100 μ M protein concentration) were transferred to 1.6 mm diameter suprasil EPR tube (Wilmad) and shock-frozen in liquid nitrogen.

Ubiquitin chain variants were assembled, purified and spin labelled as well as the UBDs and the DUB utilized in this study by Andreas Kniss from the Lab of Prof. Volker Dötsch at the Goethe-University. The detailed experimental procedures stated below were put down by Andreas Kniss and are reprinted in this thesis for completeness.

The human ubiquitin and all cysteine variants, cloned into pETM60, were expressed in T7 Express competent *E.coli* cells (NEB). The purification was achieved as described [131, 158]. The enzymes for K48- and K63-linked chain synthesis Cdc34, Ubc13, Uev1a, cloned into a pGEX6p1 vector, and Ube1 sub cloned into a pET21d vector were expressed and purified as described in [159] and [160], respectively.

His6-GST tagged OTUB1 C91A and OTUD7B (Cezanne) (53-446, C194S) were expressed as previously reported in [161].

Codon-optimized synthetic genes of the Cue1 CUE domain (45-115), gp78CUE (453-503 Cue2 CUE1 domain (6-54), a single chain construct of Ubc7 (1-165) and the U7BR of Cue1 (147-203, C147S) connected via a GG-linker were expressed as tobacco etch virus (TEV) cleavable His10-tagged ubiquitin fusion proteins. A C-terminally truncated version of the human Ube2S, Ube2S Δ C (1-156), was expressed containing a C-terminal TEV protease cleavage site followed by a hexahistidine (6His) tag. In short, expression was performed in a T7 Express competent *E.coli*. The cells were grown in Terrific Broth (TB) medium and induced for 20h at 18°C with 0.5 mM isopropyl- β -D-1-thiogalactopyranoside (IPTG). Purification was achieved by immobilized metal chelate affinity chromatography (IMAC), tag removal by TEV (except for Cue2 CUE1), a reversed IMAC step, followed by size exclusion chromatography using a HiLoad Superdex S75 column (GE Healthcare). Proximally 6His-tag capped cysteine-containing ubiquitin chains were enzymatically assembled in vitro as previously described [131]. K48-linkages were synthesized using Cdc34, K63- linked chains were generated by Ubc13 and Uev1a and K11-linkages were introduced using Ube2S Δ C (1-156) [162]. To avoid K63-linkage impurities during K11-linked chain synthesis all ubiquitin variants additionally contained a K63R mutation. Assembly of K48-linked tri- and tetraubiquitin chains required an iterative chain assembly protocol, in which the desired reaction products were purified (by NiNTA purification and subsequent gel filtration) and reemployed in further preparative chain elongation reaction. Wildtype K48-linked chains of defined length for ITC experiments were synthesized in a single 20 mL reaction using 1 μ M E1, 10 μ M Cdc34, 1500 μ M wildtype Ub in buffer containing 50 mM Tris (pH 7.8), 20 mM ATP, 0.9 mM DTT, 9 mM MgCl₂ at 37°C overnight. Ub chains were diluted in 50 mM ammonium acetate (pH 4.5), filtered through a 0.2

μm syringe filter, applied in aliquots onto a MonoS column (GE Healthcare) and eluted using a salt gradient with 0.5 M NaCl as target concentration. Peak fractions were further purified using a 16/60 Superdex 75 gel filtration column. Cysteine containing ubiquitin chains variants (100 μM) were labelled with a 20-fold excess over the cysteine amount of 1-Oxyl-2,2,5,5-tetramethylpyrroline-3-methyl (MTSSL) 1x PBS buffer at room temperature for 1h. Unreacted MTSSL was removed by buffer exchange to deuterated PBS buffer (pD 7.2) utilizing Amicon Ultra centrifugal filter units. 20% d8-glycerol were added to each sample as a cryoprotectant. The Q-Band samples (5-10 μl with 50 or 100 μM protein concentration, see Table 6.3) were transferred to 1.6 mm diameter suprasil EPR tube (Wilmad) and shock-frozen in liquid nitrogen.

6.2.2 X-Band CW EPR Measurements

The X-band CW measurements on spin labelled *anaOmp85* POTRA variants were obtained Dr. Reza Dastvan, a former Ph.D. student in the group of Prof. Thomas F. Prisner, who is currently a Postdoctoral researcher at Vanderbilt University in the group of Prof. Hassane S. Mchaourab. The X-band CW experiments on spin labelled ubiquitin variants were performed by the author herself.

Room-temperature cw X-band spectra were acquired on a Bruker Elexsys E500 cw X-band EPR spectrometer equipped either with a standard rectangular Bruker EPR cavity (ER4102ST7934), at a quality factor Q of about 3000 (*anaOmp85* POTRA domains), or a SHQE (ER4122 011 SHQE-W1), at a quality factor Q of about 4500 (ubiquitin variants). The microwave frequency was determined using a Systron Donner (6054D) frequency counter. The magnetic field was measured with a Bruker gaussmeter (ER035M).

The measurements were accomplished with a frequency of ~ 9.4 GHz and a centre magnetic field of 3360 G, with a sweep width of 120 G. Measurement on *anaOmp85* POTRA domain variants and ubiquitin chain variants were accomplished with 512 scans and 1024 scans, respectively. The modulation amplitude had a value of 1.5 G (*anaOmp85* POTRA domain variants) or 1 G (ubiquitin chain variants) and a modulation frequency of 100 kHz. The microwave power was ~ 2 mW and a receiver gain of 75 dB or 55 dB for measurements on *anaOmp85* POTRA domain variants or ubiquitin chain variants, respectively.

6.2.3 PELDOR Data Collection and Data Analysis

Pulsed EPR data were measured on an ELEXSYS E580 EPR spectrometer (Bruker, Billerica, MA) equipped with a Bruker PELDOR unit (E580-400U). The temperature was kept at 50 K with a continuous-flow helium cryostat (CF935) and temperature control system (ITC 502), both from Oxford Instruments (Abingdon, UK). For PELDOR experiments the dead-time free 4-pulse sequence was utilized [65]. For measurements at X-Band frequencies (9.6 GHz), a 1 kW TWT amplifier (ASE 117x) and a dielectric ring resonator or split ring resonator (MD5 W1 or MS3) were used. The measurements at Q-band frequencies (33.7 GHz) were obtained using the SuperQ-FT accessory as well as a Bruker AmpQ 10 W amplifier and a Bruker EN5107D2 resonator.

The X-band PELDOR measurements on spin labelled POTRA variants were obtained Dr. Reza Dastvan, a former Ph.D. student in the group of Prof. Thomas F. Prisner, who is currently a Postdoctoral researcher at Vanderbilt University in the group of Prof. Hassane S. Mchaourab. An exception to this were the *anaP1-anaP2* variants related to Q259C and Q374C and *anaP1-anaP3* variant Q259C-L448C, which were performed by the author herself. The typical pulse lengths for the probe pulses and the pump pulse were 32 ns ($\pi/2$ and π) and 12 ns, respectively. To reduce contributions from nuclear modulations the delay between the first and second probe pulses was varied between 136 and 192 or 200 and 256 ns in 8 ns steps (protonated samples) and between 456 and 848 ns in 56 ns steps (for buffer deuterated sample I292C/V460C) [163]. Dependent on the probed distances and transversal relaxation time (T_M) of the samples, the pulse separation between the second and third probe pulses was between 1.2 and 7.3 μ s. The shot repetition time was 4-5 ms. The frequency of the pump pulse was set to the resonance frequency of the over-coupled resonator ($Q \sim 50$). To obtain an optimum pumping efficiency the magnetic field was chosen such that the excitation coincides with the maximum of the nitroxide powder spectrum. The frequency of the probe pulses was chosen 70 MHz higher (80 MHz for the A319C/E344C sample). Possible orientation selective effects were probed for I292C/E344C, I292C/V370C, N265C/A319C, Q429C/A319C, Q429C/E344C, V460C/E344C by experiments using a 40 MHz offset between the pump and probe frequency. No changes in the PELDOR time traces were observed, excluding orientation selection (Only I292C/V370C is shown in Figure 6.7).

The Q-band 4-pulse PELDOR on spin labelled ubiquitin variants were performed by the author herself with pulse lengths of 32 ns ($\pi/2$ and π) for the probe pulses and 20 ns for the pump pulse. Due to the negligible effect of nuclear modulations for protons at this frequency band [164], the delay between the first and second probe pulses has not been varied. The pulse separation between the second and third probe pulses was between 3-4 μ s, depending on the probed distances and transversal relaxation time (T_M) of the samples, and a shot repetition time of 4.5 ms was used. The frequency of the pump pulse was set to the resonance frequency of the over-coupled resonator ($Q \sim 300$). The magnetic field was chosen to coincide with the maximum of the nitroxide powder spectrum to obtain optimum pumping efficiency. The frequency of the probe pulses was chosen 70 MHz lower, compared to the frequency of the pump pulse. The experiments on triubiquitin variant mA28C/dA28C and tetraubiquitin variant m1A28C/m2A28C, as well as diubiquitin variants in complex with Rpn13, were accomplished using a 150 W Q-band TWT, using pulse lengths of 32 ns ($\pi/2$ and π) for the probe pulses and 12 ns (π) for the pump pulse. Nuclear modulation averaging was achieved by a variation of the delay between the first and second probe pulses between 260 and 372 in 8 ns steps. The shot repetition time was 4.5-5 ms.

The 7-pulse CP PELDOR measurements were obtained in collaboration with Dr. Philipp E. Spindler, a Postdoctoral researcher in the group of Prof. Thomas F. Prisner at the Goethe-University. The typical pulse lengths were 32 ns ($\pi/2$ and π) and 400 ns (π) for the probe pulses and the sech/tanh pump pulses, respectively. The interpulse delays ($t_1 = 5000$ ns, $t_2 = 10400$ ns and $t_3 = 10200$ ns) for the detection sequence were chosen according to [48]. The initial pump pulse positions were $T_1 = 232$ ns, $T_2 = 300$ ns, and $T_3 = -232$ ns. These positions were incremented with $\Delta 1 = 24$ ns, $\Delta 2 = 0$, $\Delta 3 = -24$ ns. The sech/tanh pump pulses were generated with a homebuilt pulse shaping unit [165]. The pump pulses carrier frequency was set to the resonance frequency of the resonator to ensure an optimum inversion efficiency. A shot repetition time of 3 ms was used. The frequency of the pump pulse was set to the center of the over-coupled resonator ($Q \sim 300$), while the probe frequency was chosen or 65 MHz lower. The magnetic field was adjusted, such that the excitation by the pump pulses coincides with the central peak of the nitroxide powder spectrum to obtain maximum pumping efficiency.

The analysis of the experimental data on spin labelled *anaOmp85* POTRA variants were obtained Dr. Reza Dastvan, a former Ph.D. student in the group of Prof. Thomas F. Prisner, who is currently a Postdoctoral researcher at Vanderbilt University in the group of Prof. Hassane S. Mchaourab. An exception to this were the *anaP1-anaP2* variants related to Q259C

and Q374C and *anaP1-anaP3* variant Q259C-L448C, which were performed by the author herself. The analysis of the experimental data on spin labelled ubiquitin variants was performed by the author herself.

The analysis of the experimental data was performed with DeerAnalysis software package [70]. The PELDOR time traces were corrected for background decay using a homogeneous three-dimensional spin distribution. Seven pulse data was subjected to a self-consistent iterative correction procedure [48], prior to data processing with DeerAnalysis, to remove dipolar signal originating from the combinations of only one or two pump pulses. The probability of spin inversion p was found to be 0.72 (Figure 6.19A). The self-consistent iterative ‘artefact’ correction procedure, as well as background-correction, was performed by Dr. Philipp E. Spindler, a Postdoctoral researcher in the group of Prof. Thomas F. Prisner at the Goethe-University.

6.2.4 *In silico* prediction of PELDOR distance restraints

In silico spin labelling, of available Protein Data Bank (PDB) structures, was accomplished using the rotamer library approach using the Multiscale modelling of macromolecular systems (MMM) software package [38] or by the tether-in-a-cone model in mtsslWizard [43, 44].

In silico spin labelling of the X-ray structure of *anaOmp85* POTRA domain (PDB code 3mc8) was used to predict the inter-spin distances and intramolecular dipolar evolution functions for all spin label pairs. Hereby, different rotamer libraries to model the conformational flexibility of MTSSL were used for the predictions and compared to the experimental results. For rotamer libraries MMM (175 K and 298 K), Warsh and Sezer (Sezer12 and Sezer13 in 175K and 298 K mode, respectively) predictions of distance distributions and intramolecular dipolar evolution functions were directly performed in MMM. Distance distributions from MD simulation trajectories were extracted using every 40th frame by calculating the distance between geometric midpoints of N1 and O1 atoms of MTSSL. Intramolecular dipolar evolution functions for distance distributions derived from mtsslWizard, using thorough search and loose vdW restraints (cut-off 2.5Å, 5 clashes allowed), and MD simulations were simulated in a home-written MATLAB[®] script.

In silico spin labelling and prediction of distances distributions and dipolar evolution functions of the ubiquitin and polyubiquitin structures (Protein Data Bank [PDB] codes: 2PEA, 2PE9,

2O6V, 3M3J, 1ZO6, 2IVQ, 2LVP, 1AAR, 2BGF, 3AUL, 3NS8, 4DDI) was performed using the standard MMM rotamer library in 298K mode.

6.2.5 Structural Refinement of the X-ray structure of the POTRA domains

The rigid body refinements were conducted by Prof. Dr. Thomas F. Prisner at the Goethe-University and the Rosetta refinement by Dr. Oliver Mirus, a former Postdoctoral researcher in the group of Prof. Dr. Enrico Schleiff at the Goethe-University. The refinement procedures and their detailed description were already published in Dastvan et al. 2016. *Biophys J* 110:2195-2206 and are reprinted in this thesis for completeness.

Structural refinement of the X-ray structure 3MC8 was done using two approaches, a rigid body motion approach using a home-written MATLAB® script and secondly a more structure-based approach using Rosetta. The rigid body refinements were conducted by Prof. Dr. Thomas F. Prisner at the Goethe-University and the Rosetta refinement by Dr. Oliver Mirus, a former Postdoctoral researcher in the group of Prof. Dr. Enrico Schleiff at the Goethe-University.

In the first approach, the N-O midpoint coordinates of each spin label derived from rotamer libraries described in Chapter 2.4 and Chapter 6.2.4 were fixed relative to the individual *anaOmp85* POTRA domain they are attached to (rigid body assumption). The rigid bodies of domain *anaP1* and *anaP3* were then displaced (x, y, and z) and rotated (alpha, beta, and gamma) with respect to *anaP2*, to minimize the RMSD between experimental and predicted distance distribution function. Typically, 20,000 minimizations (with different starting conditions) were performed and the 100 best solutions were stored. The linker regions between the domains *anaP1*, *anaP2*, and *anaP3* of the best solutions were rebuilt using Yasara. For the second approach, a YASARA [166] Python script was developed to screen the relative orientational space of the POTRA domains (with respect to the twist and swing angles) utilizing Rosetta (www.rosettacommons.org, release 2015.05.57576). The angular space, which was explored in the MD simulations (*anaP1-anaP2* twist 0°-160°, swing 0°-120°; *anaP2-anaP3* twist 10°-105°, swing 0°-75°) was screened in steps of 18°. For in total 143 angle combinations the corresponding structure was extracted from the trajectories of the MD simulations. In case a structure with the required angle combination was not available, two structures were extracted from the trajectories, i.e. one with the required *anaP1-anaP2* angles, and another one, which fulfils the requirements for *anaP2-anaP3*. These two structures were then further processed and

joined to form a single structure, whose angles correspond to the requested angle combination for *anaP1-anaP2* as well as *anaP2-anaP3*. Any missing/superfluous MTSSLs in these structures were introduced/removed. The above-selected structures were subjected to Rosetta relax protocol [167] creating 500 models for each input structure ($143 \times 500 \approx 72,000$ Rosetta models) enforcing distance restraints to ensure that the pairwise spin label distances lie within the range of the experimentally determined distance distributions. Briefly, the better rotamer pairs match the distances associated with the highest normalized frequencies, the larger their contribution to the total Rosetta score of a model. A virtual atom was introduced at the geometric centre of the N1 and O1 atoms of each spin label by extending the MTSSL parameter file included in Rosetta. Distance restraints of type “AtomPair” were defined between these virtual atoms of spin label pairs and the experimentally determined spin label pair distance distributions were used as SPLINE functions for restraint scoring. The frequencies of each distance distribution were normalized to [0, 1]; they were multiplied with -1 to fit into Rosetta’s scoring scheme. The restraint weight was set to 4, which leads to optimal results with RosettaEPR [34]. It employs a related approach for refining structures with EPR/PELDOR data.

6.2.6 Generation of a structural ensemble of K48-linked diubiquitin

Structural modelling employing CYANA was done by Dr. Sina Kazemi from the Güntert Lab at Goethe-University. The detailed procedures stated below were put down by Sina Kazemi and are reprinted in this thesis for completeness.

In the first step, an ensemble of diubiquitin structures with a broad distance distribution between the monomers was generated using CYANA 3.9 [37]. In order to do so, a CYANA library entry for MTSSL was generated. To include the PELDOR distance restraints into the structure calculations, this entry included a virtual atom (without any interaction with other atoms) placed in the centre of the N-O bond of the nitroxide, which represented the unpaired electron and served to define the PELDOR distance restraint between the virtual atoms of an MTSSL pair. Other than in the PELDOR experiments, where only one spin pair in each sample was present, the spin labels were inserted at all positions (residue T22, E24, A28, and E34) in both monomers during the generation of the structural ensemble. During all calculations, the backbone angles ϕ and ψ of the core ubiquitin residues (residues 1 to 71) for both monomers were fixed to the values found in the first chain of the diubiquitin reference structure 2PEA, (rigid body

assumption). The flexible linker region (residues 72 to 76) and all side-chain χ angles were allowed to move freely except for the MTSSL sidechain, for which the conformations were restricted by a rotamer library generated by MMM2015.2 [38] based on 2PEA. To include the rotamer libraries for the specific residues an in-house developed extension of CYANA was used [37]. This approach allows CYANA to take into account the entire bundle of rotamers from the given rotamer library. This is realized by a new restraint that has a value of 0 (no contribution to the target function) when the MTSSL sidechain adopts a conformation in the rotamer library and increases with increasing deviation from this library. After the calculation, this restraint was checked and structures with rotamer restraint larger than a pre-defined threshold value were not further considered. Additionally, a modified lysine residue CYANA library entry was generated by deleting two of the hydrogens of the lysine's zeta nitrogen. This modified lysine was connected to the second monomer's c-terminal glycine by nine upper and lower limits with a thousand fold weight to guarantee an optimal binding geometry. For each structure calculation, five additional distances between the MTSSL pairs were set as described below.

In order to define the entire conformation space allowed by the PELDOR restraints, both the minimal and the maximal distances were extracted from the experimental distance distributions. These were 1.5-5.1 nm, 1.9-5.2 nm, 1.5-5.7 nm, 3.0-5.8 nm, and 1.6-5.7 nm for the spin labelled pairs pE24C/dE24C, pE24C/dA28C, pA28C/dA28C, pE34C/dT22C, and d34C/dE34C, respectively. Using these distance ranges a conformational ensemble was created by a systematic variation of each distance range in steps of 0.5 ± 0.25 nm (e.g. 2.75 nm as lower and 3.25 nm as upper bound for a distance of 3 nm). Thus, this conformational ensemble contains all possible combinations of five distances within each of these distance ranges. Overall 51,001 structure calculations were performed. For each distance combination, a bundle of 20 structures with the lowest target function out of 100 calculated structures was generated. All structures showing van der Waals collisions between the two ubiquitin chains or not fulfilling the above described distance ranges were dropped to generate a collision-free conformational ensemble of $\sim 3.7 \times 10^5$ models. This ensemble represents the accessible conformational space that is consistent with the upper and lower boundaries of the PELDOR measurements.

To calculate the population distribution within this conformational space each conformation of this ensemble was weighted by a pseudo probability. Taking the PELDOR distance restraints as a density distribution (with an integral of unity) a combined probability factor for any given structure was calculated. The height of the PELDOR distance distribution was used as a pseudo probability for each distance. For any given structure, all five pseudo probabilities were multiplied to obtain an overall probability factor. The resulting values for each structure were

then divided by the maximum probability obtained in these calculations such that the structure with the highest value was assigned the probability of one. This created a relative pseudo probability that allows the comparison of the relative weights of specific conformations. Hereafter, all structures with a relative pseudo probability of less than 1% were dropped.

To visualize the distribution of the distal ubiquitin relative to the proximal ubiquitin with respect to the assigned probabilities a three-dimensional grid was generated. The backbone atoms of the proximal ubiquitin (only residues 1 to 71) were superimposed. For the representation, a subset of 3000 structures that showed a probability distribution similar to the full set was selected. Each distal ubiquitin was represented as a truncated 3D Gaussian (1) around its geometric centre (with coordinates C_{ix} , C_{iy} , C_{iz}).

$$G_i(x, y, z) = p_i \cdot e^{-\frac{(x-c_{ix})^2 + (y-c_{iy})^2 + (z-c_{iz})^2}{2r_0^2}} \quad \text{Eq. 6.1}$$

Each Gaussian with $r_0 = 5.3 \text{ nm}$ was scaled such that the maximum equals the probability p_i of the specific structure. All values above a certain truncation radial distance of $r_0^2/2$ were set to zero in the grid. The grids containing Gaussians for each structure of the ensemble were merged into one grid by taking the maximum value of each grid-point. Showing hyper-surfaces covering regions above threshold values (as in three-dimensional contour lines) for this probability grid in PyMOL results in overlapping globes where the radius of each globe represents the probability of a representative conformation at this point.

6.2.7 Molecular Dynamic simulations of POTRA domains

The MD and REMD simulation were carried out by Dr. Oliver Mirus, a former Postdoctoral researcher in the group of Prof. Dr. Enrico Schleiff at the Goethe-University. The detailed procedures were already published in Dastvan et al. 2016. Biophys J 110:2195-2206 and are reprinted in this thesis for completeness.

Molecular Dynamics Simulations - Wild-Type: The rotational freedom of the *anaOmp85* the POTRA domains was explored by REMD simulations across 128 replicas in the temperature range from 300 to 405 K. A webserver (<http://folding.bmc.uu.se/remd/> [168]) was used to calculate the exponential temperature distribution of the replicas with an exchange probability of 0.2. The 20 ns REMD simulation (20 ns x 128 replicas = 2,560 ns) using the AMBER03

force field [169] was performed with Gromacs 5.0.4. A rhombic dodecahedron was selected as the shape of the simulation box with the protein being at least 18 Å away from the periodic boundaries. A 5 fs time step was enabled by converting hydrogen atoms to virtual sites (pdb2gmx option `-vsite hydrogens`). The Verlet cut-off scheme was used for neighbour searching [170]. The short-range cut-off was 1.4 nm. Long-range electrostatics were calculated with PME [171]. The PME order was 4 and the Fourier spacing 0.16 nm. Two groups (protein, water/ions) were used for temperature coupling with a time constant of 0.1 ps using the V-rescale thermostat [172]. Isotropic pressure coupling was performed with a Parrinello-Rahman barostat [173, 174] using a time constant of 2.0 ps to keep the pressure at 1.0 bar. The 1 μs wild-type MD simulation of *anaOmp85* POTRA domains used the same parameters as described for the REMD setup, but the temperature was set to 300 K.

Molecular Dynamics Simulations – Spin labelled Variants: For spin labelled variants, MTSSL was modelled, quantum mechanically optimized with YASARA [175] and introduced into the X-ray of the *anaOmp85*-POTRA domains (PDB code 3mc8) at appropriate sites. In total 5 sets of variants were constructed, which carry MTSSLs at the following positions in *anaP1* and *anaP3*: (i) Q259, I292, Q429, V460, (ii) N265, Q429, (iii) Q259, I292, L448, (iv) Q259, I292, V457, (v) G233, V460. For each set 3 MD simulations were performed, where *anaP2* carries MTSSL at residue A319, E344 or V370, respectively. The spin label combinations of these variants minimize the number of required simulations as well as the putative contact between the SLs. MD simulations were performed with YASARA using the AMBER03 force field [169]. The structures were put in cubic simulation boxes of 128Å side length with periodic boundaries. The three POTRA domains of the initial (X-ray) conformation of *anaOmp85* span about 9nm; also a fully elongated (~10.5 nm) structure can be accommodated in the box. Placement of water and ions, as well as pKa prediction of protonatable groups of the protein, were performed with YASARA's neutralization experiment [176]. The van-der-Waals interactions were cut off at 10.48 Å and Coulomb interactions were calculated with PME [171]. Proteins were simulated for 100 ns at 298 K.

Bibliography

- [1] J.H. Han, S. Batey, A.A. Nickson, S.A. Teichmann, J. Clarke, The folding and evolution of multidomain proteins, *Nat Rev Mol Cell Biol*, 8 (2007) 319-330.
- [2] A. Roy, D.P. Hua, C.B. Post, Analysis of Multidomain Protein Dynamics, *Journal of Chemical Theory and Computation*, 12 (2016) 274-280.
- [3] N. Ban, P. Nissen, J. Hansen, P.B. Moore, T.A. Steitz, The complete atomic structure of the large ribosomal subunit at 2.4 Å resolution, *Science*, 289 (2000) 905-920.
- [4] P. Cramer, D.A. Bushnell, R.D. Kornberg, Structural basis of transcription: RNA polymerase II at 2.8 Å resolution, *Science*, 292 (2001) 1863-1876.
- [5] B. Loll, J. Kern, W. Saenger, A. Zouni, J. Biesiadka, Towards complete cofactor arrangement in the 3.0 Å resolution structure of photosystem II, *Nature*, 438 (2005) 1040-1044.
- [6] R.P. Rambo, J.A. Tainer, Super-resolution in solution X-ray scattering and its applications to structural systems biology, *Annu Rev Biophys*, 42 (2013) 415-441.
- [7] H.D. Mertens, D.I. Svergun, Structural characterization of proteins and complexes using small-angle X-ray solution scattering, *J Struct Biol*, 172 (2010) 128-141.
- [8] M.H. Stowell, A. Miyazawa, N. Unwin, Macromolecular structure determination by electron microscopy: new advances and recent results, *Curr Opin Struct Biol*, 8 (1998) 595-600.
- [9] J. Kim, S. Wu, T. Tomasiak, C. Mergel, M.B. Winter, S.B. Stiller, Y. Robles-Colmanares, R.M. Stroud, R. Tampé, C.S. Craik, Y. Cheng, Subnanometer resolution cryo-EM structure of a nucleotide free heterodimeric ABC exporter, *Nature*, 517 (2015) 396-400.
- [10] W. Kühlbrandt, Cryo-EM enters a new era, *eLife*, 3 (2014) e03678.
- [11] K. Wüthrich, *NMR of Proteins and Nucleic Acids*, Wiley, 1986.
- [12] R.R. Ernst, *Nuclear Magnetic Resonance Fourier Transform Spectroscopy* (Nobel Lecture), *Angewandte Chemie International Edition in English*, 31 (1992) 805-823.
- [13] A.M. Bonvin, R. Boelens, R. Kaptein, NMR analysis of protein interactions, *Current opinion in chemical biology*, 9 (2005) 501-508.
- [14] M. Hong, Y. Zhang, F. Hu, Membrane protein structure and dynamics from NMR spectroscopy, *Annu Rev Phys Chem*, 63 (2012) 1-24.

-
- [15] A.B. Barnes, G.D. Paëpe, P.C.A. van der Wel, K.N. Hu, C.G. Joo, V.S. Bajaj, M.L. Mak-Jurkauskas, J.R. Sirigiri, J. Herzfeld, R.J. Temkin, R.G. Griffin, High-Field Dynamic Nuclear Polarization for Solid and Solution Biological NMR, *Appl. Magn. Reson.*, 34 (2008) 237-263.
- [16] D. Marion, An Introduction to Biological NMR Spectroscopy, *Molecular & Cellular Proteomics : MCP*, 12 (2013) 3006-3025.
- [17] N. Tjandra, A. Bax, Direct Measurement of Distances and Angles in Biomolecules by NMR in a Dilute Liquid Crystalline Medium, *Science*, 278 (1997) 1111-1114.
- [18] C. Camilloni, M. Vendruscolo, A Tensor-Free Method for the Structural and Dynamical Refinement of Proteins using Residual Dipolar Couplings, *The Journal of Physical Chemistry B*, 119 (2015) 653-661.
- [19] G.M. Clore, J. Iwahara, Theory, practice, and applications of paramagnetic relaxation enhancement for the characterization of transient low-population states of biological macromolecules and their complexes, *Chemical reviews*, 109 (2009) 4108-4139.
- [20] N.J. Anthis, G.M. Clore, Visualizing transient dark states by NMR spectroscopy, *Q Rev Biophys*, 48 (2015) 35-116.
- [21] D.W. Piston, G.-J. Kremers, Fluorescent protein FRET: the good, the bad and the ugly, *Trends Biochem Sci*, 32 (2007) 407-414.
- [22] M.A. Hemminga, L.J. Berliner, ESR Spectroscopy in Membrane Biophysics, in: *Biological Magnetic Resonance*, Vol. 27, Springer, New York, USA, 2007.
- [23] J.P. Klare, Site-directed spin labeling EPR spectroscopy in protein research, *Biol. Chem.*, 394 (2013) 1281-1300.
- [24] L.J. Berliner, J. Reuben, Spin Labeling - Theory and Applications, in: *Biological Magnetic Resonance*, Vol. 8, Springer US, 1989.
- [25] L.J. Berliner, Spin Labeling The Next Millennium, in: L.J. Berliner (Ed.) *Biological Magnetic Resonance*, Vol. 14, Kluwer Academic Publishers, USA, 2002.
- [26] A.D. Milov, K.M. Salikhov, M.D. Shirov, Use of the double resonance in electron-spin echo method for the study of paramagnetic center spatial distribution in solids, *Fizika Tverdogo Tela*, 23 (1981) 975-982.
- [27] A.D. Milov, A.B. Ponomarev, Y.D. Tsvetkov, Electron Electron Double-Resonance in Electron-Spin Echo - Model Biradical Systems and the Sensitized Photolysis of Decalin, *Chem Phys Lett*, 110 (1984) 67-72.
- [28] L. Loura, M. Prieto, FRET in Membrane Biophysics: An Overview, *Frontiers in Physiology*, 2 (2011) Article 82.

- [29] G. Jeschke, DEER Distance Measurements on Proteins, *Ann. Rev. Phys. Chem.*, 63 (2012) 419-446.
- [30] C. Altenbach, T. Marti, H.G. Khorana, W.L. Hubbell, Transmembrane protein structure: spin labeling of bacteriorhodopsin mutants, *Science*, 248 (1990) 1088-1092.
- [31] R. Langen, K.J. Oh, D. Cascio, W.L. Hubbell, Crystal Structures of Spin Labeled T4 Lysozyme Mutants: Implications for the Interpretation of EPR Spectra in Terms of Structure†, *Biochemistry*, 39 (2000) 8396-8405.
- [32] A. Šali, T.L. Blundell, Comparative Protein Modelling by Satisfaction of Spatial Restraints, *J. Mol. Biol.*, 234 (1993) 779-815.
- [33] A. Fiser, A. Šali, Modeller: Generation and Refinement of Homology-Based Protein Structure Models, in: *Methods in Enzymology*, Volume 374, Academic Press, 2003, pp. 461-491.
- [34] S.J. Hirst, N. Alexander, H.S. McHaourab, J. Meiler, RosettaEPR: an integrated tool for protein structure determination from sparse EPR data, *J Struct Biol*, 173 (2011) 506-514.
- [35] N.S. Alexander, R.A. Stein, H.A. Koteiche, K.W. Kaufmann, H.S. McHaourab, J. Meiler, RosettaEPR: rotamer library for spin label structure and dynamics, *PLoS One*, 8 (2013) e72851.
- [36] P. Güntert, Automated structure determination from NMR spectra, *Eur Biophys J*, 38 (2009) 129-143.
- [37] P. Güntert, L. Buchner, Combined automated NOE assignment and structure calculation with CYANA, *J Biomol NMR*, 62 (2015) 453-471.
- [38] Y. Polyhach, E. Bordignon, G. Jeschke, Rotamer libraries of spin labelled cysteines for protein studies, *Phys Chem Chem Phys*, 13 (2010) 2356-2366.
- [39] D. Sezer, J.H. Freed, B. Roux, Simulating electron spin resonance spectra of nitroxide spin labels from molecular dynamics and stochastic trajectories, *J Chem Phys*, 128 (2008) 165106.
- [40] D. Sezer, J.H. Freed, B. Roux, Parametrization, molecular dynamics simulation, and calculation of electron spin resonance spectra of a nitroxide spin label on a polyalanine alpha-helix, *J Phys Chem B*, 112 (2008) 5755-5767.
- [41] M.R. Fleissner, D. Cascio, W.L. Hubbell, Structural origin of weakly ordered nitroxide motion in spin-labeled proteins, *Protein Sci.*, 18 (2009) 893-908.
- [42] D.T. Warshaviak, L. Serbulea, K.N. Houk, W.L. Hubbell, Conformational analysis of a nitroxide side chain in an alpha-helix with density functional theory, *J Phys Chem B*, 115 (2011) 397-405.

-
- [43] G. Hagelueken, R. Ward, J.H. Naismith, O. Schiemann, MtsslWizard: In Silico Spin-Labeling and Generation of Distance Distributions in PyMOL, *Appl Magn Reson*, 42 (2012) 377-391.
- [44] G. Hagelueken, D. Abdullin, R. Ward, O. Schiemann, mtsslSuite: In silico spin labelling, trilateration and distance-constrained rigid body docking in PyMOL, *Molecular Physics*, 111 (2013) 2757-2766.
- [45] N.M. Atherton, N.M. Atherton, *Principles of electron spin resonance*, Ellis Horwood/PTR Prentice Hall, New York [etc.], 1993.
- [46] A. Schweiger, G. Jeschke, *Principles of Pulse Electron Paramagnetic Resonance* Oxford University Press, New York, 2001.
- [47] J.A. Weil, J.R. Bolton, *Electron Paramagnetic Resonance*, in: *Elementary Theory and Practical Applications*, John Wiley & Sons, Inc., Hoboken, New Jersey, 2007.
- [48] P.E. Spindler, I. Waclawska, B. Endeward, J. Plackmeyer, C. Ziegler, T.F. Prisner, Carr–Purcell Pulsed Electron Double Resonance with Shaped Inversion Pulses, *The Journal of Physical Chemistry Letters*, 6 (2015) 4331-4335.
- [49] M.H.L. Pryce, A Modified Perturbation Procedure for a Problem in Paramagnetism, *Proceedings of the Physical Society. Section A*, 63 (1950) 25.
- [50] A. Abragam, M.H.L. Pryce, Theory of the Nuclear Hyperfine Structure of Paramagnetic Resonance Spectra in Crystals, *Proceedings of the Royal Society of London. Series A. Mathematical and Physical Sciences*, 205 (1951) 135-153.
- [51] W. Gerlach, O. Stern, Das magnetische Moment des Silberatoms, *Zeitschrift für Physik*, 9 (1922) 353-355.
- [52] W. Gerlach, O. Stern, Der experimentelle Nachweis des magnetischen Moments des Silberatoms, *Zeitschrift für Physik*, 8 (1922) 110-111.
- [53] E. Zavoisky, Paramagnetic Absorption in Perpendicular and Parallel Fields for Salts, Solutions and Metals, in, Kazan State University, 1944.
- [54] E. Zavoisky, Spin-magnetic resonance in paramagnetics, *J. Phys. U.S.S.R*, 9 (1945) 211-245.
- [55] E. Fermi, Über die magnetischen Momente der Atomkerne, *Zeitschrift für Physik*, 60 (1930) 320-333.
- [56] O. Schiemann, T.F. Prisner, Long-range distance determinations in biomacromolecules by EPR spectroscopy, *Q Rev Biophys*, 40 (2007) 1-53.

[57] A.D. Milov, A.G. Maryasov, Y.D. Tsvetkov, Pulsed electron double resonance (PELDOR) and its applications in free-radicals research, *Appl. Magn. Reson.*, 15 (1998) 107-143.

[58] C. Altenbach, A.K. Kusnetzow, O.P. Ernst, K.P. Hofmann, W.L. Hubbell, High-resolution distance mapping in rhodopsin reveals the pattern of helix movement due to activation, *Proc. Natl. Acad. Sci. U.S.A.*, 105 (2008) 7439-7444.

[59] M. Grote, Y. Polyhach, G. Jeschke, H.J. Steinhoff, E. Schneider, E. Bordignon, Transmembrane signaling in the maltose ABC transporter MalFGK2-E: periplasmic MalF-P2 loop communicates substrate availability to the ATP-bound MalK dimer, *J. Biol. Chem.*, 284 (2009) 17521-17526.

[60] J. Bhatnagar, J.H. Freed, B.R. Crane, Rigid body refinement of protein complexes with long-range distance restraints from pulsed dipolar ESR, *Methods Enzymol*, 423 (2007) 117-133.

[61] D. Hilger, Y. Polyhach, E. Padan, H. Jung, G. Jeschke, High-resolution structure of a Na⁺/H⁺ antiporter dimer obtained by pulsed electron paramagnetic resonance distance measurements, *Biophys J*, 93 (2007) 3675-3683.

[62] D. Hilger, Y. Polyhach, H. Jung, G. Jeschke, Backbone structure of transmembrane domain IX of the Na⁺/proline transporter PutP of *Escherichia coli*, *Biophys J*, 96 (2009) 217-225.

[63] R. Dastvan, E.M. Brouwer, D. Schuetz, O. Mirus, E. Schleiff, T.F. Prisner, Relative Orientation of POTRA Domains from Cyanobacterial Omp85 Studied by Pulsed EPR Spectroscopy, *Biophys J*, 110 (2016) 2195-2206.

[64] R.E. Martin, M. Pannier, F. Diederich, V. Gramlich, M. Hubrich, H.W. Spiess, Determination of end-to-end distances in a series of TEMPO diradicals of up to 2.8 nm length with a new four-pulse double electron electron resonance experiment, *Angew. Chem.-Int. Edit.*, 37 (1998) 2834-2837.

[65] M. Pannier, S. Veit, A. Godt, G. Jeschke, H.W. Spiess, Dead-time free measurement of dipole-dipole interactions between electron spins, *J. Magn. Reson.*, 142 (2000) 331-340.

[66] A.D. Milov, A.G. Maryasov, Y.D. Tsvetkov, J. Raap, Pulsed ELDOR in spin-labeled polypeptides, *Chem Phys Lett*, 303 (1999) 135-143.

[67] A.D. Milov, Y.D. Tsvetkov, F. Formaggio, M. Crisma, C. Toniolo, J. Raap, The secondary structure of a membrane-modifying peptide in a supramolecular assembly studied by PELDOR and CW-ESR spectroscopies, *J Am Chem Soc*, 123 (2001) 3784-3789.

[68] B.E. Bode, D. Margraf, J. Plackmeyer, G. Dürner, T.F. Prisner, O. Schiemann, Counting the Monomers in Nanometer-Sized Oligomers by Pulsed Electron–Electron Double Resonance, *J Am Chem Soc*, 129 (2007) 6736-6745.

- [69] B.E. Bode, R. Dastvan, T.F. Prisner, Pulsed electron-electron double resonance (PELDOR) distance measurements in detergent micelles, *Journal of Magnetic Resonance*, 211 (2011) 11-17.
- [70] G. Jeschke, V. Chechik, P. Ionita, A. Godt, H. Zimmermann, J. Banham, C.R. Timmel, D. Hilger, H. Jung, DeerAnalysis2006 - a comprehensive software package for analyzing pulsed ELDOR data, *Appl Magn Reson*, 30 (2006) 473-498.
- [71] A.N. Tikhonov, A. Goncharsky, V.V. Stepanov, A.G. Yagola, *Numerical Methods for the Solution of Ill-Posed Problems*, Springer Netherlands, 1995.
- [72] Yevhen Polyhach and Gunnar Jeschke, MMM_UserManual2015.1, in, ETH Zurich, 2015.
- [73] D. Toledo Warshaviak, V.V. Khramtsov, D. Cascio, C. Altenbach, W.L. Hubbell, Structure and dynamics of an imidazoline nitroxide side chain with strongly hindered internal motion in proteins, *Journal of Magnetic Resonance*, 232 (2013) 53-61.
- [74] N. Alexander, M. Bortolus, A. Al-Mestarihi, H. McHaourab, J. Meiler, De novo high-resolution protein structure determination from sparse spin-labeling EPR data, *Structure*, 16 (2008) 181-195.
- [75] P. Koenig, O. Mirus, R. Haarmann, M.S. Sommer, I. Sinning, E. Schleiff, I. Tews, Conserved Properties of Polypeptide Transport-associated (POTRA) Domains Derived from Cyanobacterial Omp85, *J. Biolog. Chem.*, 285 (2010) 18016-18024.
- [76] B. Clantin, A.-S. Delattre, P. Rucktooa, N. Saint, A.C. Meli, C. Loch, F. Jacob-Dubuisson, V. Villeret, Structure of the membrane protein FhaC: A member of the Omp85-TpsB transporter superfamily, *Science*, 317 (2007) 957-961.
- [77] S. Kim, J.C. Malinverni, P. Sliz, T.J. Silhavy, S.C. Harrison, D. Kahne, Structure and function of an essential component of the outer membrane protein assembly machine, *Science*, 317 (2007) 961-964.
- [78] P.Z. Gatzeva-Topalova, T.A. Walton, M.C. Sousa, Crystal Structure of YaeT: Conformational Flexibility and Substrate Recognition, *Structure*, 16 (2008) 1873-1881.
- [79] D.A. Stroud, T. Becker, J. Qiu, D. Stojanovski, S. Pfannschmidt, C. Wirth, C. Hunte, B. Guiard, C. Meisinger, N. Pfanner, N. Wiedemann, Biogenesis of mitochondrial beta-barrel proteins: the POTRA domain is involved in precursor release from the SAM complex, *Mol Biol Cell*, 22 (2011) 2823-2833.
- [80] F. Ertel, O. Mirus, R. Bredemeier, S. Moslavac, T. Becker, E. Schleiff, The evolutionarily related beta-barrel polypeptide transporters from *Pisum sativum* and *Nostoc PCC7120* contain two distinct functional domains, *J. Biol. Chem.*, 280 (2005) 28281-28289.
- [81] F. Jacob-Dubuisson, V. Villeret, B. Clantin, A.-S. Delattre, N. Saint, First structural insights into the TpsB/Omp85 superfamily, *Biol. Chem.*, 390 (2009) 675-684.

- [82] A. Hahn, M. Stevanovic, O. Mirus, E. Schleiff, The TolC-like protein HgdD of the cyanobacterium *Anabaena* sp. PCC 7120 is involved in secondary metabolite export and antibiotic resistance, *J. Biol. Chem.*, 287 (2012) 41126-41138.
- [83] R. Bredemeier, T. Schlegel, F. Ertel, A. Vojta, L. Borissenko, M.T. Bohnsack, M. Groll, A. Von Haeseler, E. Schleiff, Functional and phylogenetic properties of the pore-forming beta-barrel transporters of the Omp85 family, *J. Biol. Chem.*, 282 (2007) 1882-1890.
- [84] S. Guedin, E. Willery, J. Tommassen, E. Fort, H. Drobecq, C. Locht, F. Jacob-Dubuisson, Novel topological features of FhaC, the outer membrane transporter involved in the secretion of the *Bordetella pertussis* filamentous hemagglutinin, *J. Biol. Chem.*, 275 (2000) 30202-30210.
- [85] L.R. Warner, P.Z. Gatzeva-Topalova, P.A. Doerner, A. Pardi, M.C. Sousa, Flexibility in the Periplasmic Domain of BamA Is Important for Function, *Structure*, 25 (2017) 94-106.
- [86] T. Arnold, K. Zeth, D. Linke, Omp85 from the Thermophilic Cyanobacterium *Thermosynechococcus elongatus* Differs from Proteobacterial Omp85 in Structure and Domain Composition, *J. Biol. Chem.*, 285 (2010) 18003-18015.
- [87] P.Z. Gatzeva-Topalova, L.R. Warner, A. Pardi, M.C. Sousa, Structure and Flexibility of the Complete Periplasmic Domain of BamA: The Protein Insertion Machine of the Outer Membrane, *Structure*, 18 (2010) 1492-1501.
- [88] T. Sinnige, M. Weingarth, M. Renault, L. Baker, J. Tommassen, M. Baldus, Solid-state NMR studies of full-length BamA in lipid bilayers suggest limited overall POTRA mobility, *J Mol Biol*, 426 (2014) 2009-2021.
- [89] T. Sinnige, K. Houben, I. Pritisanic, M. Renault, R. Boelens, M. Baldus, Insight into the conformational stability of membrane-embedded BamA using a combined solution and solid-state NMR approach, *J. Biomol. NMR*, 61 (2015) 321-332.
- [90] L. Han, J. Zheng, Y. Wang, X. Yang, Y. Liu, C. Sun, B. Cao, H. Zhou, D. Ni, J. Lou, Y. Zhao, Y. Huang, Structure of the BAM complex and its implications for biogenesis of outer-membrane proteins, *Nature structural & molecular biology*, 23 (2016) 192-196.
- [91] J. Bakelar, S.K. Buchanan, N. Noinaj, The structure of the β -barrel assembly machinery complex, *Science*, 351 (2016) 180-186.
- [92] Y. Gu, H. Li, H. Dong, Y. Zeng, Z. Zhang, N.G. Paterson, P.J. Stansfeld, Z. Wang, Y. Zhang, W. Wang, C. Dong, Structural basis of outer membrane protein insertion by the BAM complex, *Nature*, 531 (2016) 64-69.
- [93] J. Guérin, N. Saint, C. Baud, A.C. Meli, E. Etienne, C. Locht, H. Vezin, F. Jacob-Dubuisson, Dynamic interplay of membrane-proximal POTRA domain and conserved loop L6 in Omp85 transporter FhaC, *Mol Microbiol*, 98 (2015) 490-501.

- [94] T.J. Knowles, M. Jeeves, S. Bobat, F. Dancea, D. McClelland, T. Palmer, M. Overduin, I.R. Henderson, Fold and function of polypeptide transport-associated domains responsible for delivering unfolded proteins to membranes, *Mol Microbiol*, 68 (2008) 1216-1227.
- [95] R. Ward, M. Zoltner, L. Beer, H. El Mkami, I.R. Henderson, T. Palmer, D.G. Norman, The Orientation of a Tandem POTRA Domain Pair, of the Beta-Barrel Assembly Protein BamA, Determined by PELDOR Spectroscopy, *Structure*, 17 (2009) 1187-1194.
- [96] M. Renault, M.P. Bos, J. Tommassen, M. Baldus, Solid-State NMR on a Large Multidomain Integral Membrane Protein: The Outer Membrane Protein Assembly Factor BamA, *J Am Chem Soc*, 133 (2011) 4175-4177.
- [97] S.O. Merouch, K.Z. Bencze, D. Heseck, M. Lee, J.F. Fisher, T.L. Stemmler, S. Mobashery, Three-dimensional structure of the bacterial cell wall peptidoglycan, *Proc Natl Acad Sci U S A*, 103 (2006) 4404-4409.
- [98] L. Gan, S. Chen, G.J. Jensen, Molecular organization of Gram-negative peptidoglycan, *Proc Natl Acad Sci U S A*, 105 (2008) 18953-18957.
- [99] M. Fussenegger, D. Facius, J. Meier, T.F. Meyer, A novel peptidoglycan-linked lipoprotein (ComL) that functions in natural transformation competence of *Neisseria gonorrhoeae*, *Mol Microbiol*, 19 (1996) 1095-1105.
- [100] E.B. Volokhina, F. Beckers, J. Tommassen, M.P. Bos, The beta-barrel outer membrane protein assembly complex of *Neisseria meningitidis*, *J Bacteriol*, 191 (2009) 7074-7085.
- [101] K. Anwari, S. Poggio, A. Perry, X. Gatsos, S.H. Ramarathinam, N.A. Williamson, N. Noinaj, S. Buchanan, K. Gabriel, A.W. Purcell, C. Jacobs-Wagner, T. Lithgow, A modular BAM complex in the outer membrane of the alpha-proteobacterium *Caulobacter crescentus*, *PLoS One*, 5 (2010) e8619.
- [102] M. Leduc, C. Fréhel, E. Siegel, J. Van Heijenoort, Multilayered Distribution of Peptidoglycan in the Periplasmic Space of *Escherichia coli*, *Microbiology*, 135 (1989) 1243-1254.
- [103] T.J. Beveridge, Structures of gram-negative cell walls and their derived membrane vesicles, *J Bacteriol*, 181 (1999) 4725-4733.
- [104] L. Wilk, M. Strauss, M. Rudolf, K. Nicolaisen, E. Flores, W. Kuhlbrandt, E. Schleiff, Outer membrane continuity and septosome formation between vegetative cells in the filaments of *Anabaena* sp. PCC 7120, *Cell Microbiol*, 13 (2011) 1744-1754.
- [105] V.R. Matias, A. Al-Amoudi, J. Dubochet, T.J. Beveridge, Cryo-transmission electron microscopy of frozen-hydrated sections of *Escherichia coli* and *Pseudomonas aeruginosa*, *J Bacteriol*, 185 (2003) 6112-6118.

- [106] M.P. Williamson, The structure and function of proline-rich regions in proteins, *Biochem J*, 297 (Pt 2) (1994) 249-260.
- [107] C.M. Pickart, D. Fushman, Polyubiquitin chains: polymeric protein signals, *Current opinion in chemical biology*, 8 (2004) 610-616.
- [108] D. Komander, M. Rape, The ubiquitin code, *Annu Rev Biochem*, 81 (2012) 203-229.
- [109] C. Alfano, S. Faggiano, A. Pastore, The Ball and Chain of Polyubiquitin Structures, *Trends Biochem Sci*, 41 (2016) 371-385.
- [110] D. Finley, S. Sadis, B.P. Monia, P. Boucher, D.J. Ecker, S.T. Crooke, V. Chau, Inhibition of proteolysis and cell cycle progression in a multiubiquitination-deficient yeast mutant, *Molecular and Cellular Biology*, 14 (1994) 5501-5509.
- [111] A. Hershko, A. Ciechanover, The ubiquitin system, *Annu Rev Biochem*, 67 (1998) 425-479.
- [112] J.S. Thrower, L. Hoffman, M. Rechsteiner, C.M. Pickart, Recognition of the polyubiquitin proteolytic signal, *EMBO J*, 19 (2000) 94-102.
- [113] K. Flick, I. Ouni, J.A. Wohlschlegel, C. Capati, W.H. McDonald, J.R. Yates, P. Kaiser, Proteolysis-independent regulation of the transcription factor Met4 by a single Lys 48-linked ubiquitin chain, *Nat Cell Biol*, 6 (2004) 634-641.
- [114] D.D. Boehr, R. Nussinov, P.E. Wright, The role of dynamic conformational ensembles in biomolecular recognition, *Nat Chem Biol*, 5 (2009) 789-796.
- [115] W.J. Cook, L.C. Jeffrey, M. Carson, Z. Chen, C.M. Pickart, Structure of a diubiquitin conjugate and a model for interaction with ubiquitin conjugating enzyme (E2), *The Journal of biological chemistry*, 267 (1992) 16467-16471.
- [116] A.D. van Dijk, D. Fushman, A.M. Bonvin, Various strategies of using residual dipolar couplings in NMR-driven protein docking: application to Lys48-linked di-ubiquitin and validation against ¹⁵N-relaxation data, *Proteins*, 60 (2005) 367-381.
- [117] Y. Ryabov, D. Fushman, Interdomain mobility in di-ubiquitin revealed by NMR, *Proteins*, 63 (2006) 787-796.
- [118] Y. Ryabov, D. Fushman, Structural Assembly of Multidomain Proteins and Protein Complexes Guided by the Overall Rotational Diffusion Tensor, *J Am Chem Soc*, 129 (2007) 7894-7902.
- [119] J.F. Trempe, N.R. Brown, M.E. Noble, J.A. Endicott, A new crystal form of Lys48-linked diubiquitin, *Acta Crystallogr Sect F Struct Biol Cryst Commun*, 66 (2010) 994-998.

- [120] T. Hirano, O. Serve, M. Yagi-Utsumi, E. Takemoto, T. Hiromoto, T. Satoh, T. Mizushima, K. Kato, Conformational dynamics of wild-type Lys-48-linked diubiquitin in solution, *The Journal of biological chemistry*, 286 (2011) 37496-37502.
- [121] M.Y. Lai, D. Zhang, N. Laronde-Leblanc, D. Fushman, Structural and biochemical studies of the open state of Lys48-linked diubiquitin, *Biochim Biophys Acta*, 1823 (2012) 2046-2056.
- [122] H. McHaourab, M.A. Lietzow, K. Hideg, W.L. Hubbell, Motion of spin-labeled side chains in T4 lysozyme. Correlation with protein structure and dynamics, *Biochemistry*, 35 (1996) 7692-7704.
- [123] H.S. McHaourab, T. Kálai, K. Hideg, W.L. Hubbell, Motion of Spin-Labeled Side Chains in T4 Lysozyme: Effect of Side Chain Structure, *Biochemistry*, 38 (1999) 2947-2955.
- [124] G. Jeschke, Conformational dynamics and distribution of nitroxide spin labels, *Progress in nuclear magnetic resonance spectroscopy*, 72 (2013) 42-60.
- [125] I. Dikic, S. Wakatsuki, K.J. Walters, Ubiquitin-binding domains - from structures to functions, *Nat Rev Mol Cell Biol*, 10 (2009) 659-671.
- [126] W.J. Cook, L.C. Jeffrey, E. Kasperek, C.M. Pickart, Structure of Tetraubiquitin Shows How Multiubiquitin Chains Can Be Formed, *J. Mol. Biol.*, 236 (1994) 601-609.
- [127] C.L. Phillips, J. Thrower, C.M. Pickart, C.P. Hill, Structure of a new crystal form of tetraubiquitin, *Acta Crystallogr D Biol Crystallogr*, 57 (2001) 341-344.
- [128] R. Varadan, M. Assfalg, S. Raasi, C. Pickart, D. Fushman, Structural Determinants for Selective Recognition of a Lys48-Linked Polyubiquitin Chain by a UBA Domain, *Molecular Cell*, 18 (2005) 687-698.
- [129] M.J. Eddins, R. Varadan, D. Fushman, C.M. Pickart, C. Wolberger, Crystal structure and solution NMR studies of Lys48-linked tetraubiquitin at neutral pH, *J Mol Biol*, 367 (2007) 204-211.
- [130] S. Liu, Y. Chen, J. Li, T. Huang, S. Tarasov, A. King, Allan M. Weissman, R.A. Byrd, R. Das, Promiscuous Interactions of gp78 E3 Ligase CUE Domain with Polyubiquitin Chains, *Structure*, 20 (2012) 2138-2150.
- [131] M. von Delbrück, A. Kniss, V.V. Rogov, L. Pluska, K. Bagola, F. Lohr, P. Guntert, T. Sommer, V. Dotsch, The CUE Domain of Cue1 Aligns Growing Ubiquitin Chains with Ubc7 for Rapid Elongation, *Mol Cell*, 62 (2016) 918-928.
- [132] R.S. Kang, C.M. Daniels, S.A. Francis, S.C. Shih, W.J. Salerno, L. Hicke, I. Radhakrishnan, Solution structure of a CUE-ubiquitin complex reveals a conserved mode of ubiquitin binding, *Cell*, 113 (2003) 621-630.

[133] K. Husnjak, I. Dikic, Ubiquitin-binding proteins: decoders of ubiquitin-mediated cellular functions, *Annu Rev Biochem*, 81 (2012) 291-322.

[134] P. Schreiner, X. Chen, K. Husnjak, L. Randles, N. Zhang, S. Elsassser, D. Finley, I. Dikic, K.J. Walters, M. Groll, Ubiquitin docking at the proteasome through a novel pleckstrin-homology domain interaction, *Nature*, 453 (2008) 548-552.

[135] K. Husnjak, S. Elsassser, N. Zhang, X. Chen, L. Randles, Y. Shi, K. Hofmann, K.J. Walters, D. Finley, I. Dikic, Proteasome subunit Rpn13 is a novel ubiquitin receptor, *Nature*, 453 (2008) 481-488.

[136] D. Komander, M.J. Clague, S. Urbe, Breaking the chains: structure and function of the deubiquitinases, *Nat Rev Mol Cell Biol*, 10 (2009) 550-563.

[137] Y. Ye, G. Blaser, M.H. Horrocks, M.J. Ruedas-Rama, S. Ibrahim, A.A. Zhukov, A. Orte, D. Klenerman, S.E. Jackson, D. Komander, Ubiquitin chain conformation regulates recognition and activity of interacting proteins, *Nature*, 492 (2012) 266-270.

[138] T. Satoh, E. Sakata, S. Yamamoto, Y. Yamaguchi, A. Sumiyoshi, S. Wakatsuki, K. Kato, Crystal structure of cyclic Lys48-linked tetraubiquitin, *Biochem Biophys Res Commun*, 400 (2010) 329-333.

[139] D. Fushman, O. Walker, Exploring the linkage dependence of polyubiquitin conformations using molecular modeling, *J Mol Biol*, 395 (2010) 803-814.

[140] M.H. Glickman, A. Ciechanover, The Ubiquitin-Proteasome Proteolytic Pathway: Destruction for the Sake of Construction, *Physiol. Rev.*, 82 (2002) 373-428.

[141] C.M. Pickart, Mechanisms Underlying Ubiquitination, *Ann. Rev. Biochem.*, 70 (2001) 503-533.

[142] M.D. Petroski, R.J. Deshaies, Mechanism of lysine 48-linked ubiquitin-chain synthesis by the cullin-RING ubiquitin-ligase complex SCF-Cdc34, *Cell*, 123 (2005) 1107-1120.

[143] M.J. Eddins, C.M. Carlile, K.M. Gomez, C.M. Pickart, C. Wolberger, Mms2-Ubc13 covalently bound to ubiquitin reveals the structural basis of linkage-specific polyubiquitin chain formation, *Nature structural & molecular biology*, 13 (2006) 915-920.

[144] S. Rahighi, I. Braunstein, N. Ternette, B. Kessler, M. Kawasaki, R. Kato, T. Matsui, Thomas M. Weiss, A. Stanhill, S. Wakatsuki, Selective Binding of AIRAPL Tandem UIMs to Lys48-Linked Tri-Ubiquitin Chains, *Structure*, 24 (2016) 412-422.

[145] K.N. Swatek, D. Komander, Ubiquitin modifications, *Cell Res.*, 26 (2016) 399-422.

[146] K.E. Wickliffe, S. Lorenz, D.E. Wemmer, J. Kuriyan, M. Rape, The mechanism of linkage-specific ubiquitin chain elongation by a single-subunit E2, *Cell*, 144 (2011) 769-781.

- [147] T. Tenno, K. Fujiwara, H. Tochio, K. Iwai, E.H. Morita, H. Hayashi, S. Murata, H. Hiroaki, M. Sato, K. Tanaka, M. Shirakawa, Structural basis for distinct roles of Lys63- and Lys48-linked polyubiquitin chains, *Genes Cells*, 9 (2004) 865-875.
- [148] Meredith B. Metzger, Y.-H. Liang, R. Das, J. Mariano, S. Li, J. Li, Z. Kostova, R.A. Byrd, X. Ji, Allan M. Weissman, A Structurally Unique E2-Binding Domain Activates Ubiquitination by the ERAD E2, Ubc7p, through Multiple Mechanisms, *Molecular Cell*, 50 (2013) 516-527.
- [149] K. Bagola, M. von Delbrück, G. Dittmar, M. Scheffner, I. Ziv, Michael H. Glickman, A. Ciechanover, T. Sommer, Ubiquitin Binding by a CUE Domain Regulates Ubiquitin Chain Formation by ERAD E3 Ligases, *Molecular Cell*, 50 (2013) 528-539.
- [150] S. Raasi, C.M. Pickart, Rad23 ubiquitin-associated domains (UBA) inhibit 26 S proteasome-catalyzed proteolysis by sequestering lysine 48-linked polyubiquitin chains, *The Journal of biological chemistry*, 278 (2003) 8951-8959.
- [151] S. Raasi, I. Orlov, K.G. Fleming, C.M. Pickart, Binding of Polyubiquitin Chains to Ubiquitin-associated (UBA) Domains of HHR23A, *J. Mol. Biol.*, 341 (2004) 1367-1379.
- [152] E. Sakata, S. Bohn, O. Mihalache, P. Kiss, F. Beck, I. Nagy, S. Nickell, K. Tanaka, Y. Saeki, F. Förster, W. Baumeister, Localization of the proteasomal ubiquitin receptors Rpn10 and Rpn13 by electron cryomicroscopy, *Proceedings of the National Academy of Sciences*, 109 (2012) 1479-1484.
- [153] J. Hamazaki, S. Hirayama, S. Murata, Redundant Roles of Rpn10 and Rpn13 in Recognition of Ubiquitinated Proteins and Cellular Homeostasis, *PLOS Genetics*, 11 (2015) e1005401.
- [154] Y. Zhang, L. Vukovic, T. Rudack, W. Han, K. Schulten, Recognition of Poly-Ubiquitins by the Proteasome through Protein Refolding Guided by Electrostatic and Hydrophobic Interactions, *J Phys Chem B*, 120 (2016) 8137-8146.
- [155] Y.C. Juang, M.C. Landry, M. Sanches, V. Vittal, C.C. Leung, D.F. Ceccarelli, A.R. Mateo, J.N. Pruneda, D.Y. Mao, R.K. Szilard, S. Orlicky, M. Munro, P.S. Brzovic, R.E. Klevit, F. Sicheri, D. Durocher, OTUB1 co-opts Lys48-linked ubiquitin recognition to suppress E2 enzyme function, *Mol Cell*, 45 (2012) 384-397.
- [156] R. Wiener, X. Zhang, T. Wang, C. Wolberger, The mechanism of OTUB1-mediated inhibition of ubiquitination, *Nature*, 483 (2012) 618-622.
- [157] M.J. Lee, B.H. Lee, J. Hanna, R.W. King, D. Finley, Trimming of ubiquitin chains by proteasome-associated deubiquitinating enzymes, *Mol Cell Proteomics*, 10 (2011) R110 003871.
- [158] C.M. Pickart, S. Raasi, Controlled synthesis of polyubiquitin chains, *Methods Enzymol*, 399 (2005) 21-36.

- [159] W. Mansour, M.A. Nakasone, M. von Delbruck, Z. Yu, D. Krutauz, N. Reis, O. Kleifeld, T. Sommer, D. Fushman, M.H. Glickman, Disassembly of Lys11 and mixed linkage polyubiquitin conjugates provides insights into function of proteasomal deubiquitinases Rpn11 and Ubp6, *The Journal of biological chemistry*, 290 (2015) 4688-4704.
- [160] C.E. Berndsen, C. Wolberger, A spectrophotometric assay for conjugation of ubiquitin and ubiquitin-like proteins, *Anal Biochem*, 418 (2011) 102-110.
- [161] T.E. Mevissen, M.K. Hospenthal, P.P. Geurink, P.R. Elliott, M. Akutsu, N. Arnaudo, R. Ekkebus, Y. Kulathu, T. Wauer, F. El Oualid, S.M. Freund, H. Ovaa, D. Komander, OTU deubiquitinases reveal mechanisms of linkage specificity and enable ubiquitin chain restriction analysis, *Cell*, 154 (2013) 169-184.
- [162] K.C. Dong, E. Helgason, C. Yu, L. Phu, D.P. Arnott, I. Bosanac, D.M. Compaan, O.W. Huang, A.V. Fedorova, D.S. Kirkpatrick, S.G. Hymowitz, E.C. Dueber, Preparation of distinct ubiquitin chain reagents of high purity and yield, *Structure*, 19 (2011) 1053-1063.
- [163] G. Jeschke, Y. Polyhach, Distance measurements on spin-labelled biomacromolecules by pulsed electron paramagnetic resonance, *Phys Chem Chem Phys*, 9 (2007) 1895-1910.
- [164] Y. Polyhach, E. Bordignon, R. Tschaggelar, S. Gandra, A. Godt, G. Jeschke, High sensitivity and versatility of the DEER experiment on nitroxide radical pairs at Q-band frequencies, *Phys Chem Chem Phys*, 14 (2012) 10762-10773.
- [165] P.E. Spindler, Y. Zhang, B. Endeward, N. Gershernzon, T.E. Skinner, S.J. Glaser, T.F. Prisner, Shaped optimal control pulses for increased excitation bandwidth in EPR, *J Magn Reson*, 218 (2012) 49-58.
- [166] E. Krieger, G. Vriend, YASARA View - molecular graphics for all devices - from smartphones to workstations, *Bioinformatics*, 30 (2014) 2981-2982.
- [167] M.D. Tyka, D.A. Keedy, I. Andre, F. Dimairo, Y. Song, D.C. Richardson, J.S. Richardson, D. Baker, Alternate states of proteins revealed by detailed energy landscape mapping, *J Mol Biol*, 405 (2011) 607-618.
- [168] A. Patriksson, D. van der Spoel, A temperature predictor for parallel tempering simulations, *Phys Chem Chem Phys*, 10 (2008) 2073-2077.
- [169] Y. Duan, C. Wu, S. Chowdhury, M.C. Lee, G. Xiong, W. Zhang, R. Yang, P. Cieplak, R. Luo, T. Lee, J. Caldwell, J. Wang, P. Kollman, A point-charge force field for molecular mechanics simulations of proteins based on condensed-phase quantum mechanical calculations, *J Comput Chem*, 24 (2003) 1999-2012.
- [170] S. Páll, B. Hess, A flexible algorithm for calculating pair interactions on SIMD architectures, *Comput. Phys. Commun.*, 184 (2013) 2641-2650.

- [171] U. Essmann, L. Perera, M.L. Berkowitz, T. Darden, H. Lee, L.G. Pedersen, A smooth particle mesh Ewald method, *J. Chem. Phys.*, 103 (1995) 8577-8593.
- [172] G. Bussi, D. Donadio, M. Parrinello, Canonical sampling through velocity rescaling, *J. Chem. Phys.*, 126 (2007) 014101.
- [173] M. Parrinello, A. Rahman, Polymorphic transitions in single crystals: A new molecular dynamics method, *J. Appl. Phys.*, 52 (1981) 7182-7190.
- [174] S. Nosé, M.L. Klein, Constant pressure molecular dynamics for molecular systems, *Mol. Phys.*, 50 (1983) 1055-1076.
- [175] J.J. Stewart, MOPAC: a semiempirical molecular orbital program, *J Comput Aided Mol Des*, 4 (1990) 1-105.
- [176] E. Krieger, J.E. Nielsen, C.A.E.M. Spronk, G. Vriend, Fast empirical pKa prediction by Ewald summation, *J. Mol. Graph. Model.*, 25 (2006) 481-486.

List of Amino Acids

Amino Acid	Three letter code	One letter code
Alanine	Ala	A
Arginine	Arg	R
Asparagine	Asn	N
Aspartic Acid	Asp	D
Cysteine	Cys	C
Glutamic acid	Glu	E
Glutamine	Gln	Q
Isoleucine	Ile	I
Leucine	Leu	L
Lysine	Lys	K
Serine	Ser	S
Threonine	Trp	T
Valine	Val	V

List of Figures

Chapter: 1

Figure 1.1: SDSL scheme of an EPR active label. 3

Chapter 2:

Figure 2.1: Electron-Zeeman splitting of the energy levels of an electron spin within a magnetic field. 7

Figure 2.2: Interactions of the electron spin $S = 1/2$ in a nitroxide radical with the nuclear spin I of ^{14}N ($I=1$). 9

Figure 2.3: Anisotropic CW EPR spectrum of the nitroxide spin label MTSSL attached to a protein. 10

Figure 2.4: The effect of the dipolar coupling between two electron spins A and B. 12

Figure 2.5: Dead-time free 4-pulse PELDOR sequence. 13

Figure 2.6: 7-pulse CP PELDOR sequence. 16

Figure 2.7: Conventional PELDOR data analysis: Left: Primary PELDOR time trace. 18

Figure 2.8: The five torsion angles (χ_1 - χ_5) of the MTSSL side chain. 22

Chapter 3:

Figure 3.1: Ribbon representation of 3MC8 indicating the spin labelled residues. 24

Figure 3.2: Comparison of intra-POTRA domain PELDOR time traces generated by MMM and MtsslWizard with experimental traces. 26

Figure 3.3: Comparison of experimentally obtained intra-POTRA domain distance distributions with distributions generated by MMM and MtsslWizard. 27

Figure 3.4: Cartoon representation of 3MC8 indicating the spin labelled residues in each domain for the inter-domain variants. 29

Figure 3.5: Comparison of inter-POTRA domain PELDOR time traces for *anaP3* and *anaP2* generated by MMM and MtsslWizard with the experimental traces. 30

Figure 3.6: Comparison of inter-POTRA domain distance distributions for *anaP3* and *anaP2* generated by MMM and MtsslWizard with experimental distance distributions. 31

Figure 3.7: Comparison of inter-POTRA domain PELDOR time traces for *anaP1* and *anaP2* generated by MMM and MtsslWizard with experimental traces. 31

Figure 3.8 Comparison of inter-POTRA domain PELDOR distance distributions for <i>anaP1</i> and <i>anaP2</i> generated by MMM and MtsslWizard with experimental traces.	34
Figure 3.9: Comparison of inter-POTRA domain time traces and distance distributions for <i>anaP3</i> and <i>anaP1</i> generated by MMM and MtsslWizard with the experimental data.	35
Figure 3.10: Comparison of experimental and simulated intra-molecular distance distributions from MD and the X-ray structure 3MC8.	38
Figure 3.11: Comparison of experimental and simulated intra-molecular dipolar evolution functions from MD and 3MC8.	39
Figure 3.12: Illustration of the rigid body refinement.	41
Figure 3.13: Comparison of experimental (grey) and simulated intra-molecular distance distributions from the rigid body refinement for all inter-POTRA domain restraints.	42
Figure 3.14: Comparison of experimental (grey) and simulated intramolecular dipolar evolution functions from the rigid body refinement for all inter-POTRA domain restraints.	43
Figure 3.15: Comparison of the orientational space of pairs of <i>anaOmp85</i> -POTRA domains obtained by MD simulations of spin labelled POTRA domains and REMD simulations to models obtained from structure refinements using the experimental PELDOR distance restraints.	46
Figure 3.16: Putative orientation of the <i>anaOmp85</i> POTRA domains to the β -barrel and integration into the cellular environment.	50
Figure 3.17: Spin label flexibility in doubly spin labelled Cys-variants in monoubiquitin.	52
Figure 3.18: Experimental PELDOR Data for five K48-linked diubiquitin variants.	53
Figure 3.19: Comparison of the experimental inter-ubiquitin distance distributions for various diubiquitin variants to distance distributions generated by MMM2015.2 [38] in 298K mode.	54
Figure 3.20: Analysis of the conformational space of K48-linked diubiquitin.	56
Figure 3.21: The effect of ubiquitin binding domains (UBDs) and deubiquitinating enzymes (DUBs) on the conformational flexibility of diubiquitin.	58
Figure 3.22: The effect of Cue1 on the conformational space of K48-linked diubiquitin.	60
Figure 3.23 Investigation of Cue1 binding deficient pE24C/dA28C K48-linked diubiquitin variants.	61
Figure 3.24: Equilibrium binding model for diubiquitin using two independent Cue1 binding sites.	62
Figure 3.25: The Effect of OTUB1i on the conformational space of K48-linked diubiquitin.	64
Figure 3.26: Conformational flexibility of K48-linked polyubiquitin chains.	65

Figure 3.27: PELDOR distance restraints indicated on the X-ray structure of tetraubiquitin (2O6V).....	67
Figure 3.28 Conformational flexibility of K48-linked polyubiquitin chains.	68
Figure 3.29: Influence of chain length and diubiquitin position within a chain on the conformational flexibility of diubiquitin.	69
Figure 3.30: The effect of different UBDs and a DUB on the conformational flexibility of K48-linked tri- and tetraubiquitin chains.....	71
Figure 3.31: Ribbon representation of the X-ray structure 1UBQ of monoubiquitin.	72

Chapter 6:

Figure 6. 1: Q-band calibration.....	91
Figure 6.2: Experimental results on intra-POTRA domain restraints.	92
Figure 6.3: cw EPR spectrum of the single-Cys variant V370C in <i>anaP2</i>	93
Figure 6.4: The X-ray structure of the three <i>anaOmp85</i> POTRA domains, indicating the spin labelled residues in each domain for the inter-domain residues.....	93
Figure 6.5: Experimental PELDOR data on inter-POTRA domain restraints.	94
Figure 6.6: Inter-POTRA domain distance distributions obtained by Tikhonov.	95
Figure 6.7: Orientation selectivity test for the inter-POTRA domain variant I292C/V370C. .	95
Figure 6.8: Comparison of experimental (grey) and simulated intra-molecular distance distributions from the rigid body and Rosetta refinement for all inter-POTRA domain restraints.	96
Figure 6.9: Comparison of experimental (grey) and simulated intramolecular dipolar evolution functions from the rigid body and Rosetta refinement for all inter-POTRA domain restraints.	97
Figure 6.10: Comparison of experimental intra-molecular distance distributions for all inter-POTRA domain restraints in comparison to distributions obtained via MD or REMD simulations.....	98
Figure 6.11: Orientational space of <i>anaOmp85</i> POTRA domains of wildtype Alr2269 sampled by REMD simulations in comparison to structure refinement.	99
Figure 6.12: Hahn Echo experiment for the determination of T_M	102
Figure 6.13: Structure of diubiquitin.	102
Figure 6.14: Modelling of the conformational space of K48-linked diubiquitin.	103

Figure 6.15: Modelling of the conformational space of K48-linked diubiquitin in complex with the CUE domain of Cue1.	104
Figure 6.16: Primary 4-pulse PELDOR Data for the Cue1 binding deficient pE24C/dA28C K48-linked diubiquitin variants.	105
Figure 6.17: Modelling of the conformational space of K48-linked diubiquitin in complex with OTUB1i.	106
Figure 6.18: Analysis of 4-pulse PELDOR on doubly spin labelled tri- and tetraubiquitin variants pE24C/dA28C using different intermolecular decay functions.	107
Figure 6.19: Primary 7-pulse CP PELDOR Data.	108
Figure 6.20: Primary PELDOR Data for the effect of chain elongation.	109
Figure 6.21: The effect of pH on the conformational space of di- and tetraubiquitin.	109
Figure 6.22: Primary 7-pulse CP PELDOR Data for the effect of Cue1, gp78CUE and OUTB1i on the conformational space on tri- and tetraubiquitin.	110

List of Tables

Chapter 3:

Table 3.1: Deviation factor DF (Eq. 3.1) of the experimental and predicted distance distributions from different rotamer libraries for all intra-POTRA domain variants (N=7).	28
Table 3.2: Deviation factor DF (Eq. 3.1) of the experimental and predicted distance distributions from different rotamer libraries for all inter-POTRA domain variants (N=20).	36
Table 3.3 Comparison of the deviation factor (DF; Eq. 3.1) of the distance distributions predicted for different rotamer libraries and the refined distributions for all inter-POTRA domain variants (N=20).	44

Chapter 6:

Table 6.1: Comparison of simulated mean distances $\langle r \rangle$ obtained for different rotamer libraries on the basis of the X-ray structure 3MC8.	100
Table 6.2: Comparison of mean distance $\langle r \rangle$ of the PELDOR restraints with the X-ray structure, MD simulations of <i>in silico</i> -spin labelled <i>anaOmp85</i> POTRA domains and the best refined model of either rigid body or Rosetta refinement.	101
Table 6.3: Fitting parameters for data analysis with Gaussian model fits.	111